ABSTRACT

Title of Dissertation: IDENTIFICATION AND QUANTIFICATION OF REGIONAL AEROSOL TRENDS AND IMPACT ON CLOUDS OVER THE NORTH ATLANTIC OCEAN

Andrew R. Jongeward, Doctor of Philosophy, 2017

Directed by: Professor Zhanqing Li
Department of Atmospheric and Oceanic Science (AOSC)
and Earth System Science Interdisciplinary Center (ESSIC)

Aerosols and clouds contribute to atmospheric variability and Earth's radiative balance across local, regional, and global scales. Originating from both natural and anthropogenic sources, aerosols can cause adverse health effects and can interact directly with solar radiation as well as indirectly through complex interactions with clouds. Aerosol optical depth (AOD) has been observed from satellite platforms for over 30 years. During this time, regional changes in emissions, arising from air quality policies and socioeconomic factors, have been suggested as causes for some observed AOD trends. In the United States, the Clean Air Act and amendments have produced improvements in air quality. In this work the impacts of improved air quality on the aerosol loading and aerosol direct and indirect effects over the North Atlantic Ocean are

explored using satellite, ground, and model datasets on the monthly timescale during 2002 to 2012.

It is established that two trends exist in the total AOD observed by MODIS over the North Atlantic. A decreasing AOD trend between −0.02 and −0.04 per decade is observed over the mid-latitude region. Using the GOCART aerosol model it is shown that this trend results from decreases in anthropogenic species. Ground based aerosol networks (AERONET and IMPROVE) support a decreasing trend in AOD and further strengthen links to anthropogenic aerosol species, particularly sulfate species. This anthropogenic decrease occurs primarily during spring and summer. During the same time period, MODIS also observes an increasing AOD trend of 0.02 per decade located in the sub-tropical region. This trend is shown to occur during summer and is the result of natural dust aerosol. Changes in the North African environment seen in the MERRA reanalysis suggest an accelerated warming over the Saharan Desert leads to changes in the African Easterly Jet, related Easterly Waves, and baroclinicity playing a role in an increase and northward shift in African dust.

Both the direct and indirect impacts of the aerosol trends are investigated. Using the SBDART radiative transfer model, estimates of the shortwave direct radiative forcing are calculated. The decrease in anthropogenic AOD produces an increase of 2.0 ± 0.3 W/m^2 per decade in the Earth-system absorbance over the mid-latitude site (37.5ºN, −68.5ºE). The increase in natural AOD results in a decrease of −1.1 ± 0.2 W/m^2 per decade in the Earth-system absorbance over the sub-tropical site (23.5ºN, −55.5ºE).

Evaluation of the first indirect effect demonstrates agreement with Twomey theory when considering the North Atlantic domain on the whole. A regional analysis reveals the existence of counter-Twomey behavior along the U.S. Atlantic coast. Using a daily dataset during summertime with focus on warm, non-precipitating clouds, it is found that aerosol-cloud interaction in this coastal region is sensitive to vertical velocity and aerosol size. Cases experiencing updrafts ($\omega < 0$ Pa/s) and cases of mainly coarse-mode aerosol demonstrate good agreement with Twomey theory. Additionally, cases with low specific humidity near the cloud base show non-Twomey behavior for clouds with low liquid water path.

IDENTIFICATION AND QUANTIFICATION OF REGIONAL AEROSOL TRENDS AND IMPACT ON CLOUDS OVER THE NORTH ATLANTIC OCEAN

By

Andrew R. Jongeward

Dissertation submitted to the Faculty of the Graduate School of the
University of Maryland, College Park, Maryland, USA
In partial fulfillment of the requirements of the degree of
Doctor of Philosophy
2017

Advisory Committee:
Professor Zhanqing Li, Chair/Advisor
Professor Russell Dickerson
Professor Shunlin Liang
Professor Ross Salawitch
Dr. Jack Xiong (NASA)

Dedication

To my family and friends -- thank you for keeping me on an even-keel.

Acknowledgements

First, I must express my sincere gratitude and thanks to my advisor Dr. Zhanqing Li for his continued support, advice, questions, and patience throughout this study. He has provided much encouragement and direction for my research as well as helped to improve and revise this thesis. I also must acknowledge my committee members: Drs. Dickerson, Salawitch, Xiong, and Liang. Thank you for your patience and involvement with both my research and development as a scientist. Your feedback and probing has added to the depth of this study. I also must thank the Earth System Science Interdisciplinary Center (ESSIC) at the University of Maryland, who's funding through the ESSIC-NASA master grant supported me throughout this research.

I would also like to thank numerous members of the atmospheric/climate community and my peers for their help, advice, discussion, direction, and friendship. These people include (but are not limited to): Dr. Rob Levy, Dr. Danny Rosenfeld, Dr. Bill Lau, Dr. Derek Posselt, Dr. Hao He, and Ms. Maureen Cribb. Conversations with you have spurred new thoughts and perspectives on my research as well as provided mentorship over my own development. To Pat Kablick, Youtong Zheng, and Jungbin Mok: thank you for being a sounding board, offering suggestions, and being friendly and open peers. Thank you to those involved (past and present) in Dr. Li's research group who have provided feedback during this work. Additionally, I would like to thank all the data product scientists and providers for access to their data products used in this work. Finally, I am grateful to the staff within AOSC and ESSIC, who make the professors, scientists, and students' lives easier.

My deepest thanks and gratitude are extended to my family and friends. To my parents, Bob and Barb: I cannot thank you enough for the love and support you have unconditionally and unselfishly given me in so many ways throughout my life and my studies. It is without hesitation that I say I would not be here today without you. To my sisters, Sarah and Katy: thank you for your love and conversation from afar and your company during our visits throughout the years. It is a joy to watch your own families continuing to grow. I thank my friends both near and far for the jokes we share, beers we drink, and experiences we make. I extend a profound appreciation to Adam, Steve, and Bogus: your friendship, constant contact, texts, banter, and nights of unwinding have helped keep me focused and of sound mind. Finally, I must thank my dog, Rossby. Your presence at the beginning and end of each day cannot be appreciated enough.

Finally, I must acknowledge those that came before me, as my contributions were only possible by standing on their shoulders.

Table of Contents

Dedication ii
Acknowledgements iii
Table of Contents v
List of Tables viii
List of Figures x
List of Acronyms and Symbols xviii

Chapter 1: Introduction 1
1.1 Motivation 1
1.2 Background on Aerosols 3
1.2.1 Aerosol Composition 3
1.2.2 Forward Radiative Transfer 7
1.2.3 Aerosol Remote Sensing 9
1.3 Aerosol Influences 13
1.3.1 Long-term AOD Trends 13
1.3.2 Aerosol Direct Effects 15
1.3.3 Aerosol Indirect Effects 18
1.3.4 Aerosol Impacts on Humans and Legislation 21
1.4 Objectives and Outline 24

Chapter 2: Data and Methods 27
2.1 Observational Datasets 27
2.1.1 Moderate Resolution Imaging Spectroradiometer (MODIS) 27
2.1.2 Aerosol Robotic Network (AERONET) 30
2.1.3 Interagency Monitoring of Protected Visual Environments (IMPROVE) network 31
2.1.4 Clouds and the Earth's Radiant Energy System (CERES) 32
2.2 Model Datasets 33
2.2.1 Modern Era-Retrospective Analysis for Research and Applications (MERRA) 33
2.2.2 Goddard Chemistry and Aerosol Radiation and Transport (GOCART) model 34
2.2.3 Santa Barbara DISORT Atmospheric Radiative Transfer (SBDART) model 37
2.3 Methods of Analysis 39
2.3.1 Deseasonalizing and Trending 39
2.3.2 Dust/Anthropogenic Estimation Following Kaufman et al. (2005a,b) 42
2.3.3 Direct Effect – Attenuation of Radiation 45
2.3.4 First Indirect (Twomey) Effect – Aerosol-Cloud Interaction (ACI) 48

Chapter 3: Decreasing Aerosol Trend over the Mid-latitude North Atlantic Ocean 53
3.1 Aerosol Trends and Correlation with AERONET 54
3.2 GOCART Species Aerosol Trends 59
3.3 IMPROVE Surface Particulate Matter (PM) Trends 62
3.4 Seasonality of Aerosol Trends 66
3.5 Chapter 3 Summary 72

Chapter 4: Increasing Aerosol Trend over the Sub-tropical North Atlantic Ocean 74
4.1 Identification as Dust Aerosol 75
4.2 Trends in Dust Mass Loading and Mass Flux 78
4.3 Potential Causes for Observed Dust Trends 82
4.3.1 Short-term Changes in the North African Environment 82
4.3.2 Analysis of AEJ Potential Vorticity 90
4.3.3 Possible Linkage to Decreasing Anthropogenic AOD via Atlantic SST 96
4.4 Chapter 4 Summary 100

Chapter 5: Direct Effect of Aerosol Trends 101
5.1 Aerosol DRF Example 101
5.2 SBDART Inputs – Setup for Various Simulations 105
5.2.1 Deciding on Clear Sky 107
5.2.2 Supplementary Aerosol Properties 110
5.3 Total Aerosol DRFs 111
5.4 Anthropogenic Aerosol DRFs 115
5.4.1 Using K05 and GCT for τ_{NAT} 115
5.4.2 Estimating "natural" SSA(λ), g(λ), and AE(λ) 121
5.4.3 Adjusted for Daytime 125
5.5 Assessing Trend Uncertainty 131
5.5.1 Assumed Atmosphere/Aerosol Properties 131
5.5.2 Applying Flux Uncertainty and Determining a Range for Trends 133
5.6 Chapter 5 Summary 137

Chapter 6: First Indirect (Twomey) Effect of Aerosol Load 139
6.1 ACI Analysis with Monthly Mean Data 140
6.1.1 Domain-wide ACI Analysis 140
6.1.2 Local 3º x 3º ACI Analysis 143
6.1.3 Discussion 145
6.2 ACI Analysis with Daily Mean Data 150
6.2.1 Overview of Parameter PDFs 151

6.2.2 Aerosol and Cloud Correlations with Environmental Factors 154
6.2.3 Summertime ACI from Daily Data 157
6.2.3.1 ACI Using AOD versus AI as CCN Proxy 157
6.2.3.2 ACI Based on ω Regime 160
6.2.3.3 ACI Based on LTS Regime 162
6.2.3.4 ACI Based on Specific Humidity Regime 165
6.2.3.5 ACI Based on FMF Regime 167
6.3 Chapter 6 Summary 170

Chapter 7: Conclusions and Future Work 172
7.1 Summary of Results 172
7.2 Limitations to Present Work 176
7.3 Recommendations for Future Work 177

References 181

List of Tables

Table	Description	Page
Table 2.1	Parameters of the inst(3/U)_3D_asm_Cp MERRA reanalysis dataset (Ostrenga, 2010).	34
Table 2.2	Aerosol properties used in GOCART for conversion from column mass loading to AOD. Optical properties are based on the Global Aerosol Data Set (GADS; Kopke et al., 1997). rm is modal radius, re is effective radius, σg is geometric standard deviation in lognormal size distribution, and Q is the extinction coefficient. All values for dry aerosols at 500 nm. Dust and sea salt contain multiple bins. Table is from Chin et al. (2002). (*assuming a maximum radius at 0.5 μm).	37
Table 2.3	Boundary layer aerosol input parameters and description (Ricchiazzi, 2002). Note that parameters with an * are those modified with user-defined values for aerosol direct radiative forcing calculations (see Chapter 5).	38
Table 4.1	JJA trends in total monthly mean mass for four individual boxed regions (bounds listed in bold). Values highlighted in yellow are for entire N-S domain, values in blue are for entire E-W domain, and value in green for whole domain. Values with * are those significant > 95% level. Units are g/m2 per decade. Values in parenthesis denote the combination of domains.	81
Table 5.1	Description of inputs for various aerosol simulations with SBDART model. Boundary layer aerosol SBDART input codes are tbaer = AOD at 550 nm, qbaer = AOD(λ), wbaer = SSA(λ), and gbaer = g(λ). K05 simulations denote modifying MODIS-Aqua total AOD by removal of an anthropogenic AOD computed with the K05 method. GCT simulations denote modifying MODIS-Aqua total AOD by retaining only the percentage that is SS+DU AOD species climatology from GOCART. a-superscript and b-superscript denote two different experiments (“basic” and “2box”, respectively) using different assumptions to fulfill AOD(λ), SSA(λ), and g(λ) for “natural” aerosol loads (see text for description). “MYD C6 L3” denotes the MODIS-Aqua Collection 6 Level 3 monthly mean product, C5 refers to Collection 5.1 used for g (discontinued in C6).	107

Table 5.2 A comparison between SBDART (SBD) and CERES (CER) TOA daytime monthly mean fluxes for the "2003" year and "FULL" dataset (July 2002 to December 2012). Provided are the means of SBDART and CERES fluxes, their correlation coefficient (Corr.Coef), the mean difference between the two datasets (CER-SBD), and that mean relative to the mean CERES fluxes ([CER-SBD]/CER). 128

Table 5.3 Standard deviations (σ) in SW fluxes (W/m^2) computed for the 15625 aerosol combinations and (separately) 5 atmospheric profiles. "tot" denotes total (natural+anthropogenic) aerosol load, "nat" denotes natural aerosol load using the "K05-2box" method. 132

Table 5.4 Mean (μ) and standard deviation (σ) of aerosol properties (at 550 nm) for the total and natural simulations at the midL and subT locations (90 samples per value). All values are unitless. "tot" denotes total (natural+anthropogenic) aerosol load, "nat" denotes natural aerosol load using the "K05-2box" method. 132

Table 6.1 Table of correlation coefficients (R) between variables (along left column) and aerosol, cloud, and environment parameter (along top row). Values in BOLD are correlations that are statistically significant (i.e. $p < 0.05$). CRE is r_e, SpH is specific humidity(SpHum), and OMG is ω. 155

List of Figures

Figure	Description	Page
Figure 1.1	Idealized aerosol number distribution as a function of particle diameter. From Hinds (1999).	4
Figure 1.2	(left) Aerosol volume distribution ($dV/d\log(D_p)$) as a function of particle diameter (D_p) at four southern California locations. From Seinfeld (1986) after Hidy et al. (1975). (right) Idealized aerosol mass distribution as a function of particle diameter. From Seinfeld (1986).	6
Figure 1.3	AERONET site locations as of 2016. Note not all sites are permanent. From the AERONET website: http://aeronet.gsfc.nasa.gov/.	11
Figure 1.4	Zonal mean clear-sky anthropogenic aerosol DRF from 16 models in the AeroCom Phase II study. From Myhre et al. (2013).	16
Figure 1.5	Cartoon depiction of various ACI comparing (top) pristine and (bottom) hazy aerosol situations. From Rosenfeld et al. (2008).	20
Figure 1.6	Reduction in (top) NO_x and (bottom) SO_2 emissions from power plant stations in five mid-Atlantic states (colors; solid linear trend line fitted) from 1996 to 2012. Data from the EPA Continuous Emissions Monitoring System (CEMS), following after He et al. (2013; 2016).	23
Figure 2.1	Example of deseasonalizing and trend algorithm using the GSFC AERONET record of AOD(550nm) from 2000 to 2012. (top) Native record with trend = −0.051 per decade (not significant). (bottom) Deseasonalized record with trend = −0.055 per decade (significant beyond 95%). (right) Mean annual cycle.	40
Figure 2.2	Schematic depiction of relevant spectral flux quantities in the solar SW spectrum calculated with SBDART. Quantities include TOA and BOT upward (u-subscript) and downward (d-subscript) fluxes. Three additional derived fluxes are computed as in the box in the upper left: ES_a, ATM_a, and SFC_a absorbances (a-subscript).	46

Figure 2.3	Example of ACI_r computation. Data are from MODIS-Aqua C6 monthly mean product from 07-2002 to 12-2012 over the mid-latitude domain (80º-40ºW, 30º-50ºN) within 90 < LWP < 100 g/m^2. Gray points (n=6168) are all AOD-r_e pairs within the LWP bin while the colored points are the mean(AOD)-mean(r_e) pairs in AOD bins sized 0.01. The color represents the number of observations (see colorbar) for each binned pair and is used as a weight in the linear fitting.	52
Figure 3.1	Mean climatological circulation over the western North Atlantic Ocean during 07-2002 to 12-2012. Also shown are the locations of surface AERONET and IMPROVE sites. The white box outlines the mid-latitude domain of interest (80º-40ºW; 30º-50ºN).	54
Figure 3.2	Deseasonalized AOD trends from MODIS-Aqua for (a) Collection 5.1 and (b) Collection 6 over the North Atlantic Ocean during July 2002 to December 2012. Dots and crosses represent statistically significant trends at the 90% and 95% levels, respectively. AOD trends are per decade. Figure from Jongeward et al. (2016).	56
Figure 3.3	Deseasonalized AOD(500nm) records for three eastern U.S. AERONET sites during July 2002 to December 2012. Thick red line represents a statistically significant (> 95%) linear trend reported in the figure. Figure from Jongeward et al. (2016).	57
Figure 3.4	Spatial distribution of deseasonalized AOD temporal correlation between MODIS-Aqua and (left) GSFC and (right) CCNY during July 2002 to December 2012 over the North Atlantic. Crosses represent statistically significant correlations at the 95% level. Figure from Jongeward et al. (2016).	58
Figure 3.5	Deseasonalized AOD trends during January 2001 to December 2009 from GOCART over the North Atlantic Ocean. Dots and crosses represent trends significant at the 90% and 95% level, respectively. All trends are per decade. (a) TOT, (b) natural (SS+DU), and (c) anthropogenic (SU+BC+OC). Figure from Jongeward et al. (2016).	60
Figure 3.6	Same as Fig. 3.5 except for each individual aerosol species from GOCART: (a) TOT, (b) SU, (c) DU, (d) SS, (e) OC, and (f) BC. Figure from Jongeward et al. (2016).	62

Figure 3.7	Records of $PM_{2.5}$ composition observed from the Washington D.C. IMPROVE network site (38.88ºN, -77.03ºE) from July 2002 to December 2012. Species shown are the sum total (TOT; black) of ammonium sulfate (AS; yellow), ammonium nitrate (AN; red), particulate organic matter (POM; green), light-absorbing carbon (LAC; grey), soils (SOIL; brown), and sea salt (SS; blue) species. Displayed are the time series of the native (upper left), relative contribution (upper right), and deseasonalized (bottom) records. The calculated linear regressions are superimposed on the deseasonalized time series. Emboldened are the species (AS, POM, and TOT) who report a trend beyond the 95% significant level. The deseasonalized LAC time series (gray, bottom) is difficult to resolve due to its small variance (0.06 µg/m3) compared to other series (e.g. var(TOT) = 9.5µg/m3), thus the LAC series lies near the abscissa. Figure from Jongeward et al. (2016).	64
Figure 3.8	Decadal trends in $PM_{2.5}$ for the four IMPROVE network surface sites during July 2002 to December 2012. Species shown are the sum total (TOT; black) of ammonium sulfate (AS; yellow), ammonium nitrate (AN; red), particulate organic matter (POM; green), light-absorbing carbon (LAC; grey), soils (SOIL; brown), and sea salt (SS; blue) species. Trend units are in $\mu m/m^3$ per decade. Pink star denotes that a trend is statistical significance at the 95% level. Figure from Jongeward et al. (2016).	66
Figure 3.9	Seasonal trends of deseasonalized AOD from MODIS-Aqua (C6) during July 2002 to December 2012 over the North Atlantic. Dots and crosses represent statistically significant trends at the 90% and 95% levels, respectively. AOD trends are per decade. Figure from Jongeward et al. (2016).	68
Figure 3.10	Seasonal trends of deseasonalized AOD CCNY, MDSC, and GSFC AERONET sites during July 2002 to December 2012. Statistically significance (> 95%) of AOD trends denoted by thick red line with trend value (per decade) reported in-figure. Figure from Jongeward et al. (2016).	69
Figure 3.11	Seasonal trends in $PM_{2.5}$ observed at each of the four surface IMPROVE network sites during July 2002 to December 2012 for the sum total (TOT; top row) of all species and for only AS (bottom row). Statistical significance at the 95% level noted by pink stars. All trends are in $\mu m/m^3$/decade.	70

Figure from Jongeward et al. (2016).

Figure 3.12 Calculated statistical significance for seasonal $PM_{2.5}$ species trends at each of the four surface IMPROVE network sites during July 2002 to December 2012. Legend denotes significance up to specified value. 72

Figure 4.1 Deseasonalized AOD trends during July 2002 to December 2012 for MODIS-Aqua (top left) and January 2001 to December 2009 from GOCART over the North Atlantic Ocean. Dots and crosses represent trends significant at the 90% and 95% level, respectively. All trends are per decade. (top left) MODIS total AOD, (top right) GOCART TOT AOD, (bottom left) GOCART natural (SS+DU) AOD, and (bottom right) GOCART anthropogenic (SU+BC+OC) AOD. 76

Figure 4.2 Deseasonalized total AOD (a,c) and dust AOD (b,d) trends during July 2002 to December 2012 from MODIS-Aqua over the North Atlantic Ocean. Trends for annual time series are on top (a,b) while trends for JJA are on bottom (c,d). Dots and crosses represent trends significant at the 90% and 95% level, respectively. All trends are per decade. Dust AOD is calculated following the Kaufman et al. (2005a) method described in Section 2.3.2. 78

Figure 4.3 JJA deseasonalized trends in (a) M_d and (b) F_d over the North Atlantic Ocean during 2002 to 2012. Also shown are the contours (in black) of mean JJA M_d at intervals of 0.2, 0.5, 0.8, and 1.0 g/m^2 with highest concentrations near the African coast. M_d trends are in units of g/m^2 per decade and F_d trends are in units Tg/month per decade. Trends statistically significant at the 95% (90%) level are marked with a cross (dot). 79

Figure 4.4 JJA mean fields of (a) U_{700}, (b) $\partial u/\partial z$, and (c) RV during 2002 to 2012. Below each are the deseasonalized time series for each variable and each grid point within the three micro-regions M1 (d,e,f), M2 (g,h,i) and M3 (j,k,l) outlined in pink. Trend lines have been fitted (red). Trends that are statistically significant above the 95% level are denoted with a red diamond along the abscissa and trend value (b; per decade) reported in-figure. Black contours in (a,b,c) denote the 0 contour with warm (cool) colors used for contours > 0 (< 0). White contours in (a) are every 2.5 m/s, in (b) are every 3 m/s, and in (c) are every 10^{-5} 1/s. Values for RV in 86

(f,i,l) have been scaled by a factor of 10^5.

Figure 4.5 (a) Mean position of the WAHL during JJA and (b) indices of the mean JJA North African environment: NAFDI (black, aqua), LLAT (red (>2410 m) and green (> 2425 m)), T_{10m} (orange), and P (blue). Areas in white are locations where the 925 hPa height were unavailable due to elevated terrain. The statistical significance of trends (per decade) reported in (b) is >90% except where * denoted >95%. The units for NAFDI and LLAT are m, T_{10m} is K, and P is kg/km^3. Grid points used to calculate NAFDI are outlined in pink in (a), and contours are 2425m (inner) and 2410 m (outer). 88

Figure 4.6 (black) Mean $\partial u/\partial z$ at 925 hPa during the JJA season from 2002 to 2012 along 5ºW longitude. At each latitude is the (red) positive or (negative) decadal trend in $\partial u/\partial z$, added to the mean $\partial u/\partial z$ curve. Trends marked with * are significant beyond the 95% level. 92

Figure 4.7 JJA seasonal trends in (left) barotropic, (middle) baroclinic, and (left) all terms of Eq. 4.5. Pink contour denotes the −10 m/s contour of the JJA seasonal mean U wind. Other contours represent 0.2 x 10^{-11} 1/s contours, orange are positive, green negative, and black the 0 contour of the respective term. Trends are 10^{-11} 1/s per decade, crosses (dots) are trends significant at the 95% (90%) level. 93

Figure 4.8 Deseasonalized time series (blue), JJA mean (red dot), and JJA trend (red line) for AITG index (top) and near-equatorial V_{10m} wind speed (bottom) during July 2002 to December 2012. Also reported are the value of the JJA trend and Tscore of its significance (Tscore > 1.3 is 90% significant, Tscore > 1.8 is 95% significant). 98

Figure 5.1 Example of downward spectral fluxes ($F(\lambda)$) for TOA down (blue), BOT down (red), and BOT up (green). The solar spectrum used for SBDART calculations is MODTRAN_3 (blue). Inset: step in wavelength (WL step; blue) used and internal sea water albedo (green: albedo = F^u_{BOT}/F^d_{BOT}) used for spectral flux calculations. 102

Figure 5.2 Example of downward spectral fluxes ($F(\lambda)$) from aerosol DRE calculation for the indicated flux quantity (see text and Fig.2.2 for description). SBDART configured as described in this section. Listed to the right is the integrated TDRF value using Eqn. 2.11. The total aerosol TDRF uses total 105

aerosol minus clean sky (i.e. no aerosol).

Figure 5.3 Trends in the total aerosol TDRFs during July 2002 to December 2012 for a) TOA_u, b) ES_a, c) BOT_d, d) SFC_a, e) BOT_u, and f) ATM_a. All trends are in W/m^2 per decade; note the different and uneven scales. 112

Figure 5.4 Trends in the anthropogenic aerosol ADRFs during July 2002 to December 2012 for a-d) ES_a, e-h) ATM_a, and i-l) SFC_a for simulations using "K05-basic" (first column) or "GCT-basic" (third column) for the clear sky. Also shown are trends in the natural aerosol NDRFs using "Clean" for the clear sky and "K05-basic" (second column) or "GCT-basic" (third column) for the aerosol sky. All trends are in W/m^2 per decade; note the different and uneven scales. Scales are the same as those used in Fig. 5.3 for total aerosol TDRFs. See Table 5.1 for description of aerosol/clear-sky cases. 117

Figure 5.5 Monthly mean fractional make up of natural aerosol to the total aerosol load for the K05 (columns 1 and 3) and GCT (columns 2 and 4) methods. Fractional value x100 provides percent makeup. The 0.5 (50%) contour is drawn in black. Note monthly means for K05 cover July 2002 to December 2012 while those for GCT only cover January 2001 to December 2009. 119

Figure 5.6 Monthly mean fractional make up of natural aerosol to the total aerosol load for the K05 (red) and GCT (black) methods for a mid-latitude (left) and sub-tropical (right) region during July 2002 to December 2012. Fractional value x100 provides percent makeup. See text for domain limits on mid-latitude and sub-tropical regions. 120

Figure 5.7 Trends in the anthropogenic aerosol ADRFs (a,b,g,h,m,n) and natural aerosol NDRFs (d,e,j,k,p,q) during July 2002 to December 2012 for (a,b,d,e) ES_a, (g,h,j,k) ATM_a, and (m,n,p,q) SFC_a for simulations using "K05-basic" (left) or "K05-2box" (center) methods for separating natural and anthropogenic aerosol load and properties. Also shown are the differences (right column) for a given aerosol DRF. All trends are in W/m^2 per decade; note the different and uneven scales. Scales are the same as those used in Fig. 5.3 and 5.4. See Table 5.1 for description of aerosol/clear-sky cases. 122

Figure 5.8 (top) 2002 to 2012 "basic" mean and (bottom) mean 125

	difference ("basic" minus "2box") in supplementary aerosol properties of (left) SSA, (center) g, and (right) AE at 550nm.	
Figure 5.9	Trends in the daytime total aerosol TDRFs during July 2002 to December 2012 for a) ES_a, b) ATM_a, and c) SFC_a. All trends are in W/m^2 per decade; note the different and uneven scales.	129
Figure 5.10	Trends in the daytime aerosol DRFs during July 2002 to December 2012 for a,b) ES_a, c,d) ATM_a, and e,f) SFC_a for simulations using the "K05-2box" method for separating natural and anthropogenic aerosol load and properties. (a,c,e) anthropogenic aerosol ADRF, (b,d,f) natural aerosol NDRF. All trends are in W/m^2 per decade; note the different and uneven scales. Scales are the same as those used in Fig. 5.9. See Table 5.1 for description of aerosol simulations.	130
Figure 5.11	PDF of trends analysis for ES_a (top), ATM_a (middle), and SFC_a (bottom) daytime fluxes during July 2002 to December 2012 using the "K05-2box" method. (left) anthropogenic aerosol ADRF; (right) natural aerosol NDRF. Green (orange) are results for the midL (subT) site. All trends are W/m^2/decade. 625 random combinations used for each PDF. Also reported is the PDF μ and σ, and displayed graphically with diamond and horizontal line. %sig is the percent of trends that are beyond the 95% significant threshold.	135
Figure 6.1	Domain-wide ACI_r computation. LWP bounds for each LWP bin listed in title. ACI_r and number of AOD-r_e pairs within each LWP bin (as n) listed in plot. Nobs making up each mean(AOD)-mean(r_e) pair represented by the color of the point (blue = few pairs, red = many pairs).	141
Figure 6.2	Same as Fig. 6.1 except for ACI_d. Note the y-axis scales are not constant across LWP bins.	142
Figure 6.3	Results of local 3º x 3º ACI analysis for ACI_r (top) and ACI_d (bottom). Green contour denotes the ACI = 0 contour. LWP bin boundaries are same as used in domain-wide ACI analysis (i.e. Fig. 6.1 and 6.2); the upper limit to each boundary is listed in each title.	144
Figure 6.4	PDFs for month and latitude within each of the 12 LWP bins used in domain-wide ACI analyses (i.e. Section 6.1.1).	145
Figure 6.5	From the local 3º x 3º analysis (i.e. Section 7.1.2) and in	147

same 12 LWP bins: (top) Statistical mode month at each location, (middle) the absolute difference between mode 1 and mode 2 months, and (bottom) percent represented by modes 1 and 2 for that grid point (black lines are the 40% and 60% contours).

Figure 6.6 PDFs of (top) aerosol, (middle) cloud, and (bottom) atmospheric properties from for the summertime daily dataset. Blue denotes JJA during 2003 and 2004, red denotes JJA during 2010 and 2011, and DIFF refers to the difference (JJA-1011 – JJA-0304). An offset has been added to the DIFF such that it fits within the y-axis bounds. Note: AOD and AI have a logarithmic x-axis. 152

Figure 6.7 ACI analysis using (top) cloud effective radius (ACI_r) and (bottom) cloud optical thickness (ACI_d) using (left) AOD and (right) AI as the proxy for CCN. Thin lines denote the uncertainty envelope of the ACI estimation with 95% confidence. Dashed lines at ±0.33 denote the plausible limits of Twomey behavior. 158

Figure 6.8 Number of observations (Nobs) within each LWP bin for both summer periods and all summers combined. Also shown is the upper limit (LWP_UP) of each LWP bin (in g/m^2), which by definition is quasi-linear in log(LWP) space and based on the LWP observed for the entire daily dataset. 160

Figure 6.9 ACI analysis using (top) cloud effective radius (ACI_r) and (bottom) cloud optical thickness (ACI_d) for (left) ascending and (right) descending grids using AI as the proxy for CCN. Thin lines denote the absolute (relative to zero-line) uncertainty of the ACI estimation. 161

Figure 6.10 Plots of (a) PDF and CDF of ω, (b) LTS versus ω with linear fit, and (c) PDF and CDF of LTS. Green lines denote ω = 0 Pa/s and LTS = 12.25 K. Red line in (b) denotes linear fit. PDF correspond to left axis, CDF to right axis. Data points in (b) are mean(LTS)-mean(ω) in ω bins of width 0.005 Pa/s. 163

Figure 6.11 Same as Fig. 6.9 except using LTS = 12.25 K as threshold. 164

Figure 6.12 Same as Fig. 6.9 except using SpHum = 0.01 kg/kg as threshold. 166

Figure 6.13 Same as Fig. 6.9 except using FMF = 0.75 as threshold. 168

List of Acronyms and Symbols

2box	AE, SSA, and g for SBDART using 2box methodology (see Section 5.2.2)
ACAD1	Acadia, ME IMPROVE site
ACI	Aerosol cloud interaction
ACI_d	ACI using COD
ACI_r	ACI using CRE
ADM	Angular distribution model
ADRF	Anthropogenic aerosol DRF
AE	Ångström exponent [unitless]
AEJ	African Easterly Jet
AERONET	Aerosol Robotic Network
AI	Aerosol index [unitless]
AIE	Aerosol indirect effects
AITG	Atlantic Interhemispheric Temperature Gradient [K]
AN	Ammonium nitrate
AOD	Aerosol optical depth [unitless]
AOSC	(Department of) Atmospheric and Oceanic Science
AS	Ammonium sulfate
ATM_a	Atmospheric absorbance [W m^{-2}]
ATM(z)	MERRA atmospheric profile (p, T, [H_2O], [O_3])
AVHRR	Advanced Very High Resolution Radiometer
BC	Black carbon
BOT	Bottom of atmosphere (i.e. surface)
BOT_d	BOT downward flux [W m^{-2}]
BOT_u	BOT upward flux [W m^{-2}]
BRIG1	Brigantine, NJ IMPROVE site
basic	AE, SSA, and g for SBDART using basic methodology (see Section 5.2.2)
C6	Collection 6 (MODIS)
CACO1	Cape Cod, MA IMRPOVE site
CALIOP	Cloud-Aerosol Lidar with Orthogonal Polarization
CCN	Cloud condensation nuclei
CCNY	City College of New York AERONET site
CDF	Cumulative distribution function
CEMS	Continuous Emissions Monitoring System
CERES	Clouds and the Earth's Radiant Energy System
Clear	SBDART simulation with all aerosol parameters turned off
COADS	Comprehensive Ocean-Atmosphere Dataset
COD	Cloud optical depth [unitless]
COT	Cloud optical thickness [unitless]
CRE	Cloud effective radius [m]
CTT	Cloud top temperature [K]

DAS	Data assimilation system
DISORT	Discrete Ordinates Radiative Transfer
DJF	December, January, February (winter)
DMS	Dimethyl sulfide
DRE	Direct radiative effect
DRF	Direct radiative forcing
DU	Dust
EOS	Earth Observing System
EPA	Environmental Protection Agency
ERBE	Earth Radiation Budget Experiment
ES_a	Earth system absorbance [W m^{-2}]
ESSIC	Earth System Science Interdisciplinary Center
$F(\lambda)$	Electromagnetic spectral flux [W m^{-2} m^{-1}]
F_a	Spectral flux for aerosol sky
F_c	Spectral flux for clean sky
F_d	Zonal dust mass flux [Tg $month^{-1}$]
F_{sun}	Extraterrestrial solar flux [W m^{-2}]
FMF	Fine-mode fraction [unitless]
f	Coriolis parameter
f_t, f_m, f_d, f_a	Total FMF, marine FMF, dust FMF, anthropogenic FMF
GCT	GOCART-based method to determine "natural" aerosol (see Section 5.2)
GEOS	Goddard Earth Observing System
GEOS-5	GEOS atmospheric model, v5.2.0
GES-DISC	Goddard Earth Sciences Data and Information Services Center
GFED	Global Fire Emissions Database
Giovanni	GES-DISC Interactive Online Visualization and Analysis Infrastructure
GMT	Greenwich Mean Time
GOCART	Goddard Chemistry Aerosol Radiation and Transport
GSFC	Goddard Space Flight Center AERONET site
g	Aerosol asymmetry parameter [unitless]
$[H_2O]$	Water vapor density [g m^{-2}]
I_λ	Spectral intensity of electromagnetic radiation [W sr^{-1} m^{-1}]
IMPROVE	Interagency Monitoring of Protected Visual Environments
IPCC	Intergovernmental Panel on Climate Change
IR	Infrared electromagnetic radiation
ITCZ	Inter-tropical convergence zone
JJA	June, July, August (summer)
JJA-0304	Analyses using JJA months during 2003 and 2004
JJA-1011	Analyses using JJA months during 2010 and 2011
JJA-BOTH	Analyses using both JJA-0304 and JJA-1011
K05	Kaufman et al. (2005a)-based method to determine "natural" aerosol (see Section 5.2)
$\hat{k}$	Unit vector in the vertical (0,0,1)
L	Longitudinal length [m]

LAC	Light absorbing carbon
LLAT	Low-level atmospheric thickness [m]
LST	Local Solar Time
LTS	Lower Tropospheric Stability [K]
LUT	Look-up table
LWC	Liquid water content [g kg^{-1}]
LWP	Liquid water path [g m^{-2}]
M	Mass loading per unit area [g m^{-2}]
M_d	Dust mass loading [g m^{-2}]
MAM	March, April, May (spring)
MD	Maryland
MDSC	Maryland Science Center AERONET site
MERRA	Modern Era Retrospective Analysis for Research and Applications
MISR	Multi-angle Imaging Spectroradiometer
MODIS	Moderate Resolution Imaging Spectroradiometer
MYD	MODIS-Aqua instrument
midL	Mid-latitude location for DRF trend uncertainty (See Section 5.5.1)
N_a	Aerosol number concentration [m^{-3}]
N_d	Cloud droplet number concentration [m^{-3}]
N_s^2	Brunt-Väisälä frequency [s^{-2}]
NAAQS	National Ambient Air Quality Standards
NAFDI	North African Dipole Intensity [m]
NASA	National Aeronautics and Space Administration
NDRF	Natural aerosol DRF
NO_x	Nitrogen oxide species (e.g. NO, NO_2)
Nobs	Number of AOD-r_e observation pairs used in ACI analyses
n(r)	Aerosol number distribution (aerosol number of radius r per volume) [m^{-1} m^{-3}]
$[O_3]$	Ozone density [g m^{-2}]
OC	Organic carbon
OH	Ohio
P	Sahel precipitation [kg km^{-3}]
PA	Pennsylvania
PATMOS-x	Pathfinder Atmosphere extended
PDF	Probability distribution function
PM	Particulate matter
$PM_{2.5}$	PM with diameter less than 2.5 μm
PM_{10}	PM with diameter less than 10 μm
POLDER	Polarization and Directionality of Earth's Reflectances
POM	Particulate organic matter
PV	Potential vorticity [s^{-1}]
p	Atmospheric pressure [Pa]
$p(\Omega', \Omega)$	Scattering phase function [unitless]
Q_e,Q_s, Q_a	Extinction, scattering, and absorption cross section [m^{-2}]
QGPV	Quasi-geostrophic potential vorticity [s^{-1}]
q	PV of the atmospheric base-state [s^{-1}]

R	Gas constant for dry air (287 J kg^{-1} K^{-1})
RCP8.5	Representative Concentration Pathway for 8.5 W m^{-2}
RH	Relative Humidity (%)
RV	Relative vorticity (horizontal component) [s^{-1}]
r_e	Effective radius [m]
SAM	Stratospheric Aerosol Measurement
SBDART	Santa Barbara DISORT Atmospheric Radiative Transfer
SFC_a	Surface absorbance [W m^{-2}]
SOIL	Soil
SON	September, October, November (fall)
SPM	Summary for Policymakers
SpHum	Specific Humidity [kg kg^{-1}]
SS	Sea salt
SSA	Single scattering albedo [unitless]
SSF	Single scanner footprint (CERES dataset)
SST	Sea surface temperature [K]
SU	Suflate
SW	Shortwave electromagnetic radiation
SeaWiFS	Sea-viewing Wide Field-of-view Sensor
s	Geometric distance [m]
subT	Sub-tropical location for DRF trend uncertainty (See Section 5.5.1)
T	Atmospheric temperature [K]
T_{10m}	Atmospheric temperature at 10 m [K]
TDRF	Total aerosol DRF
TMI	TRMM Microwave Imager
TOA	Top of atmosphere
TOA_d	TOA downward flux [W m^{-2}]
TOA_u	TOA upward flux [W m^{-2}]
TOT	Total (sum total of IMPROVE $PM_{2.5}$ species or GOCART AOD species)
Total	SBDART simulation with full aerosol load (total = natural + anthropogenic)
TRMM	Tropical Rainfall Measuring Mission
U	Zonal wind speed [m s^{-1}]
U_{700}	Zonal wind speed at 700 hPa [m s^{-1}]
U_{925}	Zonal wind speed at 925 hPa [m s^{-1}]
U.S.	United States (of America)
USA	United States of America
UV	Ultraviolet electromagnetic radiation
u	Zonal wind speed of the atmospheric base-state [m s^{-1}]
u_g	Zonal geostrophic wind speed [m s^{-1}]
u_T	Thermal wind [m s^{-1}]
V_{10m}	Meridional wind speed at 10 m [m s^{-1}]
VA	Virginia
VIIRS	Visible Infrared Imaging Radiometer Suite
VOCs	Volatile organic compounds

$\vec{v}$	Horizontal components of the wind vector (u,v) [m s^{-1}]
WAHL	West African Heat Low
WASH1	Washington, D.C. IMPROVE site
WV	West Virginia
α	Ångström exponent [unitless]
β	Meridional gradient in the Coriolis parameter [s^{-1} m^{-1}]
β_e, β_s, β_a	Extinction, scattering, and absorption coefficients [m^{-1}]
η	Weighting for MODIS fine-mode AOD, equivalently FMF [unitless]
λ	Wavelength [m]
μ	Statistical mean
ρ	Density [g m^{-3}]
ρ_λ	Spectral reflectance [unitless]
σ	Statistical standard deviation
τ, τ_{NAT}, τ_t, τ_m, τ_d, τ_a	Aerosol optical depth (AOD), natural-component AOD, total AOD, marine AOD, dust AOD, anthropogenic AOD [unitless]
τ_d	Cloud optical depth (COD) [unitless]
Φ	Geopotential height [m]
ψ	Geostrophic streamfunction [m^2 s^{-1}]
Ω', Ω	Source-target and Target-observation geometry [radian]
ω	Vertical pressure velocity [Pa s^{-1}]
ω'	Solid angle [steradian]
$\tilde{\omega}$	Single scattering albedo [unitless]

Chapter 1: Introduction

1.1 Motivation

Atmospheric aerosols contribute to atmospheric variability and to Earth's radiative balance through direct radiative forcing effects (scattering and absorption) and indirectly via complex aerosol-cloud interactions (ACI) (Kaufman et al., 2002; IPCC, 2013). Aerosol optical depth (AOD), a first-order quantity of aerosols direct radiative interaction, has been observed from surface and space platforms for several decades (Holben et al., 1998; Zhao et al., 2008). Aerosol indirect effects (AIE; alternatively aerosol-cloud interactions (ACI)) include the role of aerosols in modifying cloud properties (both micro- and macro- physical) and the resultant radiative forcing (Feingold and Siebert, 2009; IPCC, 2013). Aerosols can also play a role in the biosphere by playing an important part in biogeochemical cycles (Mahowald et al., 2010), impacting

human mortality (Anderson, 2009), and affecting plant life and degrading man-made materials (Seinfeld, 1986).

Aerosols and their impacts have gained much interest in the last decade or two. In addition to increasing atmospheric concentrations of CO_2, the industrialization during much of the 20th Century also contributed elevated aerosol emissions (Lamarque et al., 2010; Smith et al., 2011). Anthropogenic aerosols are mainly scatterers in the solar visible (with the exception of black carbon aerosols which absorb; Bond et al., 2013; IPCC 2013). These rising aerosol emissions (by increasing atmospheric scatter) have been linked to a period of decreased incident radiation at the surface during 1950-80, with some additional contribution from ACI effects (Kvalevåg and Myhre, 2007; Wild, 2012). More recently, emissions decreases (e.g. over Europe and the United States) have been suggested to be driving reductions in aerosol loadings and subsequent increases in surface solar radiation over these regions (Ruckstuhl et al., 2008; Streets et al., 2009). However, other regions around the globe are experiencing increases in aerosols (e.g. East and South Asia; Streets et al., 2009). Anthropogenic aerosols over the North Atlantic have been hypothesized to impact underlying sea-surface temperatures (SSTs; Booth et al, 2012), through which subsequent impacts may influence the tropical Atlantic climate (Chang et al., 2011), precipitation in the Sahel and African dust (Biasutti and Giannini, 2006; Wang et al., 2012) and the frequency of Atlantic tropical storms (Dunstone et al., 2013). Understanding aerosol spatiotemporal variability is important to understanding its role in and impacts on the Earth's climate system.

1.2 Background on Aerosols

1.2.1 Aerosol Composition

Atmospheric aerosols consist of solid particles and/or liquid droplets suspended in the ambient atmosphere. Aerosol sizes typically range from 0.01 to 10 μm in diameter, many orders of magnitude larger than the typical diameter (~ 0.0003 μm) for ambient and well-mixed atmospheric gases (e.g. N_2; Seinfeld, 1986). Aerosols come from a wide range of sources, both natural and anthropogenic. Natural sources of aerosols include soil dust, sea salt, plant debris and emission, volcanoes, forest fires, and gas-to-particle conversions (Prospero et al., 1983; Hinds, 1999). Anthropogenic sources of aerosols can arise from transportation, electrical generation, burning (both trash and fuel), agriculture, and various industrial processes and can come from both primary pollutants (directly emitted) and secondary pollutants (evolving within the atmosphere; Seinfeld, 1986; Hand et al., 2012). Once emitted from their source, both natural and anthropogenic aerosols can undergo changes during dispersion and transport, including coagulation, chemical reactions, and cloud processing. Removal processes for aerosols include deposition, rainout, and gravitational settling. Typical residence time for tropospheric aerosols is typically on the order of a week or less (Prospero et al., 1983). The total number concentration of aerosol particles can range from 10^3 cm^{-3} in more remote locations to 10^5-10^6 cm^{-3} in polluted urban areas. Aerosol particles are also most abundant near their source region, both horizontally and vertically. Aerosol particle concentrations fall off

exponentially with height, with most mass in the lower troposphere before giving way to background concentrations aloft (> 5 km) of around 300 cm^{-3} (Pruppacher and Klett, 1978). It is worth noting a small, quasi-stable stratospheric aerosol layer (colloquially "The Junge Layer") located between 15-20 km with concentrations of sulfate particles on the order of 10^{-2} cm^{-3} (Junge and Manson, 1961). This layer can be perturbed by strong volcanic eruptions, which can elevate stratospheric aerosol concentrations for months to years after the initial eruption (Sato et al., 1993).

While in the atmosphere, aerosol particles take on sizes across three or more orders of magnitude with varying amounts, known as the aerosol number distribution. These are generally split into three categories based on three modes in the number distribution (see Figure 1.1): nuclei, accumulation, and coarse modes. The aerosol number distribution can roughly be modeled by an inverse power law distribution (shown as dash-dotted line in Fig. 1.1) or a log-normal distribution.

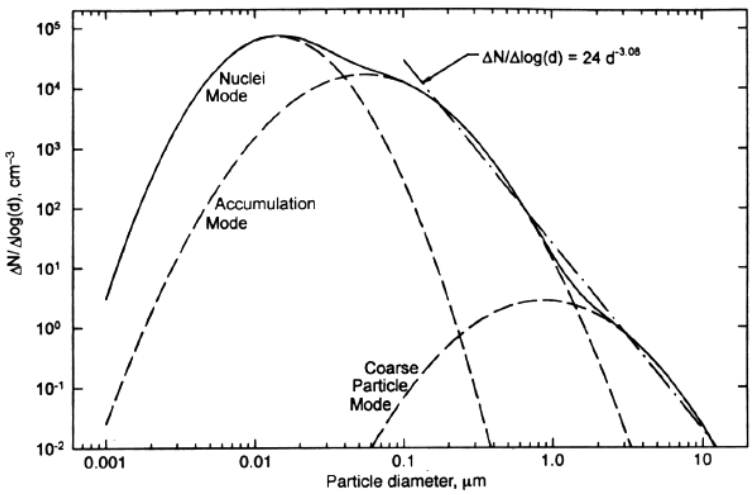

Figure 1.1: Idealized aerosol number distribution as a function of particle diameter. From Hinds (1999).

The nuclei mode is composed mainly of combustion particles and those formed by gas-to-particle conversion. These particles tend to coagulate rapidly and thus have short lifetimes before joining the accumulation mode. Additional accumulation mode aerosols include photochemical smog. Removal mechanisms for accumulation mode include rainout and further coagulation into coarse mode particles. Coarse mode aerosols are mainly comprised of dust, sea salts, and mechanically generated anthropogenic aerosols (e.g. from farming). Due to their large size, coarse mode particles are removed by gravitational settling or impacting upon surfaces (Hinds, 1999).

Additional ways to show the aerosol distribution include surface area and volume distributions. Distributions like these can separate the large number of small particles (having a smaller contribution to the volume distribution) from the small number of large particles (having a larger contribution to the volume distribution). Figure 1.2 (left) shows an example volume distribution at four southern California locations: the volume distribution of motor vehicle emissions has a strong mode in the accumulation (or fine) mode while the distribution of sea salt has a strong mode in the coarse mode. Using the volume distribution (or the roughly equivalent mass distribution, Fig. 1.2 right), a clear separation becomes apparent between primarily anthropogenic aerosols, with smaller radii in the fine mode, and natural aerosols, with larger radii in the coarse mode.

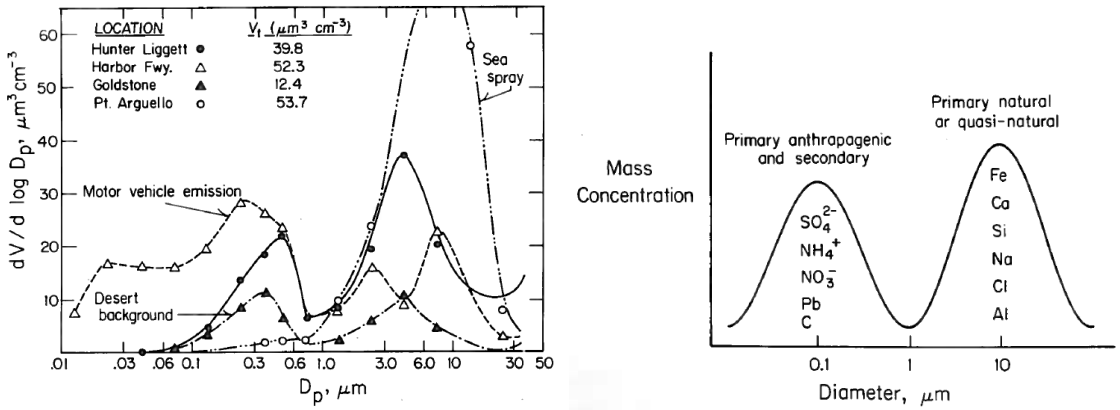

Figure 1.2: (left) Aerosol volume distribution ($dV/d\log(D_p)$) as a function of particle diameter (D_p) at four southern California locations. From Seinfeld (1986) after Hidy et al. (1975). (right) Idealized aerosol mass distribution as a function of particle diameter. From Seinfeld (1986).

Originating from a wide range of sources, the chemical composition of natural versus anthropogenic and urban versus rural aerosols can have substantial differences. For example, urban areas can have substantially elevated amounts of black carbon from combustion, organic compounds near chemical and industrial plants, sulfate compounds from coal-based electrical production, and photochemical smog (reaction of hydrocarbons and nitrogen oxides to form ozone; Seinfeld, 1986). Rural areas can have larger fractional composition of particulate organic matter (from vegetation) as well as elevated ammonium nitrate compounds from agriculture (Pitchford et al., 2009; Hand et al., 2012). Marine environments, remote islands, and coastal areas can have elevated contributions from natural sea salt aerosols (e.g. Hand et al., 2012), while dust source and down-wind regions have dominant contributions from natural dust aerosols (contributions from Si, Na, Mg, Al, K, Ca, and Fe compounds; e.g. Chen et al., 2011).

1.2.2 Forward Radiative Transfer

The chemical composition, number, and size distribution of an aerosol loading all determine the optical attenuation of electromagnetic radiation propagation. After attenuation of ultraviolet radiation aloft by oxygen and ozone, there are two dominant attenuating regimes for visible and near-visible solar radiation (roughly 0.4 to 1.0 μm) within the troposphere: Rayleigh scatter for particles smaller than 10 nm and Mie scatter for particles between around 10-100 nm to 10 μm (Petty, 2006). Rayleigh scatter is inversely proportional to the fourth power of the wavelength of light and explains why much of the sky we see is blue: shorter (blue) wavelengths experience significantly more scattering than longer (red) wavelengths. Mie scatter (or more appropriately Mie theory) describes the interaction of light with spherical particles that are approximately of the same size as the wavelength of light, a good approximation for most aerosols (Liou, 2002). Non-spherical aerosol loadings employ more complex retrieval theory (e.g. T-matrix method; Liou, 2002; Dubovik et al., 2002).

Remote sensing of AOD with Mie theory is based on Beer's law of light attenuation, which describes the loss in intensity of electromagnetic radiation as it propagates through a medium:

$$dI_\lambda \equiv I_\lambda(s + ds) - I_\lambda(s) = -I_\lambda(s)\beta_e(s)ds \qquad \text{(Eq. 1.1a)}$$

$$\frac{dI_\lambda}{I_\lambda} = -\beta_e ds = -(\beta_s + \beta_a)ds \qquad \text{(Eq. 1.1b)}$$

where I_λ is spectral intensity (W sr^{-1} m^{-1}), s is geometric distance (m), and β_e is the extinction coefficient (unitless, sum of scattering (β_s) and absorption (β_a) coefficients; after Petty, 2006). Given a number distribution of aerosol particles (n(r)), the extinction coefficient can be written as:

$$\beta_e = \int_0^\infty n(r) Q_e(r)\, \pi r^2 dr \qquad \text{(Eq. 1.2)}$$

where Q_e is the extinction cross section of a sphere and is a function of the size and complex index of refraction (using Q_s and Q_a for β_s and β_a respectively). Here, it is implied that Q_x and thus β_x can also have a spectral dependence. As can be seen, information (or assumptions) of the aerosol number, size, and chemical composition are needed.

Direct attenuation is not the only contribution to the intensity observed; there can be substantial contribution from scattering events not in the direct line-of-sight that scatter radiation into the direction observed. To account for this, Eq. 1.1b needs to be modified as:

$$dI_\lambda = -I_\lambda \beta_e ds + \frac{\beta_s}{4\pi} \int_{4\pi} I_\lambda(\Omega') p(\Omega', \Omega) d\omega'\, ds \qquad \text{(Eq. 1.1c)}$$

where the second term represents the intensity gained by single scatter from the source-particle geometry Ω' into the particle-observation geometry Ω using the scattering phase

function p(Ω',Ω), integrated over all infinitesimal steradians dω' of a sphere (with nominal unit surface area of 4π). The phase function p(Ω',Ω) can be thought of as the probability that light with incident geometry Ω' is scattered into the Ω observed geometry. Introducing optical depth as $\tau = \beta_e s$ (or in differential: $d\tau = \beta_e\, ds$), Eq. 1.1c now becomes:

$$\frac{dI_\lambda(\Omega)}{d\tau} = -I_\lambda(\Omega) + \frac{\tilde{\omega}}{4\pi}\int_{4\pi} I_\lambda(\Omega')p(\Omega',\Omega)d\omega' \qquad \text{(Eq. 1.1d)}$$

where $\tilde{\omega}$ is the single scattering albedo ($\tilde{\omega}=\beta_s/\beta_e$). The phase function itself takes on a complex form using Legendre polynomials and also depends on the particle size and complex index of refraction. One construction of the phase function used in Mie theory and aerosol studies is the Henyey-Greenstein phase function, which parameterizes p(Ω',Ω) by the asymmetry parameter (g; $-1 \le g \le 1$) which is the normalized spherical integral of p(Ω',Ω) (Petty, 2006). Its bounds suggest the probable likelihood light will be scattered in the forward (g = 1) or backward (g = −1) direction.

1.2.3 Aerosol Remote Sensing

The most fundamental aerosol property that has been observed the longest is atmospheric turbidity, an early term related to AOD and the total aerosol loading. Turbidity is determined from surface observations by comparing the intensity of direct sunlight at different zenith angles, a method which eliminates the need for exact

characterization of the intensity emitted (Volz, 1969; Shaw, 1983). With the development of more advanced surface networks and techniques (e.g. the AErosol RObotic NETwork (AERONET); Holben et al., 1998), spectral radiometers that observe sun and sky radiance measurements over a range of viewing angles can be used to infer additional properties of the aerosol loading such as number distribution and phase function. These methods utilize an inversion technique relying on a priori assumptions about the aerosol loadings that are expected to be observed (i.e. number/size distribution and complex index of refraction) and use statistical optimization methods to best match the observed radiances with those calculated with the aerosol properties using a forward model (Dubovik and King, 2000). Aerosol retrievals from ground only provide information about the aerosol loading in the vicinity of the observation site. Indeed, even with an expansive observational network like AERONET (see Figure 1.3) there still remain substantial gaps in spatial coverage of ground-based aerosol observations, especially over oceanic regions.

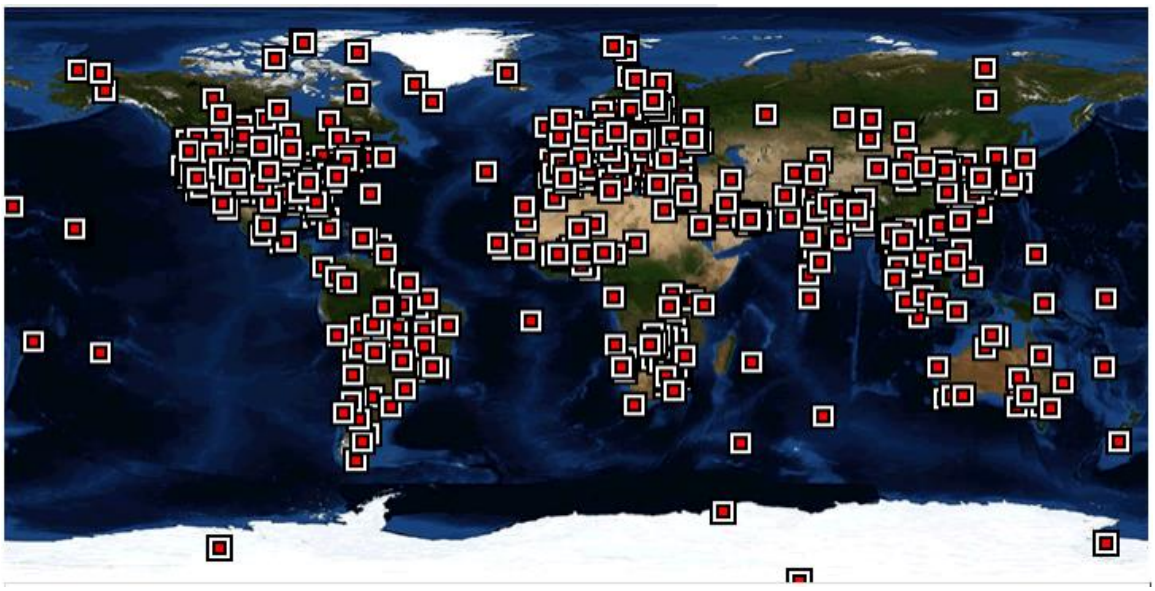

Figure 1.3: AERONET site locations as of 2016. Note not all sites are permanent. From the AERONET website: http://aeronet.gsfc.nasa.gov/.

Evolving alongside surface aerosol observations have been satellite platforms with capabilities to derive various properties of aerosols. Satellite aerosol remote sensing has a long and rich history of platforms observing the spatiotemporal variation, columnar properties, and vertical profiles of aerosols (King et al., 1999; Lee et al., 2009). These platforms have made use of single (Stratospheric Aerosol Measurement (SAM) instrument, McCormick et al., 1979) and multiple wavelengths (Advanced Very High Resolution Radiometer (AVHRR), Stowe et al., 1997; and Moderate Resolution Imaging Spectroradiometer (MODIS), Remer et al., 2005), single (AVHRR, MODIS) and multiple viewing geometries (Multiangle Imaging SpectroRadiometer (MISR), Kahn et al., 2005), polarization (Polarization and Directionality of Earth's Reflectances (POLDER), Deuzé et al., 1999; and Cloud-Aerosol Lidar with Orthogonal Polarization (CALIOP), Winker et al., 2009), and passive (AVHRR, MODIS) and active (CALIOP) sensors. Depending on sensor, retrievals can derive a range of aerosol properties

including AOD, aerosol extinction coefficient, effective radius, Ångström exponent (AE; the spectral dependence of AOD), and aerosol index (AI; AI = AOD * AE). Aerosol retrieval from space is made more difficult (compared to ground retrievals) due to the need for screening of cloudy pixels and also the inclusion of surface reflectance. Two additional factors that complicate comparison among satellite aerosol products are sensor calibrations and also using differing aerosol models and inversion methods (e.g. Li et al., 2009).

Of the numerous space-based platforms, the most intriguing for long-term aerosol studies are polar-orbiting sensors, including AVHRR and MODIS. Numerous AVHRR instruments have been flying since the late 1970s and use one (0.63 μm) or two (0.63 and 0.85 μm) wavelengths for aerosol retrieval (e.g. Stowe et al., 1997; Zhao et al., 2008a). The MODIS sensor was designed to have continuity with several sensors already flying (including AVHRR) while also providing upgrades in both technology, calibration, and retrievals (Salomonson et al., 2006). The MODIS aerosol algorithms make use of observations at seven wavelengths (0.47 to 2.1 μm; Levy et al., 2009) and will be used extensively in this work (described in Chapter 2). Like MODIS, the more recent Visible Infrared Imaging Radiometer Suite (VIIRS) sensor is designed to provide continuity to the existing long-term data records (including those from AVHRR and MODIS) and provide some improvements as technological advances have allowed (Jackson et al., 2013). In general, these sensors fly in sun-synchronous polar orbits at altitudes around 700-800 km with a viewing swath around 2500 km wide. These orbits provide near-global coverage within two days (at varying spatial resolutions) for these sensors.

1.3 Aerosol Influences

1.3.1 Long-term AOD Trends

The development of technologies and products to monitor aerosols globally from space for 30+ years affords scientists the opportunity to study long-term trends in aerosol loading, typically using AOD observations. Yet, there remains disagreement in global AOD trend assessments. For example, Mishchenko et al. (2007) identified a statistically significant globally decreasing AOD trend over oceans beginning in the 1990s using AVHRR observations. Work by Zhang and Reid (2010) report a statistically negligible increase in global over-ocean AOD from 2000 to 2009 using MODIS and MISR observations. A weakly positive AOD trend over ocean is suggested by Hsu et al. (2012) using Sea-viewing Wide Field-of-view Sensor (SeaWiFS) observations during 1998 to 2010. Aforementioned differences in calibration, cloud screening, aerosol inversion, and surface influences can affect AOD retrievals and monitoring of long-term trends (Li et al., 2009; Mishchenko et al., 2012; Zhao et al., 2013).

The spatiotemporal variability inherent in atmospheric aerosol loading complicates assessments of global AOD trends (Kaufman et al., 2002; Remer et al., 2008; Li et al., 2014). Because of subtleties seen in retrieved global AOD, the reconciliation of discrepancies across sensors and products hinges on regional analyses where trends are

expected to be stronger and easier to detect and quantify compared to global trends (Mishchenko and Geogdzhayev, 2007). For instance, trends using AVHRR, MODIS, and SeaWiFS show agreement over Southeast Asia (positive trend) and over Europe and the United States (negative trend; Zhao et al., 2008a; Zhang and Reid, 2010; Hsu et al., 2012). These studies suggest rapid economic growth and energy use in Southeast Asia and air quality legislations over Europe and the U.S. are likely causes for these respective trends. Trend analysis of AOD from AERONET sites in these regions adds a surface-based confirmation to the satellite trends (e.g. de Meij et al., 2012; Li et al., 2014) as do AOD trend results from modeling efforts (e.g. Streets et al., 2009).

Natural aerosols may also experience changes in loading. For example, the amount of precipitation in the Sahel has been negatively correlated with dust export from North Africa on inter-decadal timescales (Prospero and Lamb, 2003; Wang et al., 2012). Sahel precipitation has been on a recovery since the drought period during the 1970-80s, and some suggest increasing greenhouse gases may play a role (e.g. Dong and Sutton, 2015; Giannini, 2015). Dust variability over the North Atlantic is also controlled by several North African features, including the African Easterly Jet and related Easterly Waves (Jones et al., 2003) and the geopotential heights associated with the West African Heat Low (Rodríguez et al., 2015). A warming over the Saharan desert has been seen in reanalyses and linked to changes in the geopotential heights (Cook and Vizy, 2015) which may have an impact on dust aerosol.

1.3.2 Aerosol Direct Effects

As mentioned in Section 1.1, aerosols directly interact with electromagnetic radiation mainly in the visible to near-visible infrared spectral region (the "solar" region); this is known as the aerosol direct radiative effect (DRE). The early work by Charlson and Pilat (1969) suggested the basic effect of a backscattering aerosol load would be to cool the Earth system by increasing TOA reflectance. The DRE produces a direct radiative forcing (DRF) when examining the shortwave (SW) solar fluxes between aerosol laden and clean sky conditions. Yu et al. (2006) provide a review of measurement-based DRE using satellites and aerosol chemical transport models together; they estimate a global ocean clear-sky total aerosol DRF at TOA (surface) to be -5.5 ± 0.2 (-8.8 ± 0.7) W/m^2. This is the effect the total (natural + anthropogenic) aerosol load has (compared to none at all).

Intrinsic to the total aerosol DRF is the anthropogenic aerosol DRF (also called the "direct climate forcing by anthropogenic aerosols" in Yu et al. (2006)). This is the radiative effect from the anthropogenic component of the total aerosol load. The anthropogenic DRF is more difficult to ascertain, as it depends on correct determination of anthropogenic aerosol properties (i.e. number and size distribution and complex index of refraction) and contrast with the natural background aerosol. Kaufman et al. (2005b) employed MODIS observations to estimate the clear-sky TOA anthropogenic aerosol DRF over global ocean as -1.4 ± 0.4 W/m^2. The same quantity estimated by Zhao et al.

(2008b) was −1.25 ± 0.43 W/m^2 using Clouds and the Earth's Radiant Energy System (CERES) fluxes and the Goddard Chemistry Aerosol Radiation and Transport (GOCART) model. These values are in line with the range from pure modeling efforts in the AeroCom Phase II project shown in Figure 1.4. Note the largest anthropogenic aerosol DRF is located in the northern latitudes between 30º and 60ºN where much of the industrialized population is located.

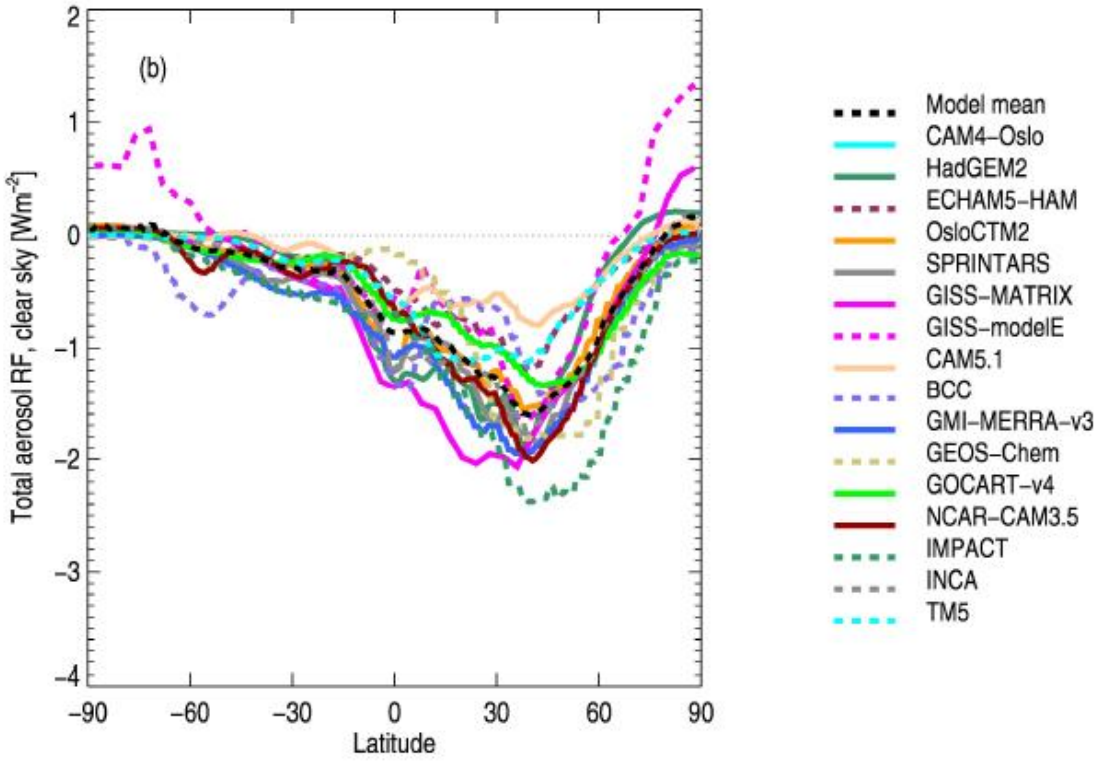

Figure 1.4: Zonal mean clear-sky anthropogenic aerosol DRF from 16 models in the AeroCom Phase II study. From Myhre et al. (2013).

As aerosol may scatter and absorb solar radiation to cool and heat the atmosphere respectively, aerosol radiative forcing can be positive or negative depending on the underlying surface reflectance (e.g. Haywood and Shine, 1995). Recently, black carbon aerosols have received increasing attention due to their absorbing nature. Bond et al.

(2013) provides a comprehensive review of black carbon impacts, and lists the anthropogenic forcing (for the industrial-era or 1750-2005) as 0.71 W/m^2 (with bounds of 0.08 to 1.27 W/m^2). However, black carbon is also co-emitted with other aerosol species from energy-related sources, and together the forcing is limited to 0.22 W/m^2 (with bounds of −0.50 to 1.08 W/m^2; Bond et al., 2013).

When considering long-term aerosol emissions, trends, and the DRE together with increases in CO_2, it has been suggested that the DRF of aerosols from industrialization may have acted to mask some of the greenhouse warming signal from CO_2 (e.g. Coakley et al., 1983; Andreae et al., 2005). For example, Wild et al. (2007) argue that a period of "solar dimming" (reduced solar radiation at the surface) caused by elevated aerosol loads during the 1960s to 1980s muted the temperature rise during this time. However, after the 1980s, when countries in Europe and North America started to improve their air quality (and thus reduce aerosol emissions), an accelerated temperature rise has been seen during surface "solar brightening". Studies by Rucksthul et al. (2008) and Streets et al. (2006, 2009) provide further support for reductions in anthropogenic aerosol loading while Wild et al. (2005) highlights the subsequent increases in surface solar radiation over these regions. Indeed, the competing forcing from aerosols and CO_2 is recognized in the latest Intergovernmental Panel on Climate Change (IPCC) report: "There is *high confidence* that aerosols and their interactions with clouds have offset a substantial portion of global mean forcing from well-mixed greenhouse gases." (IPCC, 2013, SPM, pp. 13). Thus, in addition to knowing the static DRF it is also informative to identify any trends existing in the DRF and specifically anthropogenic DRF.

1.3.3 Aerosol Indirect Effects

Aerosol indirect effects, more generally aerosol-cloud interactions (ACI), encompass a wide range of effects aerosols have on clouds via their participation as cloud condensation nuclei (CCN). Aerosols have been recognized as important to cloud droplet formation since as early as the late 19th Century (Aitken, 1880). A rigorous theory of heterogeneous nucleation put forth by Köhler (1936). More recently, the work by Twomey (1974) noted the correlation between aerosol number concentration and cloud drop number concentration: given constant cloud water content, the cloud droplets are smaller and more numerous (and thus the cloud more reflective) in cases of elevated aerosol number concentration. This effect has collectively been known in various literatures as the Twomey effect, first indirect effect, cloud microphysical effect, and cloud albedo effect. Conversely, clouds can also affect aerosols via cloud processing, including washout, convective redistribution, coalescence and chemical processing, and new particle formation (Feingold and Siebert, 2009). Cloud processing is complex and important in its own right yet these processes cannot be observed directly by satellites and will not be discussed further in this work.

From aerosols acting as CCN and modifying the microphysics of cloud droplets comes a host of macrophysical reflections of ACIs. These can include impacts on cloud optical thickness (Coakley et al., 1987), on cloud lifetime (Albrecht, 1989) and fraction

(Fan et al., 2013), on cloud vertical development (Li et al., 2011) and on updraft speeds (Koren et al., 2005). These effects may alter precipitation. In general, aerosols suppress light and enhance heavy precipitation (Rosenfeld et al., 2008; Wang et al., 2011). Figure 1.5 is a schematic of the various impacts aerosols have on clouds; while originally for deep convective clouds in growing (left), mature (center), and dissipating (right) phases, some interactions can be extended in principle to other clouds. Depicted is the reduction in cloud droplet size and increase in droplet number along with the suppression of light rain in Fig. 1.5 (left). Increasing aerosol leads to more numerous but smaller droplets that are less likely to precipitate out and more likely to reach the freezing level; then freezing releases latent heat to invigorate updrafts and increase cloud top heights, as shown in Fig. 1.5 (middle). Figure 1.5 (right) shows that the delayed light precipitation and increased water content in the cloud foster heavy precipitation, an increased anvil area, increased ice particles aloft (which can sublimate and alter the water vapor budget aloft), and potentially spawn new cloud systems, thus increasing the cloud cover/lifetime.

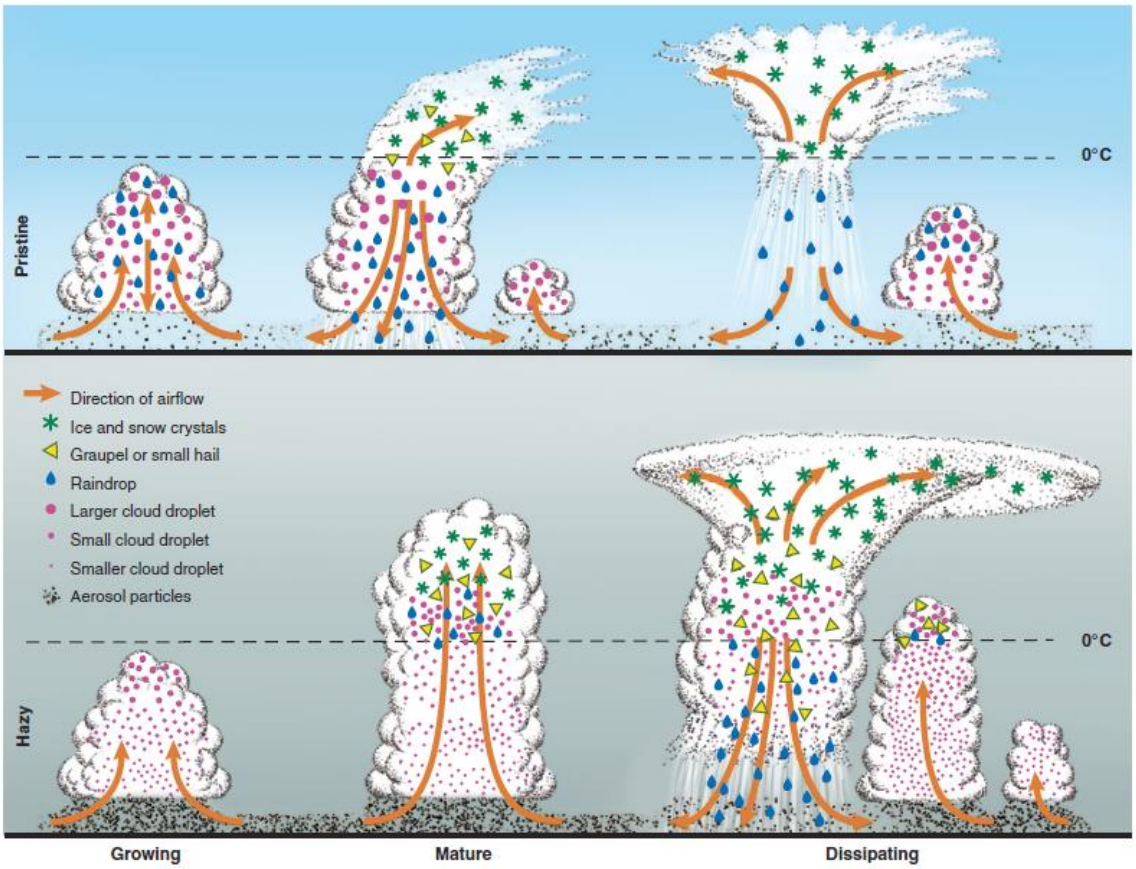

Figure 1.5: Cartoon depiction of various ACI comparing (top) pristine and (bottom) hazy aerosol situations. From Rosenfeld et al. (2008).

One additional effect aerosols have on clouds is known as the "semi-direct" effect. This is more common for light-absorbing aerosols. By absorbing solar radiation, these aerosols tend to warm the atmosphere at the height where they are present. The semi-direct effect can affect clouds by both burning off clouds (e.g. Ackerman et al., 2000) or by inhibiting their development through increasing atmospheric stability below the aerosol layer and decreasing stability above (Lohmann and Feichter, 2005; Wang et al., 2013; Li et al., 2016).

The radiative forcing resulting from ACI is difficult to quantify and can result in either a positive or negative forcing. For example, studies put the all-sky direct radiative forcing at TOA between −0.5 to −2.0 W/m^2 over oceans with methods using a percentage perturbation on AOD (Nakajima et al., 2001) and by separating natural from total AOD (Su et al., 2013). A positive TOA forcing can be seen from aerosol mediated changes to deep convective clouds and anvils (e.g. Koren et al., 2010; Yan et al., 2014). Assessment of the cloud radiative forcing resulting from ACI is further complicated by uncertainties in assessing the strength of ACI, and can potentially lead to a range between −3 and −10 W/m^2 (McComiskey and Feingold, 2008). This variability can come from using different approaches, different proxies for the aerosol, and constraints on cloud liquid water path. At present, the radiative forcing by cloud adjustments due to aerosols has one of the largest uncertainties of our understanding of climate change (IPCC, 2013).

1.3.4 Aerosol Impacts on Humans and Legislation

Briefly mentioned in the Section 1.1 were aerosol impacts on human well-being. Heavy and rapid industrialization occurred with minimal care to environmental and human impacts, a situation which may still exist in some developing parts of the world today. Lethal smog events in Belgium in 1930 (Nemery et al., 2001), in the United States in 1948 (Seinfeld, 2004), and in England in 1956 (Bell and Davis, 2001) have been linked to heavy pollution from sulfate and carbon emissions. Other pollutants such as nitrogen oxides (NO_x) and volatile organic compounds (VOCs) undergo photochemical reactions

to produce ground-level ozone, which contributes to photochemical smog in places like California (Haagen-Smit, 1952) and Mexico (Gold et al., 1999). Ammonium-nitrate and -sulfate salts can dissociate in aqueous solutions within cloud drops, causing an acidic solution and the phenomenon of acid rain which can negatively affect terrestrial and aquatic biological life and human structures (Seinfeld, 1986; 2004).

Recognizing that these problems result from anthropogenic emissions, efforts within the United States have since been undertaken aiming to reduce air pollutants and improve air quality. The establishment of the Environmental Protection Agency (EPA) in 1970 formed a government entity that monitors the environment and enforces standards from environmental laws. Legislations such as the Clean Air Act in 1970 (and subsequent amendments in 1977 and 1990) allow the EPA to establish and administer National Ambient Air Quality Standards (NAAQS) to control air pollution on a national level (U.S. EPA, 2004a,b). The NAAQS have been reviewed several times, including in 1971, 1987, 1997, and 2004 (U.S. EPA, 2004a). The stricter (through time) NAAQS have led to significant reductions in emissions of various harmful pollutant gases. For example, Figure 1.6 shows the reductions in NO_x and sulfur dioxide (SO_2) from power plants in the mid-Atlantic U.S. states (see also He et al., 2013; 2016). On a larger scale, Xing et al. (2013) developed an emission inventory for the U.S. during 1990 to 2010 covering 49 emissions sectors (e.g. electrical power generation, mobile vehicles, and industrial processes) which shows substantial reductions in pollutants and precursor emissions.

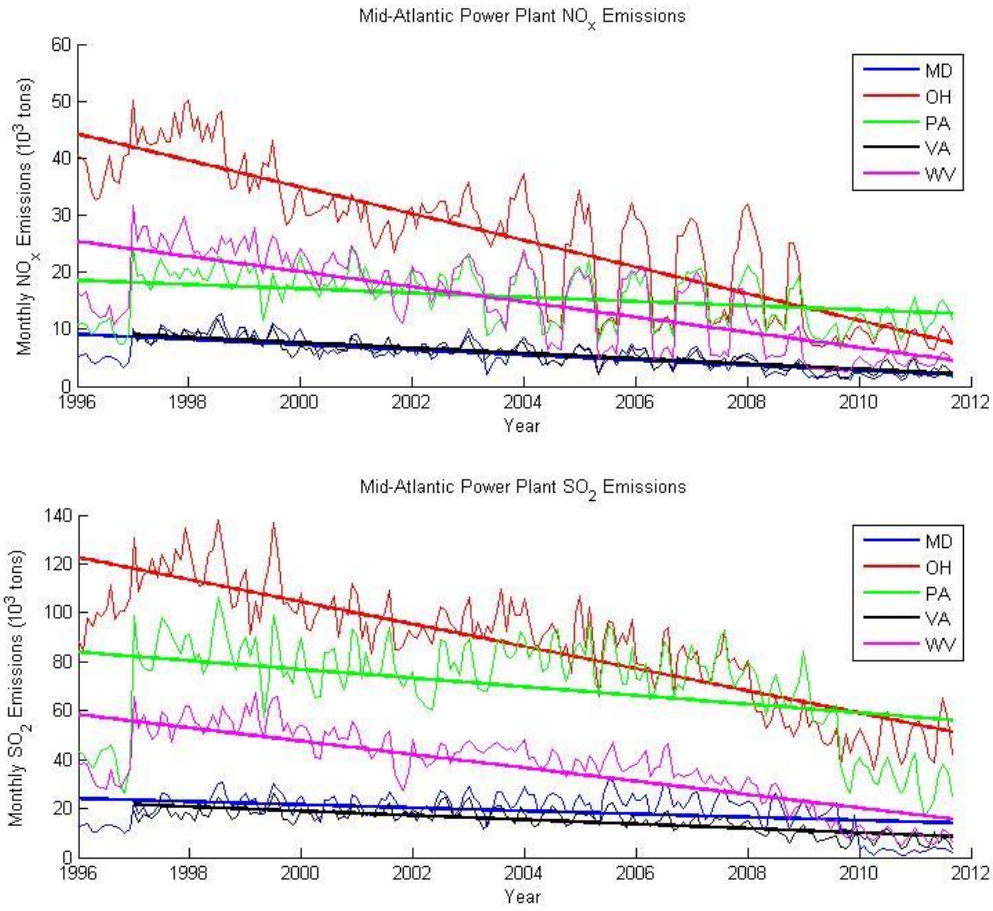

Figure 1.6: Reduction in (top) NO_x and (bottom) SO_2 emissions from power plant stations in five mid-Atlantic states (colors; solid linear trend line fitted) from 1996 to 2012. Data from the EPA Continuous Emissions Monitoring System (CEMS), following after He et al. (2013; 2016).

As mentioned in Section 1.2.1, aerosol emissions come from primary pollutants (directly emitted particles) and secondary pollutants (evolving within the atmosphere). Aerosols are often measured in terms of particulate matter (PM) at or near ground level. Those aerosol particles with aerodynamic diameter under 2.5 μm are commonly known as $PM_{2.5}$. Many attempts have been made to estimate $PM_{2.5}$ from AOD by virtue of correlations between them, including studies by Wang and Christopher (2003), Engel-Cox et al. (2004), and Webber et al. (2010). Alston et al. (2012) demonstrate decreasing trends in surface $PM_{2.5}$ and satellite AOD over regions of the eastern U.S. AOD-$PM_{2.5}$

correlations suffer from large uncertainties due to unknown vertical distribution of aerosol loading, boundary layer or mixing-layer height, hygroscopic growth, and aerosol size distribution. As such, AOD-$PM_{2.5}$ correlations remain around $R > 0.7$ and improve when using 24-hr versus hourly PM data (Green et al., 2009; Hoff and Christopher, 2009).

Recent work has begun to explore the direct and indirect effects of decreasing trends in $PM_{2.5}$ and subsequent AOD. For example, Leibensperger et al. (2012) uses historical U.S. emissions inventories in model simulations to show a reduction in magnitude of both aerosol direct and indirect forcings over the eastern U.S. from 1980 through 2010. Analysis using surface networks of PM and radiation measurements from Gan et al. (2014) support these modeling results: decreases in AOD and $PM_{2.5}$ occur while increases in both clear- and all-sky downward SW radiation at the surface. Finally, in a more global study, Yu et al. (2013) find a reduction in anthropogenic emission of 20% in the Northern Hemisphere reduces AOD by 0.02 to 0.04 and increases the all-sky DRF 0.4 to 0.6 W/m^2 (0.6 to 1.0 W/m^2) at the TOA (surface), depending on region, and shows the global impact of regional reductions.

1.4 Objectives and Outline

This study aims to investigate the aerosol loading, identify any trends, and explore their direct and indirect effects over the North Atlantic Ocean during 2002 to 2012. It is

anticipated (from past studies of emissions inventories and PM monitoring; see Section 1.3.4) that a reduction in anthropogenic emissions from the eastern U.S. will be seen in the aerosol loading as a decreasing AOD trend downwind over the mid-latitude ocean. Observations from the MODIS sensor onboard the Aqua spacecraft are used to examine the total AOD and quantify its trend. Analysis of AOD from surface AERONET sites upwind over the U.S. provides ground-based confirmation near the anthropogenic emission source (i.e. the eastern U.S.). Aerosol speciation from ground-based $PM_{2.5}$ observations and chemical transport model output are then used to attribute natural versus anthropogenic causes to any trends seen. Additionally, a method using solely MODIS observations is applied to distinguish natural from anthropogenic aerosol. An unrelated positive AOD trend in the sub-tropics is linked to African dust and hypothesized to be a result of changes in the summertime North African environment.

The impacts that aerosol trends have on the direct and indirect effects are also explored. Using the Santa Barbara DISORT Atmospheric Radiative Transfer (SBDART) program, several radiative transfer simulations are performed for the total, anthropogenic, natural, and "zero-aerosol" skies, assuming clear-sky conditions. Several methods are studied to attempt to separate natural and anthropogenic components from the total aerosol load, both for the AOD itself as well as assumed optical properties (i.e. AE, SSA, and g). Calculations made are initially representative of an instantaneous aerosol DRE and subsequently improved to cover a monthly mean average daytime DRE. The separation of anthropogenic from natural contributions allows an estimate of the anthropogenic DRE. The aerosol indirect effect is also examined, focusing on the first

indirect effect or Twomey effect. After establishing the general agreement with Twomey theory in the domain from monthly mean data, the Twomey effect using summertime daily mean data is further explored along the U.S. coast to identify nuances in the ACI. While a radiative forcing is not explored here, an attempt is made to highlight differences in the ACI seen early (with increased aerosol load) and late (with decreased aerosol load) during the time period of study.

The outline for this work is as follows. In Chapter 2 the data sets and methods used in this work are detailed. Chapter 3 explores a decreasing AOD trend in the mid-latitude North Atlantic Ocean and identifies it as anthropogenic in nature. In Chapter 4 an increasing AOD trend in the sub-tropics is seen and linked to summertime changes in dust aerosols across the sub-tropical North Atlantic originating from North Africa. Having identified two aerosol trends (one each natural and anthropogenic), the total and anthropogenic DRE are calculated and trends determined in Chapter 5. Chapter 6 establishes the existence of the Twomey effect over the western North Atlantic in a general sense and explores the impact a changing anthropogenic aerosol load may have on ACI in a near-coastal region along the U.S. East Coast. Finally, Chapter 7 provides a summary and limitations of the present work as well as recommendations for the direction of future work.

Chapter 2: Data and Methods

2.1 Observational Datasets

2.1.1 Moderate Resolution Imaging Spectroradiometer (MODIS)

The MODIS instrument is a key component of NASA's Earth Observing System (EOS) mission and has been vital to studying the Earth system (King et al., 1995; 2003). MODIS spans wavelengths from 0.41 to 14.2 μm with 36 spectral bands and spatial resolution of 0.25, 0.5, or 1.0 km depending on band. Both the reflective solar bands (0.41 to 2.11 μm) and thermal emissive bands (3.7 to 14.2 μm) are calibrated separately onboard during orbit and provide accuracy, stability, and degradation monitoring (Xiong et al., 2009). MODIS instruments currently fly on NASA's Terra and Aqua platforms.

Both are in near sun-synchronous polar orbits at an altitude of 705 km. Terra (Aqua) has an equatorial crossing time of 1030 (1330) local solar time (LST), has a 2330 km cross-track by 10 km (at nadir) along-track swath, and can individually provide near-global coverage in less than 2 days (Xiong et al., 2009). This work primarily employs the MODIS Atmosphere Collection 6 (C6) Level-3 monthly mean products (MxD08_M3; Hubanks et al., 2015) of AOD (at 550 nm), liquid cloud optical thickness (COT), effective radius (CRE), and water path (LWP). Aerosol (MxD04_L2 product) and cloud (MxD06_L2 product) properties are spatially averaged from their initial resolutions of 10 km and 1 km (respectively) to a 1º x 1º global grid for the Level-3 product.

AOD from the Level-2 aerosol product is derived using precomputed radiative transfer look-up tables (LUTs) at wavelengths of 0.47, 0.55, 0.65, 0.86, 1.2, 1.6, and 2.1 μm. The observed radiation field is compared with the LUTs for a range of lognormal aerosol models (refractive index, geometric radius, standard deviation, effective radius, extinction coefficient, single scattering albedo, and asymmetry parameter), Sun-Earth-Satellite geometry, atmospheric scattering, and underlying surface parameters (Levy et al., 2009). Over the ocean the algorithm finds the "best" AOD at 550 nm as the weighted (η) combination of reflectances from one (of four) fine (ρ_λ^f) and one (of five) coarse (ρ_λ^c) modes:

$$\rho_\lambda^{LUT}(\tau_{0.55}^{tot}) = \eta\rho_\lambda^f(\tau_{0.55}^{tot}) + (1-\eta)\rho_\lambda^c(\tau_{0.55}^{tot}) \qquad \text{(Eq. 2.1)}$$

that minimize the fitting error between observed and the simulated (ρ_λ^{LUT}) reflectances (Levy et al., 2009). The MODIS Level-2 Collection 5 aerosol product agrees with AERONET retrievals to within the predicted uncertainty (±0.03±0.05*AOD) over ocean (Remer et al., 2005). The update to C6 has modified the expected error over ocean and is now (0.04+10%, -0.02-10%) and exhibits a high bias at low AOD (Levy et al., 2013).

Cloud properties (COT, CRE, and LWP) from the Level-2 product are derived by comparing forward model calculations to observations from non-absorbing (visible/near-infrared) and absorbing (shortwave infrared) channels (Platnick et al., 2015). The 0.65, 0.86, 1.2, 1.6, and 2.1 μm bands are used and compared with cloud LUTs generated for a range of Sun-Earth-Satellite geometry, COT, CRE, and underlying surface albedos (King et al., 1997). LWP is derived from COT and CRE following Stevens (1978) as LWP = (2ρ/3)*COT*CRE, where ρ is the density of water.

Through the course of the present investigations, additional MODIS products are relied upon for additional insight. Data from MODIS Level-3 Collection 5.1 are used to provide a comparison between collections and assess the stability of results given updates to their derivation methods. Additionally, four summers (June, July, and August) worth of the MODIS C6 Level-3 daily mean product are used to provide a better analysis of aerosol-cloud interactions. Additional aerosol products including Ångström exponent (AE or α) and fine-mode AOD are used to provide additional insight into the aerosol loading and its gross size make-up. Finally, the asymmetry parameter (g) from

Collection 5.1 is used to provide a supplementary aerosol property needed in SBDART simulations (note: g was removed from the latest Collection 6).

2.1.2 Aerosol Robotic Network (AERONET)

AERONET is a global network of ground-based sun photometers that provide automatic, high-quality observations of spectral AOD (Holben et al., 1998). AERONET has a proven record of providing a "ground truth" for use in validating satellite aerosol products, including MODIS (e.g. Levy et al., 2010). Spectral AOD at visible wavelengths is derived from direct sun measurements using the Beer-Lambert-Bouguer law and accounting for non-aerosol attenuators (i.e. ozone, water vapor, Rayleigh scatter) (Shaw, 1983; Holben et al., 1998). AERONET sites at Goddard Space Flight Center (GSFC) in Greenbelt, MD (38.992ºN, −76.840ºE), Maryland Science Center (MDSC) in Baltimore, MD (39.283ºN, −76.617ºE), and City College of New York (CCNY) in New York, NY (40.821ºN, −73.949ºE) are used. The aerosol product is monthly mean AOD at 500 nm from the Level 2.0 product using the Version 2 Direct Sun Algorithm (Holben et al., 2006).

2.1.3 Interagency Monitoring of Protected Visual Environments (IMPROVE) network

The IMPROVE network consists of ground-based aerosol and particulate matter (PM) speciation observations at national wilderness and park locations across the United States. Established in 1988, the IMPROVE network collects 24-hour air samples every third day by passing air through four independent sampling filter modules to collect both fine (PM < 2.5 μm; $PM_{2.5}$) and course particles (PM < 10 μm; PM_{10}; http://vista.cira.colostate.edu/Improve/improve-program/). Data from the IMPROVE network have been used throughout the U.S. to monitor the absolute mass concentration, relative contribution, and seasonality of various $PM_{2.5}$ species (e.g. Malm et al., 1994; Hand et al., 2011). Data from the "IMPROVE Aerosol, RHR (New Equation)" (code: IMPRHR2) at four sites in the eastern U.S. are used: Washington D.C. (WASH1; 38.876ºN, −77.034ºE), Cape Cod, MA (CACO1; 41.976ºN, −70.024ºE), Acadia ME (ACAD1; 44.337ºN, −68.261ºE), and Brigantine, NJ (BRIG1; 29.465ºN, −70.024ºE). Six species are considered, including ammonium sulfate (AS), ammonium nitrate (AN), particulate organic matter (POM), light-absorbing carbon (LAC), soil (SOIL), and sea salt (SS) as well as their sum total (TOT). A simple monthly mean is constructed for each species.

2.1.4 Clouds and the Earth's Radiant Energy System (CERES)

Like MODIS, the CERES instrument is a key component of NASA's EOS mission for studying the Earth system. CERES is a broadband scanning radiometer providing observations of the Earth in the shortwave (SW; 0.3 – 5.0 μm), total (0.3 – 200 μm) and window (8 – 12 μm) regions of the electromagnetic spectrum. CERES flies on both Terra (1030 LST equator crossing time) and Aqua (1330 LST equator crossing time) platforms and has a spatial resolution of approximately 20 km (Wielicki et al., 1996, 1997). Data for this work comes from CERES flying on Aqua and the Single Scanner Footprint (SSF) dataset (Geier et al., 2003).

The CERES SSF product provides CERES measured instantaneous top-of-atmosphere (TOA) fluxes combined with complementary observations of the viewing scene from MODIS (e.g. clouds and aerosol; Geier et al., 2003). The instantaneous fluxes are inverted from the unfiltered CERES observed radiances (at the TOA) by applying scene-appropriate angular distribution models (ADMs) that relate radiance to flux at the overpass time (Green et al., 1997). TOA fluxes are then sorted by space and time, and an Earth Radiation Budget Experiment (ERBE) -like temporal averaging (using AMDs of albedo) is applied to generate a gridded monthly mean flux product (Young et al., 1997). Clear-sky SW fluxes at the TOA from the CERES SSF1deg Monthly Mean product for Aqua (ed. 4A) are used for this work, specifically to validate SBDART simulations in Chapter 6.

2.2 Model Datasets

2.2.1 Modern Era-Retrospective Analysis for Research and Applications (MERRA)

MERRA is NASA's atmospheric reanalysis product. A reanalysis is a method of running a model while simultaneously assimilating observations (not constrained to be regular in space and time) to produce gridded model output which spans an observational record (Rienecker et al., 2011). MERRA is run using NASA's Goddard Earth Observing System (GEOS) atmospheric model (v5.2.0; GEOS-5) and data assimilation system (DAS) and is documented fully in Rienecker et al. (2008). MERRA was motivated by the desire to improve the representation of the hydrological cycle over prior reanalyses in which the water cycle was inadequate for weather and climate studies (Rienecker et al., 2011). A full list of assimilated observations is found in Rienecker et al. (2011).

MERRA produces instantaneous output at a horizontal resolution of 0.50º latitude by 0.66º longitude on 42 vertical levels at 3 hr intervals. The dataset used in this work is the "inst(3/U)_3d_asm_Cp" which is the 3-D assimilated state on pressure levels. This dataset is for instantaneous output at 3 hr intervals (00, 03, 06, .., 21 GMT) where the "3" indicates 3-hourly output and the "U" indicates monthly means of 3-hourly output (note: "U" provides the monthly mean diurnal cycle and is not the entire monthly mean). Table

2.1 lists the parameters of the inst(3/U)_3d_asm_Cp dataset. Those used in this work include SLP, H, O3, QV, T, U, V, EPV, OMEGA, and model vertical pressure grid.

Variable Name	Dims	Description	Units
SLP	2D	Sea-level pressure	Pa
PS	2D	Surface pressure	Pa
PHIS	2D	Surface Geopotential	m2s-2
H	3D	Geopotential height	m
O3	3D	Ozone mixing ratio	kg kg-1
QV	3D	Specific humidity	kg kg-1
QL	3D	Cloud liquid water mixing ratio	kg kg-1
QI	3D	Cloud ice mixing ratio	kg kg-1
RH	3D	Relative humidity	percent
T	3D	Air temperature	K
U	3D	Eastward wind component	m s-1
V	3D	Northward wind component	m s-1
EPV	3D	Ertel potential vorticity	K m2 kg-1s-1
OMEGA	3D	Vertical pressure velocity	Pa sec-1

Table 2.1: Parameters of the inst(3/U)_3D_asm_Cp MERRA reanalysis dataset (Ostrenga, 2010).

2.2.2 Goddard Chemistry Aerosol Radiation and Transport (GOCART) model

GOCART is a global chemical transport model capable of simulating aerosol components within the troposphere throughout their lifetime, with processes including emission, chemistry, advection, boundary layer mixing, moist convection, and wet and dry deposition (Chin et al., 2002). Meteorology for GOCART comes from the MERRA reanalysis, and data is output on a 2.0º latitude by 2.5º longitude grid with 72 vertical levels (Chin et al., 2014). The time step for all processes is 60 min except for advection,

convection, and diffusion which occur on a 20 min time step (Chin et al., 2000). GOCART simulates sulfate (SU), dust (DU), organic carbon (OC), black carbon (BC), sea salt (SS), and combined total (TOT) components of the AOD.

Emissions of natural aerosols in GOCART are parameterized using a variety of methods. Foliar density and biome-dependent emissions factors are used for land-based organic carbon emissions (Guenther et al., 1995). Desert dust is parameterized using surface elevation, bareness, wetness, and 10 m wind (Ginoux et al., 2001). Volcanic emissions of SO_2 are from the Global Volcanism Program at the Smithsonian Institution (http://www.volcano.si.edu/). Dimethyl sulfide (DMS) emissions from the ocean are parameterized using DMS concentration, water viscosity, and the 10 m wind (Lana et al., 2011). Finally, the 10 m wind is used to parameterize sea salt emission (Chin et al., 2002).

Anthropogenic emissions from the A2-ACCMIP and A2-MAP datasets are used within the GOCART model (Diehl et al., 2012; Chin et al., 2014; and references therein). Monthly fossil fuel emissions are interpolated based on the Representative Concentration Pathway for 8.5 W/m^2 (RCP8.5) projections for the years 2000, 2005, and 2010. Ten land-based sectors are interpolated to a constant yearly emission. International shipping emissions are interpolated from year 2000 using the EDGAR 23FT2000 dataset. Biomass burning emissions for A2-ACCMIP are derived from the Global Fire Emissions Database (GFED), version 2. Lastly, monthly aircraft emissions are interpolated from 1992 with projections for 2015 are used.

GOCART computes AOD for each species based on modeled column mass concentration and assumed size, optical, and density properties (Chin et al., 2002). A lognormal size distribution is assumed for each aerosol type, and using the aerosol properties in Table 2.2, AOD is computed as:

$$\tau = \frac{3QM}{4\rho r_e} \qquad \text{(Eq. 2.2)}$$

where Q is the extinction coefficient calculated from Mie-scattering theory, M is the mass loading per unit area, ρ is the particle density, and r_e is the effective radius. A higher resolution GOCART run was made available for the period 2001 to 2009 and configured at horizontal resolution of 0.50º latitude by 1.25º longitude with 3-hourly output. Monthly mean column AOD at 500 nm has been calculated for each species and the total loadings. Additional monthly mean spectral single scattering albedo (SSA(λ)) have also been computed to provide supplementary aerosol properties for use in SBDART simulations. SSA is provided at wavelengths of 0.35, 0.45, 0.55, 0.65, 0.9, 1.0, and 1.5 μm.

Aerosol type	Density (g cm^{-3})	r_m (μm)	r_e (μm)	σ_g (μm)	Q at 500 nm	Refractive index at 500 nm
Sulfate*	1.7	0.0695	0.156	2.03	1.343	$1.43 - 10^{-8}i$
OC*	1.8	0.0212	0.087	2.20	0.680	$1.53 - 0.005i$
BC*	1.0	0.0118	0.039	2.00	0.557	$1.75 - 0.45i$
Dust	2.6	0.0421	0.14	2.00	1.298	$1.53 - 0.0078i$
	2.6	0.0722	0.24	2.00	2.201	$1.53 - 0.0078i$
	2.6	0.1354	0.45	2.00	2.768	$1.53 - 0.0078i$
	2.6	0.2407	0.80	2.00	2.682	$1.53 - 0.0078i$
	2.6	0.4212	1.40	2.00	2.421	$1.53 - 0.0078i$
	2.6	0.7220	2.40	2.00	2.277	$1.53 - 0.0078i$
	2.6	1.3540	4.50	2.00	2.178	$1.53 - 0.0078i$
Sea salt	2.2	0.228	0.80	2.03	2.696	$1.50 - 1.55 \times 10^{-8}i$
	2.2	1.64	5.73	2.03	2.143	$1.50 - 1.55 \times 10^{-8}i$

Table 2.2: Aerosol properties used in GOCART for conversion from column mass loading to AOD. Optical properties are based on the Global Aerosol Data Set (GADS; Kopke et al., 1997). r_m is modal radius, r_e is effective radius, σ_g is geometric standard deviation in lognormal size distribution, and Q is the extinction coefficient. All values for dry aerosols at 500 nm. Dust and sea salt contain multiple bins. Table is from Chin et al. (2002). (*assuming a maximum radius at 0.5 μm).

2.2.3 Santa Barbara DISORT Atmospheric Radiative Transfer (SBDART) model

The SBDART model is a radiative transfer algorithm written in FORTRAN and tailored for a variety of applications in satellite remote sensing and atmospheric radiation budget studies. SBDART provides spectral coverage from ultraviolet to infrared wavelengths and includes all important attenuating processes within this region. Model output includes spectral and integrated (using the trapezoid rule) radiative fluxes (Ricchiazzi et al., 1998).

SBDART can accept a myriad of inputs, both user- and pre-defined. The model can be configured for a given Sun-Earth-(Sensor) scenario or can use a time of day, date, and location to determine relevant geometries. Solar spectra, surface spectral reflectance properties, and atmospheric profile can be defined or use pre-determined values. While

not used in the present work, SBDART includes a module to include up to five cloud layers and relevant properties for each. Outputs from SBDART include upward, downward, and direct spectral radiative fluxes at two model heights. Further information about input/output options can be found in the SBDART Read-Me document by Ricchiazzi (2002). Here in this work output is specified for the surface (0 km) and TOA (100 km) and is integrated to provide the total flux from 0.2 μm to 5.0 μm.

Aerosol Parameter	**Parameter Description**
IAER*	Boundary layer aerosol type selector; options include none, predefined, and user defined spectral dependence
RHAER	Sets the spectral dependence relative humidity sensitivity used in the predefined boundary layer aerosol models; has no effect on user defined aerosol model
VIS	(Horizontal Path) Visibility (km) at 0.55μm due to boundary layer aerosols. VIS does not set the optical depth for the user defined aerosol model but does affect it through the vertical structure.
ZBAER	Altitude grid for custom aerosol vertical profile (km). If not set, VIS sets the exponential scale height between 1.05 and 1.51 km.
DBAER	Aerosol density at ZBAER altitude grid points.
TBAER*	Vertical optical depth of boundary layer aerosols at 0.55μm.
QBAER *	QBAER is the extinction efficiency. When TBAER is set, QBAER sets the spectral dependence of the extinction optical depth as: $\tau(\lambda) = \tau(0.55\mu m) * Q_{ext}(\lambda)/Q_{ext}(0.55\mu m)$
WLBAER *	Wavelengths (μm) for user defined aerosol spectral dependence.
WBAER *	Single scattering albedo of boundary layer aerosols at λ = WLBAER.
GBAER *	Asymmetry factor of boundary layer aerosols at λ = WLBAER.
PMAER	Legendre moments of the scattering phase function of boundary layer aerosols. Supersedes GBAER when set.
ABAER *	Wavelength (Ångström model) exponent used to extrapolate BLA extinction efficiency to wavelengths outside the range of WLBAER using $Qext \approx \lambda \wedge -ABAER(\lambda)$

Table 2.3: Boundary layer aerosol input parameters and description (Ricchiazzi, 2002). Note that parameters with an ***** are those modified with user-defined values for aerosol direct radiative forcing calculations (see Chapter 5).

Important to the present work is the boundary layer (tropospheric) aerosol module. In addition to four built-in aerosol types, SBDART can accept user input for

tropospheric aerosols, which provides utility for the use of observational data in calculations. A description of the boundary layer aerosol inputs is in Table 2.3. Further specification of the inputs used for each aerosol parameter and for a given experiment setup are provided in Section 5.1.

2.3 Methods of Analysis

All analyses are performed using the MATLAB software except for SBDART radiative transfer calculations which use FORTRAN.

2.3.1 Deseasonalizing and Trending

One of the main methods utilized in this work is an algorithm to determine the trend in time series and is shown in Fig. 2.1. The trends of interest are those that potentially span several years or more and not those that may exist across shorter timescales such as between a few months. The first step taken is to deseasonalize a time series by removing the mean annual cycle (i.e. seasonality) for the period considered:

$$\tau_d(m, y) = \tau_n(m, y) - \tau_c(m) \qquad \text{(Eq. 2.3)}$$

where $\tau_n(m,y)$ is the native AOD time series, $\tau_c(m)$ is the mean annual AOD climatology, $\tau_d(m,y)$ is the deseasonalized AOD time series, and m and y are the month and year, respectively. This formulation is also generalized to other variables in addition to AOD. In addition to annual trends, some analyses are performed for seasonal trends. The seasons are defined as winter (December, January, and February; DJF), spring (March, April, and May; MAM), summer (June, July, and August; JJA), and fall (September, October, and November; SON). Using a deseasonalized time series (again, to focus on the interannual trend), the months relevant to a given season are averaged for a given year.

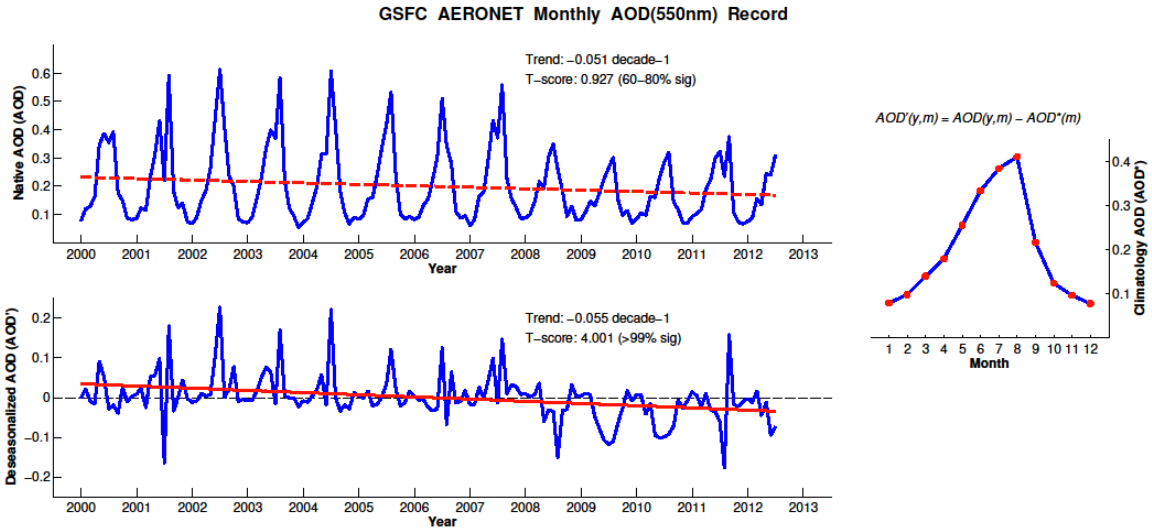

Figure 2.1: Example of deseasonalizing and trend algorithm using the GSFC AERONET record of AOD(550nm) from 2000 to 2012. (top) Native record with trend = −0.051 per decade (not significant). (bottom) Deseasonalized record with trend = −0.055 per decade (significant beyond 95%). (right) Mean annual cycle.

The trend for a time series is determined using a simple linear regression of the form Y=a+b*X, where X is time, Y is the estimated value from the regression, and a and b are the least-squares estimates of the offset and slope for the regression. The statistical

significance of a calculated trend is determined using the student's t-test and Eq. (2.4a) below:

$$T = \frac{b}{\sigma/\sqrt{S}} \qquad \text{(Eq. 2.4a)}, \qquad T = |R|\sqrt{\frac{n-1}{1-R^2}} \qquad \text{(Eq. 2.4b)}$$

where b is the slope of the fit, σ is the standard deviation of the fit errors, and $S = \sum(X_i - \bar{X})^2$ (von Storch and Zwiers, 1999). The statistical significance of an aerosol component trend is tested against the respective total so as to focus on component trends that are significant in the context of the total loading. A correlation analysis is performed between AERONET sites and MODIS observations, and the significance is tested according to Eq (2.4b) above where R is the correlation coefficient and n the degrees of freedom (i.e. number of months). The T-scores computed are compared against a table for the student's T distribution and thresholds for both the 90% and 95% confidence intervals using a null hypothesis $H_0 = 0$: for trend studies this is equivalent to a time series with no trend (i.e. H_0: b = 0) while for correlation studies this assumes no correlation (i.e. H_0: R = 0). The formulations in Eq. (2.4) reflect these null hypotheses and are dependent on the degrees of freedom (i.e. number of months) considered.

The significance of a trend (i.e. Eq. 2.4a) is a trade-off between several factors. These include the magnitude of the trend, the standard deviation of errors between the data and assumed fit, and the number of degrees of freedom (or length of record). Given a certain value b for a trend, the significance of this trend can increase if the standard deviation of the fit errors is small (i.e. a very good fit) and/or there are many degrees of

freedom (i.e. a long record). Uncertainties in the observations of aerosols (for example) can come from inaccurate calibration, inaccurate surface correction, and uncertainties in the aerosol inversion. Increasing uncertainty in these aspects can cascade into uncertainty in the aerosol product and further into uncertainty in the trend assessment via large standard deviation in the fit errors. This can be ameliorated by assessing trends on a long period, where the increase in observations (degrees of freedom) can offset some uncertainty from the fit errors. As will be shown through the subsequent chapters, the datasets used permit the determination of broad regional trends at the 95% statistical significance level.

2.3.2 Dust/Anthropogenic Estimation Following Kaufman et al. (2005a,b)

In addition to examining GOCART specieated AOD trends, a method pioneered by Kaufman et al. (2005a) is explored. The value of this method comes from using actual observations to estimate marine, dust, and anthropogenic contributions to the total aerosol load. The MERRA reanalysis will be used to provide the necessary winds. The method and assumptions made are briefly summarized here; full discussion is offered in Kaufman et al. (2005a). It is assumed that the total AOD (τ_t) observed by MODIS is the linear sum of AOD from marine (τ_m), dust(τ_d), and anthropogenic (τ_a) components:

$$\tau_t = \tau_m + \tau_d + \tau_a \qquad \text{(Eq. 2.5)}$$

The marine AOD can be reasonably parameterized as a function of oceanic surface wind speed (W_{1000}; e.g. Smirnov et al., 2003):

$$\tau_m = 0.007 * W_{1000} + 0.02 \quad \text{(Eq. 2.6)}$$

It is assumed that the fine-mode of each aerosol type also linear sum to the fine-mode of the total aerosol loading:

$$f_t * \tau_t = f_m * \tau_m + f_d * \tau_d + f_a * \tau_a \quad \text{(Eq. 2.7)}$$

where f_x is the appropriate fine-mode fraction. While f_t was a part of the MODIS aerosol product for Collection 5, it is no longer reported in Collection 6. Instead, the AOD of the fine-mode is reported, and f_t is thus determined as the ratio of fine-mode AOD to total AOD. Fine-mode fractions for the components are $f_m = 0.3$, $f_d = 0.5$, and $f_a = 0.9$. These f_x have been determined in regions where that component is assumed to be the dominant aerosol type making up the total loading: f_m in the South Indian Ocean, f_d west of the African coast, and f_a over the mid-latitude Western Atlantic Ocean (see Kaufman et al. (2005b) for domains).

From Eq. (2.5) and (2.7) we have a system of two equations with six unknowns (τ_x and f_x). Using MODIS for τ_t and f_t, Eq. (2.6) for τ_m, and estimates of f_m, f_d, and f_a the system is reduced to two unknowns (τ_d and τ_a) for which either can be solved for. The expression for τ_d is thus:

$$\tau_d = \frac{1}{f_a - f_d} * [\tau_t(f_a - f_t) - \tau_m(f_a - f_m)] \quad \text{(Eq. 2.8)}$$

and a similar expression can also be derived for τ_a (as in Kaufman et al. (2005b)):

$$\tau_a = \frac{1}{f_d - f_a} * [\tau_t(f_d - f_t) - \tau_m(f_d - f_m)] \quad \text{(Eq. 2.9)}$$

Kaufman et al. (2005a) extends this method and provide estimates of the dust mass loading (M_d) and zonal dust flux (F_d). An expression equivalent to that used in GOCART to convert from mass to optical depth (see Eq. 2.2) is used and provides a mass to optical thickness conversion ratio (M_d/τ_d) of 2.7±0.4 g/m^2. Finally, with the knowledge that dust transport across the North Atlantic occurs at heights around 2-5 km (e.g. Yu et al., 2015) and is also heavily influenced by the African Easterly Jet and Waves near West Africa (e.g. Jones et al., 2003), F_d is parameterized as the product of M_d, zonal wind speed at 700 hPa (U_{700}), and longitudinal length L through which the flux is computed:

$$F_d = (-1) * M_d * U_{700} * L \quad \text{(Eq. 2.10)}$$

where the factor of −1 is included to ensure $F_d > 0$ due to $U_{700} < 0$ in the main dust transport region between 5ºN and 25ºN. Kaufman et al. (2005a) estimates uncertainties of 15% in τ_d, 30% in M_d for AOD in the 0.2 to 0.4 range, and 35% in F_d. Thus, it is

believed that this method provides sufficient estimates for an observational estimate of dust loading.

2.3.3 Direct Effect – Attenuation of Radiation

As noted in Section 1.3.2 ("Aerosol Direct Effects"), aerosols interact directly with solar radiation through the attenuation processes of scattering and absorption. Aerosols play a role in determining the radiative balance and forcing of the Earth system in the shortwave (SW) region of the electromagnetic spectrum. For a given quantity (e.g. top-of-atmosphere (TOA) outgoing SW flux), the direct radiative forcing (DRF) due to aerosols is expressed as:

$$DRF_{TOA} = \int F_a(\lambda) - F_c(\lambda) d\lambda \qquad \text{(Eq. 2.11)}$$

where $F(\lambda)$ is the outgoing spectral flux for an atmosphere with aerosol loading (F_a) and for clean sky (F_c), and is integrated over wavelengths λ that comprise the relevant part of the electromagnetic spectrum (here, the SW portion is taken to be $0.2 < \lambda < 5$ μm). The aerosol DRFs assessed in this work are for cloud-free skies.

The aerosol DRF (and how it may be changing) is a component of this work, and the SBDART model (described in Section 2.2.3) will be used to simulate numerous situations with varying assumptions of atmospheric aerosol load. Using Eqn. 2.11 the

aerosol DRFs can be computed for a given quantity (TOA outgoing radiation in the case of Eqn. 2.11) from the 8 flux calculations performed with SBDART (4 each (TOA and bottom (BOT) downward and upward fluxes) for 2 cases (clean and aerosol-laden sky)) in addition to three additional derived fluxes (Earth system (ES_a), atmospheric (ATM_a), and surface (SFC_a) absorbance). A schematic diagram of relevant fluxes is shown in Figure 2.2.

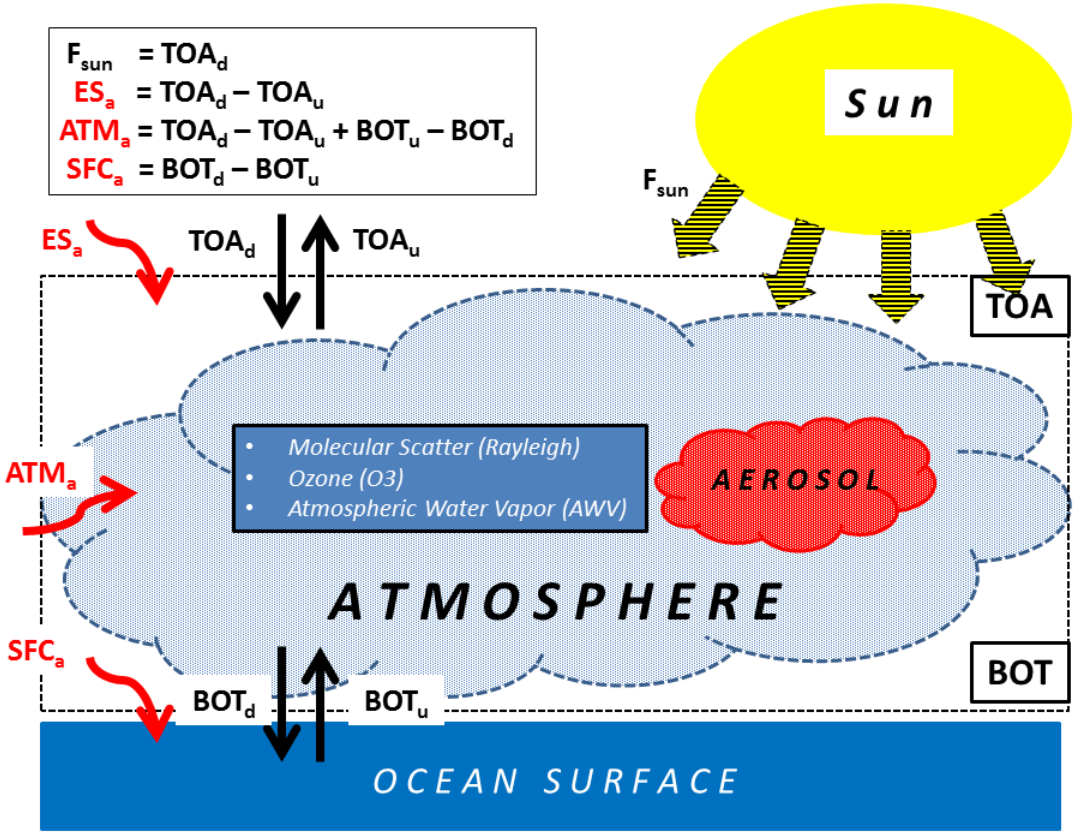

Figure 2.2: Schematic depiction of relevant spectral flux quantities in the solar SW spectrum calculated with SBDART. Quantities include TOA and BOT upward (u-subscript) and downward (d-subscript) fluxes. Three additional derived fluxes are computed as in the box in the upper left: ES_a, ATM_a, and SFC_a absorbances (a-subscript).

The most elementary calculation of the aerosol DRF uses appropriate aerosol properties for an aerosol-laden simulation and switches off all aerosol parameters within

the SBDART model to simulate a completely "clean" clear sky. This "clean" sky scenario is acknowledged to be an exaggeration, as the atmosphere is never completely devoid of aerosol particles. However, this "clean" sky scenario is informative as it provides an estimate of the total aerosol DRF and can provide an upper bound on the anthropogenic aerosol DRF. In addition to this "clean" clear sky scenario, four other clear sky cases are constructed with the goal of removing the anthropogenic contribution to the aerosol load while remaining simple enough to still rely on aerosol parameters readily available from both MODIS and GOCART datasets. These cases consist of two methods to separate the anthropogenic AOD from the total AOD (thus retaining an estimate of the natural AOD) and two methods of supplying supplemental aerosol properties (i.e. spectral SSA, g, and AE).

Detailed discussion of the methods can be found in Section 5.2. Briefly, the anthropogenic AOD at 550 nm is estimated using either the percent contribution seen in the GOCART model or a method from Kaufman et al. (2005b) (see Section 2.3.2). One method for providing the supplemental aerosol properties (spectral SSA, g, and AE) relies on the observed g from MODIS Collection 5.1 (parameter not included in C6), the monthly mean climatology of SSA from GOCART, and the observed AE from MODIS C6 total AOD (unaltered, still represents the total aerosol load). The other method attempts to modify these supplemental properties to values more representative of non-anthropogenic impacted aerosol loads over the North Atlantic Ocean. To do this, a zonal profile of each supplemental property is created in the sub-tropics (20ºN to 30ºN) to capture the predominant coexistence of dust and marine components (especially the

seasonality of dust loading), a spatial mean of properties representative of a mainly oceanic loading within a mid-latitude region (50ºW to 30ºW, 35ºN to 45ºN) over the entire mid-latitudes (35ºN to 50ºN), and providing a linear blending for the latitudes between the two regions (i.e. 30ºN to 35ºN). These two methods of removing anthropogenic AOD and two methods for estimating supplemental properties provide four unique clear sky scenarios that can be used with the base scenario for total AOD to assess the anthropogenic aerosol DRF (and the methods employed to arrive at anthropogenic aerosol DRF) and compare it to the total aerosol DRF computed with the "clean" (i.e. no aerosols; results in a total aerosol DRF) clear sky scenario.

2.3.4 First Indirect (Twomey) Effect – Aerosol-Cloud Interaction (ACI)

The presence of aerosol is necessary for the formation of clouds from heterogeneous nucleation at ambient temperature and relative humidity conditions (Rogers and Yau, 1989). Additionally, as noted in Section 1.3.3, interaction of aerosols with clouds can have profound impact. These impacts, known as aerosol indirect effects, compare clouds from "clean" and "polluted" aerosol loadings. They include (but are not limited to) effects such as decreasing cloud effective radii, altering precipitation pattern/intensity, invigorating cloud updrafts, and modifying cirrus properties/fraction (e.g. Rosenfeld et al., 2008).

In this work, the first indirect effect (or Twomey effect, after Twomey (1974)) is explored. A theoretical derivation was provided by Feingold et al. (2001; 2003). For a homogeneous cloud, with constant cloud liquid water content (LWC) and droplet number concentration N_d, Twomey (1977) showed that:

$$\tau_d \propto N_d^{1/3} \quad \text{(Eq. 2.12)}$$

where τ_d is the cloud optical depth (COD). Assuming that the N_d and N_a (aerosol number concentration) share a power law relation:

$$N_d \propto N_a^x \quad \text{(Eq. 2.13)}$$

it can be shown that:

$$r_e \propto \tau_a^{-x/3} \quad \text{(Eq. 2.14)}$$

where r_e is the cloud effective radius (CRE) and τ_a the aerosol optical depth. This proportionality can conveniently be written as a power law relationship or in linear form in log-log (all log assumed $\log_{10}$) space as:

$$r_e = 10^b * \tau_a^m \quad \text{(Eq. 2.15a)}$$

$$\log r_e = m * \log \tau_a + b \quad \text{(Eq. 2.15b)}$$

where b (represented as 10^b in Eq. 2.15a) is the constant of proportionality and the slope m of the linear fit in Eq. 2.15b is the exponent −x/3 in Eq. 2.14. Eq. 2.15b provides a convenient way to quantify the aerosol-cloud interaction (ACI_r) simply as the value of the slope m:

$$ACI_r = \frac{\log r_e}{\log \tau_a} = m = \frac{-x}{3} \geq -0.33 \qquad \text{(Eq. 2.16)}$$

where ACI_r is theoretically bounded by x = 0 and x = 1 to produce bounds of $-0.33 < ACI_r < 0$. A characteristic value of $ACI_r = -0.23$ is found by using x = 0.7 (e.g. Feingold et al., 2003, following after Pruppacher and Klett, 1997). This method of determining ACI_r has been used extensively from ground, airborne, satellite, and satellite+model studies (e.g. summarized in Table 1 of McComiskey and Feingold (2012)) and has a range of values from 0.04 to 0.25 across various cloud types, methods, meteorology, parameters used, spatiotemporal scales, and constraint on LWC. The lack of negative sign is due to some authors electing to maintain a negative factor on the log/log, thus producing positive ACI_r values. This may lead to some confusion, as ACI_d (the aerosol-cloud interaction between AOD and COD) is derived analogously with the exception of a negative sign:

$$ACI_d = \frac{\log \tau_d}{\log \tau_a} = m = \frac{x}{3} \leq 0.33 \qquad \text{(Eq. 2.17)}$$

with framework that was laid out by Feingold et al. (2001). Thus, the magnitudes of

ACI_r and ACI_d should be similar while differing in sign, and effort will be made to exaggerate this point when talking about either ACI_r or ACI_d.

An algorithm was developed to determine ACI from observation triplets of r_e (or COT), AOD, and LWP. In order to constrain cloud LWC, LWP (the vertical integral of LWC) is used. 12 bin boundaries are determined based off the cumulative distribution function of log(LWP) in an effort to have similar numbers of cloud-aerosol pairs in each LWP bin. Within each LWP bin, mean(AOD)-mean(r_e) pairs are determined by binning AOD in bins of 0.01. The number of observations that determine each mean(AOD)-mean(r_e) pair are then used as the weights to a linear fit of the mean pairs. Finally, the slope of this weighted linear fit in log-log space of mean(AOD)-mean(r_e) pairs is reported as the ACI_r value for that LWP bin. An example of this method is displayed in Figure 2.3 for clouds with 90 g/m^2 < LWP < 100 g/m^2 and results in $ACI_r = -0.11$.

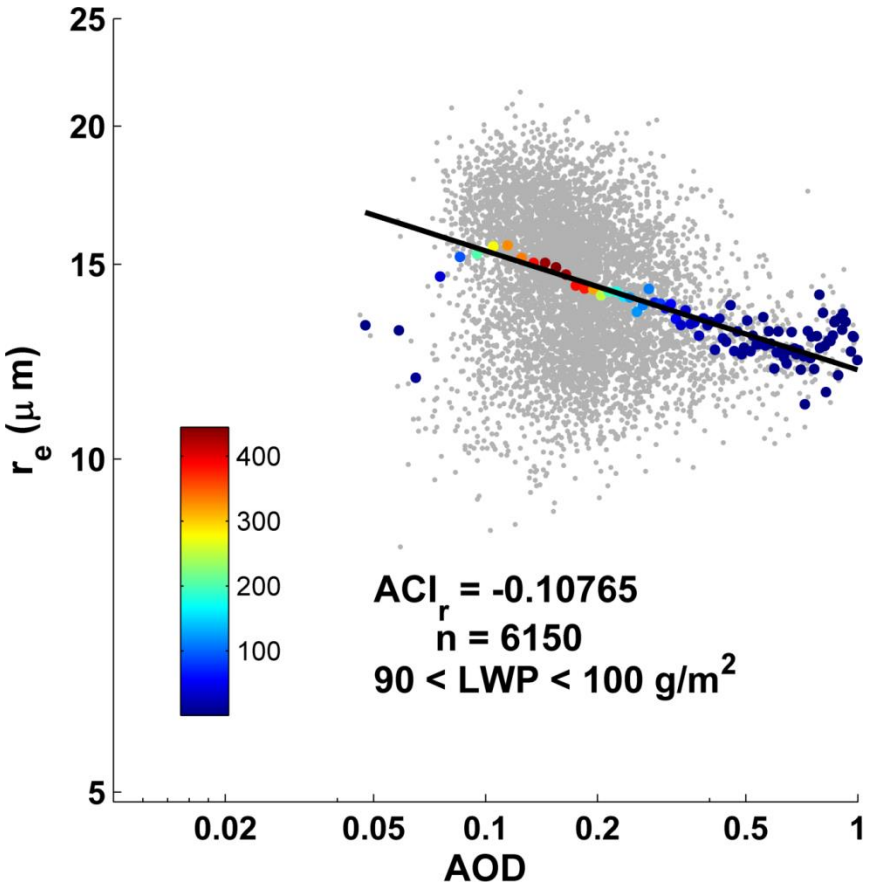

Figure 2.3: Example of ACI_r computation. Data are from MODIS-Aqua C6 monthly mean product from 07-2002 to 12-2012 over the mid-latitude domain (80º-40ºW, 30º -50ºN) within 90 < LWP < 100 g/m^2. Gray points (n=6168) are all AOD-r_e pairs within the LWP bin while the colored points are the mean(AOD)-mean(r_e) pairs in AOD bins sized 0.01. The color represents the number of observations (see colorbar) for each binned pair and is used as a weight in the linear fitting.

Chapter 3: Decreasing Aerosol Trend over the Mid-latitude North Atlantic Ocean

This chapter details the identification and attribution of a negative trend in AOD observed by MODIS over the mid-latitude North Atlantic Ocean. Several of the results are published in the Journal of the Atmospheric Sciences (article citation):

> Jongeward, A., Li, Z., He, H., and Xiong, X. (2016). Natural and anthropogenic aerosol trends from satellite and surface observations and model simulations over the North Atlantic Ocean. Journal of the Atmospheric Sciences. Vol. 73. Pp. 4469-4485. doi:10.1175/JAS-D-15-0308.1.

The geographical domain selected for this work is the mid-latitude western North Atlantic Ocean defined by 80ºW to 40ºW and 30ºN to 50ºN (white box displayed in Fig. 3.1). Monthly mean data during July 2002 through December 2012 are examined for all

datasets except for GOCART, for which data are available during January 2001 through December 2009.

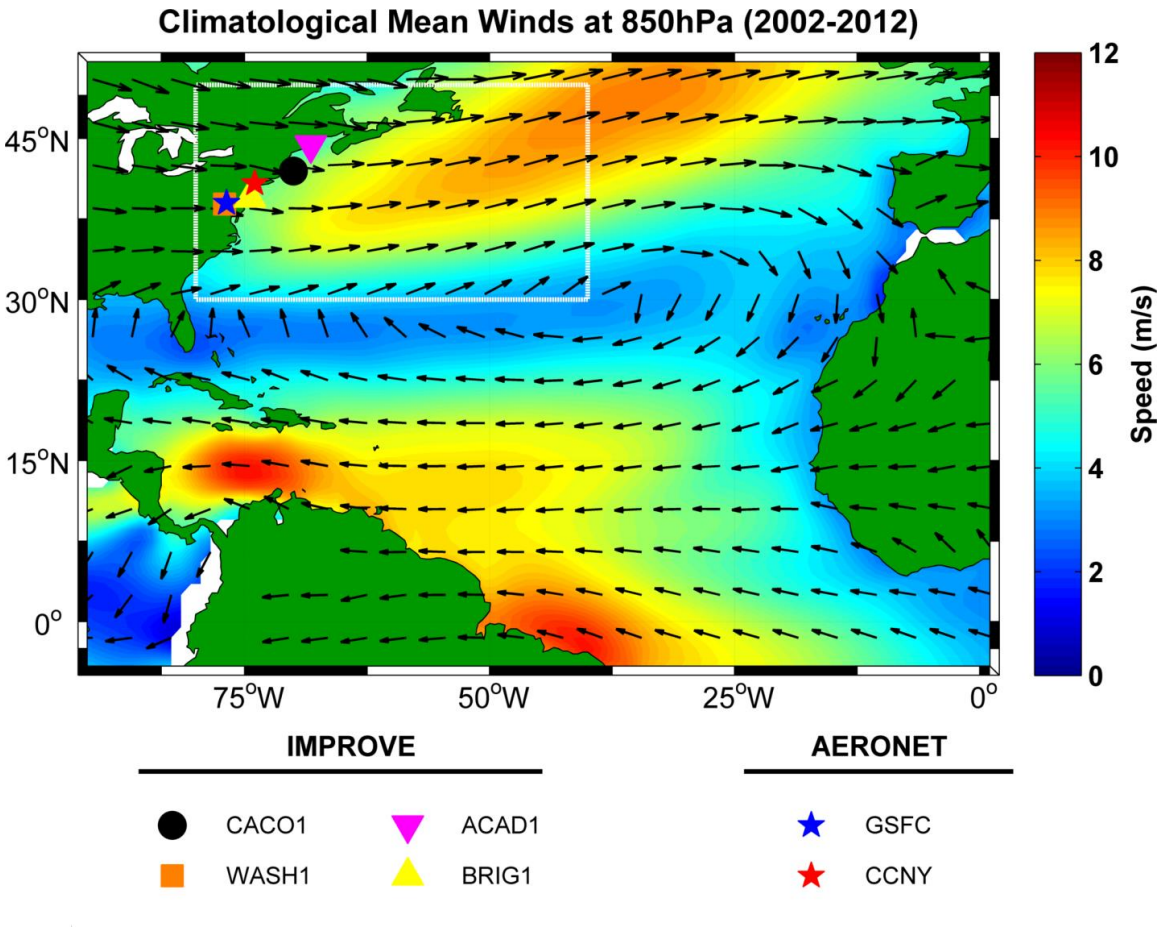

Figure 3.1: Mean climatological circulation over the western North Atlantic Ocean during 07-2002 to 12-2012. Also shown are the locations of surface AERONET and IMPROVE sites. The white box outlines the mid-latitude domain of interest (80º-40ºW; 30º-50ºN).

3.1 Aerosol Trends and Correlation with AERONET

The mean circulation (see Fig. 3.1) over the North Atlantic Ocean will tend to transport aerosol in an anticipated manner, as aerosols emitted from North America will

be advected eastward in the mid-latitudes. Therefore, it is expected that part of the changes in aerosol loading seen over the North Atlantic in the mid-latitudes may be traced back to changes in emissions over the upwind continent. Trends in the deseasonalized total AOD observed by MODIS-Aqua highlight a distinct region over the mid-latitude North Atlantic. Figure 3.2 shows the presence of a statistically significant (> 95%) negative AOD trend with magnitude around −0.02 to −0.04 decade^{-1}. This trend is both spatial coherent and extensive. A comparison of trends from Collection 5.1 (Fig. 3.2(a)) and Collection 6 (Fig. 3.2(b)) demonstrates similarity in trend behavior, location, magnitude, and statistical significance. This is a testament that, in spite of slight changes to the retrieval algorithm during the update from Collection 5 to 6 (see Levy et al., 2013), the observed trend indeed reflects an AOD decrease in the physical world and is not likely an artifact of the retrieval algorithm nor a result of the updates from Collection 5 to 6. Further adding confidence to the reported trend is its agreement with trends for the region found in similar studies. Zhang and Reid (2010) report a trend of −0.015 decade^{-1} from MODIS-Terra during 2000 to 2009 while Hsu et al. (2012) finds a trend of −0.04 decade^{-1} during 1998-2010 using the Sea-viewing Wide Field-of-view Sensor (SeaWiFS). These trends are also in agreement with a −0.02 decade^{-1} trend during 1985 to 2005 reported by Zhao et al. (2008a) using the Pathfinder Atmosphere extended (PATMOS-x) aerosol dataset from Advanced Very High Resolution Radiometer (AVHRR) instruments.

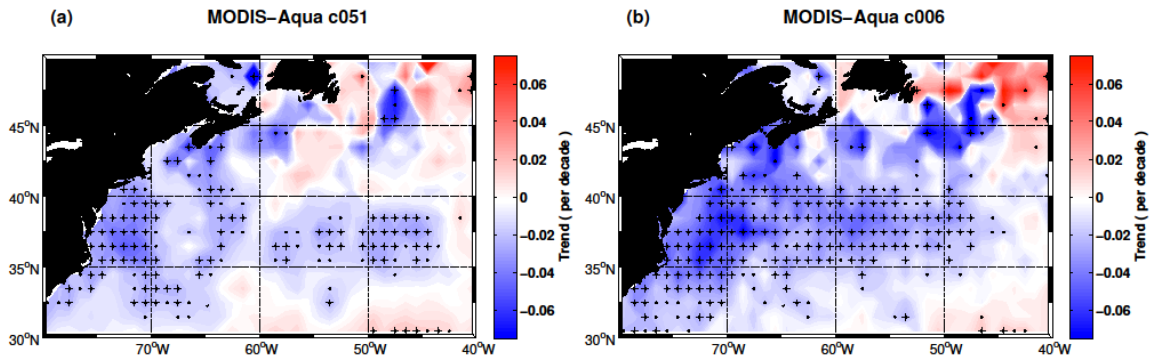

Figure 3.2: Deseasonalized AOD trends from MODIS-Aqua for (a) Collection 5.1 and (b) Collection 6 over the North Atlantic Ocean during July 2002 to December 2012. Dots and crosses represent statistically significant trends at the 90% and 95% levels, respectively. AOD trends are per decade. Figure from Jongeward et al. (2016).

To further explore if the trends seen in the deseasonalized AOD over the North Atlantic originate from changes in the upwind region, trends in deseasonalized AOD from three AERONET sites located in the eastern United States are calculated. The sites include Goddard Space Flight Center (GSFC) in Greenbelt, MD, Maryland Science Center (MDSC) in Baltimore, MD, and City College of New York (CCNY) in New York, NY. The sites are used under the consideration that they are representative of the total aerosol loading and contain species typically predominant in the upwind source region. Figure 3.3 shows the deseasonalized monthly mean AOD with linear fit and trend during the 2002 to 2012 period for the three AERONET sites. All three sites report a negative trend ranging between −0.072 to −0.082 decade^{-1} and are all found to be statistically significant at the 95% level. The trend found at GSFC also agrees with those found previously (e.g. Hsu et al., 2012). The trends at the three AERONET sites suggests a decreasing aerosol loading over the eastern U.S. and their agreement in magnitude suggests that the decreasing trend is not just local but exists on regional scales along the eastern U.S.

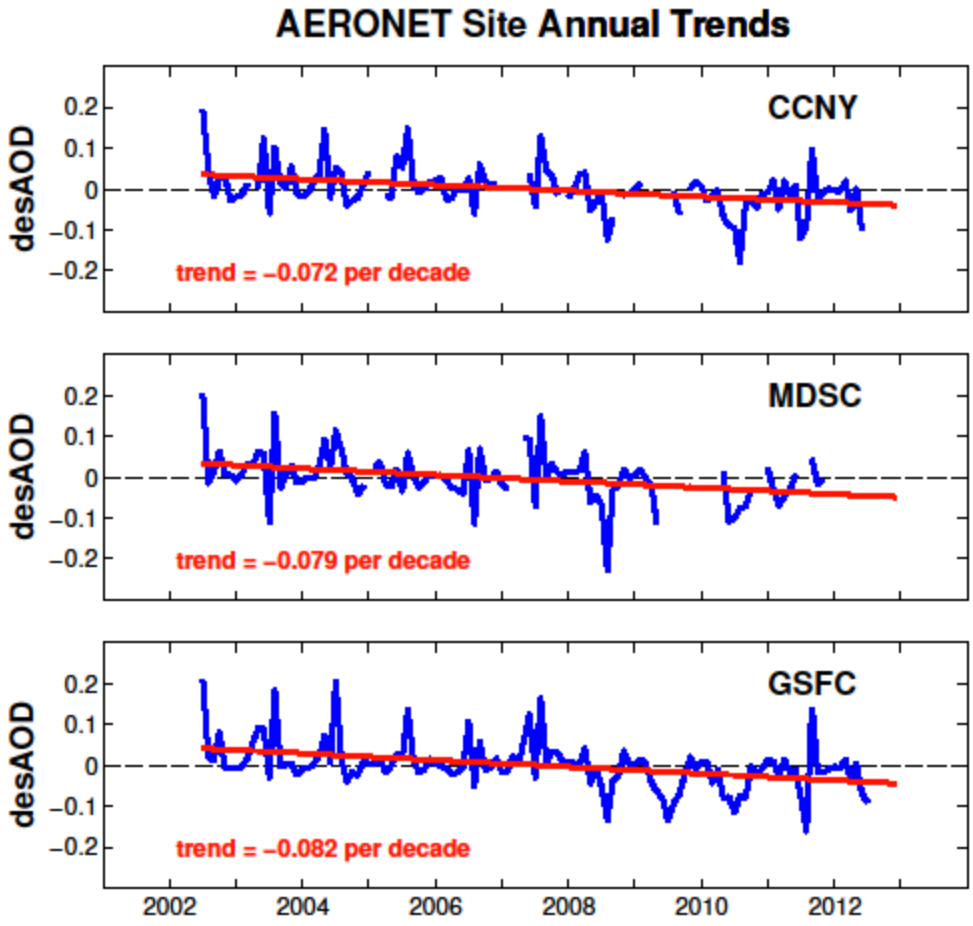

Figure 3.3: Deseasonalized AOD(500nm) records for three eastern U.S. AERONET sites during July 2002 to December 2012. Thick red line represents a statistically significant (> 95%) linear trend reported in the figure. Figure from Jongeward et al. (2016).

To further understand the spatial variability of the aerosol loading over the region during the time considered, the spatial correlation between deseasonalized AOD from MODIS-Aqua and two AERONET sites was performed. The resulting correlations show the extent to which the AOD record at a fixed location (i.e. GSFC or CCNY AERONET site) is related to the AOD field observed from space (i.e. MODIS). Figure 3.4 displays the correlation results between MODIS-Aqua and the AERONET sites at GSFC and CCNY; correlations with the MDSC site are not included as they display a similar pattern

to those using the GSFC site. The correlation analysis reveals a region in the total AOD field of MODIS in the mid-latitudes and downwind of the U.S. coast that has strong correlations ($R > 0.6$) with both the GSFC and CCNY AERONET sites. These strong correlations are also determined to be statistically significant at the 95% level.

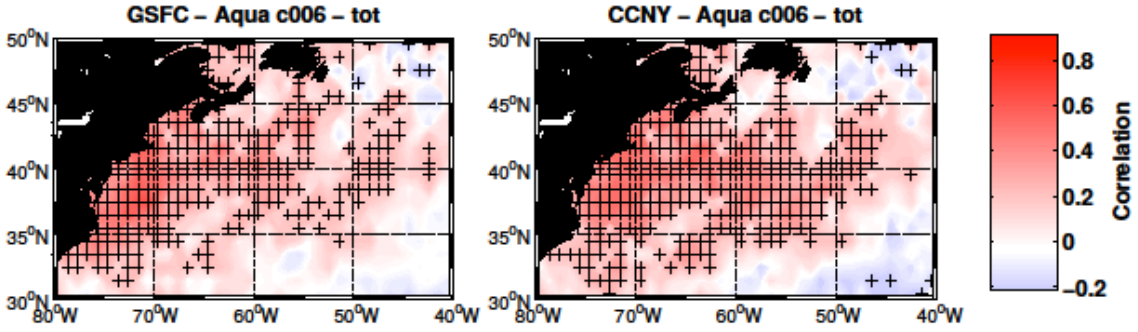

Figure 3.4: Spatial distribution of deseasonalized AOD temporal correlation between MODIS-Aqua and (left) GSFC and (right) CCNY during July 2002 to December 2012 over the North Atlantic. Crosses represent statistically significant correlations at the 95% level. Figure from Jongeward et al. (2016).

The correlation results suggest that the behavior and trend in the total AOD loading in the region is likely to result from changes in the emission and transport of the predominant aerosol species from the region upwind of the North Atlantic. These results also highlight the role of large-scale circulation (see Fig. 3.1) over the eastern U.S. and North Atlantic Ocean in blowing aerosol from west to east in the mid-latitudes. When considered in totality (Fig. 3.1–3.4), the North Atlantic region is under the influence of circulation patterns that tend to advect aerosol from upwind sources which share similar trends across surface (AERONET) and satellite (MODIS) observations.

3.2 GOCART Species Aerosol Trends

Following the identification of a negative AOD trend in the total aerosol loading from MODIS during 2002 to 2012, the question now shifts to identifying the cause for the decreasing load. As noted, MODIS is best suited to observing the total aerosol load and can provide some information on the likely size of the loading it is viewing (i.e. through either the fine-mode fraction or Ångström exponent), but lacks the capability to provide a further detailed breakdown of the aerosol species likely present in the total loading. The GOCART model is thus used to provide a desired breakdown, where the sum total of AODs from sulfate (SU), dust (DU), organic carbon (OC), black carbon (BC), and sea salt (SS) aerosol species combine to make up the total (TOT) AOD.

To begin, an assessment of the trend in the TOT AOD simulated by GOCART is compared to the trend observed by MODIS (see Fig. 3.2). Figure 3.5(a) reveals a region along the coastal U.S. experiencing a statistically significant (> 95%) negative trend in AOD (approximately −0.015 to −0.02 decade^{-1}). The TOT AOD trend in GOCART appears to be less spatially extensive than that seen by MODIS: GOCART specifically misses some of the decreasing aerosol load between 40ºN and 45ºN that is seen by MODIS. Nevertheless, the location, magnitude, and significance of the TOT AOD trend simulated by GOCART are consistent with the observed AOD decrease seen by MODIS.

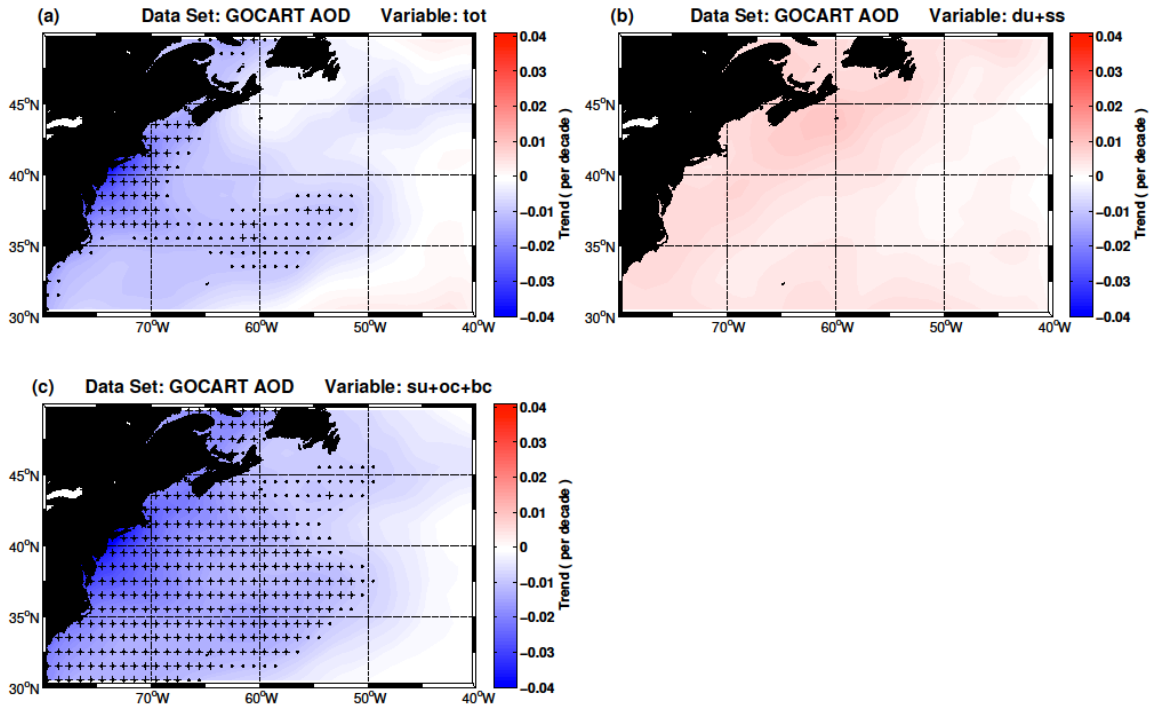

Figure 3.5: Deseasonalized AOD trends during January 2001 to December 2009 from GOCART over the North Atlantic Ocean. Dots and crosses represent trends significant at the 90% and 95% level, respectively. All trends are per decade. (a) TOT, (b) natural (SS+DU), and (c) anthropogenic (SU+BC+OC). Figure from Jongeward et al. (2016).

Following from good agreement of the trends in the total AOD from MODIS and GOCART, further trend analyses are made for AOD that are predominantly anthropogenic (SU+BC+OC) and predominantly natural (DU+SS) component species of the total aerosol composition modeled by GOCART. Also shown in Figure 3.5 are the trend analyses for natural (Fig. 3.5(b)) and anthropogenic (Fig. 3.5(c)) species over the North Atlantic. Apparent is the broad and strong decrease in anthropogenic species, which shows a strong (< -0.02 decade^{-1}) and significant ($> 95\%$; relative to the total aerosol loading) trend along the eastern U.S. coast and extending eastward over the North Atlantic. Occurring during the same time period is a very weak increase (< 0.01 decade^{-1}) in the natural component (Fig. 3.5(b)); this trend is not statistically significant relative

to the total aerosol loading. As the entire GOCART component AODs sum to make the TOT AOD, it would appear that the slight increase in natural components act to mask some of the statistically significant decrease from anthropogenic components. Figure 3.6 details a complete breakdown of the GOCART component AODs and trend analysis of each individually, and sheds additional light onto the make-up of the trends in Fig. 3.5. The SU component (Fig. 3.6(b)) can be seen to be the only anthropogenic species that is experiencing a trend (around -0.02 decade^{-1}) during the period considered. Additionally, the weak trend behavior of the natural components of Fig. 3.5(b) can further understood by considering the trend behavior of the DU (Fig. 3.6(c)) and SS (Fig. 3.6(d)) species together. The slight increase of DU is mainly found in the sub-tropics (and extends further south than the domains in Fig. 3.5 and 3.6); it is believed to be the result of changes in dust loading and/or transport of dust originating from the Saharan Desert in North Africa and will be discussed in Chapter 4. Finally, the minor increase in SS found in the mid-latitudes may result from an increase in the surface wind speed used in the SS parameterization (e.g. Chin et al., 2002) over the ocean.

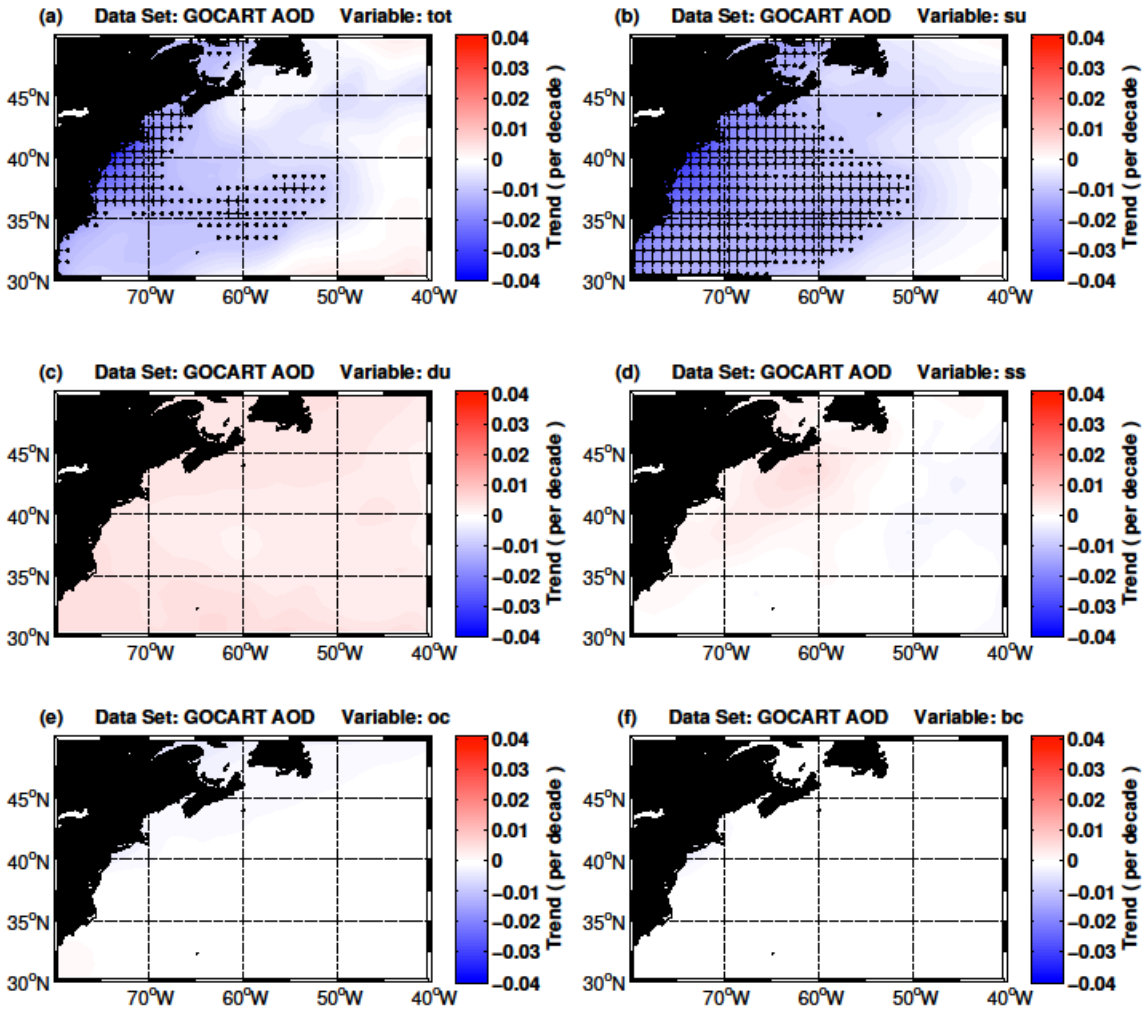

Figure 3.6: Same as Fig. 3.5 except for each individual aerosol species from GOCART: (a) TOT, (b) SU, (c) DU, (d) SS, (e) OC, and (f) BC. Figure from Jongeward et al. (2016).

3.3 IMPROVE Surface Particulate Matter (PM) Trends

The trends seen in GOCART (Fig. 3.5 and 3.6) offer a compelling breakdown of which species might be responsible (i.e. sulfate aerosols) for the decrease in aerosol loading seen by MODIS over the North Atlantic. GOCART provides a spatiotemporal

complete picture of AOD and its make-up, which provides for easy comparison with MODIS satellite observations. Yet GOCART still suffers from being a simulation of the aerosol load, relying on accurate reanalysis meteorological fields and aerosol emissions and evolution parameterizations.

To further augment and strengthen the assessment of aerosol trends and the species responsible, the particulate matter (PM) composition observed at four IMPROVE network surface sites in the eastern U.S. is examined. The four sites selected are the Washington D.C. (WASH1), Cape Cod, MA (CACO1), Acadia ME (ACAD1), and Brigantine, NJ (BRIG1) sites. As an example, the time series from 2002 to 2012 of total $PM_{2.5}$ mass and individual species masses are shown in Figure 3.7 for the WASH1 site. Notable is the large relative fraction of AS that makes up the total $PM_{2.5}$ mass load during the middle of the year (i.e. summertime): upwards of 60% of the total mass and more than twice that of any other species. Also of note is the trade-off between AS and AN species throughout the year, with AN maxima contribution occurring during the winter months while AS maxima occur during the summer months. This trade-off is a result of the equilibrium reaction to form AN: conditions during wintertime (i.e. colder temperature and higher relative humidity) favor the formation of AN as opposed to summertime, which favors AN dissociation (Renard et al., 2004). Therefore, the ammonia present during summertime has an increased likelihood to react with sulfur dioxide and sulfuric acid to form AS. During the period considered (July 2002 to December 2012), a trend of -7.726 $\mu m/m^3$/decade is seen in the total $PM_{2.5}$ mass observed by the WASH1 station; component wise, the AS species experiences a -4.278

µm/m^3/decade trend while the POM species experiences a -1.867 µm/m^3/decade. All three trends are statistically significant at the 95% level.

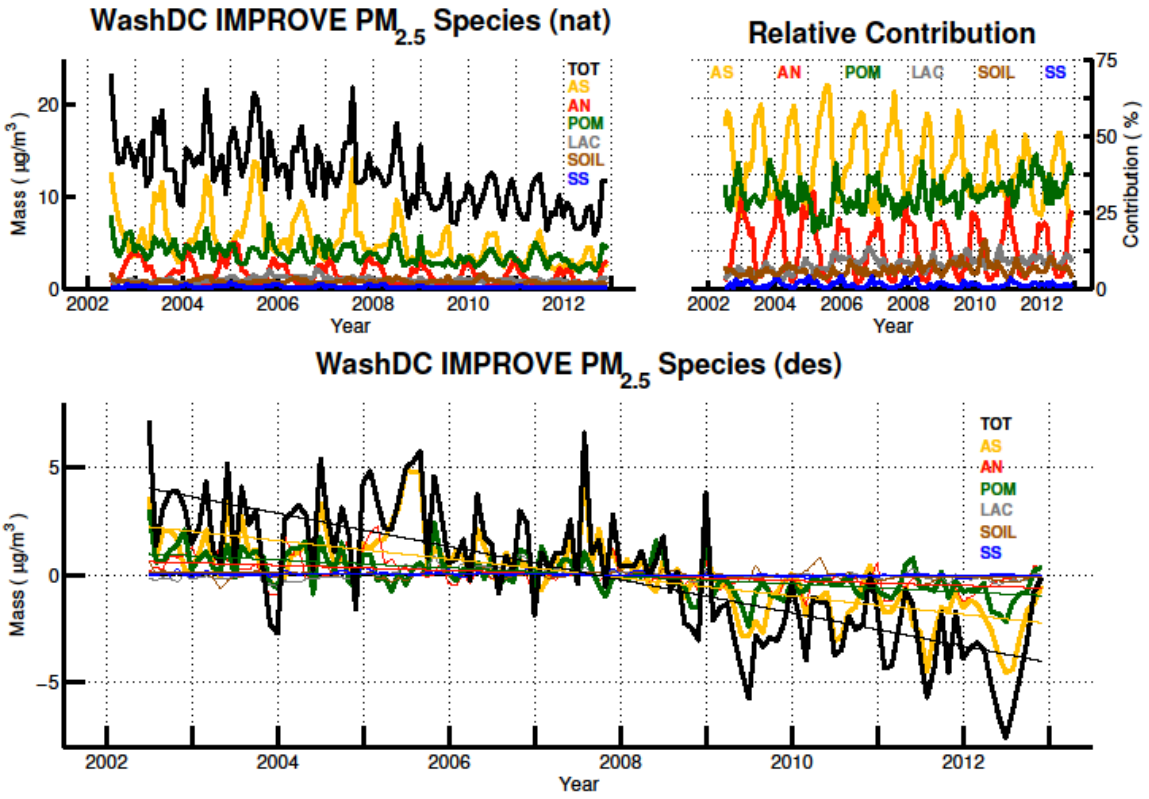

Figure 3.7: Records of $PM_{2.5}$ composition observed from the Washington D.C. IMPROVE network site (38.88ºN, -77.03ºE) from July 2002 to December 2012. Species shown are the sum total (TOT; black) of ammonium sulfate (AS; yellow), ammonium nitrate (AN; red), particulate organic matter (POM; green), light-absorbing carbon (LAC; grey), soils (SOIL; brown), and sea salt (SS; blue) species. Displayed are the time series of the native (upper left), relative contribution (upper right), and deseasonalized (bottom) records. The calculated linear regressions are superimposed on the deseasonalized time series. Emboldened are the species (AS, POM, and TOT) who report a trend beyond the 95% significant level. The deseasonalized LAC time series (gray, bottom) is difficult to resolve due to its small variance (0.06 µg/m^3) compared to other series (e.g. var(TOT) = 9.5µg/m^3), thus the LAC series lies near the abscissa. Figure from Jongeward et al. (2016).

Having an initial understanding of the PM (both TOT and component species) time series, the trend analysis is now extended to include all four IMPROVE network sites. Figure 4.8 shows the results of trend analysis at each site for each individual species and the combined sum total. For the four sites considered, each reports a

statistically significant (> 95%) decrease in the total $PM_{2.5}$ mass loading during the July 2002 to December 2012 period. The CACO1 and ACAD1 sites (located in the New England region) show a decreasing trend between −2 and −4 $\mu m/m^3$/decade while the WASH1 and BRIG1 sites (located in the New York – Washington corridor) show a stronger decrease, between −5 and −8 $\mu m/m^3$/decade. When considering each species individually, only AS is seen to have a statistically significant (> 95%) decrease at all of the four sites. The only other species that experiences a significant decreasing trend is the aforementioned POM species at the WASH1 site. This POM trend may be a result of the WASH1 site being in a more urban environment where controls on vehicular emissions including volatile organic compounds (VOCs; a precursor to POM) would be likely to be realized as compared to a non-urban (i.e. more rural) site like the ACAD1 site.

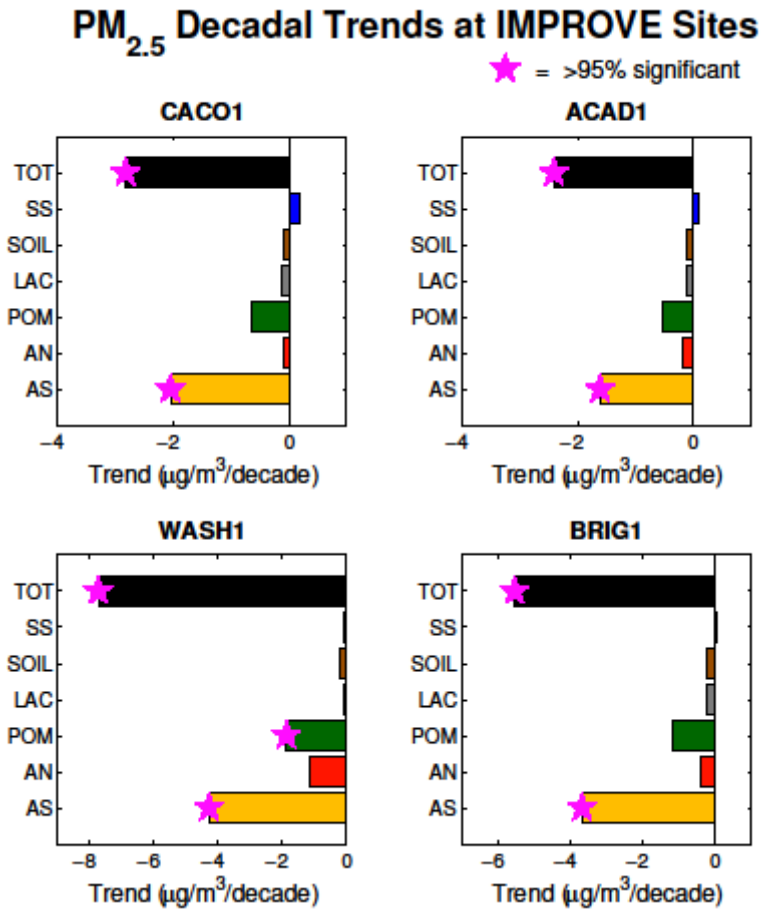

Figure 3.8: Decadal trends in $PM_{2.5}$ for the four IMPROVE network surface sites during July 2002 to December 2012. Species shown are the sum total (TOT; black) of ammonium sulfate (AS; yellow), ammonium nitrate (AN; red), particulate organic matter (POM; green), light-absorbing carbon (LAC; grey), soils (SOIL; brown), and sea salt (SS; blue) species. Trend units are in $\mu m/m^3$ per decade. Pink star denotes that a trend is statistical significance at the 95% level. Figure from Jongeward et al. (2016).

3.4 Seasonality of Aerosol Trends

The changing aerosol loading during the first decade of the 21st Century over the mid-latitude western North Atlantic Ocean is beginning to be clarified: a negative AOD trend seen by MODIS is mirrored by that in GOCART total AOD and is suspected to be consequence of decreases in the anthropogenic component (specifically sulfates, as

determined by GOCART). This picture is further made clear by an assessment of ground-based observations from the eastern U.S.: all three AERONET sites demonstrate a negative AOD trend and all four IMPROVE sites show negative trends in both the TOT $PM_{2.5}$ mass and, importantly, the AS $PM_{2.5}$ species.

The analysis is now taken one step further to investigate seasonal trends that may exist in the observational datasets during July 2002 to December 2012. Shown in Figure 3.9 is the breakdown of seasonal trend in deseasonalized total AOD observed from MODIS-Aqua while Figure 3.10 displays the seasonal trends observed in deseasonalized AOD observed at the three AERONET sites. First, it is apparent from MODIS-Aqua that the annual decrease in AOD (i.e. as seen in Fig. 3.2) is the result of strong seasonal decreases in AOD during spring (MAM) and summer (JJA) seasons; strong and statistically significant (> 95%) trends in excess of -0.05 decade^{-1} are seen. The trend during springtime appears to exist throughout the southern portion of the domain, while trend determination north of 40^0N is inconclusive (perhaps due to cloud contamination in the mid-latitude storm track). This negative trend further strengthens itself going into summertime as well as shifts northward in the domain.

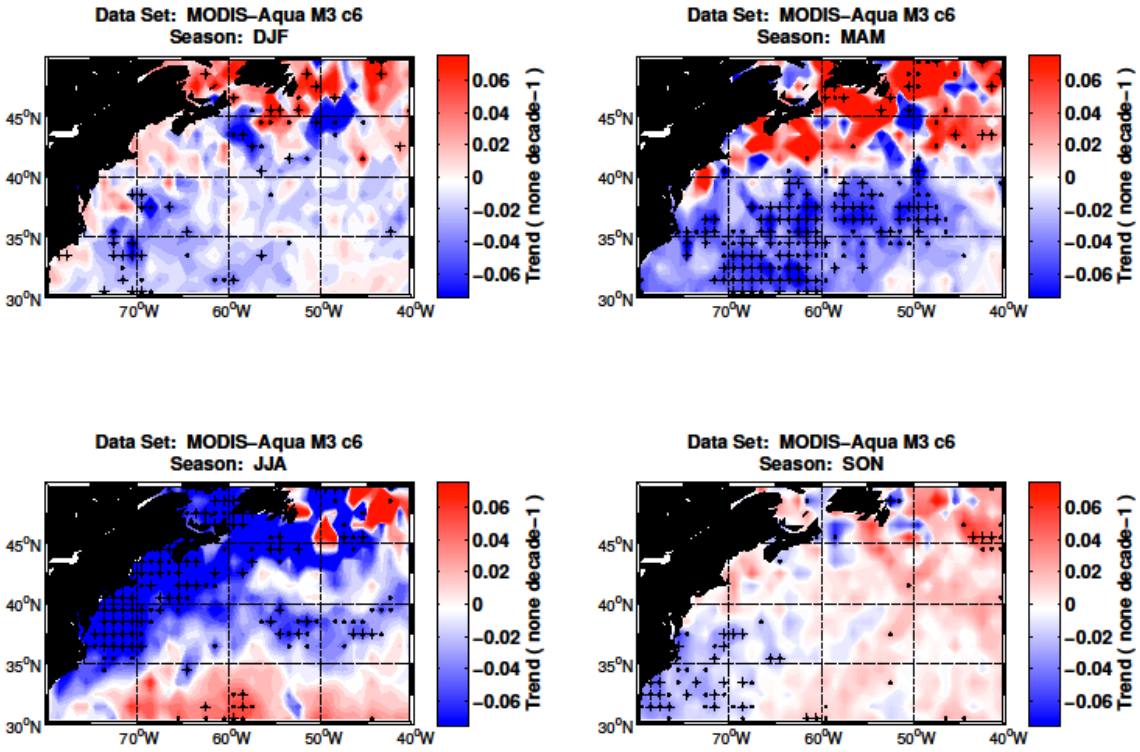

Figure 3.9: Seasonal trends of deseasonalized AOD from MODIS-Aqua (C6) during July 2002 to December 2012 over the North Atlantic. Dots and crosses represent statistically significant trends at the 90% and 95% levels, respectively. AOD trends are per decade. Figure from Jongeward et al. (2016).

The main seasons that experience the decreasing AOD (i.e. MAM and JJA) are further supported by the seasonal analysis of AOD at the three AERONET sites (Fig. 3.10). No site reports a statistically significant trend during either fall (SON) or winter (DJF) months. While the CCNY and MDSC sites do reflect some slight decrease in spring (MAM), these trends are not statistically significant. The GSFC site does however report a statistically significant decrease of −0.07 decade^{-1} occurring during MAM. Both the CCNY and GSFC site report a strong and significant decrease of −0.195 and −0.233 decade^{-1}, respectively. As with spring, the summer trend at MDSC reflects a decrease yet is not statistically significant. The lack of significance at CCNY during spring and MDSC during spring and summer is the combination of three factors: 1) too small of a

trend, 2) too large of variance in error between the estimated fit and observations, and/or 3) a smaller number of data points (degrees of freedom).

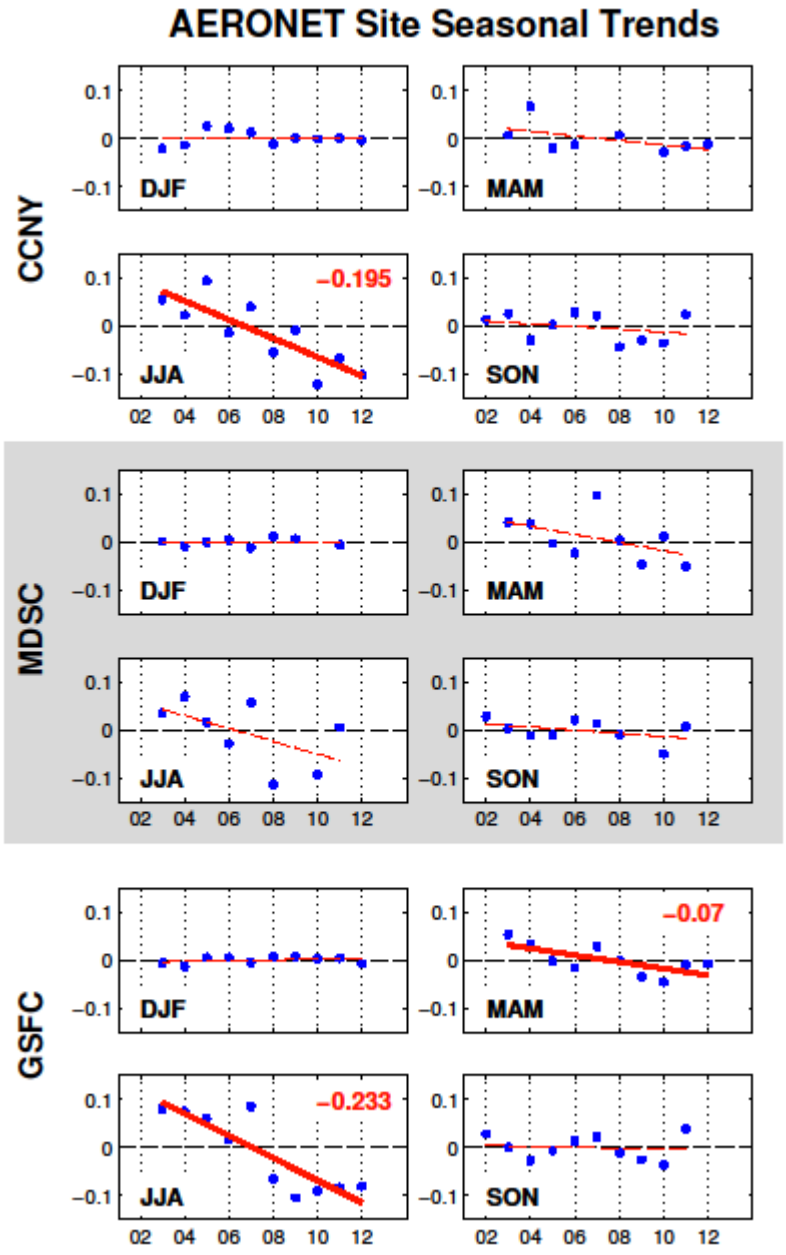

Figure 3.10: Seasonal trends of deseasonalized AOD CCNY, MDSC, and GSFC AERONET sites during July 2002 to December 2012. Statistically significance (> 95%) of AOD trends denoted by thick red line with trend value (per decade) reported in-figure. Figure from Jongeward et al. (2016).

To complete the seasonal analysis, a breakdown of seasonal trends at the four IMPROVE network sites is examined (Fig. 3.11). The negative trend seen annually in the TOT $PM_{2.5}$ mass at each of the four sites (see Fig. 3.8) is reflected in each season at all sites but the CACO1 site, where the decrease is only significant during the spring and summer months. The season experiencing the strongest decrease in $PM_{2.5}$ mass is summer at all four stations. This agrees well with summer being the season reporting the strongest decreases in AOD at the GSFC and CCNY sites (Fig. 3.10) as well as summer displaying the strongest decrease in AOD out over the western North Atlantic as seen by MODIS (Fig. 3.9).

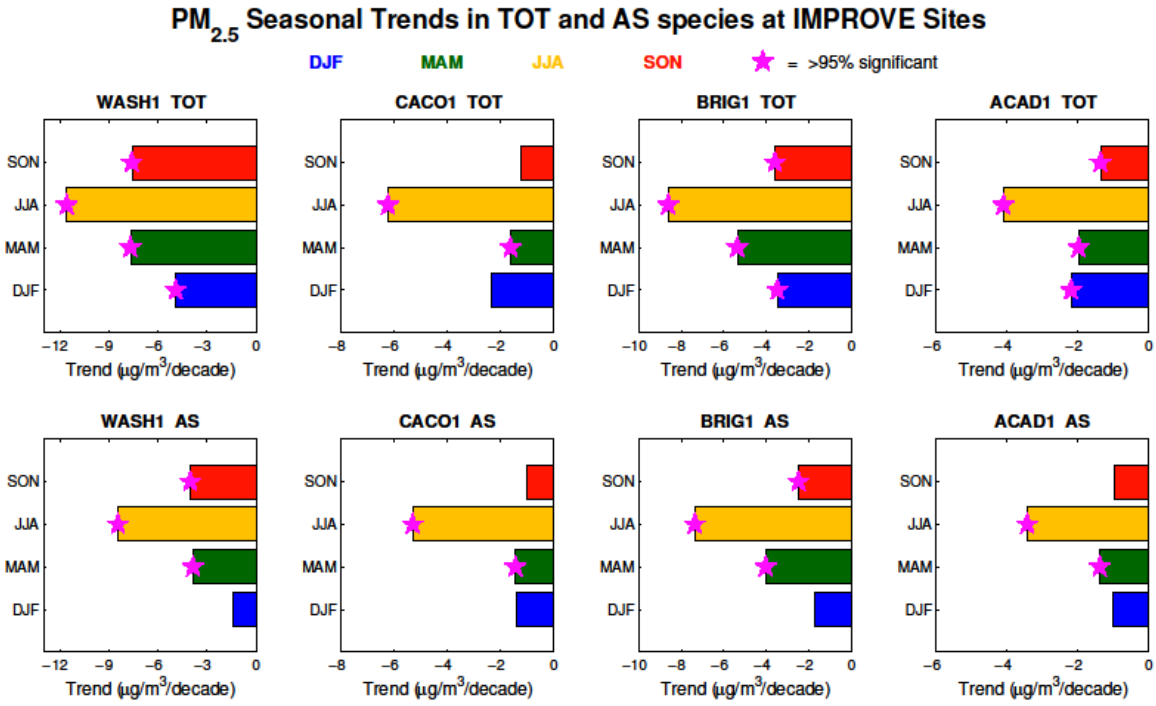

Figure 3.11: Seasonal trends in $PM_{2.5}$ observed at each of the four surface IMPROVE network sites during July 2002 to December 2012 for the sum total (TOT; top row) of all species and for only AS (bottom row). Statistical significance at the 95% level noted by pink stars. All trends are in µm/m^3/decade. Figure from Jongeward et al. (2016).

A breakdown of the seasonal trend behavior (and statistical significance) of the AS $PM_{2.5}$ species at each of the four IMPROVE sites is also displayed in Fig. 3.11. Each of the four sites reports statistical significant decreases in the AS $PM_{2.5}$ species during MAM and JJA seasons. Most notable, the magnitude of the AS decrease during the JJA season closely matches the magnitude of the TOT $PM_{2.5}$ decrease during JJA, further strengthening the connection that decreases in ammonium sulfate $PM_{2.5}$ species are predominantly responsible for the decrease in TOT $PM_{2.5}$ and, by extension, AOD during the summer months. In addition to TOT and AS species, the seasonal trend behavior for the other $PM_{2.5}$ species (AN, POM, LAC, SOIL, and SS) was also performed. Figure 3.12 displays the breakdown of statistical significance for all $PM_{2.5}$ species. Immediately apparent is the lack of statistical significance of seasonal trends calculated for AN, POM, LAC, SOIL, and SS species. None of the aforementioned species report trends that are significant beyond the 90% level. As with the analysis of AERONET seasonal trends, the lack of significance is the combination of three factors: 1) too small of a trend, 2) too large of variance in error between the estimated fit and observations, and/or 3) a smaller number of data points (degrees of freedom). Note the consistent flagging of statistical significance in TOT and AS species between Fig. 3.11 and 3.12.

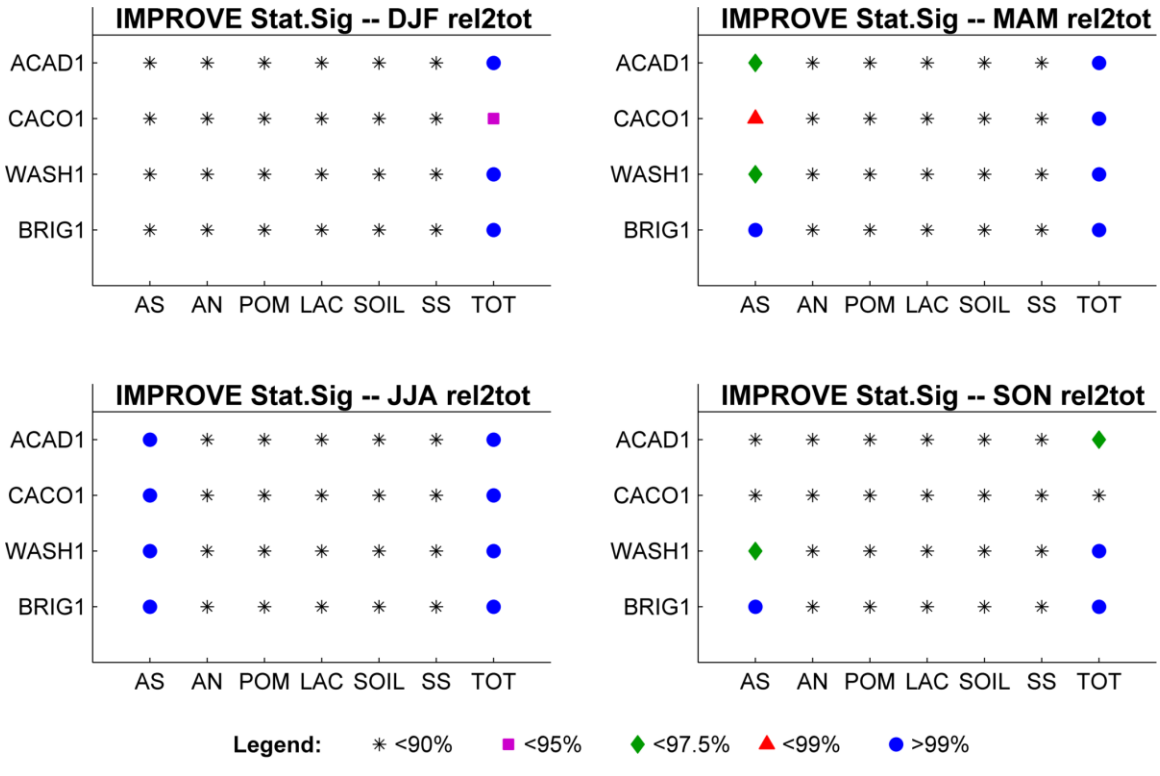

Figure 3.12: Calculated statistical significance for seasonal $PM_{2.5}$ species trends at each of the four surface IMPROVE network sites during July 2002 to December 2012. Legend denotes significance up to specified value.

3.5 Chapter 3 Summary

This chapter explores decadal trends in deseasonalized AOD from satellite, surface, and model datasets. A decreasing AOD trend of −0.02 to −0.04 decade^{-1} is observed by MODIS-Aqua over the mid-latitude western North Atlantic Ocean during July 2002 to December 2012. This trend agrees well with decreases in AOD seen at three AERONET sites along the Eastern U.S. The GOCART aerosol model reveals a decrease in total AOD that is due to decreases in predominantly anthropogenic species (sulfate, organic carbon, and black carbon aerosols) while trends in the mainly natural species

(dust and sea salt) are non-existent. Trends in $PM_{2.5}$ observed at four IMPROVE network surface sites along the U.S. Atlantic coast demonstrate significant decreases in total $PM_{2.5}$ mass and highlight the role of ammonium sulfate (AS) decreases. A seasonal breakdown of MODIS and AERONET AOD trends reveals spring (MAM) and summer (JJA) as seasons of significant decreases. This is reflected by seasonal trends in total $PM_{2.5}$ mass at the IMPROVE sites and again highlights the role of AS decreases: AS is the only $PM_{2.5}$ species to show significant seasonal trends.

Chapter 4: Increasing Aerosol Trend over the Sub-tropical North Atlantic Ocean

This chapter details the identification and attribution of a positive trend in AOD observed by MODIS over the sub-tropical North Atlantic Ocean. The main geographical domains of interest include much of the North Atlantic Ocean (90ºW to 0ºW and 0ºN to 50ºN; whole domain of Fig. 3.1) and various regions within North Africa (20ºW to 20ºE, 10ºN to 40ºN). Additional results also pertinent to determining the cause of the increasing aerosol come from the Sahel region of Africa as well as the near-equatorial North and South Atlantic Ocean. Monthly mean data during July 2002 through December 2012 are employed.

4.1 Identification as Dust Aerosol

As was shown in Chapter 3, there exists a negative AOD trend over the mid-latitudes (identified anthropogenic in origin), and upon expanding the domain to 20ºN a positive AOD trend is seen over the sub-tropical western North Atlantic Ocean (see Figure 4.1; top left). The mean circulation (see Fig. 3.1) would dictate aerosol loading from the North American continent influencing the mid-latitude trend while aerosol loading from the eastern North Atlantic Ocean (and North Africa further upwind) likely influence the sub-tropical trend. Indeed, if the domain of Fig. 3.2 and 3.5 are expanded to 20ºN, there is agreement between MODIS-Aqua and GOCART in the existence of the positive AOD trend in the sub-tropics (Fig. 4.1, top). Going one step further, GOCART natural species (i.e. DU+SS) are those responsible for this positive trend, a trend that is statistically significant (Fig. 4.1, bottom left).

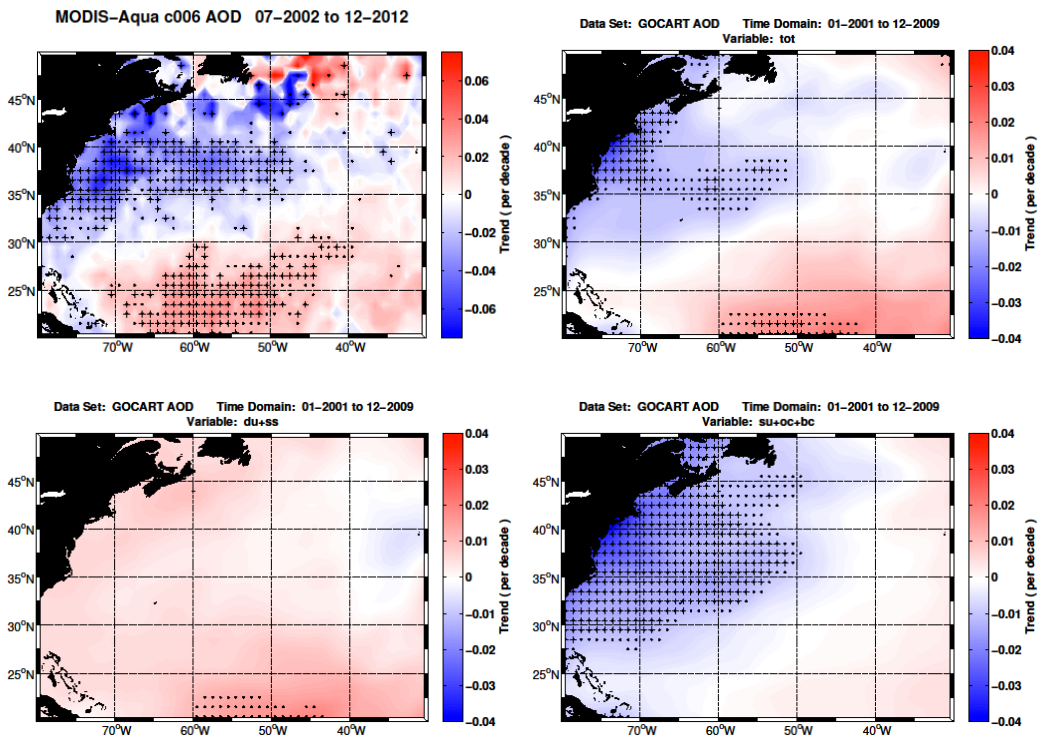

Figure 4.1: Deseasonalized AOD trends during July 2002 to December 2012 for MODIS-Aqua (top left) and January 2001 to December 2009 from GOCART over the North Atlantic Ocean. Dots and crosses represent trends significant at the 90% and 95% level, respectively. All trends are per decade. (top left) MODIS total AOD, (top right) GOCART TOT AOD, (bottom left) GOCART natural (SS+DU) AOD, and (bottom right) GOCART anthropogenic (SU+BC+OC) AOD.

The domain for calculating the aerosol trends is now expanded to include much of the entire North Atlantic Ocean basin, spanning from 0ºW to 90ºW and from the equator to 50ºN. Additionally, the method from Kaufman et al. (2005a) is used to determine the dust AOD as described in Section 2.3.2 using Eq. 2.8. The deseasonalizing, trending, and significance algorithm can now be applied to both the annual and summertime (i.e. June, July, and August (JJA)) time series of both total AOD and dust AOD. The utility of the Kaufman et al. (2005a) method in identifying dust loading and the subsequent positive trend is evident in the trend results shown in Figure 4.2. In looking at the annual trends in both total AOD (Fig. 4.2a) and dust AOD (Fig. 4.2b) one can see that the Kaufman et al. (2005a) method not only isolates the sub-tropical trend in dust AOD but also mirrors

the magnitude and significance seen in the total AOD trend. Going one step further, the Kaufman et al. (2005a) method is able to exclude the mid-latitude decreasing trend seen in the total AOD and identified in Chapter 3 as arising from anthropogenic decreased emissions (i.e. no trends seen in dust AOD in the mid-latitudes). This Kaufman et al. (2005a) method will be used to separate assumed aerosol loadings for calculation of the aerosol direct radiative effect in Chapter 5.

The summertime season (JJA) is notable for the large transport of dust westward across the sub-tropical North Atlantic Ocean (e.g. Delany et al., 1967; Carlson and Prospero, 1972; Chin et al., 2002; Yu et al., 2015), and assessing the trends during JJA further identifies the importance of dust to the increasing AOD over the sub-tropics. During JJA, MODIS-Aqua total AOD (Fig. 4.2c) experiences a wide band of statistically significant AOD increase throughout the sub-tropical region. This trend is in contrast to the strong decrease that is seen in the western mid-latitudes (and identified in Chapter 3 as originating in anthropogenic decreases). When compared to the total AOD trends during JJA (Fig. 4.2c), those seen in the estimated dust AOD (Fig. 4.2d) show this strong increase across the sub-tropics with the mid-latitude decrease again absent. This only further strengthens the confidence in the Kaufman et al. (2005a) method of distinguishing dust AOD. Interestingly, an area in the northern equatorial region (around 10º-15ºN) reports a decreasing trend in both total and dust AOD during JJA. However, the significance of this trend is less coherent than the aforementioned increasing trend to the north. The uncertainty in the significance can arise from too small of a trend (not likely), too large of variance in error between estimated fit and observations, and/or too few data

points (i.e. degrees of freedom). The latter two likely combine to lead to the uncertain statistical significance of the negative trend in this region.

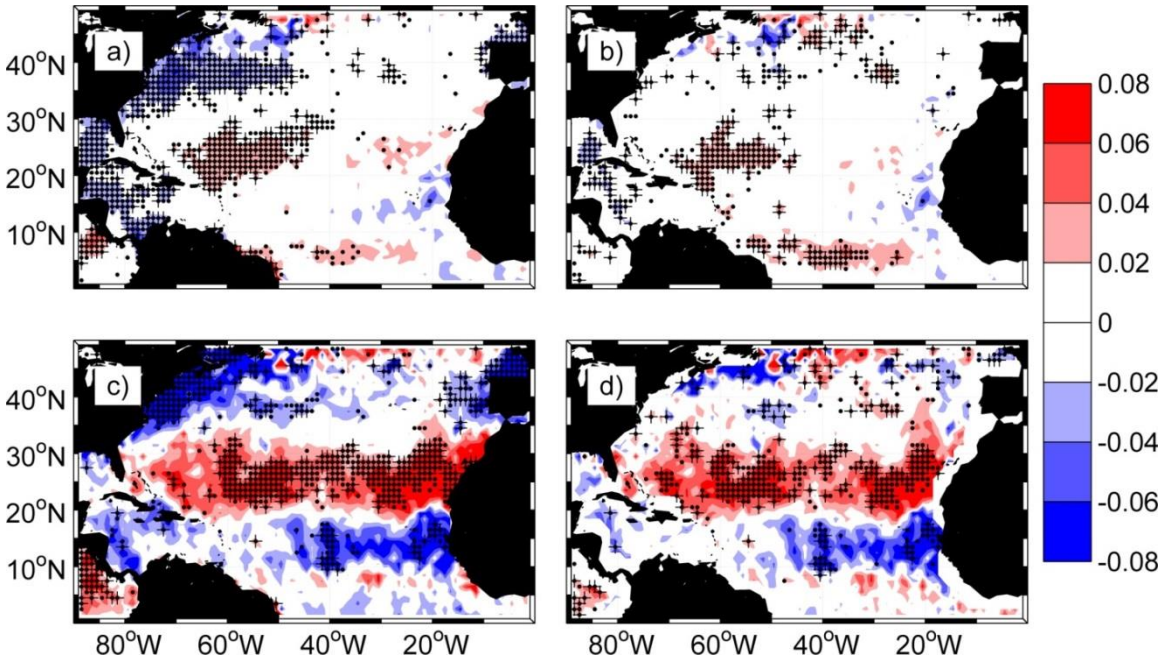

Figure 4.2: Deseasonalized total AOD (a,c) and dust AOD (b,d) trends during July 2002 to December 2012 from MODIS-Aqua over the North Atlantic Ocean. Trends for annual time series are on top (a,b) while trends for JJA are on bottom (c,d). Dots and crosses represent trends significant at the 90% and 95% level, respectively. All trends are per decade. Dust AOD is calculated following the Kaufman et al. (2005a) method described in Section 2.3.2.

4.2 Trends in Dust Mass Loading and Mass Flux

In addition to deriving dust AOD, the method put forth in Kaufman et al. (2005a) is extended to estimate dust mass loading (M_d) and zonal dust flux (F_d). As laid out in Section 2.3.2, M_d is simply a ratio of dust mass to dust AOD (2.7 ± 0.4 g/m^2) while F_d is parameterized (Eq. 2.10) as the product of M_d, the zonal wind at 700 hPa (U_{700}), and the longitudinal length (L). A factor of -1 is included to produce $F_d > 0$ in the main dust

transport region between 5ºN and 25ºN (the region of the African Easterly Jet; AEJ) due to the flow being westerly (having $U_{700} < 0$). U_{700} is used as it is around this height where westward dust transport by the AEJ occurs and correlations between U and AOD are highest (Kaufman et al., 2005a).

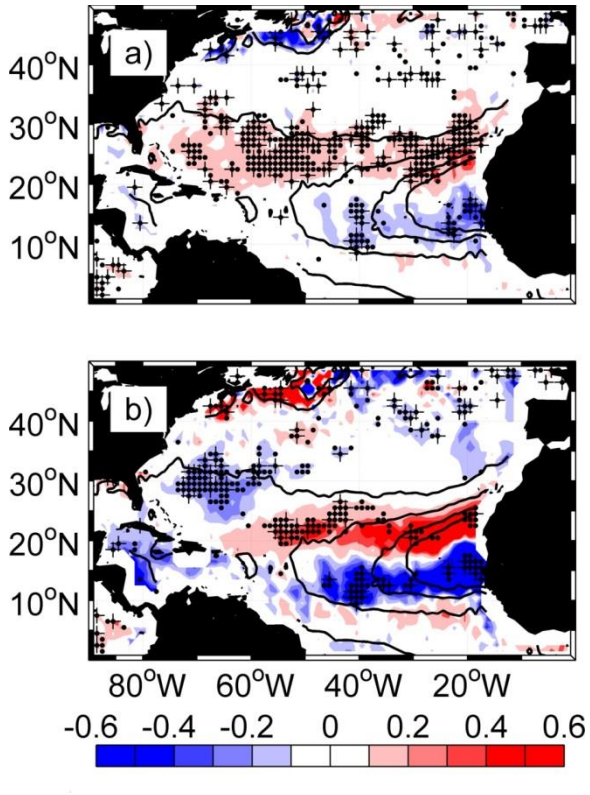

Figure 4.3: JJA deseasonalized trends in (a) M_d and (b) F_d over the North Atlantic Ocean during 2002 to 2012. Also shown are the contours (in black) of mean JJA M_d at intervals of 0.2, 0.5, 0.8, and 1.0 g/m^2 with highest concentrations near the African coast. M_d trends are in units of g/m^2 per decade and F_d trends are in units Tg/month per decade. Trends statistically significant at the 95% (90%) level are marked with a cross (dot).

Figure 4.3 shows the spatial distribution of JJA trends in dust M_d and F_d from 2002 to 2012. Across the sub-tropical North Atlantic Ocean, the increase in dust AOD (Fig. 4.2d) can be seen as the result of an increase in M_d on the order of around 0.2 g/m^2 per decade (significant at the 95% level). Taking the radius of the Earth as 6370 km, a

1ºx1º grid box (resolution of datasets used) at 25ºN translates to an area approximately 11,201 km^2. A 0.2 g/m^2 per decade increase in dust thus yields an increase of approximately $2.24x10^6$ kg of dust per decade per grid location across the positive trend region between 20ºN and 30ºN. One interesting behavior is seen in the F_d estimation (Fig. 4.3b) occurring in the western sub-tropics. Namely, this region appears to have experienced dust convergence, as positive flux trend occurs to the east (more dust entering) while a negative flux trend occurs to the west (less dust exiting).

One feature that stands out in all JJA trends (total AOD (Fig. 4.2c), dust AOD (Fig. 4.2d), M_d (Fig. 4.3a) and F_d (Fig. 4.3b)) is the region of (uncertain) negative trend in dust around 10º-15ºN. When overlaying contours of dust mass concentration (contours of M_d) in Figure 4.3, an additional question is raised. It appears that along a zonal axis in M_d (around 20ºN) there is a decrease in dust to the south mirrored by an increase in dust to the north. Not only might the amount of dust be increasing, but perhaps the dust transport path may have also shifted (and shifted to the north). As a means of further exploration, JJA trends in the total monthly mass of four individual boxed regions and five combinations of them are computed. Bounded at the west and east by 70ºW and 20ºW (respectively) and to at the south and north by 10ºN and 30ºN (respectively), four boxed regions are made by subdividing this domain along 50ºW and 20ºN. Table 4.1 contains the JJA trend results for the total monthly mass within these various regions.

		Domain A	Domain B		Whole Domain
		70°-50°W	**50°-20°W**		4.29 (AB12)
Domain 1	**20°-30°N**	3.00* (A1)	4.43* (B1)	7.39* (AB1)	
Domain 2	**10°-20°N**	0.02 (A2)	-3.12 (B2)	-3.10 (AB2)	
		2.99 (A12)	1.30 (B12)		

Table 4.1: JJA trends in total monthly mean mass for four individual boxed regions (bounds listed in bold). Values highlighted in yellow are for entire N-S domain, values in blue are for entire E-W domain, and value in green for whole domain. Values with * are those significant > 95% level. Units are g/m^2 per decade. Values in parenthesis denote the combination of domains.

What can be seen from Table 4.1 is that indeed both northern subdomains (A1 and B1) and the entirety of the northern domain (AB1) have significant JJA trends (increasing) in the total monthly mean mass. The southern subdomains (A2 and B2) do not have significant trends, and the entirety of the southern domain (AB2) seems dominated by the trend occurring between 20°-50°W (B2). When considering the domains in a north-south sense, the western domain (A12) appears to be dominated by the increase from the north (A1) with very little contribution from the south (A2). The eastern domain (B12) trend while positive is not significant and is a combination of the offsetting trends from the north (B1) and south (B2). Taken as a whole, the 10°-20°N – 70°-20°W domain (AB12) has experienced an increase in total dust mass; however, this trend is not significant. The results from Table 4.1 together with those shown in Fig. 4.2d and 4.3 suggest an increase in subtropical dust and point to a slight northward shift in the dust export/transport from North Africa across the North Atlantic.

4.3 Potential Causes for Observed Dust Trends

4.3.1 Short-term Changes in the North African Environment

The reason for increase in JJA dust across the sub-tropical North Atlantic remains unclear, thus a closer examination is undertaken to explore any summertime changes in the dust transport pathway from North Africa. Two of the main dynamical features of summertime North Africa are the African Easterly Jet (AEJ) over the African coast around 15ºN latitude and the African Easterly Waves (AEWs) that form on the north and south flanks of the AEJ. Both the AEJ and AEW play a key role in African dust transport. The AEJ is characterized by a westward zonal maximum in wind speed around 700 hPa and results from the meridional temperature gradient between the (relatively) cooler equatorial Africa and the (relatively) hot temperatures of the Saharan desert (Cook, 1999; Wu et al., 2009). The AEJ arises from the N-S temperature gradient through the thermal wind relation:

$$p\frac{\partial u_g}{\partial p} = \frac{R}{f}\left(\frac{\partial T}{\partial y}\right)_p \qquad \text{(Eq. 4.1)}$$

where u_g is the zonal geostrophic wind, p is atmospheric pressure, R is the gas constant for dry air (287 J/kg/K), f is the Coriolis parameter, T is atmospheric temperature, and the partial derivative $(\partial/\partial y)_p$ is taken on a constant pressure surface (Holton, 2004; Pp. 72,

Eq. 3.29). A simpler form of the thermal wind relates the geostrophic winds at two levels p_0 and p_1 (where $p_0 > p_1$):

$$u_T = u_g(p_1) - u_g(p_0) = -\frac{R}{f}\left(\frac{\partial\langle T\rangle}{\partial y}\right)_p \ln\left(\frac{p_0}{p_1}\right) \qquad \text{(Eq. 4.2)}$$

where <T> is the mean temperature between p_0 and p_1. In this form, it is clear to see that a positive meridional temperature gradient (∂<T>/∂y > 0) results in a negative thermal wind ($u_T < 0$), which alternatively can be thought of as negative shear in the geostrophic wind with height ($\partial u_g/\partial p < 0$). AEWs develop through convection triggered over East/Central Africa and grow through mixed barotropic-baroclinic mechanism associated with the AEJ (Hall et al., 2006; Skinner and Diffenbaugh, 2014). AEWs have been shown to play an important role in both dust mobilization (Knippertz and Todd, 2010) and its transport and variability (Jones et al., 2003).

As a starting point, the mean and evolution of the AEJ and AEWs during JJA are investigated using the MERRA monthly mean product. Shown at the top of Figure 4.4 are the 2002-2012 JJA means of zonal wind at 700 hPa (U_{700}), vertical shear of the zonal wind ($\partial u/\partial z$; taken as the difference between U at 925 and 700 hPa: $U_{700} - U_{925}$), and horizontal relative vorticity at 700 hPa (RV: $RV = \hat{k} \cdot \nabla \times \vec{v}$) over the west coast of North Africa (5º-25ºN, −30º-0ºW). Immediately recognizable is the AEJ (Fig. 4.4a) as the core in minimum zonal wind velocity (< −10 m/s) extending from the interior of West Africa out over the Atlantic Ocean around 15ºN latitude. The AEJ arises from the near-surface positive meridional temperature gradient through the thermal wind (Eq. 4.1), as verified

by the negative mean vertical wind shear of the zonal wind (Fig. 4.4b). The elevated wind speed within the AEJ relative to its flanks gives rise to cyclonic (anticyclonic) rotation in the horizontal mean flow to the south (north) of the jet, as seen by RV > 0 (RV < 0; Fig. 4.4c), which can aid in the growth and maintenance of AEWs.

The time evolution of the summertime North African atmosphere is examined for any notable trends that may influence African dust and its transport over the sub-tropical North Atlantic Ocean. Three micro-regions within the AEJ core and along either flank have been isolated. Shown in Fig. 4.4a and outlined in pink, these regions extend over 22.5º to 7.5ºW longitude where region M1 covers 19.5º to 21.5ºN, region M2 covers 14.5º to 16.5ºN, and region M3 covers 9.5º to 11.5ºN. The subsequent time series in Fig. 4.4d-l contain the deseasonalized values during the JJA months for each grid point that falls within that micro-region. There appears to be a northward shift in the position of the AEJ when considering the trends in deseasonalized U_{700} in Fig. 4.4d,g,j. The negative trend in M1 imposed on already negative U_{700} produces an acceleration of the AEJ to the north of its mean position (Fig. 4.4a) while the positive trend in M3 will lead to a deceleration of the AEJ to the south of its mean position (Fig. 4.4j). The apparent northward shift in the AEJ is accompanied by a decrease in deseasonalized $\partial u/\partial z$ in M1 (Fig. 4.4e) which increases the magnitude of vertical shear of the zonal wind. This behavior is seen to be reversed to the south of the AEJ where an increase in $\partial u/\partial z$ is seen in M3 (Fig. 4.4k). The changes in U_{700} and $\partial u/\partial z$ may be indicative of changes in the underlying horizontal temperature field (to be discussed below). The RV near the AEJ is important for AEWs, and the changes seen may suggest changes in the amount of

transient AEWs in the monthly mean dataset. In M1 to the north of the AEJ core, an increase in the deseasonalized RV is seen (Fig. 4.4f). This is interpreted as representing an increase in the number of AEWs (which would have RV > 0) through an area with climatologically anti-cyclonic (RV < 0; Fig. 4.4c) flow.

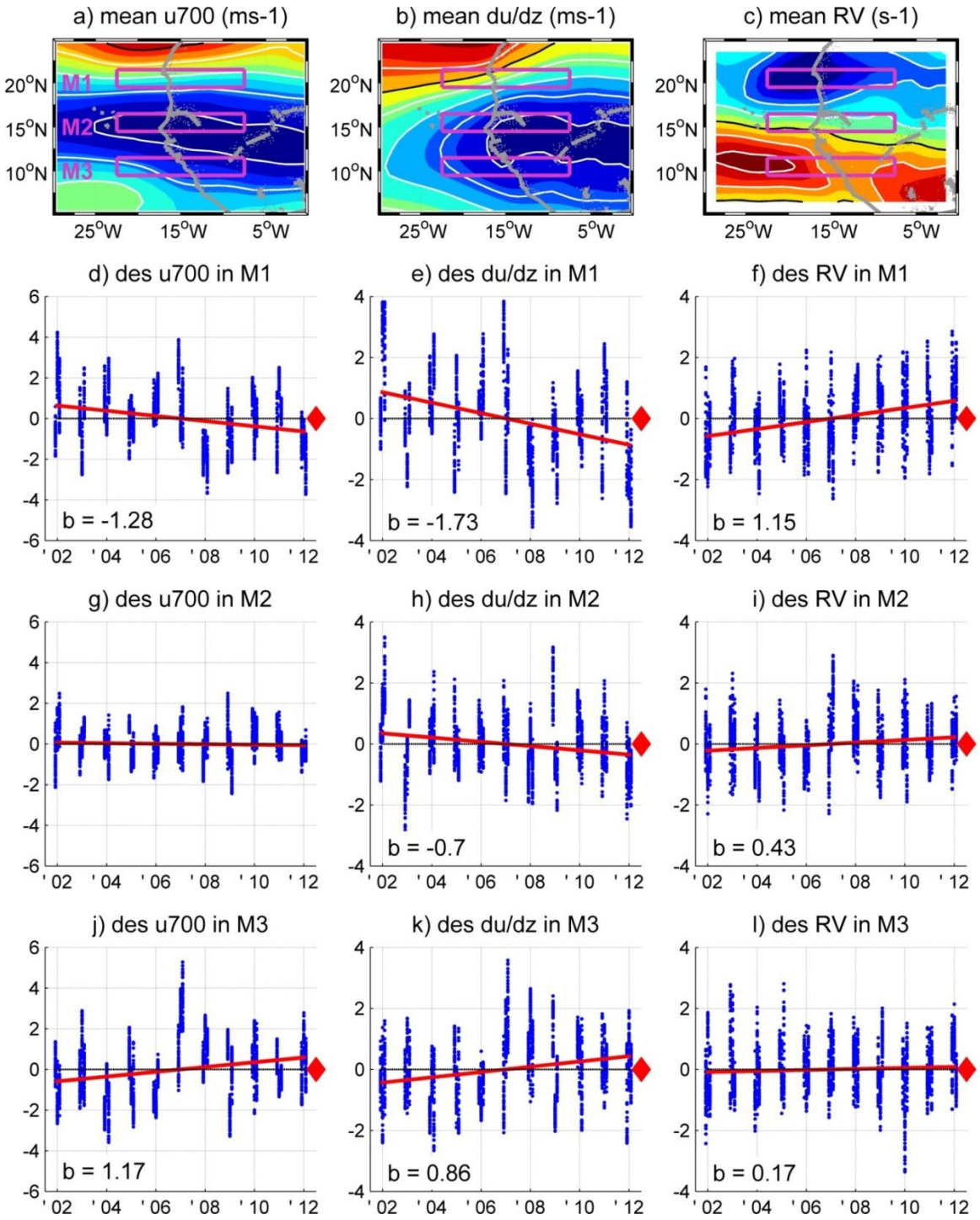

Figure 4.4: JJA mean fields of (a) U_{700}, (b) $\partial u/\partial z$, and (c) RV during 2002 to 2012. Below each are the deseasonalized time series for each variable and each grid point within the three micro-regions M1 (d,e,f), M2 (g,h,i) and M3 (j,k,l) outlined in pink. Trend lines have been fitted (red). Trends that are statistically significant above the 95% level are denoted with a red diamond along the abscissa and trend value (b; per decade) reported in-figure. Black contours in (a,b,c) denote the 0 contour with warm (cool) colors used for contours > 0 (< 0). White contours in (a) are every 2.5 m/s, in (b) are every 3 m/s, and in (c) are every 10^{-5} 1/s. Values for RV in (f,i,l) have been scaled by a factor of 10^5.

Having determined the atmospheric environment around the AEJ is evolving from 2002 to 2012, the analysis is now further extended to explore the extent to which the temperature (or heat content more accurately) over North Africa is changing and its causes, which would impact the AEJ/AEWs through the thermal wind relation. The Saharan environment is quantified using the North African Dipole Intensity (NAFDI; Rodríguez et al., 2015) and the low-level atmospheric thickness (LLAT; Lavaysse et al., 2009).

The North African dipole describes the characteristic summertime low (high) pressure over the tropics (Sahara) in the lower atmosphere associated with the African monsoon. The NAFDI is correlated with dust concentration at the Canary Islands (28ºN, 16ºW), U_{700} over North Africa, and also the transport pattern/amount over the sub-tropical North Atlantic (Rodríguez et al., 2015). The dipole can be quantified using the NAFDI which examines the difference in 700 hPa geopotential height (Φ) anomalies over Morocco (8º-5ºW, 30º-32ºN) in the north and Bamako (9º-6ºW, 10º-14ºN) in the south:

$$NAFDI = \frac{1}{10} * ((\Phi_i - \Phi_m)_M - (\Phi_i - \Phi_m)_B) \qquad \text{(Eq. 4.3)}$$

where i is a given month, m is the location's spatiotemporal mean, M is for Morocco, B is for Bamako, and 1/10 is a scaling factor. The Morocco and Bamako domains are shown in Figure 4.5a along with the behavior of deseasonalized NAFDI during JJA in Fig. 4.5b (black and aqua). From both monthly (Fig. 4.5b, black) and seasonal (Fig. 4.5b, aqua) values, the NAFDI experienced an increasing trend. Seasonal values of NAFDI estimates

the same trend as using monthly values of NAFDI. However, due to limited degrees of freedom (n=10), the seasonal NAFDI trend is not significant whereas the monthly NAFDI increase is (at the 90% level).

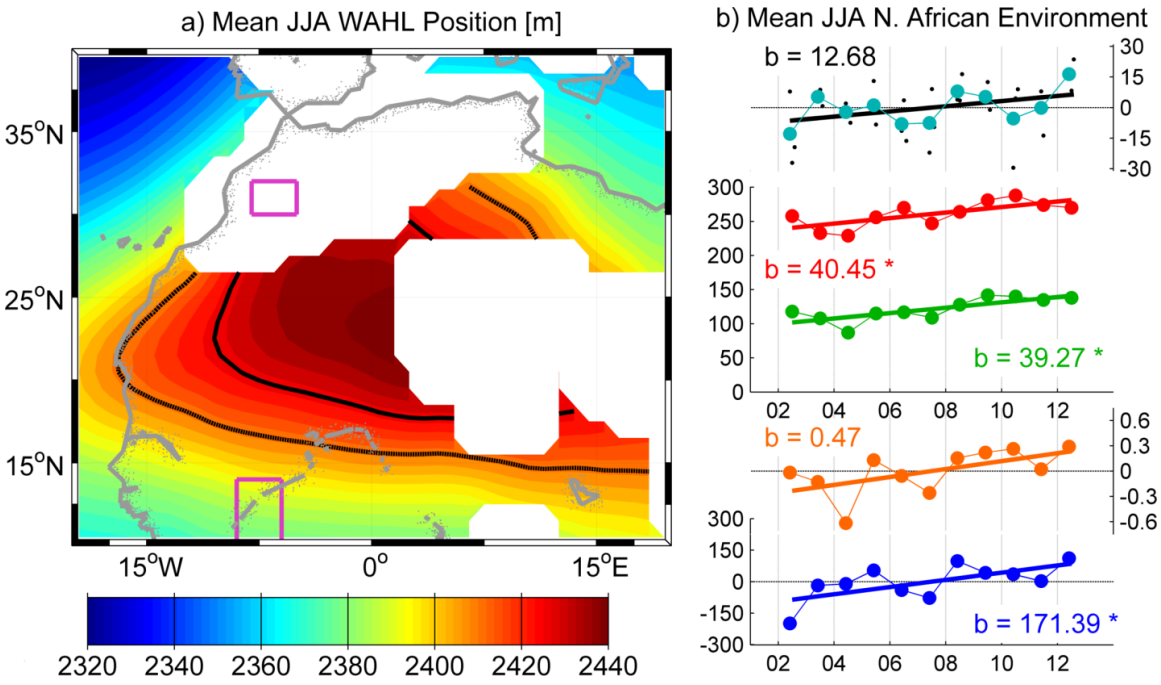

Figure 4.5: (a) Mean position of the WAHL during JJA and (b) indices of the mean JJA North African environment: NAFDI (black, aqua), LLAT (red (>2410 m) and green (> 2425 m)), T_{10m} (orange), and P (blue). Areas in white are locations where the 925 hPa height were unavailable due to elevated terrain. The statistical significance of trends (per decade) reported in (b) is >90% except where * denoted >95%. The units for NAFDI and LLAT are m, T_{10m} is K, and P is kg/km^3. Grid points used to calculate NAFDI are outlined in pink in (a), and contours are 2425m (inner) and 2410 m (outer).

Another important feature of the North African environment is the West African Heat Low (WAHL) which plays an important role in the maintenance of the AEJ (e.g. Thorncroft and Blackburn, 1999). The WAHL characterizes a dome-shaped heating feature present in the lower troposphere over western North Africa whose position can be determined by calculation of low-level atmospheric thickness (LLAT; Lavaysse et al., 2009). LLAT is determined as the difference in geopotential heights at 700 and 925 hPa.

The mean position of the WAHL (within 20ºW to 20ºE, 10ºN to 40ºN) during JJA in 2002 through 2012 is shown in Fig. 4.5a, with contours of 2410 m (outer) and 2425 m (inner).

To explore the evolution of the WAHL from 2002 to 2012, the evolution of LLAT counts (i.e. number of grid points) that exceed 2410 m and 2425 m are explored. First, the counts of LLAT for a given season that are above either threshold are tallied, then a trend and significance determined. Fig. 4.5b shows the JJA seasonal records of LLAT that exceed 2410 m (green) and 2425 m (red). The significant (> 95% level) increases seen in LLAT under both thresholds suggests that the WAHL has experienced a combination of areal expansion and strengthening. These increases in the NAFDI and LLAT during JJA are believed to be reflections of the increase in surface temperature over the Sahara (Fig. 4.5b, orange; using T_{10m} from MERRA over 10ºW to 10ºE, 20ºN to 30ºN). Indeed, an amplified Saharan warming is seen in atmospheric reanalyses (including MERRA; Cook and Vizy, 2015) and is likely brought about by an increased warming over the sub-tropics compared to the tropics (e.g. Sutton et al., 2007).

Another link to dust that deserves assessment is that with Sahel precipitation. Past studies (Prospero and Lamb, 2003; Wang et al., 2012) have noted anticorrelation between North African dust export and Sahel rainfall. If the AOD trends observed by MODIS result from this anticorrelation, it may be anticipated that a decrease in Sahel precipitation will be observed. Precipitation data from the Tropical Rainfall Measuring Mission (TRMM) Microwave Imager (TMI; product: TRMM_3A12_007_rainWater)

were obtained from NASA's Goddard Earth Sciences Data and Information Services Center (GES-DISC) Interactive Online Visualization and Analysis Infrastructure, or Giovanni, web portal (http://giovanni.gsfc.nasa.gov/giovanni/). The data cover the Sahel region (20ºW to 40ºE, 10º to 20ºN) following that used by Wang et al. (2012). Figure 4.5b contains the deseasonalized JJA record of Sahel precipitation (in blue) and reports a statistically significant increase in Sahel rainfall. This finding is in agreement with other studies which report a recovery of Sahel precipitation from a low during the 70s and 80s, and point to the role of increasing greenhouse gases as the driver for Sahel precipitation recovery (Dong and Sutton, 2015; Giannini, 2015). Thus, it is believed that the increase in dust is occurring in spite of the Sahel precipitation recovery.

4.3.2 Analysis of AEJ Potential Vorticity

An analysis of the potential vorticity along 5ºW is performed to further probe the possibility of the hypothesis that changes in AEW activity (particularly those propagating along the northern flank of the AEJ) are influencing the dust trends seen. After being triggered by convection upstream over East/Central Africa, AEWs grow through mixed barotropic-baroclinic mechanism associated with the AEJ (Hall et al., 2006; Skinner and Diffenbaugh, 2014). Various energetic analyses have been performed in the past on the North African environment, including the seminal work of Burpee (1972) and the more recent work Wu et al. (2012). These works analyze the instability of the quasi-

geostrophic potential vorticity (QGPV, PV for short). An academic treatment of PV and baroclinic instability (e.g Holton, 2004) arrives at the following equation:

$$c_i \left[\int \int \frac{\partial \bar{q}}{\partial y} \frac{\rho_0 |\psi|^2}{|\bar{u}-c|^2} dy\, dz^* - \int \varepsilon \frac{\partial \bar{u}}{\partial z^*} \frac{\rho_0 |\psi|^2}{|\bar{u}-c|^2} \right]_{z^*=0} dy \Bigg] = 0 \qquad \text{(Eq. 4.4)}$$

where q and u are the PV and zonal wind of the base-state (respectively), ρ_0 is atmospheric density, ψ is geostrophic streamfunction, c ($c = c_r + c_i$) is the complex phase speed, and y and z^* are the meridional and vertical coordinates (respectively). For unstable ψ wave modes, c_i must exist (i.e. $c_i \neq 0$), thus the two integrals must cancel (i.e. sum to zero).

This creates three interesting scenarios for instability when considering $\partial u/\partial z$ at a lower boundary $z^* = 0$ (i.e. near the surface): Case I with $\partial u/\partial z > 0$, Case II with $\partial u/\partial z = 0$, and Case III with $\partial u/\partial z < 0$. Case II is the simplest case, as $\partial u/\partial z = 0$ implies no meridional temperature gradient (a consequence of Eq. 4.1). For instabilities in Case II, $\partial q/\partial z$ must change sign within the domain (i.e. $\partial q/\partial y = 0$ somewhere). Case I is unlikely to exist in the North African domain, as $\partial u/\partial z > 0$ implies a $\partial T/\partial y < 0$ or temperatures to decrease away from the equator. This does not occur as the equatorial region during JJA is cooler than the hot Saharan desert region to the north. Finally, Case III provides the converse to Case I (i.e. $\partial u/\partial z < 0$ implies $\partial T/\partial y > 0$) and does exist over North Africa. In order to have unstable wave modes under Case III, $\partial q/\partial y < 0$ must occur within the domain. Shown in Figure 4.6 are the mean JJA seasonal and trend in $\partial u/\partial z$ at 925hPa, the lowest level across all latitudes where $\partial u/\partial z$ could be computed.

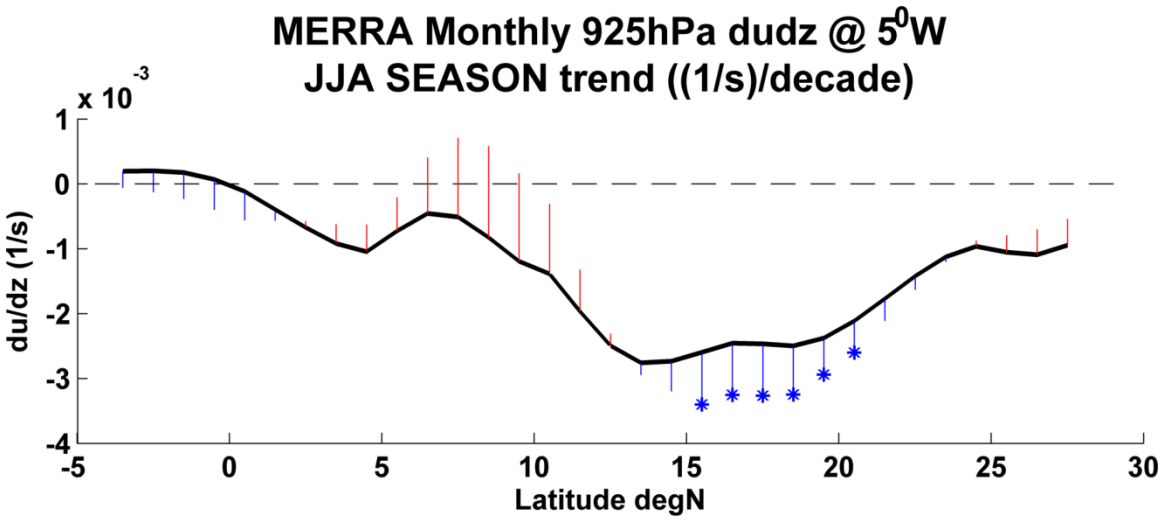

Figure 4.6: (black) Mean ∂u/∂z at 925 hPa during the JJA season from 2002 to 2012 along 5ºW longitude. At each latitude is the (red) positive or (negative) decadal trend in du/dz, added to the mean ∂u/∂z curve. Trends marked with * are significant beyond the 95% level.

As can be seen in Fig. 4.6, ∂u/∂z ≈ 0 (in a mean sense) through about 7ºN. During the period considered (2002 to 2012), the mean JJA ∂u/∂z is trending towards 0 1/s as far north as 10ºN. This is in contrast to the latitudes 10º-22ºN, which see substantially negative ∂u/∂z, and see ∂u/∂z trending more negative, perhaps as a result of the heating of the WAHL. These behaviors may also be indicative of the hypothesized northward displacement of the AEJ. The structure of ∂u/∂z also points towards locations where Case II and Case III may occur: the atmosphere is more barotropic (Case II-like) to the south of ~12ºN while it is more baroclinic (Case III-like) to the north of ~12ºN.

An analysis of the PV budget over North Africa is now presented. A latitude-height cross section at 5ºW is analyzed form −5º to 30ºN and 1000 to 100 hPa. The meridional PV gradient is calculated following Burpee (1972) in x-, y-, z- dimensional coordinates:

$$\frac{\partial \bar{q}}{\partial y} \equiv \beta - \frac{\partial^2 \bar{u}}{\partial y^2} - \frac{f_0^2}{N_s^2} \frac{1}{\rho_s} \frac{\partial \rho_s}{\partial z} \frac{\partial \bar{u}}{\partial z} - \frac{f_0^2}{N_s^2} \frac{\partial^2 \bar{u}}{\partial z^2} \qquad \text{(Eq. 4.5)}$$

where $\partial q/\partial y$ is the meridional gradient in PV, β is the meridional gradient in the Coriolis parameter (f_0), N_s^2 ($N_s^2 = (g/\theta) * d\theta/dz$; g is gravity and θ is potential temperature) is the Brunt-Väisälä frequency, and subscript s used for vertical level surfaces; simple finite differences are used to evaluate derivatives. The analysis is presented for the first two terms ($K(y) = \beta - \partial^2 u/\partial y^2$) which are barotropic terms, the last two terms which are baroclinic terms (containing $\partial u/\partial z$), and the entirety of Eq. 4.5. Figure 4.7 displays the JJA seasonal trends during 2002 to 2012 of the barotropic terms (Fig. 4.7, left), baroclinic terms (Fig. 4.7, middle), and the entire PV gradient (Fig. 4.7, right). The terms and $\partial q/\partial y$ were computed first, then deseasonalized, and finally trended.

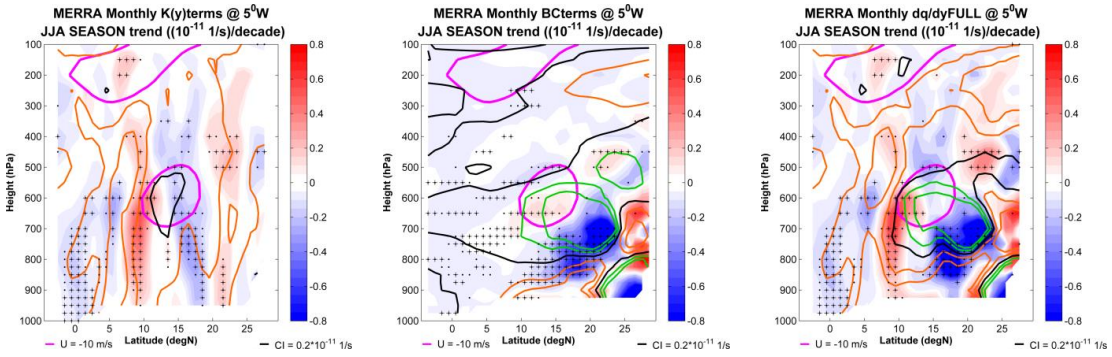

Figure 4.7: JJA seasonal trends in (left) barotropic, (middle) baroclinic, and (left) all terms of Eq. 4.5. Pink contour denotes the −10 m/s contour of the JJA seasonal mean U wind. Other contours represent 0.2 x 10^{-11} 1/s contours, orange are positive, green negative, and black the 0 contour of the respective term. Trends are 10^{-11} 1/s per decade, crosses (dots) are trends significant at the 95% (90%) level.

If it is assumed that the atmosphere is barotropic (i.e. $\partial u/\partial z = 0$), Case II instability arises solely from dynamic instability in horizontal flow and requires $\partial q/\partial y$ to

change sign (or $\partial q/\partial y = 0$ somewhere) within the domain. This can be seen in the mean sense in Fig. 4.7 (left) within the vertical corridor between 10º and 15ºN and confined between 700 and 600 hPa (along the black contour). The instability region around 12ºN arises from the cyclonic shear as the AEJ speed decreases to the south of its core. At the critical latitude y_{cr} where the barotropic term $K(y_{cr}) = 0$, conditions favorable to instability from Kuo theory occur if $K(y) > 0$ for $y < y_{cr}$ and $K(y) < 0$ for $y > y_{cr}$ (Kuo, 1949; Wu et al., 2012). Trend analysis appears to reveal a subtle northward shift in the small barotropically unstable (Case II) region, believed to be associated with a northward shift of the AEJ. This region is to the south of 15ºN latitude where according to Fig. 4.6 $\partial u/\partial z \approx 0$, thus the barotropic assumption has some standing.

To the north of 15ºN latitude, however, the atmosphere cannot be assumed barotropic and must be considered baroclinic (Case III; see Fig. 4.6). Figure 4.7 (middle) is now discussed. Above the latitude band 15º to 20ºN where $\partial u/\partial z < 0$ is a large region between 800 and 600 hPa in which $\partial q/\partial y < 0$, thus satisfying conditions for baroclinic instability according to Case III. When considering the trend behavior of the baroclinic terms (Fig. 4.7, middle), it appears that through time the baroclinic center becomes more negative and encroaches lower in the atmosphere towards the surface. This may be associated with an increase in instability to the north of the AEJ latitude and might lead to increased AEW activity and/or AEW interaction with the surface, in which dust can be mobilized and exported from the Saharan region.

Finally, consider together the barotropic and baroclinic terms that make up the whole PV gradient (Fig. 4.7, right). Several mean features and trend behaviors seen in either barotropic or baroclinic analyses are identifiable in the whole PV gradient. For example, the barotropically unstable region along the AEJ south flank is seen around 10ºN latitude, and appears to be pushed northward by the increasing $\partial q/\partial y$ trend. Likewise, the baroclinically unstable region to the north of the AEJ remains strongly identifiable, as does the behavior of its trend to extend lower in the atmosphere. The mean locations of the barotropic and baroclinic instability areas match well with processes for AEWs and latitude-height regions suggested by other authors. AEWs to the south of the jet rely on mixed barotropic-baroclinic processes and are easily identified around 700 hPa while AEWs to the north of the jet rely on baroclinic processes and are easily identified lower in the atmosphere around 850 hPa (Pytharoulis and Thorncroft, 1999; Skinner and Diffenbaugh, 2014; and references therein).

The analysis of meridional PV gradients and barotropic/baroclinic energy locations adds further confidence to the hypothesis that a warming Sahara/WAHL migrates the AEJ slightly northward which displaces the barotropic zone for AEWs along the AEJ southern flank slightly north. There is also a simultaneous intensifying and slightly lowering the baroclinic zone for AEWs along the AEJ northern flank. The lowering of the baroclinic zone may aid in dust mobilization as well as possible increased export by an increased AEW activity. This hypothesis deserves further attention, the use of higher resolution datasets, and more advanced analytic techniques, but nonetheless appears sound.

4.3.3 Possible Linkage to Decreasing Anthropogenic AOD via Atlantic SST

Atmospheric aerosols can impact the surface radiative balance through both direct and indirect effects. As will be shown in Chapters 5 and 6, the mid-latitude decrease in AOD can bring about an increase in surface radiance directly through a reduction of light attenuation and potentially indirectly through a reduction in cloud optical thickness. The converse is also true: an increased aerosol load can result in reduced surface radiation. Additionally, well-mixed greenhouse gases can substantially perturb the longwave radiative balance.

In modeling studies, the climate response to increases in aerosols during the 20th Century produces a cooler atmosphere in the Northern Hemisphere relative to the Southern Hemisphere resulting from the asymmetry in aerosol forcing (strongest in the Northern Hemisphere, see Fig. 1.4); this is on top of the global warming signal from well-mixed greenhouse gases (e.g. CO_2; Ming and Ramaswamy, 2009). In the Atlantic region, the atmospheric signal from increasing aerosol forcing may imprint itself in the oceanic sea-surface temperature (SST), producing a meridional gradient with warmer SSTs in the South Atlantic relative to the North (Chang et al., 2011). Due to the heat imbalance, signals in both the atmosphere and ocean under an increasing aerosol load (from primarily in the Northern Hemisphere mid-latitudes) can manifest in a southward positioning of the inter-tropical convergence zone (ITCZ). Might a relaxing of mid-

latitude forcing (as seen by a reduction in anthropogenic aerosol (Chapter 3)) permit a northward shift in the ITCZ with the potential to alter dust transport patterns?

As a first step, the Atlantic Interhemispheric Temperature Gradient (AITG) is calculated following Chang et al. (2011) as the difference in deseasonalized average SST between the tropical South Atlantic (5º-35ºS, 60ºW-20ºE) and the tropical North Atlantic (5º-35ºN, 0º-80ºW). Positive AITG indicates the South Atlantic is warmer than the North Atlantic. Monthly mean SST averages from MODIS-Aqua during 2002 to 2012 over the two regions were obtained from NASA's Giovanni web portal (http://giovanni.gsfc.nasa.gov/giovanni/). Figure 4.8 displays the AITG index, with JJA seasonal averages highlighted in red. There is a very weak decreasing trend (−0.078 K per decade, not significant) in the JJA seasonal AITG index, indicating a slight (yet not statistically distinguishable from an absent trend) increase in the North Atlantic SST relative to the South Atlantic. An interesting behavior, it appears as though there may be an increase in JJA South Atlantic SST until 2008 when the North Atlantic SST appears to be increasing during JJA that ultimately lead to the uncertain trend in JJA throughout 2002 to 2012.

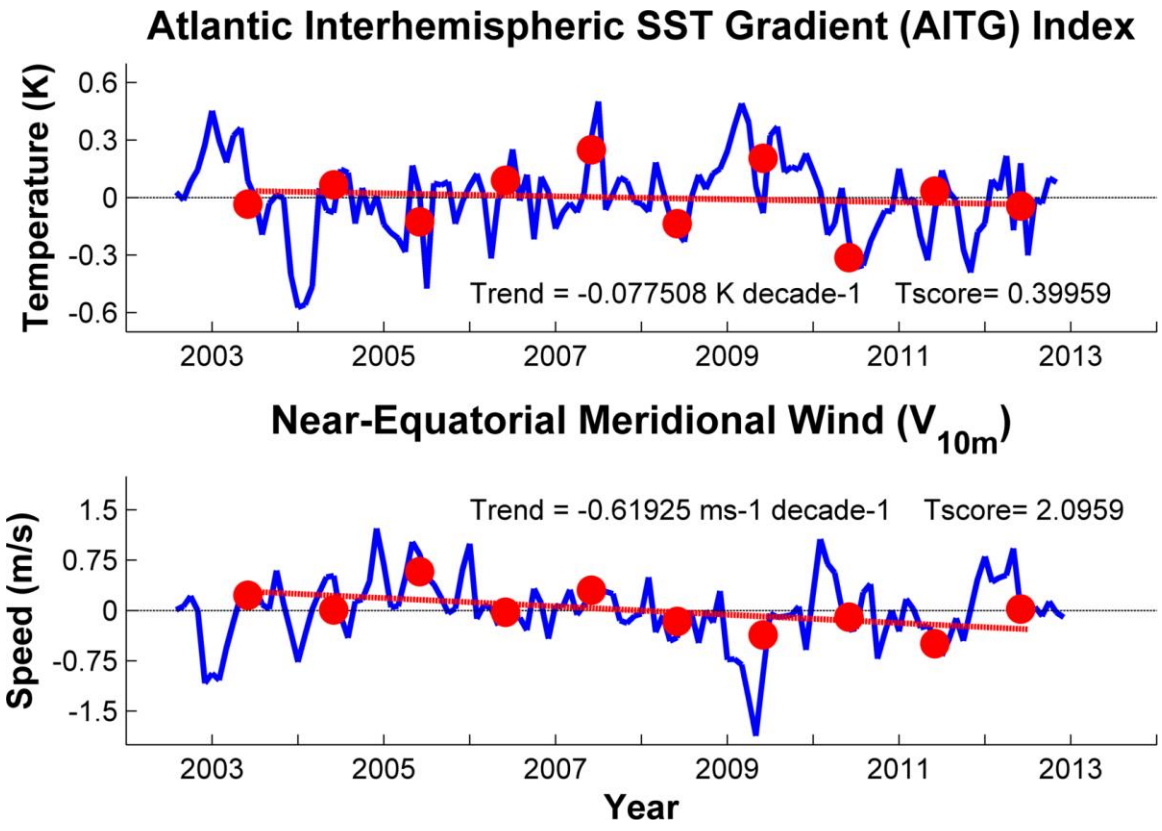

Figure 4.8: Deseasonalized time series (blue), JJA mean (red dot), and JJA trend (red line) for AITG index (top) and near-equatorial V_{10m} wind speed (bottom) during July 2002 to December 2012. Also reported are the value of the JJA trend and Tscore of its significance (Tscore > 1.3 is 90% significant, Tscore > 1.8 is 95% significant).

The AITG has been noted to influence the position of the Atlantic ITCZ through cross-equatorial winds due to small pressure gradients arising from the anomalous SST gradients (Chiang et al., 2002). Indeed, during much of the 20th Century in which the North Atlantic saw increasing aerosol load and imparted a positive AITG gradient (i.e. South Atlantic warming relative to the North Atlantic), there was a decrease trend in the surface meridional wind about the equator signaling a southward shift in the ITCZ (Chang et al., 2011). Figure 4.8 also examines the monthly mean surface equatorial meridional wind from MERRA (V_{10m}) covering the same domain as Chang et al. (2011; 50º-10ºW and 0º-6ºN) with JJA seasonal averages highlighted in red. Throughout the

JJA season during 2002 to 2012 there appears to be a slight decrease in anomalous wind speed (−0.62 m/s per decade; significant at 90% level) signifying a southward shift in the ITCZ. This is counter to the idea that a decreasing aerosol load, through producing a negative AITG (i.e. North Atlantic warming relative to the South, a feature not significantly demonstrated in Fig. 4.8) would produce a positive trend in anomalous JJA V_{10m} and suggest a northward shift in the ITCZ.

The differences between this work and Chang et al. (2011) are briefly noted. While the variables and domains investigated are the same, Chang et al. (2011) use reconstructed SSTs while satellite observed SSTs are used presently. In the same vein, Chang et al. (2011) use meridional winds from the Comprehensive Ocean-Atmosphere Dataset (COADS) whereas those used presently are from the MERRA atmospheric reanalysis. Additionally, Chang et al. (2011) assess a time period extending back to 1870, and in doing so are able to produce a more nuanced analysis. For example, in the AITG Chang et al. (2011) can distinguish Atlantic Ocean internal variability (by the Atlantic Multidecadal Oscillation) from the more long-term signal associated with aerosol increase throughout much of the 20th Century. Here the results of Fig. 4.8 represent all contributions to the AITG. Nevertheless, the seemingly southward shift in the ITCZ (deduced from Fig. 4.8) appears to cast doubt on the hypothesis that the change in dust transport pattern may result from a northward shift in the ITCZ. Extending the analysis in this Chapter (with AVHRR observations and MERRA output) back in time to the 1980s and exploring more thorough analyses is a direction for anticipated future work.

4.4 Chapter 4 Summary

An increase in AOD of 0.02 per decade is observed by MODIS-Aqua over the sub-tropical North Atlantic Ocean. Trends in total AOD and natural (dust and sea salt) AOD reflect an increase in AOD over the sub-tropics. A dust estimation method (see Kaufman et al., 2005a,b) is used to determine dust AOD from satellite along with dust mass and dust mass flux. Trends in dust AOD mirror those in total AOD both annually and during the summer (JJA) season and show an extensive basin-wide (dust) AOD increase over the sub-tropics. This is reflected in trends in JJA dust mass and mass flux. The upwind North African/Saharan region is explored for any changes that dynamically link to dust. The AEJ is shown to be shifting slightly northward from its mean JJA position along with an increase in transient AEW activity along the AEJ north flank. These changes are linked to a warming signal seen over the Saharan region (using NAFDI, LLAT, and T_{10m}) which manifests itself through changes in low-level baroclinic stability below and to the north of the AEJ mean position. It is believed the changes in AEW activity and low-level stability lead to increased dust mobility while the shift in the AEJ results in a slightly northward migration in dust export, and a combination of these two factors results in the sub-tropical dust increase.

Chapter 5: Direct Effect of Aerosol Trends

5.1 Aerosol DRE Example

As discussed in Section 2.3.3, the aerosol direct radiative effect (DRE) is the difference between fluxes for an aerosol-laden sky and a clean sky under clear-sky conditions, integrated over wavelengths corresponding to the SW region (taken be $0.2 < \lambda < 5.0$ μm) of the electromagnetic spectrum. The total aerosol DRF (TDRF) used the total aerosol loading and clean (i.e. zero aerosol) sky for DRF computation, anthropogenic DRF (ADRF) uses total aerosol loading and natural aerosol sky for DRF computation, and natural DRF (NDRF) uses natural aerosol sky and clean (i.e. zero aerosol) sky for DRF computation. An example calculation using the SBDART model has been run to aid in displaying the aerosol SW DRE. All inputs not explicitly specified here remain at their default values (see Ricchiazzi, 2002). Figure 5.1 shows the top-of-atmosphere

(TOA), surface (BOT) downward, and BOT upward fluxes for this example. The inset of Fig. 5.1 shows the wavelength step ("WL step") used and the internal sea water albedo used (albedo is the ratio of BOT up flux to BOT down).

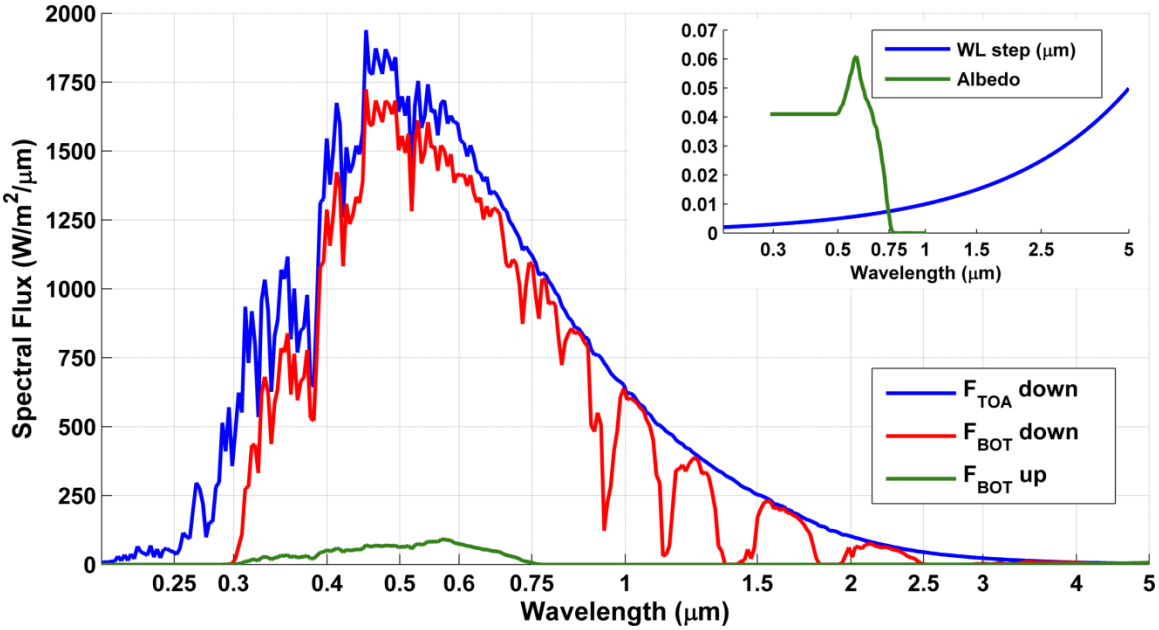

Figure 5.1: Example of downward spectral fluxes (F(λ)) for TOA down (blue), BOT down (red), and BOT up (green). The solar spectrum used for SBDART calculations is MODTRAN_3 (blue). Inset: step in wavelength (WL step; blue) used and internal sea water albedo (green: albedo = F^{u}_{BOT}/F^{d}_{BOT}) used for spectral flux calculations.

For this example, the MODTRAN_3 solar spectrum (nf = 3) from 0.2 to 5 μm (wlinf = 0.2, wlsup = 5.0) is used with varying wavelength interval (wlinc = −0.01). The model geometry was set to run for a summertime oceanic site around the 1330 LST MODIS-Aqua crossing time (iday = 182 (July 1), alat = 40 (40ºN), alon = −30 (30ºW), time = 15.5 (1530GMT or 1330LST)). The model surface albedo was set for sea water (isalb = 4), while the model atmosphere was set for mid-latitude summer (idatm = 2) with integrated water vapor amount of 3.137 cm (equivalently 3.137 g/cm^2; uw = 3.137) and integrated ozone concentration of 291.6 Dobson Units or 0.2916 atm-cm (uo3 = 0.2916).

The boundary layer aerosol model was configured with the oceanic aerosol model (iaer = 3) using a visibility at 550 nm of 20 km (vis = 20) and an AOD of 0.094 (tbaer = 0.094). The model output was configured to provide upward, downward, and direct spectral fluxes at the TOA (100 km) and BOT (0 km; iout = 1). Several interesting features can be identified in Fig. 5.1. First is the strong attenuation of UV radiation ($\lambda < 0.4$ μm) by ozone. Also notable is the attenuation in the visible ($0.4 < \lambda < 0.75$ μm) in the form of absorption by molecular oxygen, Rayleigh scatter by atmospheric gases, and Mie scatter by aerosols. The absorption by water vapor in the near-IR part of the spectrum can also be seen in bands centered on 0.94, 1.1, 1.38, and 1.87 μm. Finally, the internal sea water albedo is between 0.04 and 0.06 over much of the UV-visible portion of the SW spectrum and quickly falls to approximately 0 above 0.75 μm. This is in line with an albedo estimate of 0.07 from Coakley (2003).

Also discussed in Section 2.3.3 are the various fluxes at both the TOA and BOT either simulated directly by SBDART or computed after simulation (see also Fig. 2.2). These include the flux calculations performed by SBDART (TOA downward (TOA_d), TOA upward (TOA_u), BOT downward (BOT_d), and BOT upward (BOT_u) fluxes) in addition to three derived fluxes (Earth system absorbance (ES_a), atmospheric absorbance (ATM_a), and surface absorbance (SFC_a)). A second example SBDART simulation was run identical to that above but excluding the boundary layer aerosol (i.e. iaer = 0) and represents a "clean" clear sky. This is an exaggerated case, as the sky is never truly devoid of aerosol particles. The DRF calculated with aerosol simulation (from Fig. 5.1) and "clean" simulation represents the total aerosol TDRF. These two simple simulations

allow for an initial demonstration of how aerosol loading affects the Earth system via the aerosol DRE. Spectral total aerosol TDRFs for relevant flux quantities have been computed and are displayed in Figure 5.2 as well as a listing of their integrated SW aerosol TDRF. As can be seen, the ES_a and TOA_u total aerosol TDRFs are identical in magnitude (5.1 W/m^2) and only differ in sign. This is because TOA_d for both aerosol and clear-sky calculations is identical (i.e. F_{sun}, the extraterrestrial solar flux) and is canceled in the calculation of ES_a. The difference in sign represents a loss in energy of the Earth system due to an increase in TOA upwelling radiation from aerosol scattering. The 5.1 W/m^2 is in line with other estimates of the TOA aerosol DRE (e.g. Yu et al., 2006). The total aerosol TDRF for ATM_a (1.5 W/m^2) is representative of the slight absorption of radiation by the aerosol load, thus acting to deposit energy into the atmosphere, while the negative BOT_d total aerosol TDRF (−6.8 W/m^2) represents a decrease in flux to the surface as the result of attenuation (both scattering and absorption) by the overlying aerosol load. This decreased flux arriving at the surface further manifests as both a slight negative BOT_u total aerosol TDRF (−0.16 W/m^2) and a substantial reduction in the SFC_a (whose total aerosol TDRF is −6.6 W/m^2). Consistent with the internal sea water albedo above 0.75 μm (see Fig. 5.1, inset), the spectral BOT_u total aerosol TDRF is zero above 0.75 μm as there is no reflected solar SW radiation.

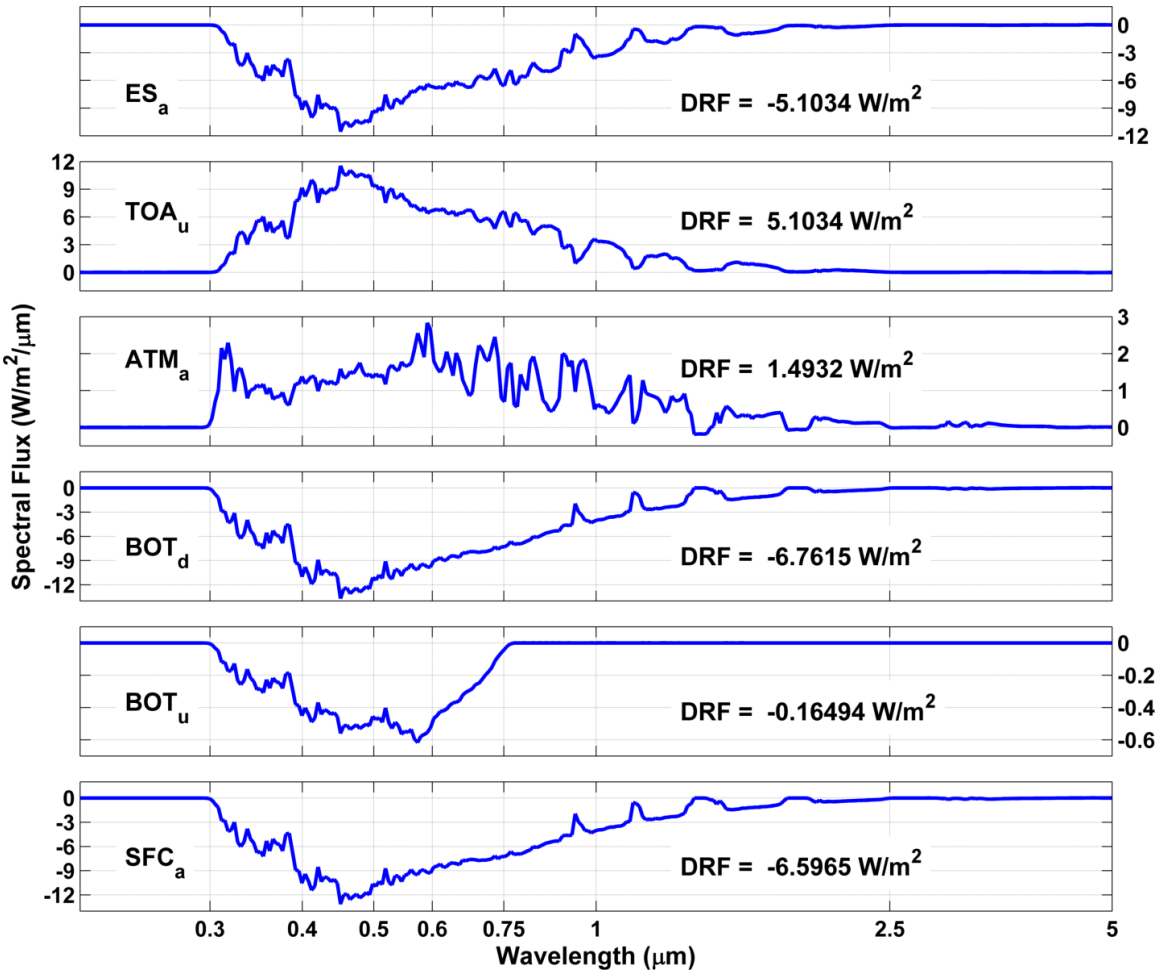

Figure 5.2: Example of downward spectral fluxes (F(λ)) from aerosol DRE calculation for the indicated flux quantity (see text and Fig.2.2 for description). SBDART configured as described in this section. Listed to the right is the integrated TDRF value using Eqn. 2.11. The total aerosol TDRF uses total aerosol minus clean sky (i.e. no aerosol).

5.2 SBDART Inputs – Setup for Various Simulations

These methods will be used to assess the direct impact the aerosol load over the North Atlantic Ocean has on the Earth system in the region. SBDART calculations will be performed for each grid point where the MODIS-Aqua C6 Level-3 monthly product has a mean oceanic AOD recorded; latitude, longitude, 14th day of the month, and 1330

LST will be used to determine relevant geometries. The underlying albedo is set to the internal sea water albedo provided in SBDART (see Fig. 5.1, inset). The MERRA monthly instU_3d_asm_Cp product will be used to provide the monthly mean surface pressure and vertical profiles of pressure (p), temperature (T), water vapor density ($[H_2O]$), and ozone density ($[O_3]$). These vertical profiles of water vapor and ozone are scaled to the column density reported in the MODIS C6 Level-3 product. The aforementioned parameters (i.e. geometry, surface, atmospheric profile) will remain constant across all simulations with varying aerosol loadings.

The aerosol DRFs (and how they may be changing) are key components of this work, and several simulations are performed under select aerosol parameterizations (briefly summarized in Table 5.1). These include one simulation ("Total") with the total aerosol loading derived from by MODIS-Aqua C6 and one simulation ("Clear") with no aerosol in the model (i.e. ibaer = 0 as in the example in Fig. 5.2). Differences between "Total" and "Clear" simulations produce the total aerosol TDRF. Four additional simulations are performed with efforts at providing a more realistic picture of the anthropogenic-free aerosol loading to be used to determine the anthropogenic aerosol DRF (ADRF) and natural aerosol DRF (NDRF). The key aerosol parameters that differ across these aerosol simulations are the AOD at 550 nm (through removal of estimated anthropogenic AOD), spectral Ångström exponent ($AE(\lambda)$ and thus spectral $AOD(\lambda)$), spectral single scattering albedo ($SSA(\lambda)$), and spectral asymmetry parameter ($g(\lambda)$).

Name	**SBDART Inputs**	**Notes**
Clean	ibaer = 0	No boundary layer aerosol
Total	ibaer = 5	User-defined aerosol
	tbaer = MYD C6 L3 AOD(550 nm) qbaer = MYD C6 L3 AOD(λ) wbaer = GOCART SSA(λ) climatology using "basic" gbaer = MYD C5 L3 g(λ) using "basic"	Fluxes simulated for total aerosol loading
K05	ibaer = 5	User-defined aerosol
	tbaer = MYD C6 L3 AOD(550nm) – AOD_{hum} from K05 [a]qbaer = MYD C6 L3 AE(λ) using "basic" [a]wbaer = GOCART SSA(λ) climatology using "basic" [a]gbaer = MYD C5 L3 g(λ) using "basic" [b]qbaer = MYD C6 L3 AE(λ) using "2box" [b]wbaer = GOCART SSA(λ) climatology using "2box" [b]gbaer = MYD C5 L3 g(λ) using "2box"	Fluxes simulated for estimated natural aerosol loading (using K05 method); uses two supplemental methods
GCT	ibaer = 5	User-defined aerosol
	tbaer = MYD C6 L3 AOD(550nm) * % SS+DU from GOCART [a]qbaer = MYD C6 L3 AE(λ) using "basic" [a]wbaer = GOCART SSA(λ) climatology using "basic" [a]gbaer = MYD C5 L3 g(λ) using "basic" [b]qbaer = MYD C6 L3 AE(λ) using "2box" [b]wbaer = GOCART SSA(λ) climatology using "2box" [b]gbaer = MYD C5 L3 g(λ) using "2box"	Fluxes simulated for estimated natural aerosol loading (using % SS+DU from GOCART); uses two supplemental methods

Table 5.1: Description of inputs for various aerosol simulations with SBDART model. Boundary layer aerosol SBDART input codes are tbaer = AOD at 550 nm, qbaer = AOD(λ), wbaer = SSA(λ), and gbaer = g(λ). K05 simulations denote modifying MODIS-Aqua total AOD by removal of an anthropogenic AOD computed with the K05 method. GCT simulations denote modifying MODIS-Aqua total AOD by retaining only the percentage that is SS+DU AOD species climatology from GOCART. a-superscript and b-superscript denote two different experiments ("basic" and "2box", respectively) using different assumptions to fulfill AOD(λ), SSA(λ), and g(λ) for "natural" aerosol loads (see text for description). "MYD C6 L3" denotes the MODIS-Aqua Collection 6 Level 3 monthly mean product, C5 refers to Collection 5.1 used for g (discontinued in C6).

5.2.1 Deciding on Clear Sky

The example from Section 5.1 was performed using two simulation runs: one with aerosol load and one completely without (due to turning all boundary aerosol layer processes off). This computation of total aerosol TDRF represent an upper limit on the

DRFs as the atmosphere is never completely free of any aerosol load. Thus, it is necessary to make some assumptions on the background aerosol load, especially if the anthropogenic aerosol ADRF is desired. Two methods are used to provide an estimate of the anthropogenic AOD at 550 nm and subsequently remove it from calculations for the clear sky with remaining natural background AOD.

The first of these two methods is identical to the method used to estimate dust (see Section 2.3.2). This method (referred to as K05) was developed by Kaufman et al. (2005a,b) and works by parameterizing the marine AOD component along with fine-mode fractions (FMF or f_x) for anthropogenic, marine, and dust components (see Section 2.3.2 or Kaufman et al. (2005a,b) for details). The total AOD (at 550 nm) is assumed a linear sum of anthropogenic, marine, and dust components while the fine-mode AOD (total AOD * FMF) is also the linear sum of species components multiplied by their respective FMF. This provides a system of two equations with six unknowns. Parameterizations for marine AOD and component FMFs reduce the unknowns to two, and the system can be solved for either dust AOD or an analogous equation for anthropogenic AOD:

$$\tau_a = \frac{1}{f_d - f_a} * [\tau_t(f_d - f_t) - \tau_m(f_d - f_m)] \qquad \text{(Eq. 2.9)}$$

The background "natural" AOD at 550 nm that remains using the K05 method is thus:

$$\tau_{NAT} = \tau_{TOT} - \tau_a \qquad \text{(Eq. 5.1)}$$

and is unique for each month.

The second method (referred to as GCT) to remove the anthropogenic AOD relies on the monthly climatology of fractional aerosol component make-up. GOCART provides five component AODs (SU, BC, OC, SS, and DU) that sum linearly to produce the total AOD (for more on GOCART see Section 2.2.1). The background "natural" AOD in this method is simply taken as the percentage that the SS and DU species contribute to the total AOD:

$$\%_{NAT} = (\tau_{SS} + \tau_{DU})/\tau_{TOT} \qquad \text{(Eq. 5.2)}$$

This is done for each month of the GOCART dataset (i.e. January 2001 through December 2009) and a monthly mean climatology is generated. This monthly climatology is then applied to the total AOD to arrive at the background "natural" AOD:

$$\tau_{NAT}(y,m) = \tau_{TOT}(y,m) * \%_{NAT}(m) \qquad \text{(Eq. 5.3)}$$

The remaining natural AOD from either K05 (Eq. 5.1) or GCT (Eq. 5.3) is then used together with supplementary aerosol properties (described next in Section 5.2.2) to produce an estimate of the clear-sky fluxes free of the influence of anthropogenic aerosol.

5.2.2 Supplementary Aerosol Properties

Two methods ("basic" and "2box") are used to estimate the supplementary aerosol properties for this background loading. After AE(λ) is determined, AOD(λ) is then computed. The first of these methods is the "basic" method and relies on the observed g from MODIS Collection 5.1 (this parameter not included in C6), the monthly mean climatology of SSA from GOCART, and the observed AE from MODIS C6 total AOD. The second of these methods is the "2box" method, employing properties in two sub-domains as representative of the "natural" background supplementary aerosol properties. This method uses a zonal profile of each supplemental property created in the sub-tropics (20ºN to 30ºN) to capture the predominant coexistence of marine and dust components, especially the seasonality of dust loading. The method also uses a spatial mean of properties representative of a mainly oceanic loading within a mid-latitude region (50ºW to 30ºW, 35ºN to 45ºN) over the entire mid-latitudes (35ºN to 50ºN). Random perturbations of up to ± 100% of the variance in either region were also added to represent some heterogeneity. Finally, the region between the sub-tropic and mid-latitude domains is blending using linear interpolation for these latitudes (i.e. 30ºN to 35ºN).

The two methods (K05 and GCT) of removing the anthropogenic AOD from the total and two methods ("2box" and "basic") for estimating supplemental properties provide four unique clear sky scenarios. They are used with the base scenario for total

AOD to assess the anthropogenic aerosol ADRF (and remaining natural aerosol NDRF) and compare it to the total aerosol TDRF computed with the "clean" (i.e. no aerosols) clear sky scenario.

5.3 Total Aerosol TDRFs

To begin, an assessment of the trends in total aerosol TDRFs are shown in Figure 5.3. These trends are computed with simulations "Total" (for aerosol laden) and "Clean" (for clear-sky) from Table 5.1. Note that these results are taken as an "extreme" case, as the atmosphere is never without aerosol. As such the results may act as an upper bound to the aerosol DRE, and here are taken to represent the total aerosol TDRF. Several features are now discussed.

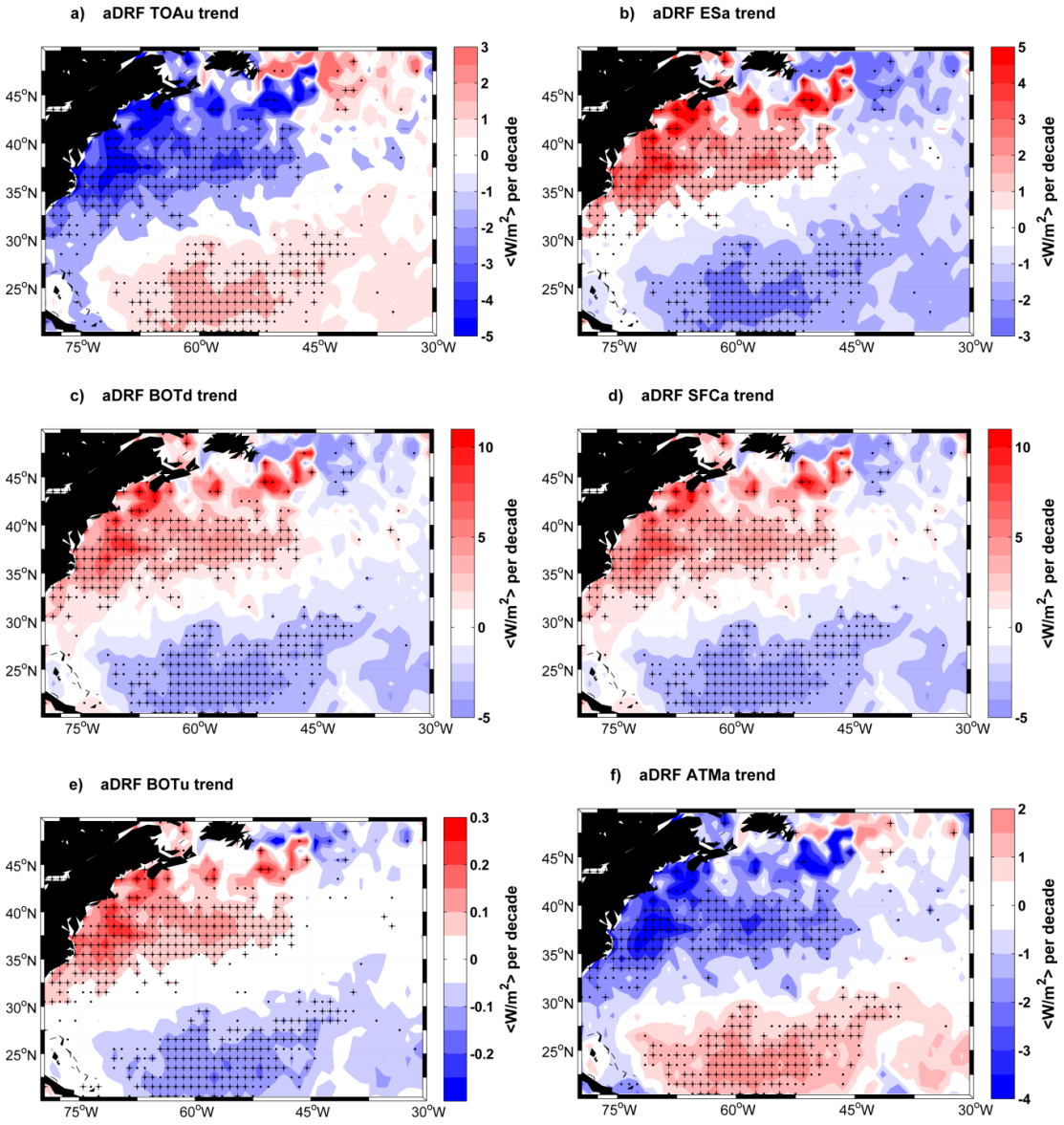

Figure 5.3: Trends in the total aerosol TDRFs during July 2002 to December 2012 for a) TOA_u, b) ES_a, c) BOT_d, d) SFC_a, e) BOT_u, and f) ATM_a. All trends are in W/m^2 per decade; note the different and uneven scales.

First, in areas where decreases in (anthropogenic) AOD are seen (i.e. western mid-latitudes) there is a decrease in TOA_u flux (Fig. 5.3a). This results from a decrease in scattering events as the aerosol load lightens. As the extraterrestrial solar flux is unchanged between simulations (i.e. TOA_d is the same in both), a decrease in outgoing radiation implies an increase in radiation trapped within the Earth system. Indeed, this is

seen in Fig. 5.3b which shows increasing ES_a, interpreted as an increase in energy being deposited into the Earth system. Conversely, an analogous yet inverted situation occurs in the sub-tropics, where increases in (natural) AOD are seen: an increasing aerosol load (which increases the scattering events) produces an increase in TOA_u flux also seen as a decrease in the ES_a (or less energy deposited into the Earth system).

Consider next the trends in total aerosol TDRF calculated at the surface for BOT_d (Fig. 5.3c) and BOT_u (Fig. 5.3e). As the overlying aerosol load is lessened in the mid-latitudes, less scattering events occur, allowing more radiation to penetrate to the surface. This is seen in both an increase in BOT_d flux and an increase in BOT_u flux (reflected from the underlying ocean surface). As with TOA_u, a similar yet mirrored scenario occurs in the sub-tropics. As a result of the increasing the aerosol load in the sub-tropical atmosphere (and thus scattering events), less radiation is permitted to transmit through to the surface, and decreases in the BOT_d (and BOT_u) total aerosol TDRF are seen.

Finally, the energy balances of the surface (SFC_a; Fig. 5.3d) and atmosphere (ATM_a; Fig. 5.3f) are examined. In the mid-latitudes and under a lightening aerosol load, an increased BOT_d total aerosol TDRF is seen (Fig. 5.3c). More flux penetrating to the surface not only offers more flux to be reflected (Fig. 5.3e), but importantly offers more flux to be absorbed by the surface. Indeed, this scenario is seen at the surface (Fig. 5.3d) where an increase in the SFC_a total aerosol TDRF represents an increase in the energy absorbed by the ocean surface. As can be computed from the simple example in Section 5.1, the BOT_u total aerosol TDRF is only on the order of 2.5% the total aerosol TDRF

from BOT_d and will contribute minimally to the ATM_a. Thus, the total aerosol TDRF for the ATM_a is mainly a balance between those at TOA_u and BOT_d. A combination of increased transmittance through to the surface and reduction of attenuation processes (both scattering and (slight) absorption) results in the decreasing total aerosol TDRF for the ATM_a. This is interpreted as a reduction in the energy deposited within the atmosphere itself for the region of lessening aerosol load (i.e. the mid-latitudes). As with all other total aerosol TDRF quantities, that for the SFC_a within the sub-tropic shows an inverted picture with decreasing flux put into the surface. The total aerosol TDRF for the ATM_a in the sub-tropics shows an increase in energy deposited within the atmosphere. These reflect the increase in aerosol load seen over the sub-tropical region.

The discussion thus far has focused on the sign of total aerosol TDRF trends: either increasing or decreasing. Briefly noted is the difference in magnitude of the total aerosol TDRF trends. Those occurring in the mid-latitudes are consistently larger in magnitude than those occurring over the sub-tropics. This is a result of the stronger decreasing trend in the total AOD seen over the mid-latitude region compared to the weaker increase in total AOD observed over the sub-tropics (see Chapters 3 and 4).

5.4 Anthropogenic Aerosol ADRFs

5.4.1 Using K05 and GCT for τ_{NAT}

The total aerosol TDRFs reported in the previous section were performed for a sky with monthly mean observed AOD from MODIS ("Total" simulation) and for a sky in which there was no aerosol load ("Clean" simulation). It is acknowledged that this "Clean" simulation is not realistic, as there is always some background aerosol in the atmosphere. To address this, two additional simulations were performed with two different ways to provide a background (or "natural") aerosol load such that the subsequent aerosol DRFs are more representative of the forcing from anthropogenic aerosol ADRF (and therefore the decrease seen in the mid-latitudes). The anthropogenic aerosol ADRFs are computed between "Total" and "K05-basic" or between "Total" and "GCT-basic" simulations. The changes here are only made to the AOD at 550 nm; the SSA(λ), g(λ), and AE(λ) are maintained as they were in the "Total" simulation (see Table 5.1). However, AOD(λ) will be affected when the original AE(λ) is applied to the new AOD at 550 nm, which has been adjusted to an estimate of the background natural aerosol load (see Section 5.2). Attention will be paid to the anthropogenic aerosol ADRFs for ES_a, SFC_a, and ATM_a due to the comparable behavior of TOA_u and BOT_d to ES_a and SFC_a (respectively) and minimal contribution from BOT_u.

Figure 5.4 displays the anthropogenic aerosol ADRFs for ES_a (a,c), ATM_a (e,g), and SFC_a (i,k) determined by using the "Total" case for aerosol sky and "K05-basic" or "GCT-basic" case for clear sky. First consider the cases using "K05-basic" as clear sky (first column): ES_a (positive), ATM_a (negative), and SFC_a (positive) all have trends in line with those over the mid-latitudes which are reported when simply using "Clean" as the clear sky case (Fig. 5.3). One feature that is strikingly absent in the three "K05-basic" ADRFs is any trend in the sub-tropics that is seen in TDRFs using "Clean" as the clear sky (Fig. 5.3). This is notable because "Total" - "Clean" was assessing the total aerosol TDRF. In developing the inputs for the "K05-basic" case, the anthropogenic aerosol was removed, thus when using the "K05-basic" case as the clear sky, anthropogenic aerosol load is absent from the clear sky simulation but natural aerosol remains. As was shown, the trend in the mid-latitudes arises from decreases in the anthropogenic load (Chapter 3), while the trend in the sub-tropics is the result of natural aerosol increases (Chapter 4). It therefore comes as no surprise when using a clear sky case which still retains the natural aerosol load that trends in the aerosol DRE are absent from the sub-tropics. Indeed, the aerosol DREs are actually reflective of the anthropogenic aerosol ADRF. Another clear sky case retaining natural aerosol was also evaluated: "GCT-basic". While the anthropogenic aerosol ADRFs for "Total" - "GCT-basic" (third column) still mirror the behavior in the mid-latitudes of the simulations using either "Clean" or "K05-basic" as the clear sky, the "GCT-basic" simulation permits some of the increase in aerosol in the sub-tropics (which is natural) to remain in the anthropogenic aerosol ADRFs.

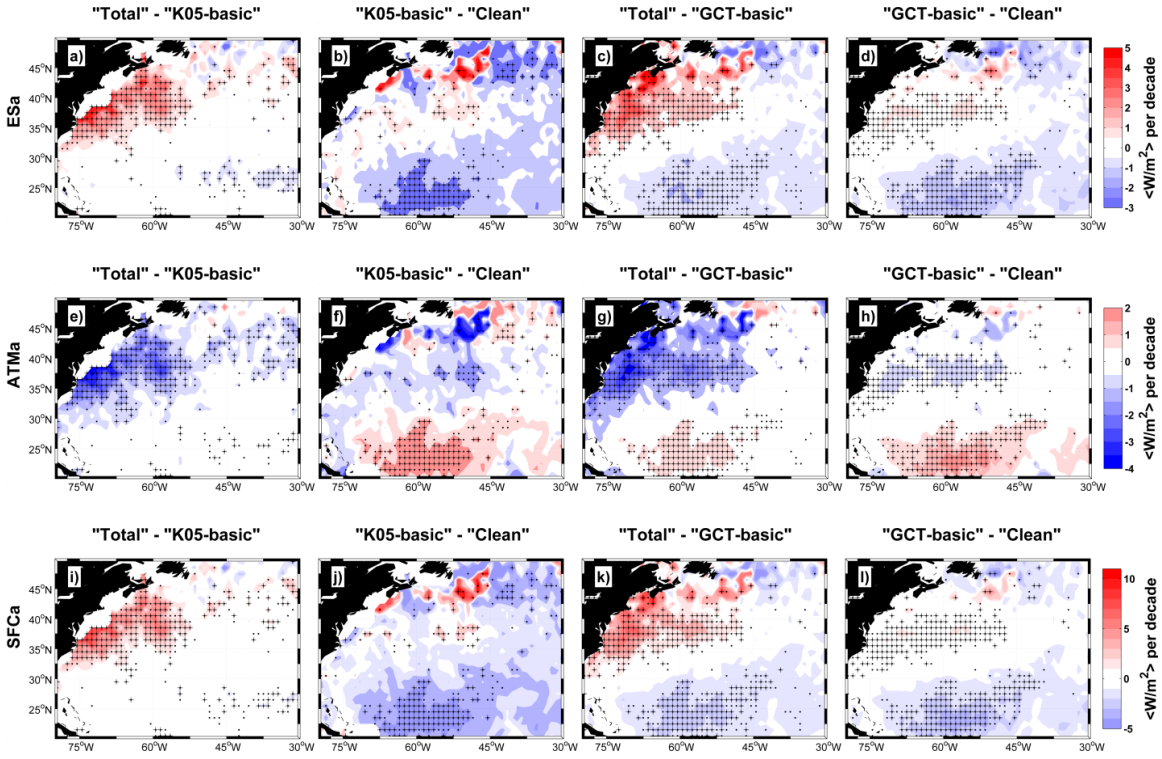

Figure 5.4: Trends in the anthropogenic aerosol ADRFs during July 2002 to December 2012 for a-d) ES_a, e-h) ATM_a, and i-l) SFC_a for simulations using "K05-basic" (first column) or "GCT-basic" (third column) for the clear sky. Also shown are trends in the natural aerosol NDRFs using "Clean" for the clear sky and "K05-basic" (second column) or "GCT-basic" (third column) for the aerosol sky. All trends are in W/m^2 per decade; note the different and uneven scales. Scales are the same as those used in Fig. 5.3 for total aerosol TDRFs. See Table 5.1 for description of aerosol/clear-sky cases.

In addition to assessing the anthropogenic aerosol ADRFs, the natural aerosol NDRFs can be computed by using either "K05-basic" or "GCT-basic" cases for the aerosol sky and "Clean" case for the clear sky; the aerosol loading has had the anthropogenic component removed and what remains is the natural loading. The natural aerosol NDRFs are also shown in Figure 5.4: second column for "K05-basic" and fourth column for "GCT-basic". Notable is the absence of any aerosol DRF trend in the mid-latitudes for the "K05-basic" cases. This is consistent with the lack of aerosol DRF trend in the sub-tropics for the "Total" - "K05-basic" case, and as with the prior assessment comes from the anthropogenic/natural apportionment. The "K05-basic" case is in slight

contrast to the “GCT-basic” case which appear to permit some of the anthropogenic aerosol (and decreasing trend information from its signal) to remain in what should be the natural aerosol loading.

A comparison of the fraction natural aerosol that makes up the total aerosol loading and the mean fractional behavior in two sub-regions offers further insights. Shown in Figure 5.5, the GCT method consistently under represents (relative to K05) the fractional makeup of the natural aerosol to the total aerosol loading. The mean makeup of the aerosol load over much of the North Atlantic appears to heavily favor anthropogenic species (SU, BC, and OC); the fractional makeup that consists of natural aerosol is mainly confined to the sub-tropical latitudes. Even still, the natural contribution used in the GCT runs is much less than that from the K05 method. An additional observation is that the K05 method confines the anthropogenic contribution much closer to the North American coast line during fall and winter months and produces an easily identifiable intrusion of anthropogenic load into the mid-latitudes beginning around April lasting through September.

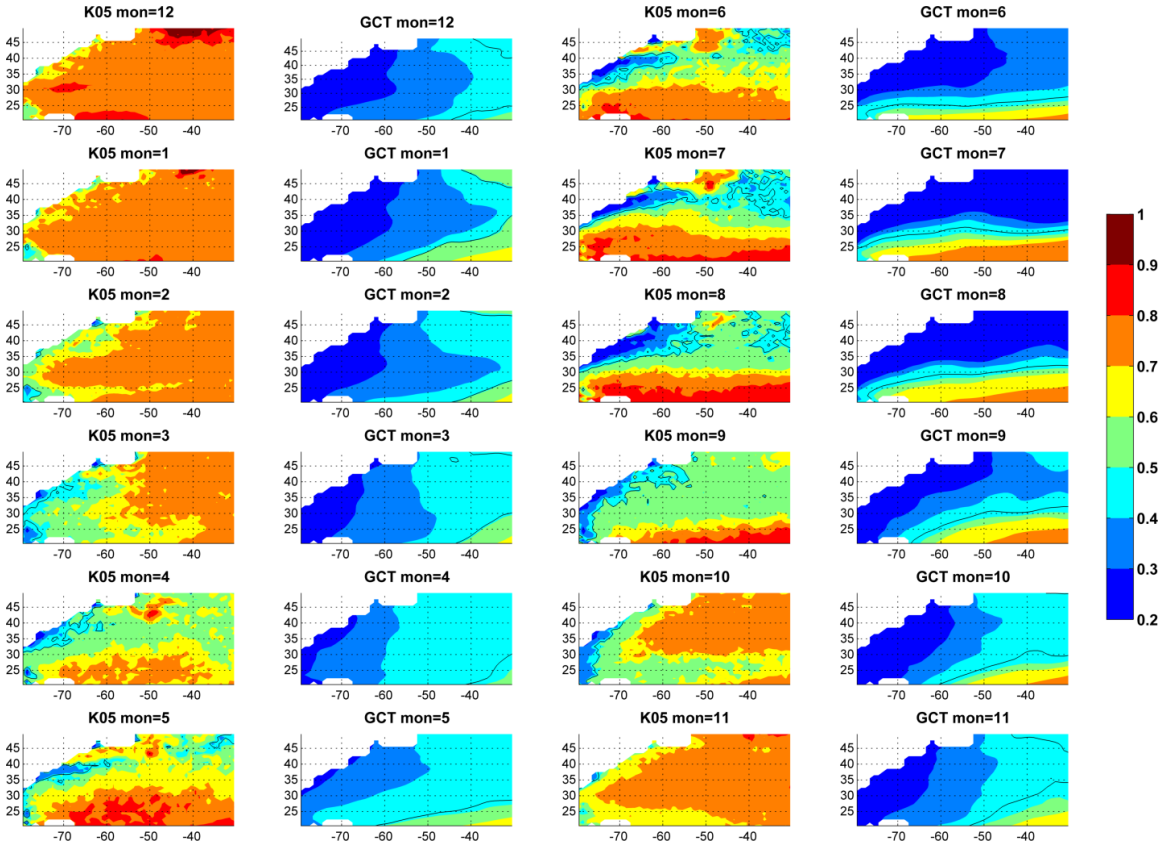

Figure 5.5: Monthly mean fractional make up of natural aerosol to the total aerosol load for the K05 (columns 1 and 3) and GCT (columns 2 and 4) methods. Fractional value x100 provides percent makeup. The 0.5 (50%) contour is drawn in black. Note monthly means for K05 cover July 2002 to December 2012 while those for GCT only cover January 2001 to December 2009.

One final additional analysis is the mean fractional behavior in two sub-regions: defined as "mid-latitude" (70º-60ºW, 32º-42ºN) and "sub-tropical" (65º-55ºW, 20º-28ºN). These time series are constructed by taking the domain-wide mean fractional contribution for each month. The first behavior to note is that the GCT fractional contribution exhibits no trend. This is because the GCT fractional contribution is constructed from the annual monthly mean climatology, thus trends in the underlying total AOD would be passed on as trends in the natural (and anthropogenic) components. This behavior is not seen in the K05 fractional contribution. This is because the K05 fractional contribution is more dynamically generated (see Section 2.3.2): it depends on the monthly mean observation

of total AOD and the fine-mode fraction makeup. As anthropogenic aerosol loads are more fine-mode dominated while natural loads more coarse-mode, the signal in the K05 method reflects both the change in the AOD as well as fractional contribution throughout the period considered. This is apparent in the mid-latitude grid (Fig. 5.6, left) as the fractional contribution of the natural AOD is seen to slowly rise and is reflective of the decreasing anthropogenic AOD load. Conversely, the sub-tropical region is not expected to have substantial anthropogenic contribution. As such, a trend in the total AOD will reflect in the natural AOD, and the fractional contribution from the natural aerosol load should remain more or less consistent with its annual climatology (Fig. 5.6, right). This is seen in the sub-tropical grid for K05 as an absence of any trend in the fractional contribution.

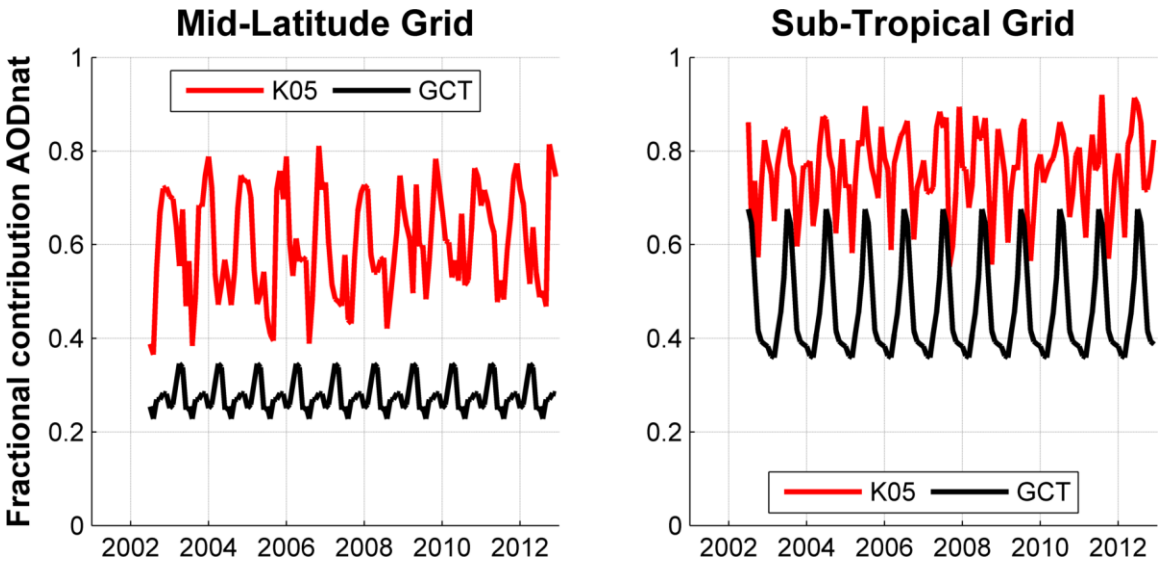

Figure 5.6: Monthly mean fractional make up of natural aerosol to the total aerosol load for the K05 (red) and GCT (black) methods for a mid-latitude (left) and sub-tropical (right) region during July 2002 to December 2012. Fractional value x100 provides percent makeup. See text for domain limits on mid-latitude and sub-tropical regions.

5.4.2 Estimating "natural" SSA(λ), g(λ), and AE(λ)

Having determined an appropriate method ("K05") to separate the natural and anthropogenic components from the total AOD, an additional step has been taken to approximate the supplemental aerosol properties (i.e. SSA(λ), g(λ), and AE(λ)) for the natural aerosol loading. SBDART simulations for the "Total" and all cases using the "basic" method have relied on the same parameterization to determine these properties, namely using climatological SSA(λ) from GOCART together with AE(λ) derived from AOD(λ) in MODIS C6 and g(λ) from MODIS Collection 5.1 (g was discontinued as a C6 product). Additional simulations were performed using the "2box" method described in Section 5.2.2. The trends in the natural aerosol NDREs and anthropogenic aerosol ADRFs using the "K05-2box" method are displayed in Figure 5.7 and are compared (via differencing) to the results obtained for simulations using the "K05-basic" method to evaluate the impact of the "2box" estimation method.

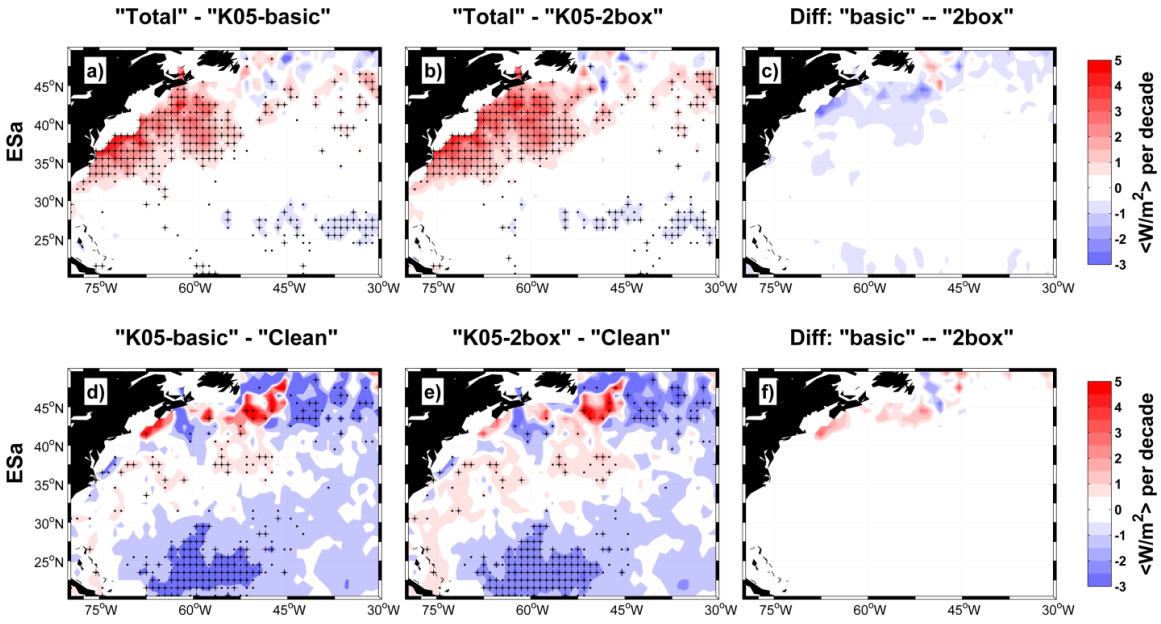

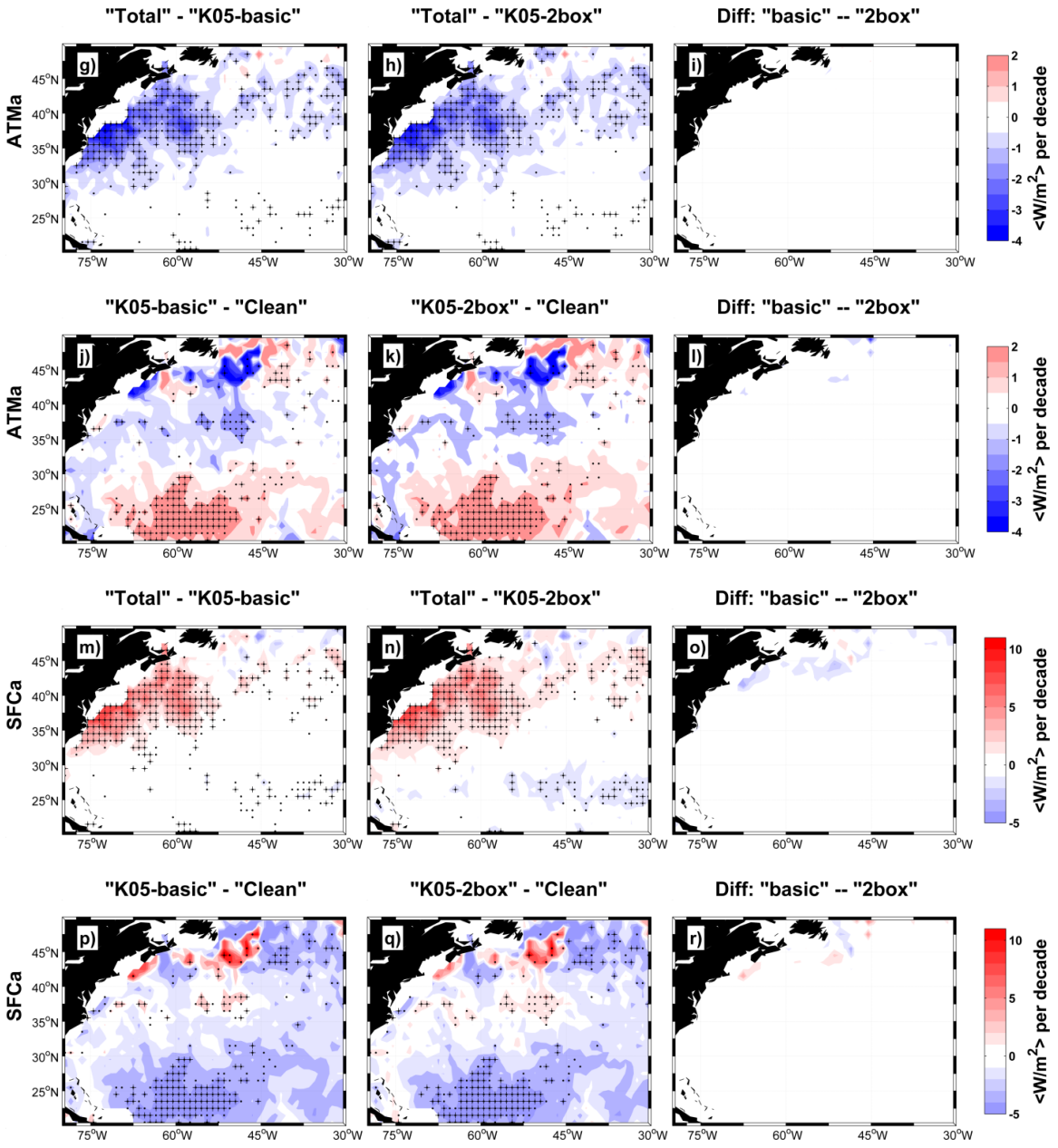

Figure 5.7: Trends in the anthropogenic aerosol ADRFs (a,b,g,h,m,n) and natural aerosol NDRFs (d,e,j,k,p,q) during July 2002 to December 2012 for (a,b,d,e) ES_a, (g,h,j,k) ATM_a, and (m,n,p,q) SFC_a for simulations using "K05-basic" (left) or "K05-2box" (center) methods for separating natural and anthropogenic aerosol load and properties. Also shown are the differences (right column) for a given aerosol DRF. All trends are in W/m^2 per decade; note the different and uneven scales. Scales are the same as those used in Fig. 5.3 and 5.4. See Table 5.1 for description of aerosol/clear-sky cases.

There is remarkable similarity in the trend behavior of the aerosol DRFs (both ADRF and NDRF) when using the "basic" or "2box" method for the aerosol supplementary properties. For instance, both methods produce the increase in

anthropogenic aerosol ADRF ES_a (Fig. 5.7a,b) seen over the mid-latitudes (also seen in the total aerosol TDRF (Fig. 5.3b)), reflecting the decrease in anthropogenic aerosol loading and decrease in scatter. Likewise, the decrease in anthropogenic aerosol loading is also seen for both "basic" and "2box" cases in the anthropogenic aerosol ADRF ATM_a (Fig. 5.7g,h) as a decrease in energy deposited into the atmosphere, presumably from a decrease in (slight) absorption by the decreasing aerosol loading and also increased transmittance allowed through to the surface. Finally, the increased transmittance to the surface manifests as a positive trend in the anthropogenic aerosol ADRF SFC_a (Fig. 5.7m,n). In addition to isolating the behavior in the mid-latitudes associated with the decrease in anthropogenic aerosol load (i.e. the anthropogenic aerosol ADRFs, Fig. 5.7a,b,g,h,m,n), the behavior in the sub-tropics associated with increases in natural aerosol load is also identified (i.e. the natural aerosol NDRFs, Fig. 5.7d,e,j,k,p,q). The increase in natural aerosol not only permits an increase in atmospheric absorbance (ATM_a; Fig. 5.7j,k) but also an increase in scatter which causes reductions in both Earth system and surface absorbance (ES_a and SFC_a; Fig. 5.7d,e and Fig. 5.7p,q, respectively). This is due to increasing scatter back to space (for ES_a) and associated increase in attenuation by the aerosol, thus transmitting less radiation to the surface (for SFC_a).

The similarity in trend behavior of the aerosol DRFs using either "basic" of "2box" method reveals that it is primarily the aerosol loading (and changes to it) that produce the trends in the resulting aerosol DRFs. Yet, in spite of the apparent similarities, there are still small differences that are informative of the impact the "basic" or "2box" method of determining the supplemental aerosol properties. These are shown

as differences in the calculated trend for a given aerosol DRF in the right column of Fig. 5.7 (Fig. 5.7c,f,i,l,o,r) and are most notable for ES_a and SFC_a with little impact on ATM_a. For example, consider the anthropogenic aerosol ADRFs (Fig. 5.7a,b,c) and natural aerosol NDRFs (Fig. 5.7d,e,f) for the ES_a using the two methods. It appears that within the mid-latitudes the "2box" method produces a slightly stronger trend in anthropogenic aerosol ADRF (Fig. 5.7c) while resulting in a slightly weaker (though not as extensive) trend in the natural aerosol NDRF. Note the behavior in the sub-tropics for natural aerosol NDRF is very similar, as demonstrated by the absence of trend difference (Fig. 5.7f). This is not surprising given the large makeup of natural aerosol to the total aerosol loading in this region, thus little is expected to be gained in using "2box" over the "basic" method. This behavior is mirrored in the SFC_a DRFs (Fig. 5.7m-r): over the mid-latitudes the "2box" case produces a slightly higher trend in the anthropogenic aerosol ADRF (Fig. 5.7m,n,o) while showing a slightly lower trend in the natural aerosol NDRF (Fig. 5.7p,q,r). Again, as with ES_a, there is little change in the trend behavior along the sub-tropical region.

These slight differences can be viewed as the changes to the underlying aerosol properties when transitioning from the "basic" (i.e. just modifying the AOD to reflect natural/anthropogenic) to the "2box" (i.e. modifying both AOD and supplementary aerosol properties to better reflect natural) method. Taking the difference between ES_a for anthropogenic aerosol ADRF using "basic" versus "2box" (Fig. 5.7c) as an example, a slight decrease in the calculated trend arises from the changes in the supplementary aerosol properties. Figure 5.8 shows the overall mean values (top) using the "basic"

method for SSA, g, and AE at 550 nm along with the mean difference (bottom) between the "basic" and "2box" method. When transitioning to the "2box" method, there is (on average) a slight decrease in SSA and AE while also a slight increase in g for the supplemental aerosol properties of the natural load. This translates into shifting the supplementary properties to be more representative of slightly larger particles (i.e. mainly sea salt versus mixed anthropogenic and sea salt load) which in theory have slightly lower SSA and spectral sensitivity in AOD (as evidenced by lower AE) and slightly higher g (increased forward scatter).

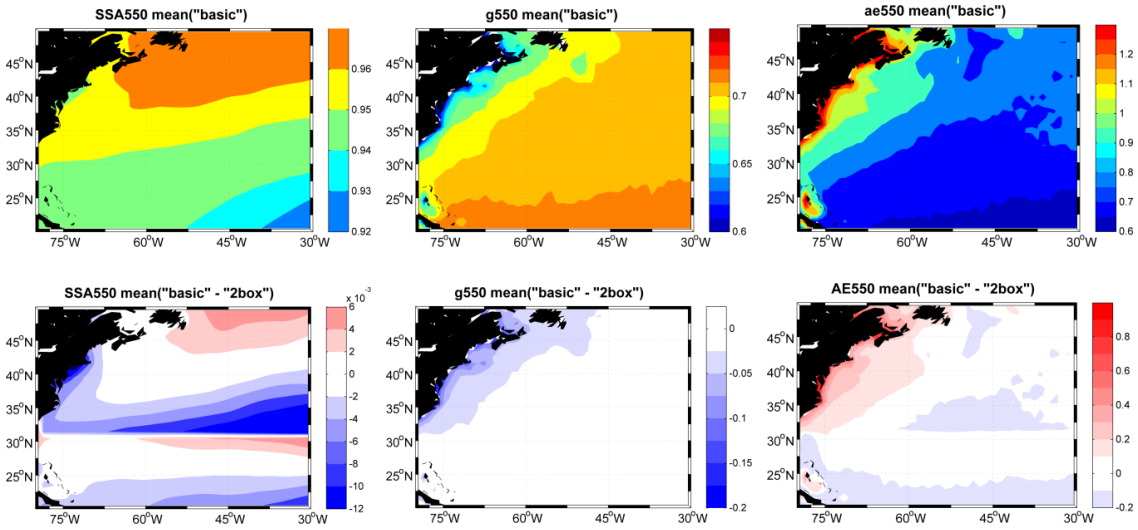

Figure 5.8: (top) 2002 to 2012 "basic" mean and (bottom) mean difference ("basic" minus "2box") in supplementary aerosol properties of (left) SSA, (center) g, and (right) AE at 550nm.

5.4.3 Adjusted for Daytime

The results to this point have consisted of linear trends of aerosol DRFs using monthly mean data. By using the Aqua overpass time of 1330 local solar time (LST), all

SBDART simulations and DRF calculations have been for an instantaneous snapshot around the 1330 LST time. The final step in this work is to extend the flux calculations (and aerosol DRF and trend determinations) from instantaneous (around 1330 LST) to encompass the full daytime solar illumination to better approximate the "true" daytime monthly mean. A method by Remer and Kaufman (2006) is adopted to convert an instantaneous flux measurement (around 1330 LST) to approximate the integrated daily flux.

The basis for the conversion process (termed "flux conversion" for short) relies on the ratio that approximates the instantaneous flux to the daytime average. Here, daytime consists of the hours between 0830 and 1830 LST (8:30a to 6:30p). To save computational time, ratios have been computed for one year (2003, 12 months) using the same monthly mean aerosol and atmosphere profiles (for both instantaneous and "flux conversion") and for five different hours during the day: 0930, 1130, 1330, 1530, and 1730 LST. Integration by summation is performed over these daytime hours as follows:

$$F_d^{TOAu} = \frac{1}{10} * \sum_{hr=1}^{5} F_i^{TOAu}(hr) \qquad \text{(Eq. 5.4)}$$

where F is the flux (here for TOA_u), subscripts d and i represent daily summation and instantaneous fluxes (respectively), and hr represents the hourly index of the five hours in chronological order. The factor 1/10 accounts for the summation of fluxes over 10 hours (two hours each). The flux conversion ratio (for a given month and location) is then calculated based on the five hourly instantaneous flux calculations per month in 2003:

$$ratio(x, y, m) = {F_d^{TOAu}}\Big/{F_i^{TOAu}(hr = 3)} \qquad \text{(Eq. 5.5)}$$

to provide the ratio of the daily mean flux estimate (F_d) to the instantaneous flux (F_i) calculated at the Aqua overpass time (1330 LST; hr = 3) for a given month m. The calculated ratio(x,y,m) produces a year-round monthly estimate for each longitude (x) and latitude (y) and can be applied to all F_i that have been previously been calculated. Similar ratios are also calculated for TOA_d, BOT_d, and BOT_u fluxes and applied for flux conversion from instantaneous to daily means of the monthly mean.

Table 5.2 provides a comparison for SBDART simulated daytime monthly mean TOA_u and TOA_d fluxes with monthly mean observed fluxes from the CERES SSF1deg product (Ed. 4) (see Section 2.1.4) for both the computed year ("2003") and applying the ratios determined from 2003 to the whole SBDART dataset ("FULL"). TOA_d fluxes compare very favorably, showing a correlation above 0.99 and a relative difference of −2.57 % in 2003 (−2.58 % for the FULL dataset). The small disagreement in TOA_d fluxes is thought to stem from slightly different solar spectra used in the CERES retrieval and SBDART simulation as well as small differences in the assumed earth-sun orbital geometry for SBDART. The TOA_u fluxes also compare favorably, almost as strongly as the TOA_d fluxes: TOA_u share a correlation of 0.7768 (0.7842) and have a relative difference of 8.08 % (7.87 %) in the 2003 (FULL) dataset. Several factors may play a part in the differences seen in TOA_u between CERES and SBDART, including solar spectra, earth-sun geometry, CERES SSF vs. MODIS pixel size/aggregation and cloud

screening (e.g. Loeb and Manalo-Smith, 2005), and the monthly evolution of the scene seen by CERES yet absent in SBDART simulations (e.g. aerosol properties, surface albedo). One factor that will affect both TOA_d and TOA_u in SBDART is the use of a 10 hour day throughout the year, while daytime during the northern summer is longer. In spite of these intrinsic differences, CERES and SBDART TOA_u fluxes compare well and provide confidence in the "flux conversion" method (Eq. 5.4 and 5.5).

Year	Flux	SBDART (W/m^2)	CERES (W/m^2)	Corr.Coef	CER-SBD (W/m^2)	Diff. relative to CERES (%)
2003	TOA_d	357.5427	344.4505	0.9955	−8.8602	−2.57 %
	TOA_u	34.2644	40.0075	0.7768	3.2342	8.08 %
FULL	TOA_d	356.9272	343.5190	0.9956	−8.8758	−2.58 %
	TOA_u	34.1046	39.6578	0.7842	3.1219	7.87 %

Table 5.2: A comparison between SBDART (SBD) and CERES (CER) TOA daytime monthly mean fluxes for the "2003" year and "FULL" dataset (July 2002 to December 2012). Provided are the means of SBDART and CERES fluxes, their correlation coefficient (Corr.Coef), the mean difference between the two datasets (CER-SBD), and that mean relative to the mean CERES fluxes ([CER-SBD]/CER).

The "flux conversion" method (Eq. 5.4 and 5.5) is now applied to convert TOA and BOT fluxes from instantaneous (around 1330 LST) monthly means to daytime monthly means. From the daytime monthly mean fluxes the daytime monthly mean total aerosol TDRFs are now calculated and trend analysis performed. Figure 5.9 shows the trend analysis for the daytime total aerosol TDRFs for ES_a, ATM_a, and SFC_a. These figures are analogous to the instantaneous total aerosol TDRFs in Fig.5.3 (b,d,f) from Section 5.3. Remarkable similarity is seen between instantaneous (Fig. 5.3) and daytime (Fig. 5.9) total aerosol TDRF with respect to trend sign, location, and significance. The main notable difference is the daytime total aerosol TDRFs are smaller in magnitude compared to their instantaneous counterparts. This is due to the "flux conversion" which

estimates the daily integral of flux over five earth-sun geometries and not just the 1330 LST geometry the instantaneous computations use. The 1330 LST is near a solar zenith angle corresponding to approximately maximum insolation for that month and location.

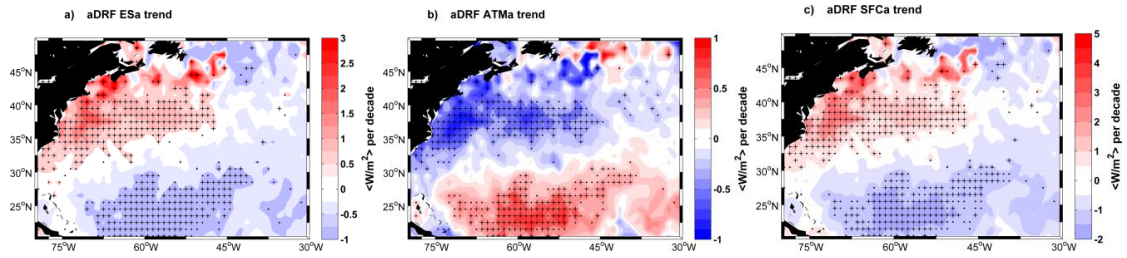

Figure 5.9: Trends in the daytime total aerosol TDRFs during July 2002 to December 2012 for a) ES_a, b) ATM_a, and c) SFC_a. All trends are in W/m^2 per decade; note the different and uneven scales.

As with the results in Section 5.3, the resulting trends seen in Fig. 5.9 are for the total aerosol TDRF using "Total" and "Clean" simulations from Table 5.1. The "flux conversion" ratios are now applied to the "K05-2box" simulation such that daytime anthropogenic aerosol ADRF ("Total" – "K05-2box" simulations) or natural aerosol NDRF ("K05-2box" – "Clean" simulations) can be determined. Figure 5.10 displays the trends in the anthropogenic aerosol ADRF (left) and natural aerosol NDRF (right) for ES_a, ATM_a, and SFC_a. As with the transition from instantaneous to daytime total aerosol TDRFs, those for anthropogenic aerosol ADRF or natural aerosol NDRF show similar trend sign, location, and significance. The separation of trends due to anthropogenic aerosol versus natural aerosol loadings is also maintained. The major difference is the lower magnitude of DRF trend in the daytime cases versus those for instantaneous (Fig. 5.3). This is due to the "flux conversion" which provides daytime fluxes less than those instantaneous around 1330 LST near local solar noon.

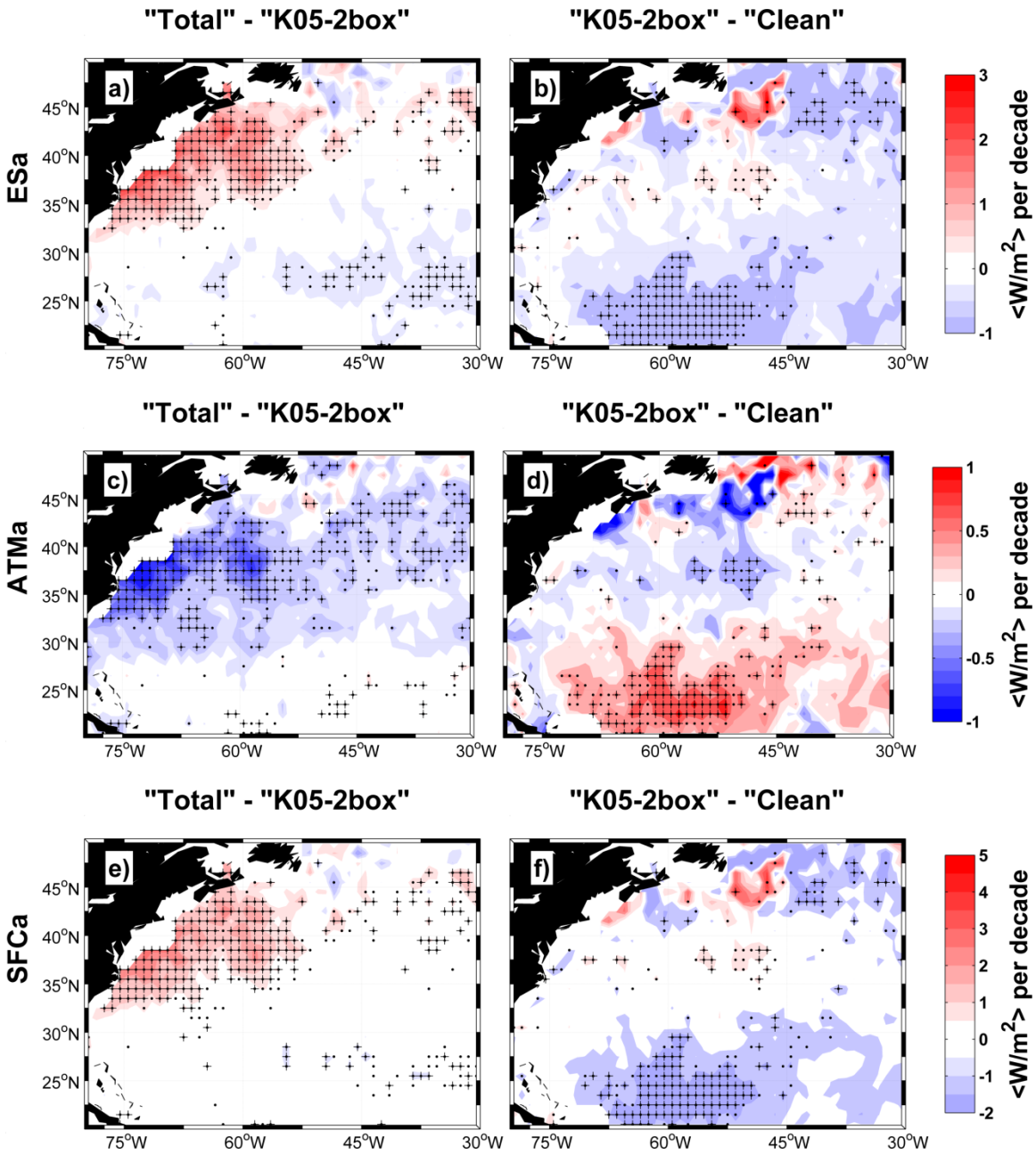

Figure 5.10: Trends in the daytime aerosol DRFs during July 2002 to December 2012 for a,b) ES_a, c,d) ATM_a, and e,f) SFC_a for simulations using the "K05-2box" method for separating natural and anthropogenic aerosol load and properties. (a,c,e) anthropogenic aerosol ADRF, (b,d,f) natural aerosol NDRF. All trends are in W/m^2 per decade; note the different and uneven scales. Scales are the same as those used in Fig. 5.9. See Table 5.1 for description of aerosol simulations.

5.5 Assessing Trend Uncertainty

An uncertainty analysis is performed to estimate some range of uncertainty on the DRF trends calculated in Section 5.4.3 (see Fig. 5.10). Several assumptions are made. First, two sites are chosen as representative of the trend behavior in their vicinity. One site (called "midL") is located in the mid-latitudes (37.5ºN, −68.5ºE) within the region of anthropogenic aerosol decreases. The other site (called "subT") is located in the sub-tropics (23.5ºN, −55.5ºE) and is representative of the natural aerosol increases. The second assumption is to perform the variability analysis during the month of July. This is chosen because the solar illumination is strongest and the resulting analysis, when applied throughout the year, is understood to represent an upper-bound to the uncertainty. A third assumption is that the uncertainty in the DRF and subsequent trend arises from imprecise knowledge of atmospheric profile and aerosol properties supplied to SBDART, an assumption elaborated below.

5.5.1 Assumed Atmosphere/Aerosol Properties

As discussed above (see Section 5.2), the main properties changing for each grid location are the monthly mean atmospheric profile (p, T, [H_2O], [O_3]; ATM(z) is taken as a whole) and spectral aerosol properties (AOD, SSA, g). To assess some variability inherent to these properties, the central grid point for both midL and subT locations and their 8 surrounding neighbors during 10 July months (2003-2012) are compiled, resulting

in 90 samples each for ATM(z), AOD, SSA, and g. One main set of SBDART simulations was performed for a static atmospheric profile and 25 random samples each for all three aerosol properties, resulting in 25^3 or 15625 combinations of AOD, SSA, and g. Additionally, one secondary set of SBDART simulations was performed for five randomly sampled ATM(z) under clean conditions (i.e. no aerosol load; ibaer = 0). Table 5.3 shows the resulting standard deviation (σ) in TOA_u, BOT_d, and BOT_u daily mean SW fluxes (following Eq. 5.4) at both midL and subT locations for total (anthropogenic+natural) and natural only ("K05-2box") aerosol scenarios. Table 5.4 shows the mean (μ) and standard deviation (σ) of the 25 AOD, SSA, and g samples used for combinations of total and natural aerosol loads over the midL and subT locations.

		TOA_u		**BOT_d**		**BOT_u**	
		midL	subT	midL	subT	midL	subT
AOD	tot	2.4988	0.3016	4.8687	4.4786	0.1479	0.1183
	nat	1.6160	0.6142	3.3864	3.9472	0.1139	0.1079
SSA	tot	0.5249	0.7475	1.6240	3.0309	0.0530	0.0859
	nat	0.1620	0.3936	0.5641	1.5363	0.0180	0.0445
g	tot	0.8227	0.1787	0.9160	0.2196	0.0214	0.0055
	nat	0.1354	0.1947	0.1511	0.2289	0.0037	0.0060
ATM(z)		0.0281	0.0218	1.6054	0.4825	0.0069	0.0024

Table 5.3: Standard deviations (σ) in SW fluxes (W/m^2) computed for the 15625 aerosol combinations and (separately) 5 atmospheric profiles. "tot" denotes total (natural+anthropogenic) aerosol load, "nat" denotes natural aerosol load using the "K05-2box" method.

		AOD		**SSA**		**g**	
		μ	σ	μ	σ	μ	σ
midL	tot	0.276	0.058	0.955	0.006	0.699	0.020
	nat	0.114	0.044	0.957	0.003	0.696	0.006
subT	tot	0.249	0.036	0.930	0.007	0.742	0.008
	nat	0.213	0.035	0.938	0.003	0.733	0.006

Table 5.4: Mean (μ) and standard deviation (σ) of aerosol properties (at 550 nm) for the total and natural simulations at the midL and subT locations (90 samples per value). All values are unitless. "tot" denotes

total (natural+anthropogenic) aerosol load, "nat" denotes natural aerosol load using the "K05-2box" method.

Several points are briefly noted. First, the σ for fluxes decreases from BOT_d to TOA_u to BOT_u. This is due to differences in the mean magnitude of the fluxes: approximately 340 W/m^2 for BOT_d, 37 W/m^2 for TOA_u, and 8 W/m^2 for BOT_u. Secondly, variations in AOD lead to the largest σ in fluxes, which would suggest that the total amount of aerosol load (AOD) is most important in determining the subsequent fluxes, while the scattering nature (SSA) and direction (g) are less important over the ranges considered. Thirdly, variations in the atmospheric profile (i.e. Rayleigh scattering) appear to only play a minor role. Finally, when comparing the statistics for the aerosol properties used, SSA and g appear relatively similar at a particular site and it is the AOD that shows the largest difference between total and natural simulations.

5.5.2 Applying Flux Uncertainty and Determining a Range for Trends

The estimated flux uncertainties in Table 5.3 are now applied to the calculated midL and subT total, natural ("K05-box"), and clean time series (i.e. those used in Section 5.4). When a calculated flux value is imported, it is perturbed 5 times for each ATM(z), AOD, SSA, and g. This produces a dataset of 5^4 or 625 perturbed time series:

$$F_p^i = F_0^i + r_1 * \sigma_{AOD}^i + r_2 * \sigma_{SSA}^i + r_3 * \sigma_g^i + r_4 * \sigma_{ATM}^i \quad \text{(Eq. 5.6)}$$

where F_p^i and F_0^i are the perturbed and unperturbed (respectively) fluxes (e.g. TOA_u) for the i locations (midL or subT), r_x is a uniformly distributed random number, and σ_x^i are the σ of AOD, SSA, g, and ATM(z) for the i locations. Thus, random perturbations of the σ_x are used to perturb F_0. Having imported each month and performed the 625 perturbations, trend analysis can then be performed on the datasets for the two locations. As with prior analyses (e.g. Section 5.4), the trends in anthropogenic aerosol ADRF and natural aerosol NDRF for ESa, ATMa, and SFCa are computed and displayed in Figure 5.11 for the midL and subT sites.

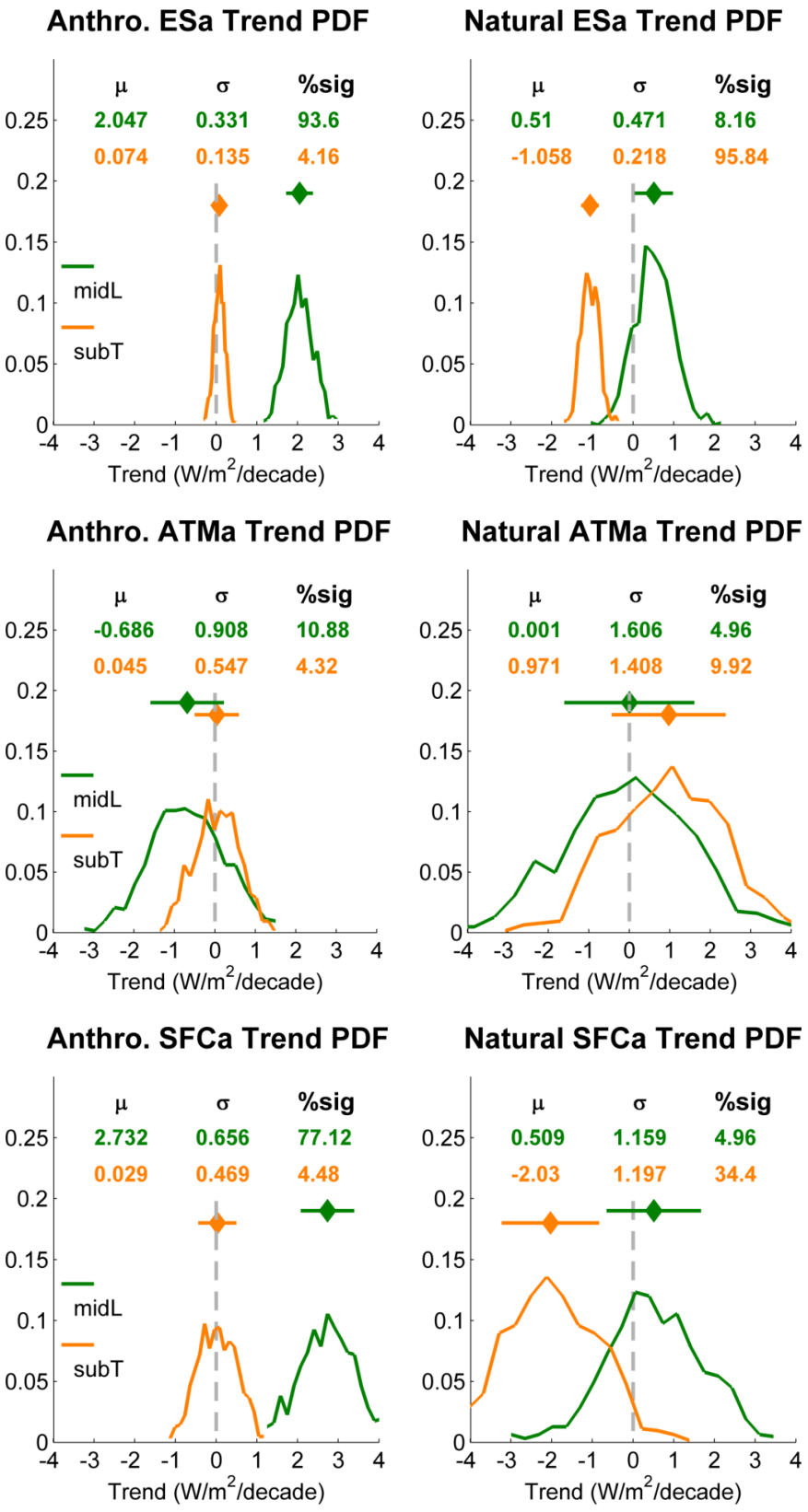

Figure 5.11: PDF of trends analysis for ES_a (top), ATM_a (middle), and SFC_a (bottom) daytime fluxes during July 2002 to December 2012 using the "K05-2box" method. (left) anthropogenic aerosol ADRF;

(right) natural aerosol NDRF. Green (orange) are results for the midL (subT) site. All trends are W/m^2/decade. 625 random combinations used for each PDF. Also reported is the PDF μ and σ, and displayed graphically with diamond and horizontal line. %sig is the percent of trends that are beyond the 95% significant threshold.

First, consider trends in ES_a (Fig. 5.11, top). It is determined that the midL site has a mean anthropogenic aerosol ADRF ES_a trend value 2.05 W/m^2/decade, that this trend has a standard deviation of 0.33 W/m^2/decade, and that 93% of the 625 random instances reflect statistical significance (> 95%). Analysis of the midL mean natural aerosol NDRF ES_a trend estimates the trend is 0.51 ± 0.47 W/m^2/decade; however, only 8% of the trends are statistically significant. Focusing on the subT location, there is no significant anthropogenic aerosol ADRF ES_a trend reported (trend = 0.07 ± 0.14 W/m^2/decade) while the natural aerosol NDRF ES_a trend is reported as −1.06 ± 0.22 W/m^2/decade, with more than 95% of instances statistically significant. These results are in agreement with the trend estimate reported in Fig. 5.10a,b.

Similar yet slightly larger in magnitude trends are seen for the SFC_a (Fig. 5.11, middle). The midL anthropogenic aerosol ADRF SFC_a trend is reported to be 2.73 ± 0.66 W/m^2/decade while the natural aerosol NDRF SFC_a trend is estimated as 0.029 ± 0.47 W/m^2/decade. The subT location reveals an anthropogenic aerosol ADRF SFC_a trend estimate as 0.51 ± 1.16 W/m^2/decade while the natural aerosol NDRF SFC_a trend is −2.03 ± 1.2 W/m^2/decade. Again, these results are in line with the estimates in Fig. 5.10e,f. The slightly larger magnitude of the SFC_a trends (relative to ES_a trends) is due to the decreasing (increasing) AOD trends in the midL (subT) allowing more (less) radiation to reach the surface. One notable difference is that the SFC_a trends appear less certain than the ES_a trends. The SFC_a has a larger trend σ as well as less percentage of instances

reporting statistically significant trend. Two mechanisms are acting to produce less certain SFC_a trends relative to ES_a: 1) the BOT_d fluxes intrinsically are more uncertain than TOP_u (see Table 5.3), and 2) when producing SFC_a two applications of the random perturbation scheme (Eq. 5.6) are applied (to BOT_d and BOT_u) whereas only one application is used for ES_a (for TOP_u).

Finally, the trend and uncertainty estimates for ATM_a (Fig. 5.11, bottom) reveal a highly uncertain estimate, casting doubt on the ATM_a trends reported in Fig. 5.10c,d. These trends (in Fig. 5.10c,d) are already very small in magnitude ($< |1|$ W/m^2/decade). The uncertainty analysis reveals these trends may have σ that is on the order of (if not larger than) the trend itself. Furthermore, less than 11% of the 625 iterations reveal statistically significant trends. These uncertainties encompass all uncertainties in the fluxes (Table 5.3) as well as three applications of the random perturbation scheme (Eq. 5.6). Furthermore, the ATM_a is highly dependent on the aerosol properties, which inherently have their own uncertainty due to using estimates and the "2box" scheme throughout this analysis.

5.6 Chapter 5 Summary

As a result of AOD trends documented in Chapters 3 and 4, the resulting impact(s) on the aerosol direct radiative effect are estimated. Numerous radiative transfer simulations using the SBDART code were performed under total, natural-only, and clean

sky (i.e. no aerosols) conditions to assess the total aerosol TDRF, anthropogenic aerosol ADRF, and natural aerosol NDRF. The dust estimation method of Kaufman et al. (2005a,b) is shown to better segregate natural from anthropogenic aerosol loads (and subsequent trends) than a method using GOCART aerosol species. The conversion of instantaneous flux (at 1330 LST) to daily fluxes (using 5 2-hr windows) performs well and produces TOA_u estimates within 8% relative difference to CERES observations. The anthropogenic AOD decrease in the mid-latitudes is expected to produce a 1.0 to 2.0 W/m^2/decade increase in ES_a, much of which is seen as SFC_a. Conversely, the natural AOD increase in the sub-tropics is expected to produce a −0.5 to −1.0 W/m2/decade decrease in ES_a, much of which comes from decreased SFC_a. A perturbation analysis is performed by altering the aerosol inputs and adding an appropriate normally distributed perturbation to the monthly mean fluxes. Uncertainty in AOD is shown to cause the largest uncertainty in flux and subsequent trend determination. The anthropogenic AOD decrease at the mid-latitude site leads to a 2.0±0.33 W/m^2/decade ADRF trend in ES_a while the natural AOD increase at the sub-tropical site leads to a −1.06±0.22 W/m^2/decade NDRF trend in ES_a.

Chapter 6: First Indirect (Twomey) Effect of Aerosol Load

The impact of aerosols on clouds (aerosol-cloud interaction, or ACI) over the western North Atlantic Ocean is now explored. Specific focus is paid to the first indirect effect, or Twomey effect, and the mid-latitude region where anthropogenic aerosol decreases are seen (Chapter 3). A variety of analyses are performed, starting with the monthly mean datasets (Section 6.1). After highlighting several combined shortcomings with this dataset, analyses are performed with a daily mean dataset (Section 6.2). This chapter uses the methodology outlined in Section 2.3.4. Only datasets for liquid clouds are considered in this analysis. ACI_r refers to the Twomey effect with respect to cloud effective radius (r_e) while ACI_d refers to that with respect to cloud optical depth/thickness (COD or COT) (i.e. Eq. 2.16 and 2.17, respectively). At this time, only aerosol impacts on cloud properties (r_e and COD) via the Twomey effect are explored. The impacts on radiation and radiative forcing are left for further work.

6.1 ACI Analysis with Monthly Mean Data

6.1.1 Domain-wide ACI Analysis

The large-scale behavior of ACI during July 2002 to December 2012 is explored in a domain-wide (80º-40ºW, 30º-50ºN) analysis of monthly mean MODIS-Aqua data using LWP-binned observations of AOD-r_e. Twelve LWP bins have been determined based the cumulative distribution function (CFD) of log(LWP) such that each bin has approximately equal number of observations. Next, for each LWP bin, mean(AOD)-mean(r_e) pairs are made in each AOD bin (sized 0.01) and number of AOD-r_e pairs (Nobs) going into that point are recorded. Finally, a weighted (by Nobs) linear fit in log-log space is calculated, with the slope of this fit reported as the ACI_r for that LWP bin. Figure 6.1 displays the domain-wide ACI_r results.

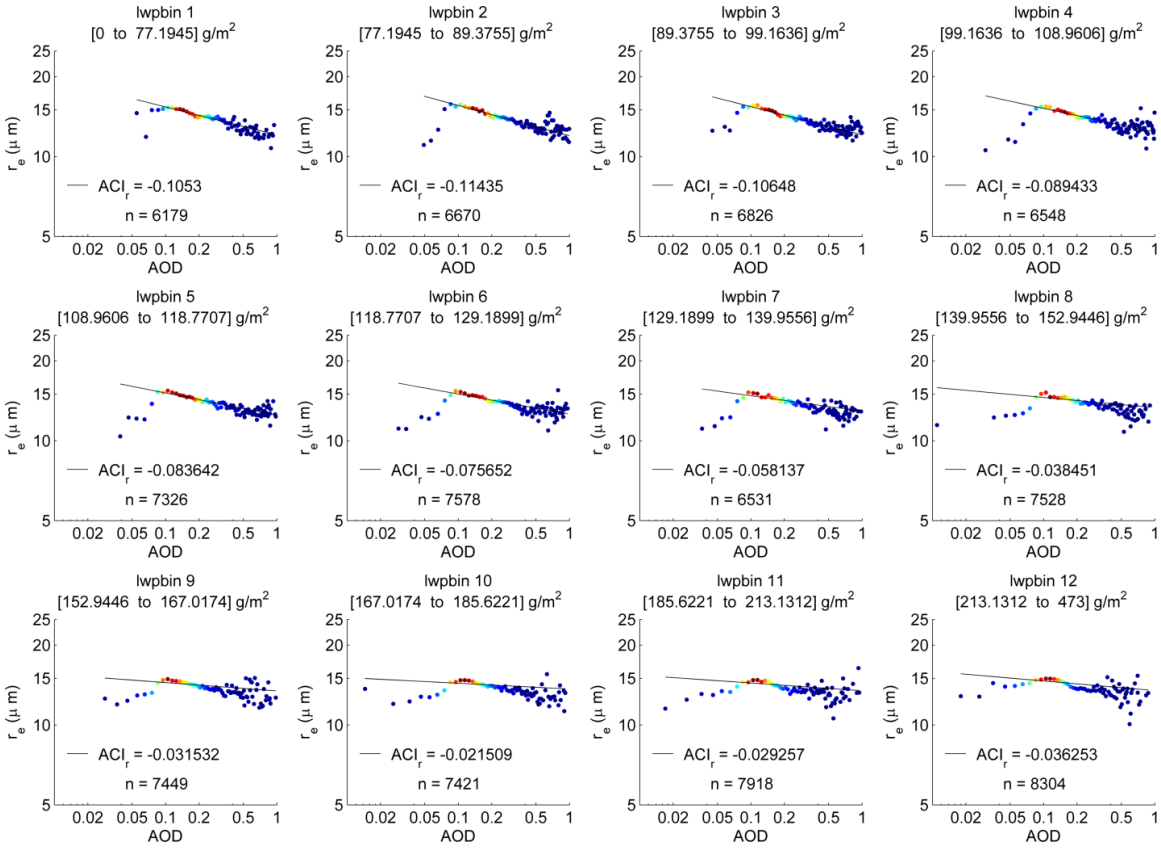

Figure 6.1: Domain-wide ACI_r computation. LWP bounds for each LWP bin listed in title. ACI_r and number of AOD-r_e pairs within each LWP bin (as n) listed in plot. Nobs making up each mean(AOD)-mean(r_e) pair represented by the color of the point (blue = few pairs, red = many pairs).

From the domain-wide ACI_r analysis, there is good and consistent agreement with Twomey theory across all LWP bins: r_e decreases as AOD increases, resulting in $ACI_r < 0$. Two interesting behaviors are seen in Fig. 6.1: 1) the apparent decrease in ACI_r magnitude as LWP increases, and 2) the increased mean(r_e) scatter at larger values of AOD. Discussion of these behaviors is deferred to Section 6.1.3.

As can be done for AOD-r_e to estimate ACI_r, the same methodology is now extended to AOD-COT to estimate ACI_d, or the cloud optical thickness response across a range of aerosol loadings. As was noted in Section 2.3.4, the derivation of ACI_r and

ACI_d (see Feingold et al., 2001) is identical except for a negative sign which provides expectation of $ACI_r < 0$ while $ACI_d > 0$. Figure 6.2 shows the same domain-wide analysis applied to AOD-COT data (using the same LWP binning scheme) to produce estimates of ACI_d.

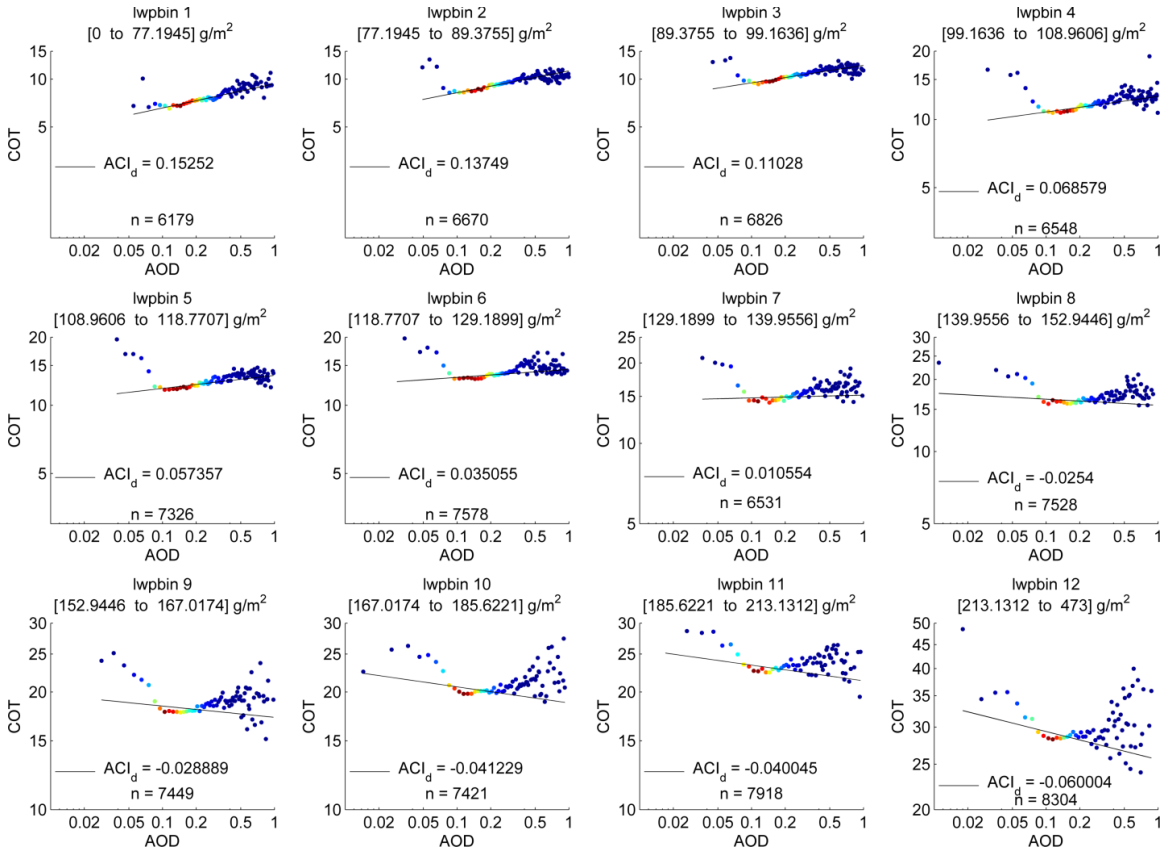

Figure 6.2: Same as Fig. 6.1 except for ACI_d. Note the y-axis scales are not constant across LWP bins.

As theory would dictate, the values of ACI_d are positive in LWP bins 1-7 (LWP < 140 g/m^2). Together with the ACI_r results from Fig. 6.2, these results show that (for clouds of similar LWP) MODIS monthly data confirm the presence of the Twomey effect over the large Western North Atlantic domain: increasing aerosol loads results in more numerous yet smaller cloud droplets, a consequence of which is increased light scattering

associated with optically thicker cloud. Analogues of the two behaviors noted for ACI_r are also present in the ACI_d analysis: 1) a decrease (and even reversal in sign) of ACI_d magnitude as LWP increases, and 2) the increased mean(COT) scatter at larger values of AOD, a behavior exaggerated at higher LWP.

6.1.2 Local 3º x 3º ACI Analysis

One shortcoming of the analysis from Section 6.2.1 is its broad domain-wide nature. As shown by Grandey and Stier (2010), large spatial domains chosen for ACI studies can introduce spurious spatial variations between aerosol and cloud, causing errors in calculated ACI. The spatial domain used in Section 6.2.1 covers 20º latitude by 40º longitude, while Grandey and Stier (2010) suggest using areas smaller than 4º latitude by 4º longitude. In this section, a local 3º x 3º analysis is constructed by appending data from the eight surrounding grid members to that of the data of the central grid member, making one vector. This method combines the localization limit suggested by Grandey and Stier (2010) with a sliding window which allows an individual grid point to participate in analyses with all surrounding grid neighbors. Once the data vectors are formed (1 variable x 126 months x 9 grids), the same ACI analysis is applied and informs the ACI_r (or ACI_d) for that particular grid point.

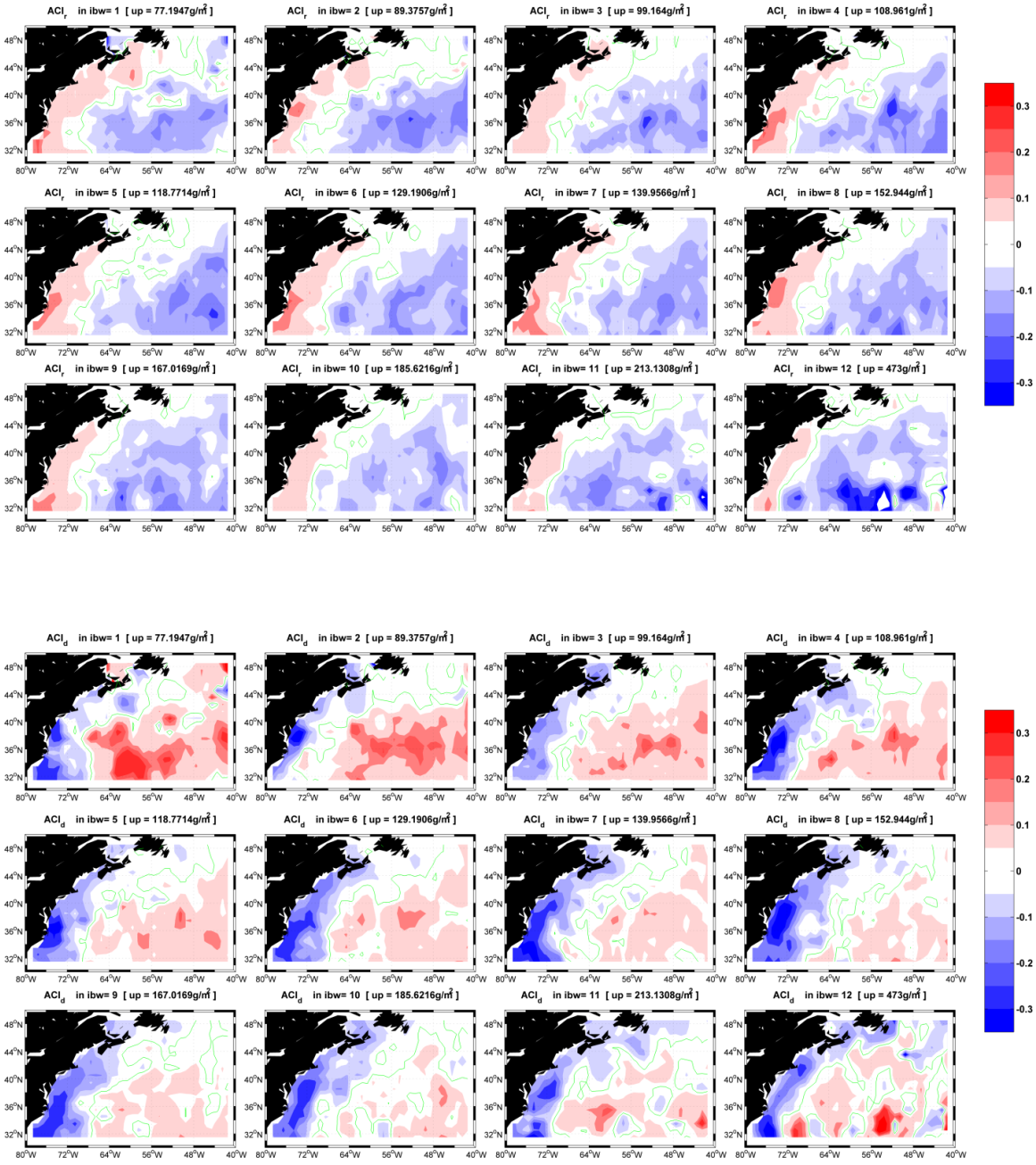

Figure 6.3: Results of local 3º x 3º ACI analysis for ACI_r (top) and ACI_d (bottom). Green contour denotes the ACI = 0 contour. LWP bin boundaries are same as used in domain-wide ACI analysis (i.e. Fig. 6.1 and 6.2); the upper limit to each boundary is listed in each title.

Using this method, the ACI_r and ACI_d results using the local 3º x 3º analysis are displayed in Figure 6.3. Immediately noticeable is the good agreement with Twomey-like behavior out to sea (east of 65ºW) with $ACI_r < 0$ and $ACI_d > 0$. The most striking

feature in Fig. 6.3 is the presence of a region along the U.S. coast that exhibits counter-Twomey behavior: that is, $ACI_r > 0$ and $ACI_d < 0$. This counter-Twomey behavior is also seen by Grandey and Stier (2010). The reason for this behavior is unknown but may be a combination of several factors, including meteorological/dynamical forcings, the presence of precipitating clouds (thus violating the constant LWP constrain), uncertainties at the aerosol/cloud retrieval level, and aggregation of observations to the monthly mean level.

6.1.3 Discussion

Before continuing ACI analyses, a few limitations of the monthly mean ACI analyses are noted. First, in performing a domain-wide ACI analysis (Section 6.1.1), certain latitudes and months are preferentially selected for certain LWP bins, as shown by Figure 6.4.

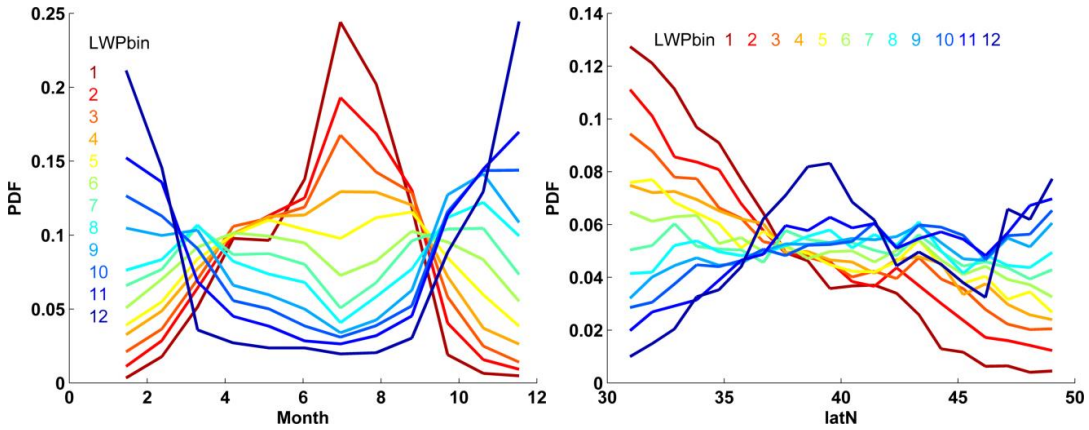

Figure 6.4: PDFs for month and latitude within each of the 12 LWP bins used in domain-wide ACI analyses (i.e. Section 6.1.1).

For example, the lowest LWP bin (LWP < 77 g/m^2) has a large representation of aerosol-cloud observations coming from the south of the domain (latitude < 35ºN) and primarily summer months (months 6, 7, and 8; June, July, and August). On the other extreme, the highest LWP bin (LWP > 213 g/m^2) contains observations during the cold winter months and latitudes around 40ºN and higher.

In extending the domain-wide ACI analysis (Section 6.1.1) to the more local 3º x 3º analysis (Section 6.1.2), behavior such as that in Fig. 6.4 (right) are avoided simply due to the more spatially local design of the analysis. However, the propensity of some months to be represented more so than others in a given LWP bin still remains. Figure 6.5 displays analysis of the first two mode months most often encountered for that grid point and LWP bin.

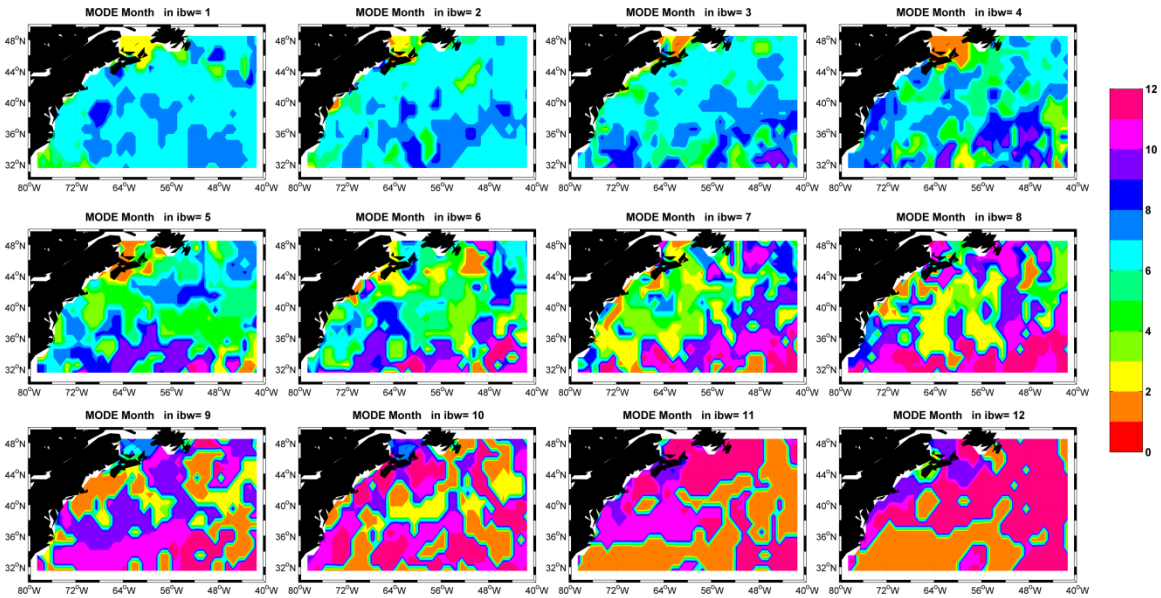

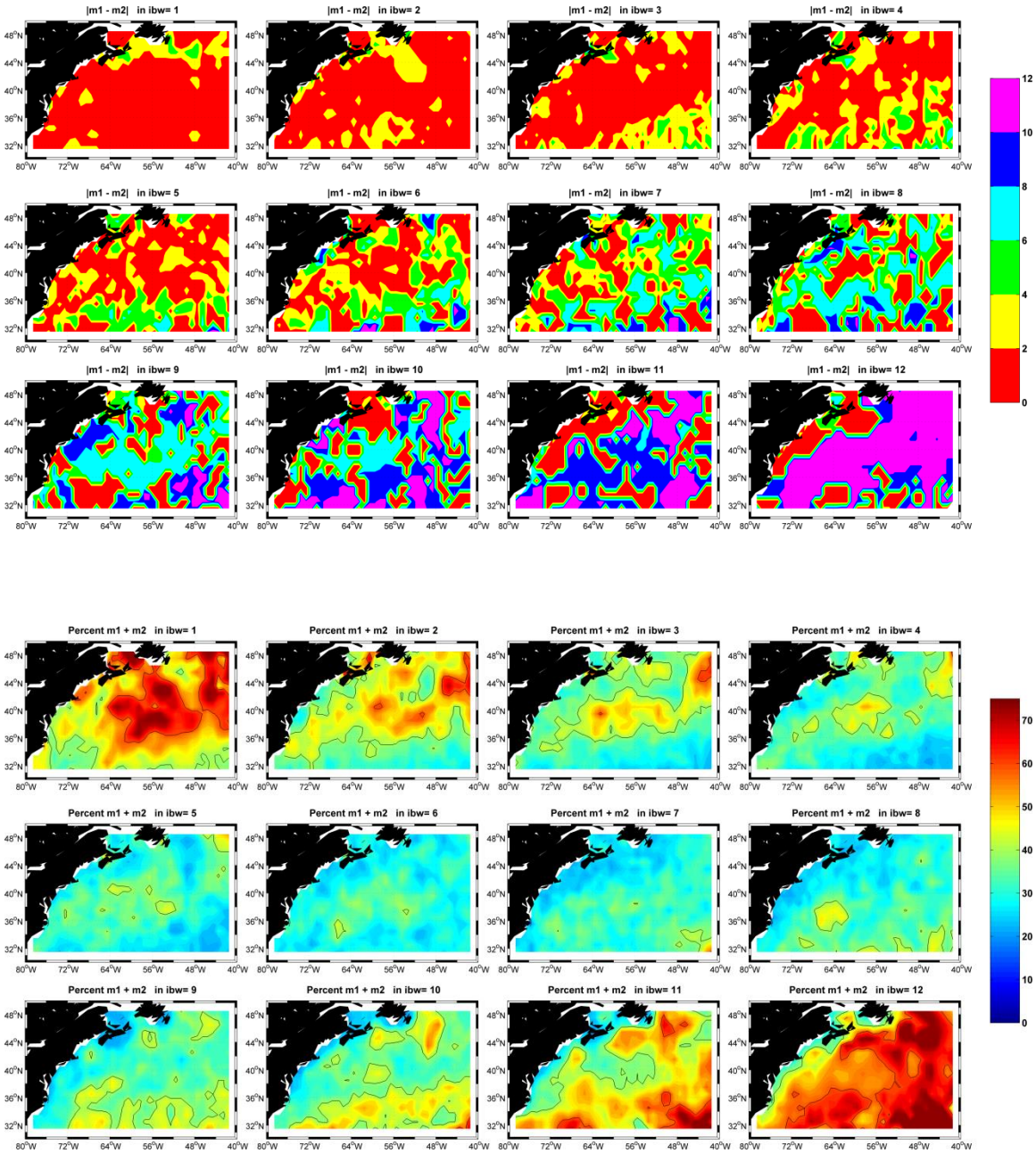

Figure 6.5: From the local 3^o x 3^o analysis (i.e. Section 7.1.2) and in same 12 LWP bins: (top) Statistical mode month at each location, (middle) the absolute difference between mode 1 and mode 2 months, and (bottom) percent represented by modes 1 and 2 for that grid point (black lines are the 40% and 60% contours).

Figure 6.5 (top) reveals that the summer months are the most frequent month encountered at low LWP, and this transitions to winter months being the most frequent at high LWP. This finding is supported when considering the two most frequent months

(mode 1 and mode 2) and the difference between them. Figure 6.5 (middle) demonstrates that for much of the domain analyzed, the difference in mode 1 and mode 2 months is less than two or more than ten, indicating that mode 1 and mode 2 months are adjacent and are likely to occur during the same season. Finally, the percent makeup of all observations for that grid point and LWP bin that mode 1 and mode 2 represent is shown in Figure 6.5 (bottom). While the spatial contribution has been improved and now more localized, the temporal contribution (or distribution of months) still remains. For example, low LWP (e.g. bins 1 and 2) observations are comprised of 50% or greater of observations that occur during the summer months while high LWP (e.g. bins 11 and 12) use 50% or greater of observations occurring during winter months.

Briefly mentioned in Section 6.1.1 were two behaviors shared in both ACI_r and ACI_d analyses: 1) the apparent decrease (increase) in ACI_r (ACI_d) magnitude as LWP increases, and 2) the increased mean(r_e) (or mean(COT)) scatter at large aerosol loading. McComiskey et al. (2009) suggest that an increase in cloud drop collision-coalescence and reduction in cloud drop number concentration when transitioning from low to moderate LWP might obscure the ACI effects. When transitioning to high LWP bins, ACI influences can be completely masked (i.e. ACI = 0 or even $ACI_d < 0$ as the case for COT) due to the presence of precipitation and the scavenging/removal of aerosol. These may underlie point (1) and the reduction in ACI sensitivity for both ACI_r and ACI_d under increasing LWP. The behavior suggested by point (2) has been noted by Feingold et al. (2001), who proposes three scenarios likely to be occurring at high aerosol loading: a) there is saturation in the r_e response (i.e. ACI = 0), b) there is an increase in droplet

concentration leading to smaller r_e (i.e. continuation of $ACI_r < 0$), and/or c) competition for vapor causes small droplets to evaporate leading to larger r_e (i.e. $ACI_r > 0$). A combination of these three responses is thought to contribute to the large spread in mean(r_e)-mean(AOD) points at larger aerosol loadings.

The use of monthly mean aerosol-cloud observations has permitted an initial demonstration that the Twomey effect is indeed seen over the broad North Atlantic domain while having nuanced behavior (including non-Twomey) from a more local point of view. However, these analyses using monthly mean data do not offer a straight forward way to assess if the long-term decrease in aerosol load (see Chapter 3) results in a cloud modification (e.g. by Twomey theory an increase in r_e and decrease in COT), and one whose strength might be changing through time. Additionally, using monthly means limits the depth of analyses that can be performed and confounds meteorological influences on clouds with potential aerosol influences. For example, ACI are sensitive to the aerosol type/size (e.g. Ghan et al., 1998; Yuan et al., 2008) as well as dynamical conditions like vertical velocity and atmospheric stability (e.g. Su et al., 2010; Andersen and Cermak, 2015). Using monthly mean data thus lacks the temporal information needed to assess finer details of ACI and the role that the range of atmospheric conditions throughout a given month may play.

6.2 ACI Analysis with Daily Mean Data

Having reached a practical limit in the temporally coarse monthly mean MODIS dataset, further ACI analyses are now performed with the MODIS Level-3 1º x 1º daily mean dataset of four years (2003, 2004, 2010, and 2011) during summertime (June, July, and August; JJA), with corresponding daily meteorological information from the MERRA reanalysis. The summertime months were selected because this season has shown the strongest decrease in AOD (see Chapter 3, e.g. Fig. 3.8). The four years were chosen which represent a period of higher AOD (2003 and 2004) and a period of lower AOD (2010 and 2011), with the aim to identify an influence from the reduction in aerosol loading. Finally, a much narrower domain is investigated: 80º to 70ºW longitude and 30º to 40ºN latitude. This is selected for two reasons, first to correspond to the near coastal counter-Twomey region seen in the local 3º x 3º analysis (Section 6.1.2, Fig. 6.3), and second to match the MODIS 1330 LST observation time with the MERRA 1800 GMT output time (centers the 45º longitude window (from 3-hr output) at 90ºW). Data from the MERRA reanalysis considered here are the vertical pressure velocity (ω) and lower tropospheric stability (LTS) at 700 hPa as well as specific humidity (SpHum) at 900 hPa.

Several restrictions are imposed on the data prior to analysis. These include using grid locations with both aerosol and cloud retrievals (i.e. no entirely clear nor entirely cloudy scenes), excluding grids with cloud top temperature (CTT) below 273 K (ensure liquid water clouds), and using clouds with LWP < 200 g/m^2 (to avoid clouds that may be precipitating). ACI analyses will be performed on the dataset as a whole and for several

segregations based on environmental conditions (ω, LTS, and SpHum) and aerosol size (FMF) based on previous studies that note the influence of dynamical conditions (e.g. Su et al. 2010; Andersen and Cermak, 2015) and aerosol type/size (e.g. Ghan et al., 1998; Yuan et al., 2008).

6.2.1Overview of Parameter PDFs

Before continuing with ACI analyses, the probability distribution functions (PDFs) of aerosol (AOD, AE, AI, and FMF), cloud (r_e, COT, LWP, CTT), and atmosphere (ω, LTS, SpHum, and relative humidity (RH)) parameters during the 4 years of summertime daily data are first examined. Special attention is paid to the PDFs for the 2003 and 2004 combined summers, 2010 and 2011 combined summers, and the difference between the two. The PDFs are displayed in Figure 6.6.

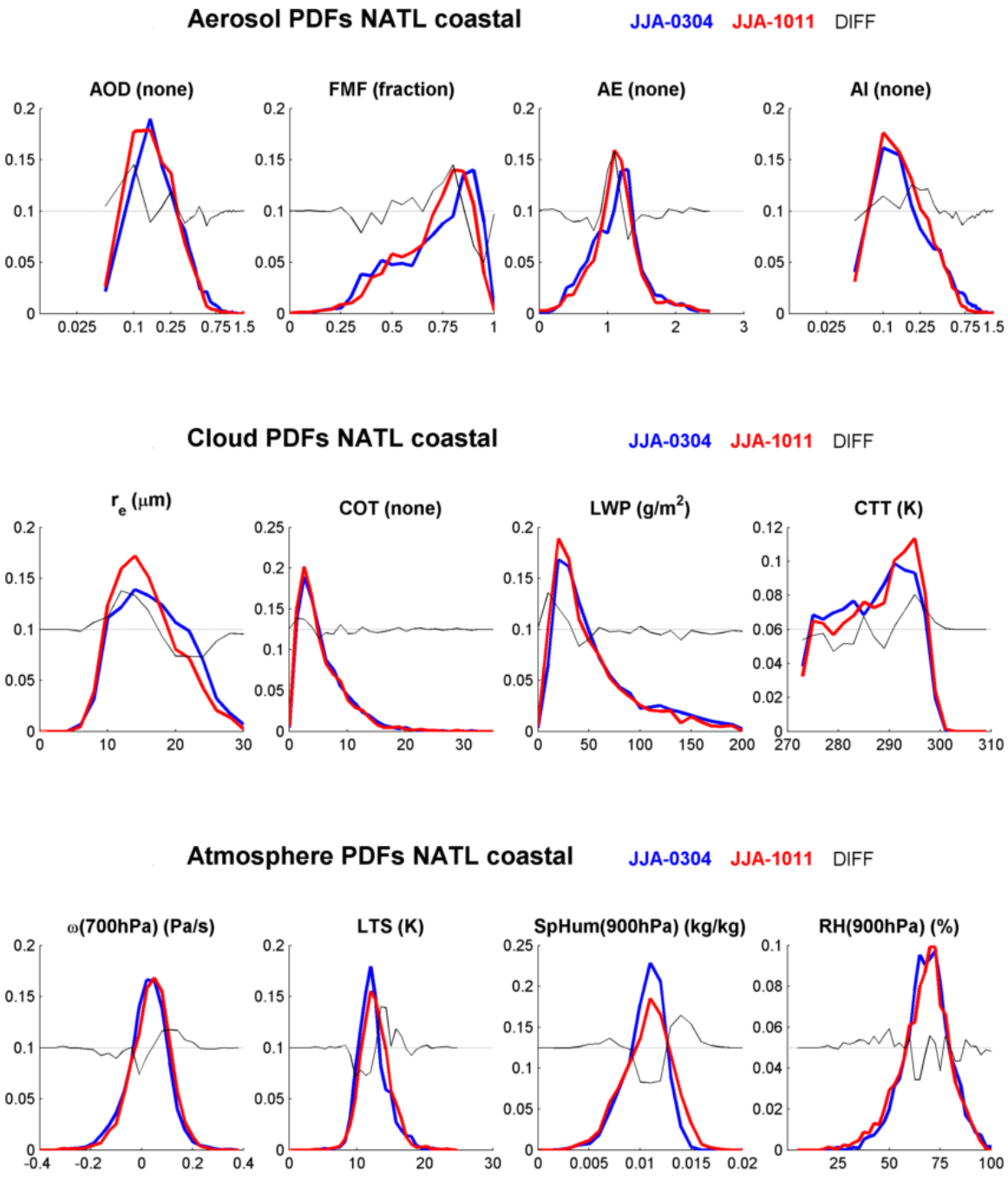

Figure 6.6: PDFs of (top) aerosol, (middle) cloud, and (bottom) atmospheric properties from for the summertime daily dataset. Blue denotes JJA during 2003 and 2004, red denotes JJA during 2010 and 2011, and DIFF refers to the difference (JJA-1011 – JJA-0304). An offset has been added to the DIFF such that it fits within the y-axis bounds. Note: AOD and AI have a logarithmic x-axis.

The reduction in anthropogenic AOD calculated in Chapter 3 using the monthly mean data is reflected by the aerosol PDFs with the daily data. For example, a decrease

in AOD would shift the aerosol PDF towards lower values. This is reflected by JJA-1011 having a higher fraction of small AOD values while JJA-0304 has a higher fraction of large AOD values. If the decrease in AOD is indeed reflective of decreases from anthropogenic species (which are typically smaller than natural species), there should be a noticeable shift in the FMF within the aerosol loading. Indeed, JJA-0304 had a larger fraction of very high FMF values (i.e. predominately small particles) while JJA-1011 shows a larger fraction of moderate FMF values (i.e. fewer small particles). This shift in the composition of the aerosol load also has an impact on the AE seen in the dataset, where larger particles have a smaller spectral dependence of AOD and translates to smaller values of AE for these particles. The size shift seen in FMF is also present in PDFs of AE: there are a larger number of small AE values around 1.0 during JJA-1011 in contrast to a larger number of high AE values (greater than around 1.3) during JJA-0304. Finally, AI mirrors the behavior seen in AOD: JJA-1011 has a larger fraction of lower AI observations compared to JJA-0304 which has a larger fraction of higher AI observations.

Cloud properties between the two periods also show some slight shifts. Clouds during JJA-1011 appear to have an increased fraction of smaller r_e while also having a reduced fraction of larger r_e when compared with clouds during JJA-0304. The shift in COT is minor and appears to mirror the shift in LWP. Clouds during JJA-1011 reveal an increased number of low LWP clouds and a decreased number of higher LWP clouds relative to JJA-0304 clouds. CTT reveals a shift towards higher occurrences of warm clouds (i.e. lower clouds) and fewer cool clouds during JJA-1011 compared to JJA-0304.

This may reflect the shifts in the other cloud properties: lower clouds during JJA-1011 do not have the same vertical thickness as those during JJA-0304, and with restricted vertical development have smaller effective radii and LWP.

Finally, there are shifts in the atmosphere PDFs between the two periods that may also contribute to the shifts in cloud PDFs. JJA-1011 appears on the whole to be relatively more stable than JJA-0304 when considering either ω or LTS. While JJA-1011 shows a sizable shift towards more occurrences of high SpHum, this is not reflected in RH which may suggest a decrease in high RH frequency compared to JJA-0304. This may be a behavior of a global warming behavior that permits an elevated water vapor mixing ratio within the lower atmosphere, yet also an increase to the saturation mixing ratio that ultimately could result in a reduced relative humidity if the increase to saturation mixing ratio is larger than the ambient mixing ratio (e.g. Byrne and O'Gorman, 2013).

6.2.2 Aerosol and Cloud Correlations with Environmental Factors

Prior to continuing with ACI analyses, raw correlation coefficients (R) were determined for select parameters within the daily dataset. Table 6.1 displays the correlation (and significance) between the selected parameters and the daily dataset. Correlations were determined via a binning method using bin sizes appropriate to the selected parameter (left column) to determine a set of mean(X)-mean(Y) points for

correlation. Here X and Y denote the two variables being correlated, for example, AOD and AI.

	AOD	FMF	AE	AI	CRE	COT	LWP	CTT	OMG	LTS	SpH
AI	**0.98**	**0.73**	**0.66**	-	0.02	0.11	-0.25	**-0.51**	**-0.36**	**-0.46**	**0.43**
FMF	-0.06	-	**0.99**	**0.96**	0.11	**-0.46**	**-0.61**	0.10	-0.11	-0.36	0.07
CRE	-0.24	-0.08	**-0.54**	0.26	-	**-0.51**	**0.82**	**0.59**	**-0.60**	**-0.86**	**0.51**
LWP	0.08	-0.13	**0.62**	0.20	**0.79**	**0.99**	-	-0.09	**-0.81**	**-0.61**	**0.68**
OMG	-0.36	0.38	0.62	-0.20	**-0.74**	**-0.28**	**-0.74**	**0.72**	-	**0.88**	**-0.93**
LTS	-0.27	**-0.46**	**-0.53**	**-0.47**	**-0.30**	**-0.48**	**-0.62**	0.17	**0.48**	-	**-0.59**
SpH	**0.89**	0.24	-0.15	**0.89**	0.34	**0.73**	**0.78**	**0.55**	**-0.80**	**-0.66**	-

Table 6.1: Table of correlation coefficients (R) between variables (along left column) and aerosol, cloud, and environment parameter (along top row). Values in **BOLD** are correlations that are statistically significant (i.e. $p < 0.05$). CRE is r_e, SpH is specific humidity(SpHum), and OMG is ω.

AI is seen to be well correlated with all aerosol parameters (AOD, FMF, and AE) and minimally correlated with r_e, COT, and LWP. Negative correlations between AI and ω or LTS may indicate either aerosol lofted above or advected above the boundary layer and thus not removed as quickly via deposition. The negative correlation with CTT may be a by-product of CTT correlations with ω. Positive correlation with SpHum suggests some influence of water vapor uptake or aerosol swelling. FMF appears well correlated with both AE and AI, which might be expected as FMF and AE both tell qualitative information about aerosol size. FMF has minimal correlation with r_e, CTT, and all environmental parameters (ω, LTS, and SpHum). FMF does show some negative correlation with COT and LWP, which may indicate here that loadings predominated by fine-mode aerosols (i.e. large FMF) perform poorly in as cloud condensation nuclei, thus

producing optically thinner and less-water laden clouds than situations with more coarse mode aerosol loadings.

Cloud parameters (r_e and LWP) show weak correlations with aerosol properties except for AE. These weak correlations may be indicative of the confounding influence of environmental forcing on the cloud system which may be stronger than any aerosol correlation. It is also noted that LWP is not constrained here, a requirement for Twomey theory. The strong correlations with AE and lack of correlations with FMF provide an unclear picture of the impact that aerosol size may have, and again may point towards other environmental forcing that must be accounted for. LWP is strongly correlated with both r_e and COT, and r_e is strongly correlated with LWP and moderately negatively correlated with COT. To the zeroth order, this manifests from the interplay between all three parameters (r_e, COT, and LWP) in producing the optical properties of a cloud: r_e and COT are inversely correlated, thus show $R < 0$. The positive correlation between r_e and CTT demonstrates the behavior (for non-precipitating clouds) of cloud droplets to grow in size as they ascend within a cloud to higher heights. Both r_e and LWP show strong negative correlations with ω and LTS, suggesting that more dynamically unstable environments ($\omega < 0$ and low LTS) permit clouds with larger effective radii and larger water content, possibly a result of the strong updrafts and/or extended vertical development. r_e and LWP both show strong correlation to SpHum, indicating that larger amounts of water vapor permit larger radii and water contents as well.

6.2.3 Summertime ACI from Daily Data

6.2.3.1 ACI Using AOD versus AI as CCN Proxy

As defined in Section 2.3.4 and used in Section 6.1, ACI has to this point been calculated using AOD as a proxy for cloud droplet number concentration (N_d) and thus condensation nuclei (CCN). While AOD is used in a wide range of satellite studies of ACI, other proxies such as aerosol index (AI) and aerosol number concentration (N_a) have also been used (see Table 1 in McComiskey and Feingold, 2012). The derivation of ACI is the same but for the aerosol proxy. Here, the result of Nakajima et al. (2001) is highlighted, demonstrating a better fit to estimated N_a when using AI as opposed to AOD from satellite. Caution was used in selecting AOD or AI for ACI studies using the monthly mean data as AI is not a provided product from the MODIS aerosol team but derived in this work a posteriori from spectral AOD (to derive AE). Thus, AI from the monthly dataset would not be considered to represent the mean AI for all aerosol loads seen throughout the month, but rather the AI seen if assuming the mean spectral AOD were valid throughout the month. Using daily data alleviates this problem and the derived AI is assumed to better represent that observed and the N_a on any given day. Figure 6.7 below compares ACI derived from the summertime datasets using both AOD (left) and AI (right) as the aerosol proxy.

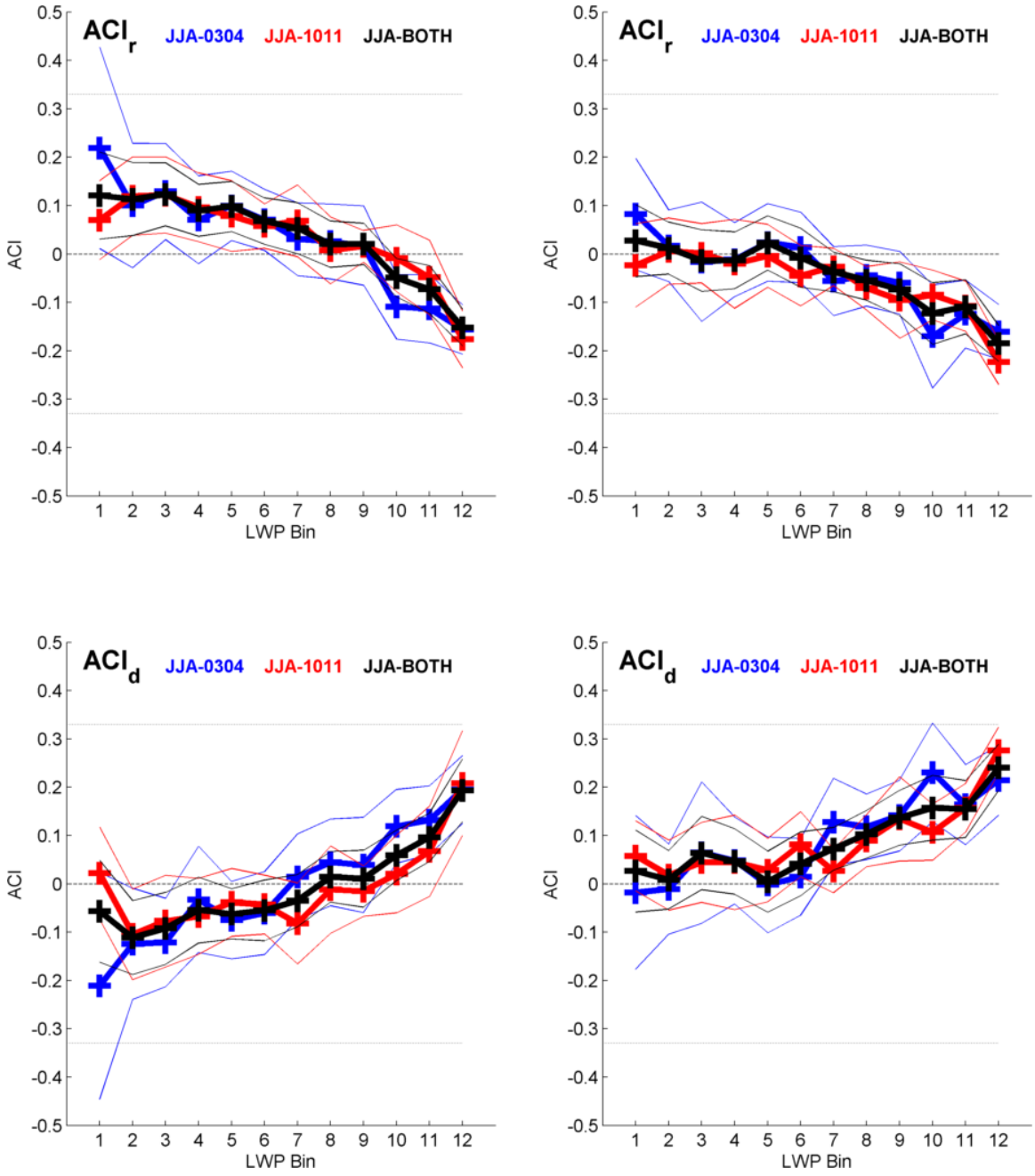

Figure 6.7: ACI analysis using (top) cloud effective radius (ACI_r) and (bottom) cloud optical thickness (ACI_d) using (left) AOD and (right) AI as the proxy for CCN. Thin lines denote the uncertainty envelope of the ACI estimation with 95% confidence. Dashed lines at ±0.33 denote the plausible limits of Twomey behavior.

Some general observation notices that using AOD suggests more counter-Twomey behavior ($ACI_r > 0$ and $ACI_d < 0$) at lower LWP bins when compared to using AI. While using AI can provide some counter-Twomey behavior at the lowest two LWP

bins (LWP < 20 g/m^2), the uncertainty in the reported ACI provides an envelope that includes Twomey behavior and an envelope which provides much less chance that the true ACI value using AOD may indeed be Twomey. Finally, based on the similarity of JJA-0304 and JJA-1011 curves, it would appear that the general ACI behavior for this dataset is consistent throughout time (i.e. similar at the beginning and ending of the aerosol decrease analyzed here). Upon seeing the ACI results from Fig. 6.7 comparing AOD versus AI, AI will be used going forward as the proxy for N_a.

One additional point to note is the apparent larger uncertainty in ACI value, especially at lower LWP, such as bin #1 for JJA-0304. In addition to spread in the mean(AI)-mean(r_e) points, some uncertainty is contributed from the relatively fewer aerosol-cloud pairs within this low LWP bin relative to the others. Figure 6.8 shows not only the number of observational pairs (Nobs) within each LWP bin but also the upper bound on the LWP bins themselves. As can be seen, each time period has around 200 ± 50 Nobs in each LWP bin, representing approximately 8-10% of that periods data per bin. The upper limits to each LWP bin resemble an exponential shape, which is expected as the bins are determined in a linear fashion from the log(LWP) distribution of the entire four summers. Thus, by construction it comes as no surprise to see quasi-constant Nobs within each LWP bin. This also has the effect of making the confidence intervals for ACI much more constant across LWP bins. Analyses were done (not shown) with custom LWP bins (linear in LWP space) that upon investigation had elevated Nobs in lower LWP bins and much fewer Nobs at higher LWP bins. The consequence of this was

to have ACI confidence intervals that became larger (or more uncertain ACI) as LWP was increased simply due to the fewer data points making up the analysis for those bins.

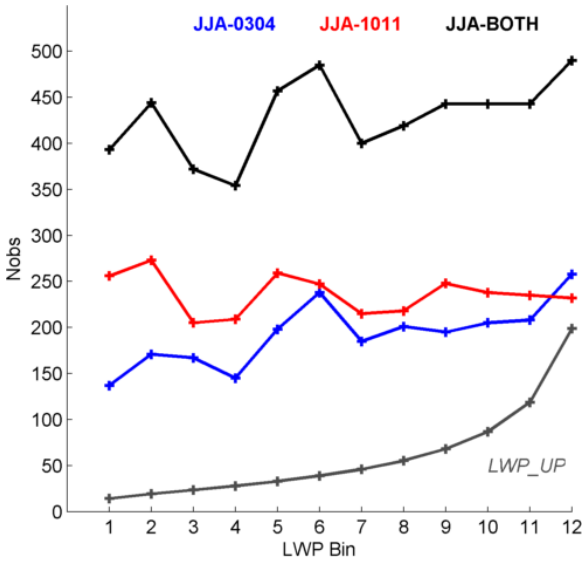

Figure 6.8: Number of observations (Nobs) within each LWP bin for both summer periods and all summers combined. Also shown is the upper limit (LWP_UP) of each LWP bin (in g/m^2), which by definition is quasi-linear in log(LWP) space and based on the LWP observed for the entire daily dataset.

6.2.3.2 ACI Based on ω Regime

To begin to separate the aerosol influence on clouds from environmental influences, ACI analyses have been performed for grids with ascending (subsiding) motion based on $\omega < 0$ ($\omega > 0$). Figure 6.9 shows the both ACI_r and ACI_d results for the three time periods and two ω scenarios.

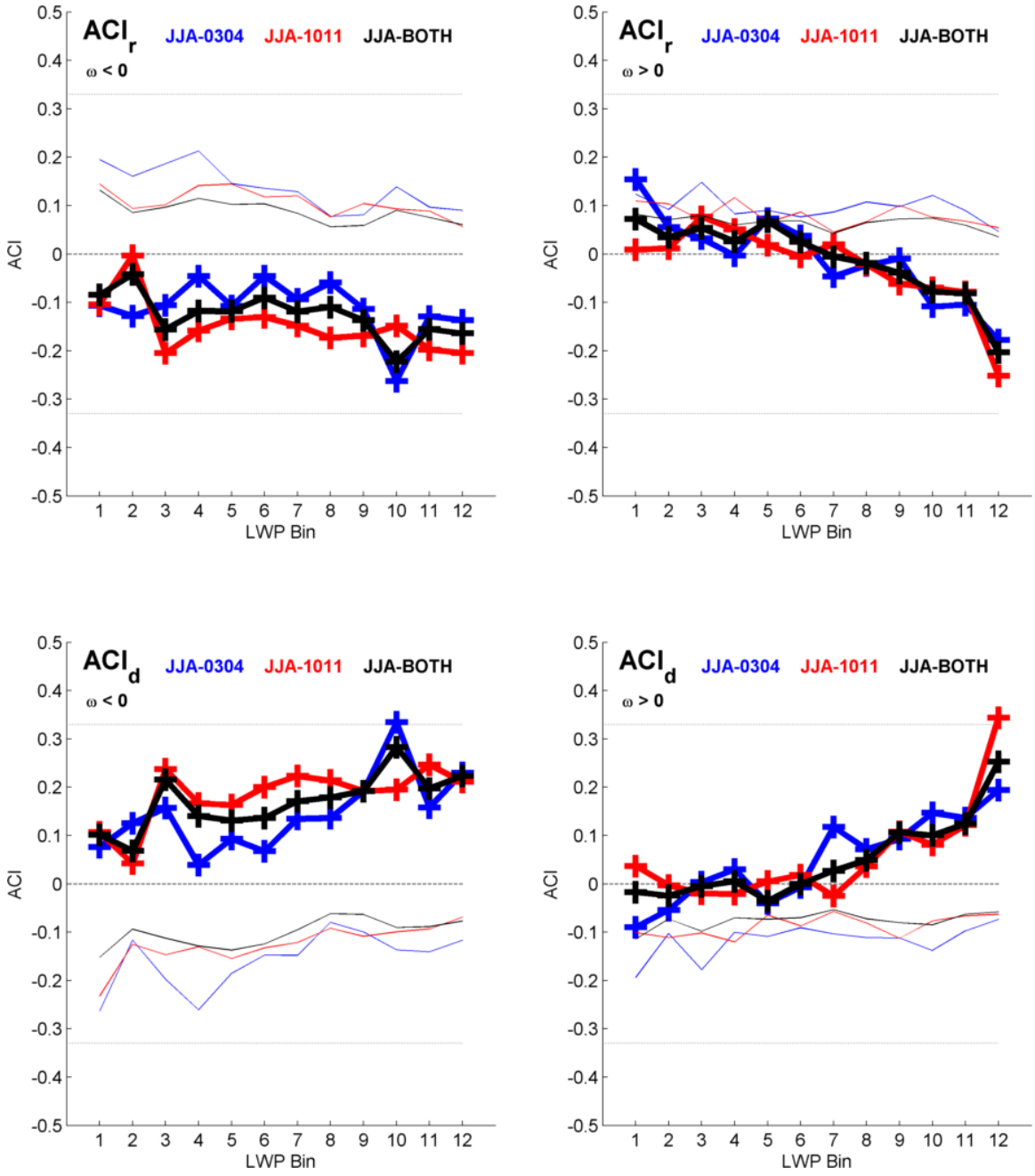

Figure 6.9: ACI analysis using (top) cloud effective radius (ACI_r) and (bottom) cloud optical thickness (ACI_d) for (left) ascending and (right) descending grids using AI as the proxy for CCN. Thin lines denote the absolute (relative to zero-line) uncertainty of the ACI estimation.

One striking difference between ascending and subsiding cases is the ACI for ascending cases is reliably Twomey-like across all LWP bins, while the behavior for subsiding cases shows counter-Twomey behavior for ACI_r (ACI_d) at lower LWP bins and

transitions to Twomey-like behavior at higher LWP bins. This is true when considering JJA-0304, JJA-1011, or JJA-BOTH. A possible cause may include subsidence-related lowering of the boundary layer (thus separating aerosols from the cloud base). Another interesting feature that is unique between ascending and subsiding cases is that while the behavior for JJA-0304 and JJA-1011 is similar for subsiding cases (Fig. 6.9, right), there is separation in the curves for the two summers in ascending cases (Fig. 6.9, left). In both ACI_r and ACI_d, it appears that the later period (JJA-1011) has a stronger aerosol-cloud interaction when compared to the early period (JJA-0304).

6.2.3.3 ACI Based on LTS Regime

While ω had an obvious choice to segregate data with (i.e. $\omega = 0$), a threshold for LTS is less clear. The PDFs and CDFs of both ω and LTS as well as the linear regression of LTS onto ω are shown in Figure 6.10 and were examined. Using $\omega = 0$ as a starting point, an approximate point in the LTS(ω) fit is determined to be 12.25 K. While approximately 32% of the data have $\omega < 0$, using 12.25 K as the cutoff for LTS divides the dataset into half. Thus, a threshold of 12.25 K for LTS is selected as it provides some relation to dynamical vertical motions (via ω) and fortuitously divides the dataset into equal halves.

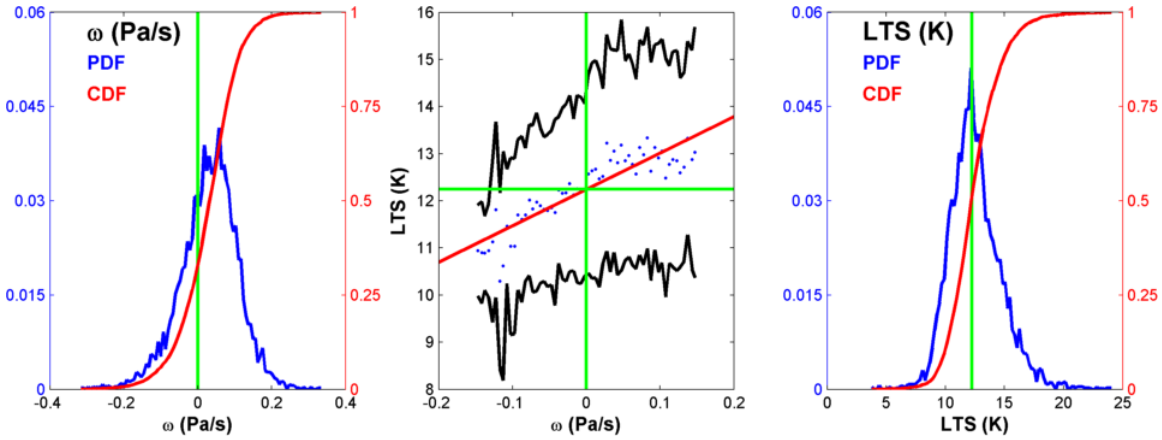

Figure 6.10: Plots of (a) PDF and CDF of ω, (b) LTS versus ω with linear fit, and (c) PDF and CDF of LTS. Green lines denote ω = 0 Pa/s and LTS = 12.25 K. Red line in (b) denotes linear fit. PDF correspond to left axis, CDF to right axis. Data points in (b) are mean(LTS)-mean(ω) in ω bins of width 0.005 Pa/s.

Figure 6.11 shows the ACI analysis for the JJA daily dataset stratified by thermodynamic stability using the LTS = 12.25 K threshold. Relative to the ω = 0 threshold, there is increased similarity in the two thermodynamic regimes. Additionally, there is little contrast between the behavior of ACI during JJA-0304 and JJA-1011. As a whole, the dataset shows little to no aerosol sensitivity at low LWP bins and increases in sensitivity as the LWP of the clouds considered increases. One contrasting behavior appears to be the strength at which the aerosol sensitivity increases: the thermodynamically unstable cases (Fig. 6.11 left) appear to show a slower increase in aerosol sensitivity at moderate to high LWP bins whereas the thermodynamically stable cases (Fig. 6.11 right) reveal a more rapid increase in aerosol sensitivity.

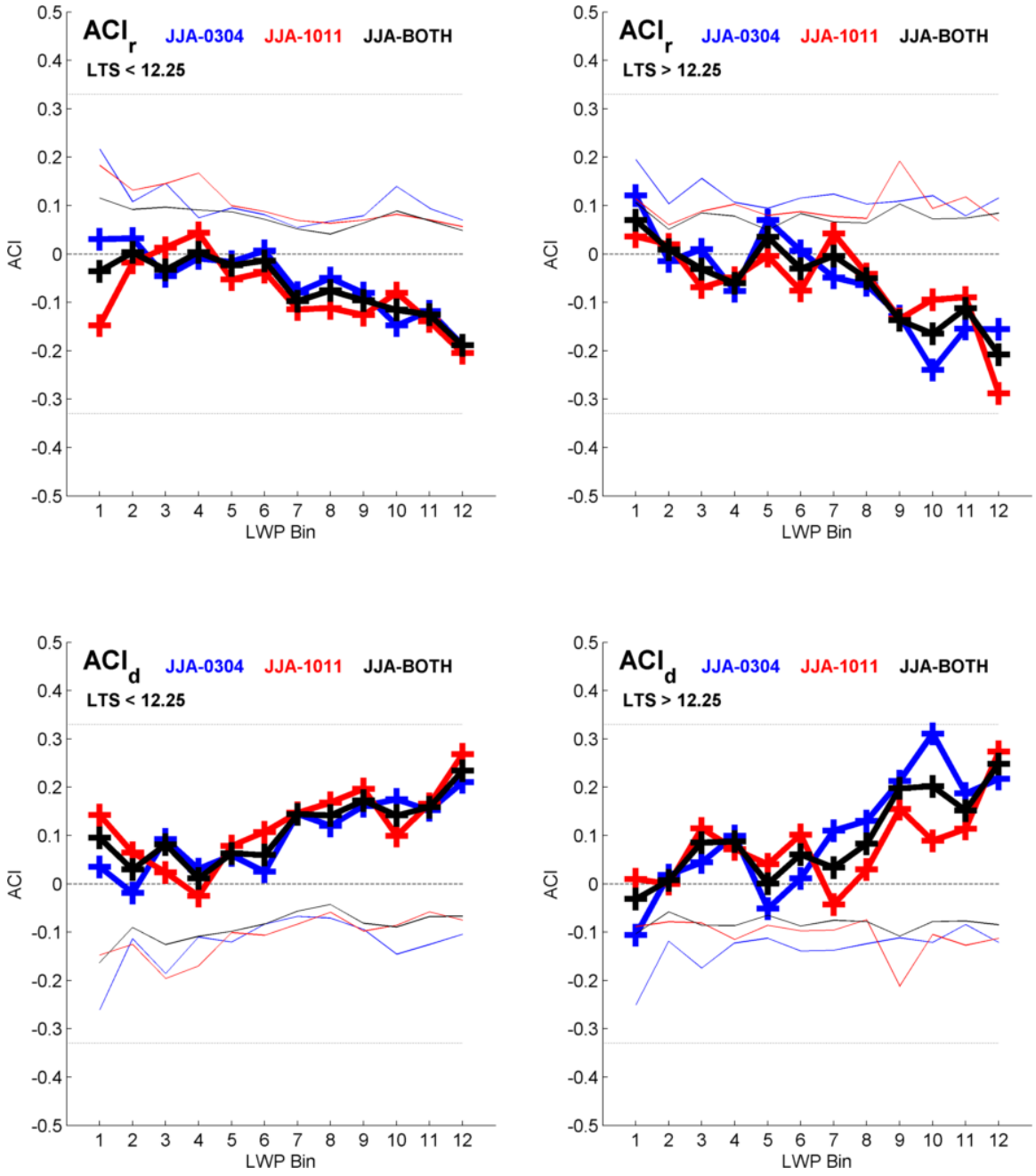

Figure 6.11: Same as Fig. 6.9 except using LTS = 12.25 K as threshold.

6.2.3.4 ACI Based on Specific Humidity Regime

Aerosol activation and cloud droplet formation occurs near the cloud base in a region of elevated supersaturation (relative to the remaining cloud above) (Rogers and Yau, 1989). Supersaturation is highly variable in space and time and is not offered as an output to modern reanalyses, including MERRA used presently. In place of supersaturation here the specific humidity (SpHum) is explored as a proxy and represents the total water vapor amount near the cloud base (here assumed at 900 hPa). Thresholds to make two quasi-equal regimes are based on SpHum = 0.01 kg/kg. ACI analyses for SpHum are shown in Figure 6.12.

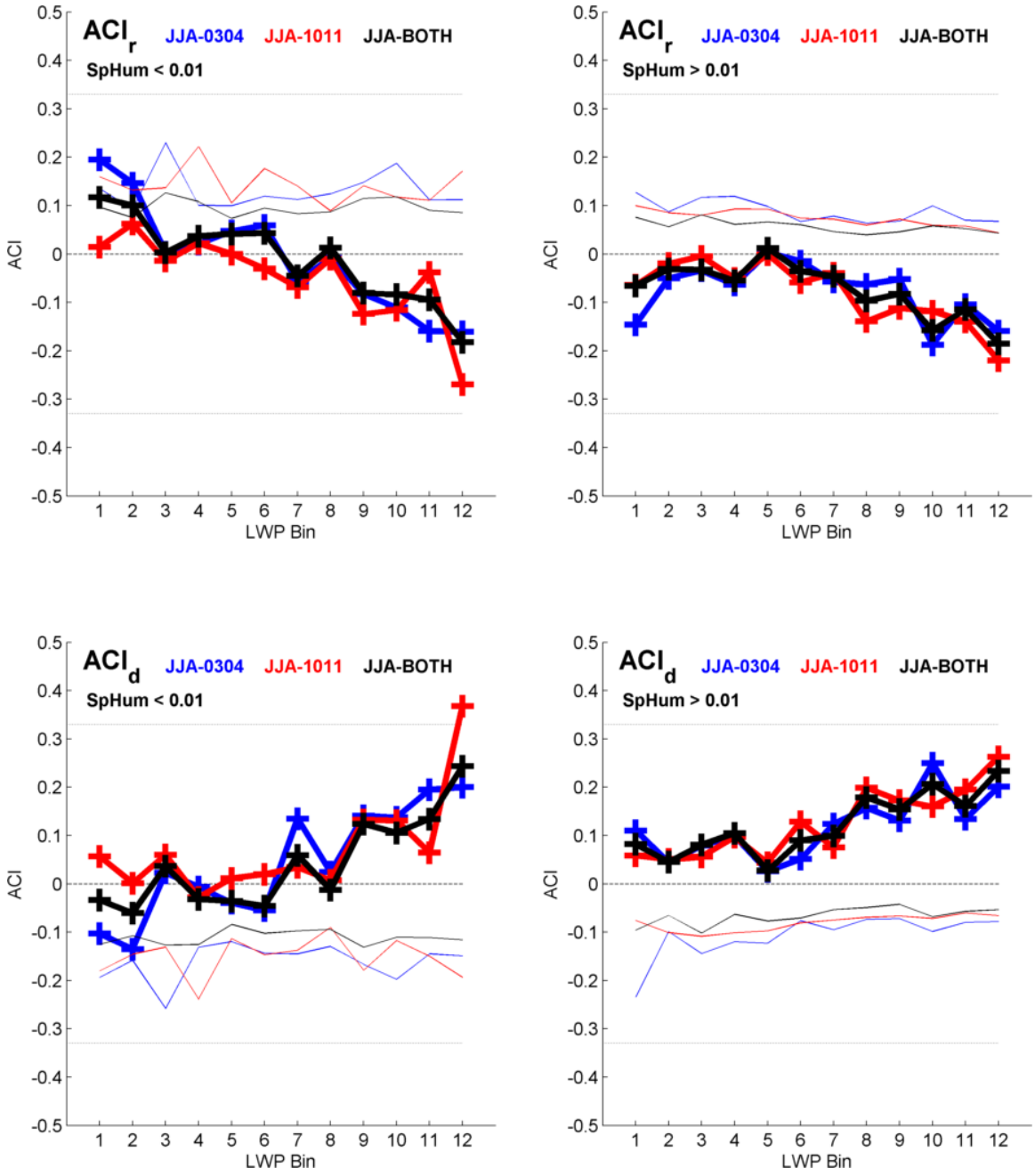

Figure 6.12: Same as Fig. 6.9 except using SpHum = 0.01 kg/kg as threshold.

One interesting feature that is evident in SpHum-based ACI analyses is that cases with larger water vapor amount near the cloud base (Fig. 6.12, right) display Twomey behavior at all LWP bins. This is likely due to the large amount of water vapor at the (assumed) cloud base being able to activate a larger number of aerosol particles

(spanning low and high aerosol loadings). An increased number of cloud droplets competing for the same amount of vapor results in an equilibrium of more numerous but smaller droplets, which in turn encompass more scattering events and increased cloud optical depth. This is in contrast to the low SpHum cases (Fig. 6.12 left), in which the amount of aerosol activated is limited, not all aerosol available can be activated, and thus an ACI insensitivity (and some counter-Twomey behavior) to aerosol loading is seen at lower LWP clouds.

6.2.3.5 ACI Based on FMF Regime

A final segregation of the JJA dataset is made based on the fine-mode fraction (FMF) of the observed aerosol load. Larger aerosol particles are favored for CCN activation over smaller aerosol particles due to the reduced critical supersaturation required to activate (Rogers and Yau, 1989; McFiggans et al., 2006). Space-based remotely sensed aerosol loads are composed of a combination of aerosol types and range of sizes, properties that are not possible to obtain from a sensor like MODIS. As described in Chapter 2, the MODIS ocean aerosol retrieval combines the reflectances of one fine mode and one coarse mode aerosol model. The weighted combination (η; see Eq. 2.1) is also called here the FMF, and provides a qualitative perspective of the assumed fine/coarse composition of the observed aerosol load. Low values of FMF represent the presence of more coarse mode aerosol than higher values of FMF. Figure

6.13 shows the ACI analysis using a threshold of FMF = 0.75, chosen again to split the data into approximate halves.

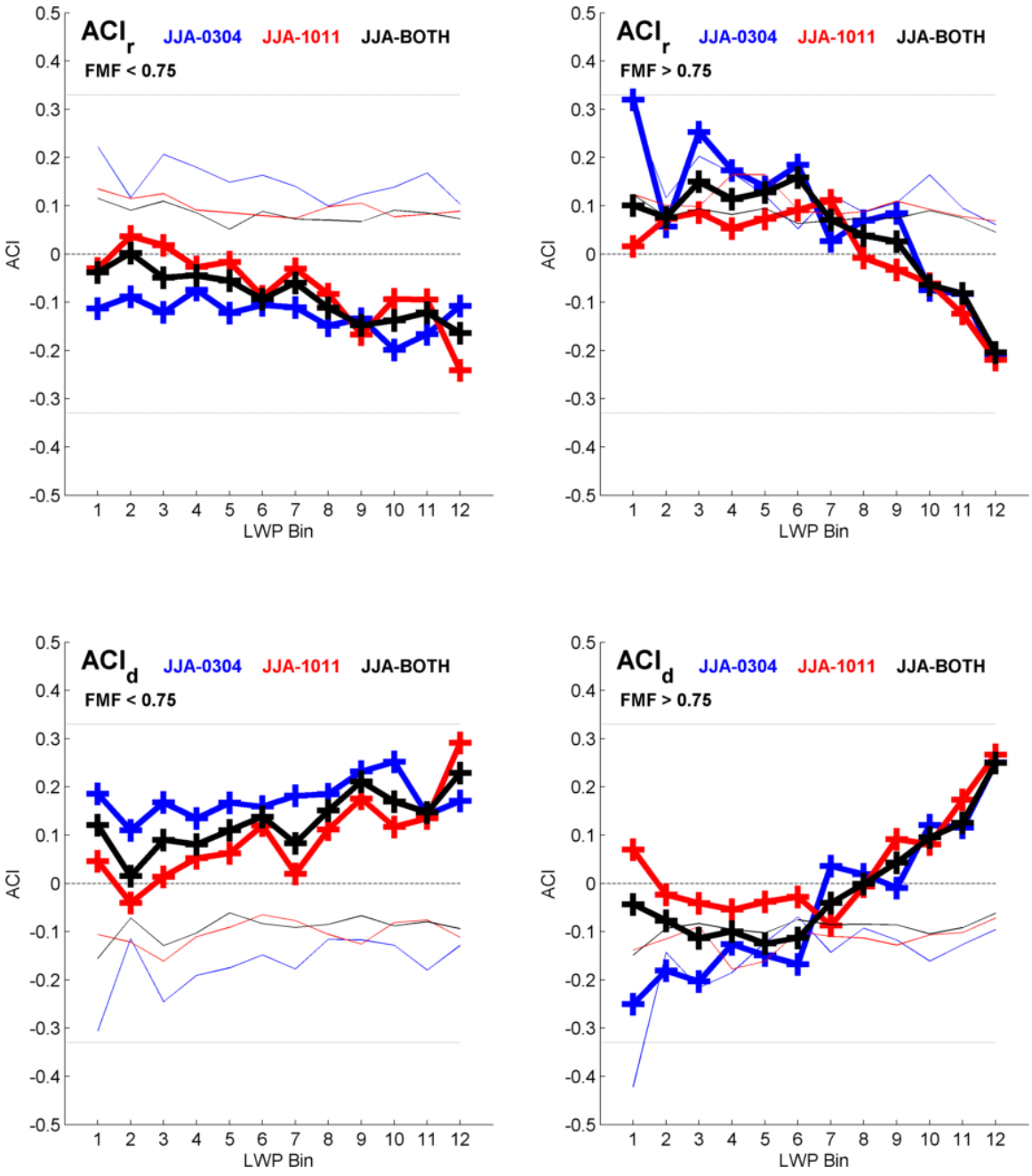

Figure 6.13: Same as Fig. 6.9 except using FMF = 0.75 as threshold.

Several interesting features are now discussed. First, aerosol loads with larger coarse mode fraction (Fig. 6.13 left) are in better agreement with Twomey theory than fine mode dominated aerosol loads (Fig. 6.13 right), especially at lower LWP. Second, across all LWP bins, the early period (JJA-0304) appears to have stronger aerosol sensitivity relative to the later period (JJA-1011) for the FMF < 0.75 cases (Fig. 6.13 left). Third, low LWP bins for FMF > 0.75 cases (Fig. 6.13 right) appear to show counter-Twomey behavior, namely positive (negative) relation between aerosol and r_e (COT). The early period (JJA-0304) appears to have stronger counter-Twomey behavior than the later period (JJA-1011). In general, this counter-Twomey behavior transitions to more Twomey like at the highest LWP bins, and the difference between the two time periods disappears.

The reasons for these behaviors are uncertain. One possible explanation for the difference in Twomey and counter-Twomey behavior in FMF < 0.75 and FMF > 0.75 cases involves the residual presence of large aerosols in the FMF> 0.75 case. The numerical modeling study by Ghan et al. (1998) investigated the impact of sea-salt particles (a typically coarse mode aerosol) on the activation of sulfate particles (typically fine mode aerosol). Their results show that at large number concentration of sulfate particles the addition of larger sea salt particles acts to reduce the supersaturation. This reduction is caused by the inherent preference of larger aerosols to be activated first, as a result of their greater size and reduced critical supersaturation required. These CCN then continue to attract vapor to condense onto itself, thereby reducing the ambient supersaturation and inhibiting the activation of smaller aerosol. In total, this acts to

reduce the overall number of aerosol activated as CCN yet allows those large particles (which are activated as CCN) to continue to grow to larger radii. This is in contrast to a high aerosol load of mainly fine-mode particles, which according to Twomey theory should result in a population of smaller radii cloud droplets (relative to a light aerosol load). The presence of few large particles is thus hypothesized to be a potential reason for the counter-Twomey behavior seen in FMF > 0.75 (Fig. 6.13 right) cases.

6.3 Chapter 6 Summary

The potential impact aerosols have on clouds via aerosol-cloud interactions (ACI) is explored through the first indirect (or Twomey) effect. Using monthly mean data, the Twomey effect is present in a domain-wide analysis over the mid-latitude North Atlantic Ocean. The strength of the ACI diminishes when looking at clouds of increasing LWP, possibly a consequence of increased cloud drop collision-coalescence and reduction in cloud droplet number concentration as well as the presence of precipitating clouds scavenging/removing aerosol. The monthly mean analysis was extended to a localized 3º x 3º analysis, which reveals good Twomey agreement at sea but a "counter-Twomey" region of ACI behavior along the U.S. coastline. Having reached the extent of monthly mean analyses, daily mean data in the near-coastal region during summers (JJA) of 2003, 2004, 2010, and 2011 are examined, which allows for additional information on the atmospheric state using ω, LTS, and SpHum. Ascending cases ($\omega < 0$) are reliably Twomey-like across all LWP bins while descending cases ($\omega > 0$) show some non-

Twomey behavior at low LWP and transition to Twomey-like at larger LWP. ACI for ascending cases during 2003 and 2004 is weaker than ACI during 2010 and 2011. There is little difference between low and high LTS cases and little difference between 2003/2004 and 2010/2011 datasets. When analyzing based on near cloud base SpHum it is shown that high SpHum cases are reliably Twomey-like across all LWP bins, possibly due to high water vapor density near the cloud base activating a large number of aerosols. Finally, analysis based on FMF regime reveals good Twomey agreement for mainly coarse-mode aerosol loadings. Interestingly, for more fine-mode loadings there exists strong counter-Twomey behavior at low LWP. A role of residual coarse-mode aerosols remaining is hypothesized to limit the activation of smaller fine-mode aerosol and subsequently decrease the supersaturation as the coarse-mode aerosols grow.

Chapter 7: Conclusions

7.1 Summary of Results

This study investigated the aerosol loading over the western North Atlantic Ocean and the direct and indirect impacts aerosols have on the climate of the region. The impetus to this work was the air quality controls imposed by the EPA, which aimed to improve air quality by reducing air pollution over the U.S., and the anticipated reduction in aerosol load downwind of the U.S. Datasets for this work come from satellite (MODIS and CERES), surface (AERONET and IMPROVE), and model (GOCART, MERRA, and SBDART) sources. The goals of this work were to (1) identify and attribute aerosol trends seen over the study area and (2) explore the impacts a changing aerosol load has on the environment through both the direct and indirect effects.

A negative trend in aerosol optical depth (AOD) is seen by MODIS in the mid-latitudes over the western North Atlantic Ocean from July 2002 to December 2012. This trend is estimated to be around −0.02 to −0.04 decade^{-1} and is statistically significant beyond the 95% level. This trend in total AOD agrees well with decreasing trends from other sensors (e.g. SeaWiFS and AVHRR). Trend analysis from three AERONET sites in the eastern U.S. also confirms this decreasing trend and shows strong spatial correlation between the surface sites and broad satellite field. Using the GOCART aerosol model, only anthropogenic species (primarily sulfate species) are shown to exhibit a decreasing AOD trend over the study region (natural species showed no trend). The anthropogenic origin of the decreases is further seen in IMPROVE surface $PM_{2.5}$ observations over the eastern U.S., where ammonium sulfate (AS) is identified as having significant decreases. A seasonal analysis showed spring (MAM) and summer (JJA) months as the main seasons for total AOD decreases, total $PM_{2.5}$ decreases, and AS decreases.

Occurring during the same time period as the mid-latitude decrease in AOD is an increase over the sub-tropics in total AOD on the order of 0.02 decade^{-1} annually as seen by MODIS. Using GOCART aerosol species, this trend is identified as coming from natural (dust and/or sea-salt) species. A seasonal breakdown reveals this trend occurring during JJA months, further suggesting changes in dust aerosol. The dust parameterization used by Kaufman et al. (2005a) is applied here and confirms the strong JJA AOD increase (0.06 to 0.08 decade^{-1}) comes from a basin-wide increase in dust aerosol. Interestingly, this sub-tropical (between 20º and 30ºN) increase overlies a less

coherent decrease in dust aerosol around 15ºN, suggesting a possible northward shift in dust generation, export, and/or transport. The MERRA reanalysis during JJA was used to examine possible upstream changes in the North African environment that may link to the change in dust. Examinations of the African Easterly Jet (AEJ; using u_{700}, $\partial u/\partial z$, and relative vorticity) suggest a northward shift in the AEJ and increase in transient African Easterly Wave (AEW) behavior along the AEJ north flank. The AEJ is linked to the underlying Saharan environment via the West African Heat Low (WAHL) and thermal wind. Three measures used to quantify the WAHL (NAFDI, LLAT, and T_{10m}) all show increases in the heat content and areal extent of the WAHL. An analysis of atmospheric instability using the meridional potential vorticity gradient along 5ºW suggests changes to the baroclinic zone along the north flank of the AEJ: the altitude of instability appears to decrease and may result in increased interaction between AEWs and dust mobilization. It is hypothesized that the changes to the WAHL are impacting the AEJ, atmospheric instability, and wave activity along its northern flank (known to influence dust transport and variability) and result in the trends seen in total (dust) AOD during JJA over the sub-tropical North Atlantic.

The aerosol direct radiative effect (DRE) and resulting direct radiative forcing (DRF) of the aerosol trends seen by MODIS were examined using radiative transfer calculations simulated with the SBDART model. On the zeroth order, the mid-latitudes (sub-tropics) seeing a decrease (increase) in AOD also see an increase (decrease) in both Earth-system and surface absorbance (ES_a and SFC_a, respectively) and decrease (increase) in atmospheric absorbance (ATM_a) for the total aerosol TDRF. Various

simulations were carried out to further refine the assumed "clean-sky", including using AOD = 0 and two methods to retain a "natural" background aerosol loading. It was determined that the method of Kaufman et al. (2005a,b) provides an appropriate way to separate anthropogenic from natural aerosol loads. A method inspired by Remer and Kaufman (2006) was used to convert 1330 LST instantaneous fluxes to daytime fluxes, and provides agreement within 8% and correlation $R > 0.75$ between SBDART-estimated and CERES-observed monthly mean top-of-atmosphere outgoing (TOA_u) fluxes. Overall, it is estimated that the broad mid-latitude anthropogenic AOD decrease leads to a 1-2 W/m^2/decade increase in daytime Earth-system absorbance (ES_a), most of which is seen as a surface absorbance. The perturbation analysis performed at one mid-latitude location revealed a trend of 2.0 ± 0.3 W/m^2/decade, a range taken to represent the upper bound on uncertainty based on assumptions presently made.

Finally, the possible impact a decrease in anthropogenic aerosol has on clouds (through the first indirect effect or Twomey effect) was investigated. Analyses were first preformed using the monthly mean dataset on hand. Results show good agreement basin-wide with Twomey theory both for aerosol impact on cloud effective radius (ACI_r) and on cloud optical depth (ACI_d). At lower liquid water paths (LWP < 140 g/m^2) higher aerosol loadings lead to smaller (larger) cloud effective radius (optical depth) than at lower aerosol loadings. At higher LWP, ACI_r continues to follow Twomey theory (albeit more weakly) while ACI_d demonstrates a counter-Twomey behavior. The potential inclusion of precipitating clouds in the monthly mean dataset may play a role in masking Twomey behavior. Recognizing the limitations in a basin-wide analysis (e.g. Grandey

and Stier, 2010), a more local 3º x 3º analysis was performed and revealed agreement with Twomey theory out to sea but counter-Twomey behavior along the U.S. coast in all LWP bins for both ACI_r and ACI_d. Limitations from using monthly mean data provided the impetus to perform analyses on daily mean data, where additional information about the atmospheric state can accurately be incorporated using the MERRA reanalysis. Restricted to warm, non-precipitating clouds during 4-years summer months in the near-coastal region, the daily analyses reveal ACI is sensitive to vertical velocity (ω) and fine-mode fraction (FMF) regime: grids with updrafts ($\omega < 0$ Pa/s) and small FMF (FMF < 0.75) showed good agreement with Twomey theory across all LWP. Additionally, these two regimes demonstrate some ACI separation between JJA-0304 and JJA-1011, suggesting an impact arising from the decrease in aerosol loading. ACI was found to be sensitivity to specific humidity at 900 hPa, where dryer cases showed non-Twomey behavior for low LWP clouds. Elevated cases of specific humidity showed consistently Twomey behavior, increasing in strength as cloud LWP increased. ACI was found to be insensitive to LTS regimes in the dataset considered, yet regardless of LTS aerosol sensitivity increased as LWP increased.

7.2 Limitations to Present Work

The present work is not without its limitations, some of which were able to be ameliorated. For example, MODIS only observes the total column AOD, thus making it difficult to attribute aerosol changes to a particular species. This restriction was reduced

by bringing in both GOCART aerosol species as well as surface PM observations. This could be further refined by also including additional qualitative information on aerosol type from other satellite sensors such as MISR and/or CALIPSO. Another limitation to the present work is the conversion of instantaneous to daytime monthly radiative fluxes from SBDART. To improve the agreement between SBDART simulated and CERES observed TOA_u fluxes, simulations at additional hours (beyond the two-hour windows used) and years (beyond 2003) could be performed. Additionally, some SBDART simulations not on the center-month date could be performed to provide information about the subtle change in Sun-Earth-viewing geometry seen throughout the month by CERES yet presently absent in SBDART simulations. A third limitation in the present work is in using one-degree gridded data to explore ACI. This mainly speaks to the separation between the analysis scale (i.e. MODIS 1º resolution or ~ 100 km) and process scale for aerosol-cloud interactions (sub-meter; e.g. McComiskey and Feingold, 2012). Further scale separation is incurred when using monthly mean data due to temporal aggregation, an issue somewhat alleviated in daily analyses.

7.3 Recommendations for Future Work

There are several areas of the current work that can be continued in future works and fall into two categories: (I) improvements to present work and (II) new and/or continuing works. Future studies could refine the direct effect calculations (Chapter 5), including expanding from five two-hour windows to ten or 12 one-hour windows. Using

more years than just one (2003) in the Remer and Kaufman (2006) ratio method may also provide a more robust daytime flux, and one that is not tied just to the mean conditions seen throughout 2003. Additionally, using more than just the center-month date, as this limits the monthly analysis to one Earth-Sun-sensor geometry per month whereas CERES observes a continuously changing geometry each day. Finally, using an observationally-based SSA dataset (e.g. from MISR) might provide a more realistic basis for how the scattering nature of the aerosol load may be evolving. This future work would fall under Category I. A new work (Category II) would include exploring the impact of aerosol and radiative flux trends on the underlying ocean, both in terms of biological impact as well as sea-surface temperature and ocean heat content.

Another area for further work is in the ACI analyses. Because using gridded data (Level-3) has its own limitations (i.e. McComiskey and Feingold, 2012) improvements and/or finer-scale nuances might be achieved using granular (Level-2) scale aerosol and cloud observations from MODIS. This is not without its own drawbacks, as aerosols and clouds cannot be retrieved at the same time. Additionally, present reanalysis (i.e. MERRA) only has output at 3-hourly intervals and 1.25º resolution (presently used) or a reduced dataset at 2/3º resolution but at 6-hourly intervals. The analysis presented in Section 6.2 could also be enhanced and uncertainties in ACI reduced with a larger data volume including additional summer months. Additionally, seasonal analysis during spring (MAM) may also be of interest given the anthropogenic AOD decrease also exists during this season. This future work would fall under both Category I and II. A continuing new work that could be performed would be to extend the ACI analysis out to

the eventual radiative impact aerosols (and their changes) produce in clouds. This work would fall under Category II.

Perhaps the most intriguing future work that could be explored is the hypothesis related to the changes in dust AOD seen in Chapter 4. Following the present analysis, it is hypothesized that an amplified warming signal seen over North Africa produces effects on the AEJ and particularly AEWs along the AEJ northern flank that result in changes in summertime dust export and/or transport, producing the trends observed. Continuing to explore these dust trends and probe further their cause will necessitate using daily data and more refined filtering techniques (e.g. Jones et al., 2003; Skinner and Diffenbaugh, 2014) to arrive at variability caused by AEWs and the associated variability in dust. Additionally, a longer dataset may also be required, as there are additional factors that have influence on atmospheric dust, including Sahel rainfall (Prospero and Lamb, 2003) and equatorial Atlantic SSTs (e.g. Chang et al., 2011; Wang et al., 2012). While MODIS data are limited to the 21st Century, including data from AVHRR could extend the AOD record back to the 1980s. This work would fall under Category II.

Moving forward in these areas can help improve the methods used here as well as to inform our understanding of Earth's climate and humankind's place in it. Expanding the domain globally would provide an opportunity to assess regional trends around the world, including areas of high aerosol loadings like India, East Asia, and Southeast Asia. Continuing studies of aerosol direct effects can offer a validation of the trend findings here and can provide an initial point of comparison with modeled aerosol direct effects

and trends. Finally, expanding on the North African dust trends will help illuminate their causes and answer questions like: is this a transient trend, existing because the perfect timeframe was used? Or is the trend indeed more long-term? Is it arising from a global warming signal as hypothesized? Or perhaps it results from the ideal alignment of internal climate variabilities during the period considered.

References

Aitken, J. (1880). On dust, fogs, and clouds. Transactions of the Royal Society of Edinburgh. Vol. 30. Pp. 337-368.

Albrecht, B.A. (1989). Aerosols, cloud microphysics, and fractional cloudiness. Science. Vol. 245. Pp. 1227-1230.

Alston, E.J., Sokolik, I.N., and Kalashnikov, O.V. (2012). Characterization of atmospheric aerosol in the US Southeast from ground- and space-based measurements over the past decade. Atmospheric Measurement Techniques. Vol. 5. Pp. 1667-1682. doi: 10.5194/amt-5-1667-2012.

Andersen, H. and Cermak, J. (2015). How thermodynamic environments control stratocumulus microphysics and interactions with aerosols. Environmental Research Letters. Vol. 10. doi: 10.1088/1748-9326/10/2/024004.

Anderson, H.R. (2009). Air pollution and mortality: A history. Atmospheric Environment. Vol. 43. Pp. 142-152. doi: 10.1016/j.atmosenv.2008.09.026.

Andreae, M.O., Jones, C.D., and Cox, P.M. (2005). Strong present-day aerosol cooling implies a hot future. Nature. Vol. 435. Pp.1187-1190.

Bell, M.L. and Davis, D.L. (2001). Reassessment of the lethal London Fog of 1952: novel indicatiors of acute and Chronic consequences of acute exposure to air pollution. Environmental Health Perspective. Vol. 109. Pp. 389-394.

Biasutti, M. and Giannini, A. (2006). Robust Sahel drying in response to late 20th century forcings. Geophysical Research Letters. Vol. 33. L11706. doi: 10.1029/2006GL026067.

Bond, T.C. et al. (2013). Bounding the role of black carbon in the climate system: a scientific assessment. Journal of Geophysical Research. Vol. 118. Pp. 5380-5552. doi: 10.1002/jgrd.50171.

Burpee, R.W. (1972). The origin and structure of easterly waves in the lower troposphere of North Africa. Journal of the Atmospheric Sciences. Vol. 29. Pp. 77-90.

Byrne, M.P. and O'Gorman, P.A. (2013). Link between land-ocean warming contrast and surface relative humidities in simulations with coupled climate models. Geophysical Research Letters. Vol. 40. Pp. 5223-5227. doi: 10.1002/grl.50971.

Chang, C.-Y. et al. (2011). Sulfate aerosol control of tropical Atlantic climate over the twentieth century. Journal of Climate. Vol. 24. Pp. 2540-2555. doi: 10.1175/2010JCLI4965.1.

Charlson, R.J. and Pilat, M.J. (1969). Climate: the influence of aerosols. Journal of Applied Meteorology. Vol. 8. Pp. 1001-1002.

Chen, G. et al. (2011). Observations of Saharan dust microphysical and optical properties from the Eastern Atlantic during NAMMA airborne field campaign. Atmospheric Chemistry and Physics. Vol. 11. Pp. 723-740. doi: 10.5194/acp-11-723-2011.

Chiang, J.C.J., Kushnir, Y., and Giannini, A. (2002). Deconstructing Atlantic Intertropical Convergence Zone variability: Influence of the local cross-equatorial sea surface temperature gradient and remote forcing from the eastern equatorial Pacific. Journal of Geophysical Research. Vol. 107. doi: 10.1029/2000JD000307.

Chin, M. et al. (2000). Atmospheric sulfur cycle simulated in the global model GOCART: Model description and global properties. Journal of Geophysical Research. Vol. 105. Pp. 24671-24687.

Chin, M. et al. (2002). Tropospheric aerosol optical thickness from the GOCART model and comparisons with satellite and sun photometer measurements. Journal of the Atmospheric Sciences. Vol. 59. Pp. 461-483.

Chin, M. et al. (2014). Multi-decadal aerosol variations from 1980 to 2009: a perspective from observations and a global model. Atmospheric Chemistry and Physics. Vol. 14. Pp. 3657-3690. doi:10.5194/acp-14-3657-2014.

Coakley, J.A., Cess, R.D., and Yurevich, F.B. (1983). The effect of tropospheric aerosols on the Earth's radiation budget: a parameterization for climate models. Journal of the Atmospheric Sciences. Vol. 40. Pp. 116-138.

Coakley, J.A., Bernstein, R.L., and Durkee, P.A. (1987). Effect of ship-stack effluents on cloud reflectivity. Science. Vol. 237. Pp. 1020-1022. doi: 10.1126/science.237.4818.1020.

Coakley, J.A. (2003). Reflectance and albedo, surface. In *Encyclopedia of Atmospheric Sciences*. Holton, Curry, and Pyle (Eds.). Academic Press. pp. 1914-1923.

Cook, K.H. (1999). Generation of the African Easterly Jet and its role in determining West African precipitation, Journal of Climate. Vol. 12. Pp. 1165-1184.

Cook, K.H. and Vizy, E.K. (2015). Detection and analysis of an amplified warming of the Sahara desert. Journal of Climate. Vol. 28. Pp.6560-6580. doi: 10.1175/JCLI-D-14-00230.1.

de Meij, A., Pozzer, A., and Lelieveld, J. (2012). Trend analysis in aerosol optical depths and pollutant emission estimates between 2000 and 2009. Atmospheric Environment. Vol. 51. Pp. 75-85. doi: 10.1016/j.atmosenv.2012.01.059.

Delany, A.C. et al. (1967). Airborne dust collected at Barbados. Geochimica et Cosmochimica Acta. Vol. 31. Pp. 885-909.

Deuzé, J.L. et al. (1999). Characterization of aerosols over ocean from POLDER/ADEOS-1. Geophysical Research Letters. Vol. 26. Pp. 1421-1424.

Diehl, T. et al. (2012). Anthropogenic, biomass burning, and volcanic emissions of black carbon, organic carbon, and SO_2 from 1980 to 2010 for hindcast model experiments. Atmospheric Chemistry and Physics Discussions. Vol. 12. Pp. 24895-24954. doi:10.5194/acpd-12-24895-2012.

Dong, B. and Sutton, R. (2015). Dominant role of greenhouse-gas forcing in the recovery of Sahel rainfall. Nature Climate Change. Vol. 5. Pp. 757-760. doi: 10.1038/NCLIMATE2664.

Dubovik, O. and King, M.D. (2000). A flexible inversion algorithm for retrieval of aerosol optical properties from Sun and sky radiance measurements. Journal of Geophysical Research. Vol. 105. Pp. 20673-20696.

Dubovik, O. et al. (2002). Non-spherical aerosol retrieval method employing light scattering by spheroids. Geophysical Research Letters. Vol. 29. doi: 10.1029/2001GL014506.

Dunstone, N.J. et al. (2013). Anthropogenic aerosol forcing of Atlantic tropical storms. Nature Geoscience. Vol. 6. Pp. 534-539. doi: 10.1038.NGEO1845.

Engel-Cox, J.A., Holloman, C.H., Coutant, B.W., and Hoff, R.M. (2004). Qualitative and quantitative evaluation of MODIS satellite sensor data for regional and urban scale air quality. Atmospheric Environment. Vol. 38. Pp. 2495-2509.

Fan, J. et al. (2013). Microphysical effects determine macrophysical response for aerosol impacts on deep convective clouds. Proceedings of the National Academy of Sciences. Vol. 110. Pp. E4581-4590. doi: 10.1073/pnas.1316830110.

Feingold, G., Remer, L.A., Ramaprasad, J., and Kaufman, Y.J. (2001). Analysis of smoke impacts on clouds in Brazilian biomass burning regions: An extension of Twomey's approach. Journal of Geophysical Research. Vol. 106. Pp. 22907-22922.

Feingold, G., Eberhard, W.L., Veron, D.E., and Previdi, M. (2003). First measurements of the Twomey indirect effect using ground-based remote sensors. Geophysical Research Letters. Vol. 30. doi: 10.1029/2002GL016633.

Feingold, G. and Siebert, H. (2009). "Cloud-Aerosol Interactions from the Micro to the Cloud Scale". *Clouds in the Perturbed Climate System: Their Relationship to Energy Balance, Atmospheric Dynamics, and Precipitation.* Ed. Heintzenberg, J. and Charlson, R.J. Strungmann Forum Reports. MIT Press. Book. ISBN: 0-262-01287-1. Ch. 14. Pp. 319-338.

Gan, C.-M. et al. (2014). Assessment of the effect of air pollution controls on trens in shortwave radiation over the United States from 1995 through 2010 from multiple observation networks. Atmospheric Chemistry and Physics. Vol. 14. Pp. 1701-1715. doi: 10.5194/acp-14-1701-2014.

Gerier, E.B. et al. (2003). CERES Data Management System: Single Satellite Footprint TOA/Surface Fluxes and Clouds (SSF) Collection Document, Release 2, Version 1.

Ghan, S.J., Guzman, G., and Abdul-Razzak, H. (1998). Competition between sea salt and sulfate particles as cloud condensation nuclei. Journal of the Atmospheric Sciences. Vol, 55. Pp. 3340-3347.

Giannini, A. (2015). Climate change comes to the Sahel. Nature Climate Change. Vol. 5. Pp. 720-721.

Ginoux, P. et al. (2001). Sources and distributions of dust aerosols simulated with the GOCART model. Journal of Geophysical Research. Vol. 106. Pp. 20255-20273.

Gold, D.R. et al. (1999). Particulate and ozone pollutant effects on the respiratory function of children in southwest Mexico City. Epidemiology. Vol. 10. Pp. 8-16.

Grandey, B.S. and Stier, P. (2010). A critical look at spatial scale choices in satellite-based aerosol indirect effect studies. Atmospheric Chemistry and Physics. Vol. 10. Pp. 11459-11470. doi: 10.5194/acp-10-11459-2010.

Green, R.N. et al. (1997). Clouds and the Earth's Radiant Energy System (CERES) Algorithm Theoretical Basis Document, CERES Inversion to Instantaneous TOA Fluxes (Subsystem 4.5), release 2.2.

Green, M., Kondragunta, S., Ciren, P., and Xu, C. (2009). Comparison of GOES and MODIS aerosol optical depth (AOD) to Aerosol Robotic Network (AERONET) AOD

and IMPROVE $PM_{2.5}$ mass at Bondville, Illinois. Journal of the Air and Waste Management Association. Vol. 59. Pp. 1082-1091. doi: 10.3155/1047-3289.59.9.1082.

Guenther, A. et al. (1995). A global model of natural volatile organic compound emissions. Journal of Geophysical Research. Vol. 100. Pp. 8873-8892.

Haagen-Smit, A.J. (1952). Chemistry and physiology of Los Angeles Smog. Industrial and Engineering Chemistry. Vol. 44. Pp. 1342-1346.

Hall, N.M.J., Kiladis, G.N., and Thorncroft, C.D. (2006). Three-dimensional structure and dynamics of African easterly waves. Part II: Dynamical modes. Journal of the Atmospheric Sciences. Vol. 63. Pp. 2231-2245.

Hand, J.L. et al. (2012). Seasonal composition of remote and urban fine particulate matter in the United States. Journal of Geophysical Research. Vol. 117. D05209. doi: 10.1029/2011JD017122.

Haywood, J.M. and Shine, K.P. (1995). The effect of anthropogenic sulfate and soot aerosol on the clear sky planetary radiation budget. Geophysical Research Letters. Vol. 22. Pp. 603-606.

He, H. et al. (2013). Trends in emissions and concentrations of air pollutants in the lower troposphere in the Baltimore/Washington airshed from 1997 to 2011. Atmospheric Chemistry and Physics. Vol. 13. Pp. 7859-7874. doi: 10.5194/acp-13-7859-2013.

He, H., Vinnikov, K.Y., Li, C., Krotkov, N.A., Jongeward, A.R., Li, Z., Stehr, J.W., Hains, J.C., and Dickerson, R.R. (2016). Response of SO_2 and particulate air pollution to local and regional emission controls: a case study in Maryland. Earth's Future. Vol. 4. doi: 10.1002/2015EF000330.

Hidy, G.M., Mueller, P.K., and Tong, E.Y. (1975). Summary of the California aerosol characterization experiment. Journal of the Air Pollution Control Association. Vol. 25. Pp. 1106-1114.

Hinds, W.C. (1999). Aerosol Technology: Properties, Behavior, and Measurement of Airborne Particles. Wiley-Interscience, 1999, New York, USA. Book. ISBN: 0-471-19410-7.

Hoff, R.M. and Christopher, S.A. (2009). Remote sensing of particulate pollution from space: have we reached the promised land? Journal of the Air and Waste Management Association. Vol. 59. Pp. 645-675. doi: 10.3155/1047-3289.59.6.645.

Holben, B.N. et al. (1998). AERONET – A federated instrument network and data archive for aerosol characterization. Remote Sensing of Environment. Vol. 66. Pp. 1-16.

Holben, B.N. et al. (2006). AERONET's Version 2.0 quality assurance criteria. Proceedings of SPIE. Vol. 6408. Remote Sensing of the Atmosphere and Clouds. 64080Q. doi:10.1117/12.706524.

Holton, J.R. (2004). An Introduction to Dynamic Meteorology (4th ed.). Elsevier Academic Press. Burlington, MA.

Hsu, N.C. et al. (2012). Global and regional trends of aerosol optical depth over land and ocean using SeaWiFS measurements from 1997 to 2010. Atmospheric Chemistry and Physics. Vol. 12. Pp. 8037-8053. doi: 10.5194/acp-12-8037-2012.

Hubanks, P., Platnick, S., King, M., and Ridgway, B. (2015). MODIS Atmosphere L3 Gridded Product Algorithm Theoretical Basis Document (ATBD) & Users Guide. Collection 006, Version 3.2. ATBD Reference Number: ATBD-MOD-30. Available online: http://modis-atmos.gsfc.nasa.gov/MOD08_M3/atbd.html. 119 pages.

IPCC. (2013). Climate Change 2013: The Physical Science Basis. Cambridge University Press. 1535 pg. doi: 10.1017/CBO9781107415324.

Jackson, J.M. et al. (2013). Suomi-NPP VIIRS aerosol algorithms and data products. Journal of Geophysical Research. Vol. 118. Pp. 12673-12689. doi: 10.1002/2013JD020449.

Jones, C., Mahowald, N., and Lou, C. (2003). The role of easterly waves on African desert dust transport. Journal of Climate. Vol. 16. Pp. 3617-3628.

Jongeward, A., Li, Z., He, H., and Xiong, X. (2016). Natural and anthropogenic aerosol trends from satellite and surface observations and model simulations over the North Atlantic Ocean from 2002 to 2012. Journal of the Atmospheric Sciences. doi:10.1175/JAS-D-15-0308.1. in press.

Junge, C.E. and Manson, J.E. (1961). Stratospheric aerosol studies. Journal of Geophysical Research. Vol. 66. Pp. 2163-2182.

Kahn, R.A. et al. (2005). Multiangle Imaging Spectroradiometer (MISR) global aerosol optical depth validation based on 2 years of coincident Aerosol Robotic Network (AERONET) observations. Journal of Geophysical Research. Vol. 110. D10S04. doi: 10.1029/2004JD004706.

Kaufman, Y.J., Tanré, D., and Boucher, O. (2002). A satellite view of aerosols in the climate system. Nature. Vol. 419. Pp. 215-223.

Kaufman, Y.J. et al. (2005a). Dust transport and deposition observed from the Terra-Moderate Resolution Imaging Spectroradiometer (MODIS) spacecraft over the Atlantic Ocean. Journal of Geophysical Research. Vol. 110. D10S12. doi:10.1029/2003JD004436.

Kaufman, Y.J. et al. (2005b). Aerosol anthropogenic component estimated from satellite data. Geophysical Research Letters. Vol. 32. L17804. doi:10.1029/2005GL023125.

King, M.D., Herring, D.D., and Diner, D.J. (1995). The Earth Observing System: a space-based program for assessing mankind's impact on the global environment. Optics and Photonic News. Vol. 6. Pp. 34-39.

King, M.D. et al. (1997). Cloud retrieval algorithms for MODIS: Optical thickness, effective particle radius, and thermodynamic phase. MODIS Algorithm Theoretical Basis Document No. ATBD-MOD-05. Version 5. Available online: https://modis.gsfc.nasa.gov/data/atbd/atmos_atbd.php. 79 pages.

King, M.D., Kaufman, Y.J., Tanré, D., and Nakajima, T. (1999). Remote sensing of tropospheric aerosols from space: past, present, and future. Bulletin of American Meteorological Society. Vol. 80. Pp. 2229-2259.

King, M.D. et al. (2003). Clouds and aerosol properties, precipitable water, and profiles of temperature and water vapor from MODIS. IEEE Transactions on Geoscience and Remote Sensing. Vol. 41. Pp. 442-458.

Knippertz, P. and Todd, M.C. (2010). The central west Saharan dust hot spot and its relation to African easterly waves and extratropical disturbances. Journal of Geophysical Research. Vol. 115. D12117. doi: 10.1029/2009JD012819.

Köhler, H. (1936). The nucleus in and the growth of hygroscopic droplets. Transactions of the Faraday Society. Vol. 32. Pp. 1152-1161. doi: 10.1039/TF9363201152.

Koren, I. et al. (2005). Aerosol invigoration and restructuring of Atlantic convective clouds. Geophysical Research Letters. Vol. 32. L14828. doi: 10.1029/2005GL023187.

Koren, I. et al. (2010). Aerosol-induced changes of convective cloud anvils produce strong climate warming. Atmospheric Chemistry and Physics. Vol. 10. Pp. 5001-5010. doi: 10.5194/acp-10-5001-2010.

Kuo, H.-L. (1949). Dynamic instability of two-dimensional nondivergent flow in a barotropic atmosphere. Journal of Meteorology. Vol. 6. Pp. 105-122.

Kvalevåg, M.M. and Myhre, G. (2007). Human impact on direct and diffuse solar radiation during the industrial era. Journal of Climate. Vol. 20. Pp. 4874-4883. doi: 10.1175/JCLI4277.1.

Lamarque, J.-F. et al. (2010). Historical (1850-2000) gridded anthropogenic and biomass burning emissions of reactive gases and aerosols: methodology and application. Atmospheric Chemistry and Physics. Vol. 10. Pp. 7017-7039. doi: 10.5194/acp-10-7017-2010.

Lana, A. et al. (2011). An updated climatology of surface dimethylsulfide concentrations and emissions fluxes in the global ocean. Global Biogeochemical Cycles. Vol. 25. GB1004. doi:10.1029/2010GB003850.

Lavaysse, C. et al. (2009). Seasonal evolution of the West African heat low: a climatological perspective. Climate Dynamics. Vol. 33. Pp. 313-330. doi: 10.1007/s00382-009-0553-4.

Lee, K.H., Li, Z., Kim, Y.J, and Kokhanovsky, A. (2009). "Atmospheric aerosol monitoring from satellite observations: A history of three decades". *Atmospheric and Biological Environmental Monitoring*. Ed. Kim, Y.J. et al. Springer Netherlands. Book. ISBN: 978-1-4020-9673-0. Pp. 13-38. doi: 10.1007/978-1-4020-9674-7.

Leibensperger, E.M. et al. (2012). Climatic effects of 1950-2050 changes in US anthropogenic aerosols – Part 1: aerosol trends and radiative forcing. Atmospheric Chemistry and Physics. Vol. 12. Pp. 3333-3348. doi: 10.5194/acp-12/3333/2012.

Levy, R.C. et al. (2009). Algorithm for remote sensing of tropospheric aerosol over dark targets from MODIS: Collections 005 and 051: Revision 2. Feb. 2009. MODIS Algorithm Theoretical Basis Document.

Levy, R.C. et al. (2010). Global evaluation of the collection 5 MODIS dark-target aerosol products over land. Atmospheric Chemistry and Physics. Vol. 10. Pp. 10399-10420. doi:10.5194/acp-10-10399-2010.

Levy, R.C. et al. (2013). The Collection 6 MODIS aerosol products over land and ocean. Atmospheric Measurement Techniques. Vol. 6. Pp. 2989-3034. doi:10.5194/amt-6-2989-2013.

Li, J., Carlson, B.E., Dubovik, O., and Lacis, A.A. (2014). Recent trends in aerosol optical properties derived from AERONET measurements. Atmospheric Chemistry and Physics. Vol. 14. Pp. 12271-12289. doi: 10.5194/acp-14-12271-2014.

Li, Z. et al. (2009). Uncertainties in satellite remote sensing of aerosols and impact on monitoring its long-term trend: a review and perspective. Annales Geophysicae. Vol. 27. Pp. 2755-2770.

Li, Z. et al. (2011). Long-term impacts of aerosols on the vertical development of clouds and precipitation. Nature Geoscience. Vol. 4. Pp. 888-894. doi: 10.1038/ngeo1313.

Li, Z. et al. (2016). Aerosol and monsoon climate interactions over Asia. Reviews of Geophysics. Vol. 54. doi: 10.1002/2015RG000500.

Liou, K.N. (2002). An Introduction to Atmospheric Radiation. 2nd Ed. Academic Press. 2002, San Diego, CA, USA. Book. ISBN: 0-12-451451-0.

Loeb, N.G. and Manalo-Smith, N. (2005). Top-of-atmosphere direct radiative effect of aerosols over global oceans from merged CERES and MODIS observations. Journal of Climate. Vol. 18. Pp. 3506-3526.

Lohmann, U. and Feichter, J. (2005). Global indirect aerosol effects: a review. Atmospheric Chemistry and Physics. Vol. 5. Pp. 715-737.

Mahowald, N.M. et al. (2010). Observed 20th century desert dust variability: impact on climate and biogeochemistry. Atmospheric Chemistry and Physics. Vol. 10. Pp. 10875-10893. doi: 10.5194/acp-10-10875-2010.

Malm, W.C. et al. (1994). Spatial and seasonal trends in particle concentration and optical extinction in the United States. Journal of Geophysical Research. Vol. 99. Pp. 1347-1370.

McComiskey, A. and Feingold, G. (2008). Quantifying error in the radiative forcing of the first aerosol indirect effect. Vol. 35. L02810. doi: 10.1029/2007GL032667.

McComiskey, A. et al. (2009). An assessment of aerosol-cloud interactions in marine stratus clouds based on surface remote sensing. Journal of Geophysical Research. Vol. 114. D09203. doi: 10.1029/2008JD011006.

McComiskey, A. and Feingold, G. (2012). The scale problem in quantifying aerosol indirect effects. Atmospheric Chemistry and Physics. Vol. 12. Pp. 1031-1049. doi: 10.5194/acp-12-1031-2012.

McCormick, M.P. et al. (1979). Satellite studies of the stratospheric aerosol. Bulletin of the American Meteorological Society. Vol. 60. Pp. 1038-1046.

Ming, Y. and Ramaswamy, V. (2009). Nonlinear climate and hydrological responses to aerosol effects. Journal of Climate. Vol. 22. Pp. 1329-1339. doi: 10.1175/2008JCLI2362.1.

Mishchenko, M.I. and Geogdzhayev, I.V. (2007). Satellite remote sensing reveals regional tropospheric aerosol trends. Optics Express. Vol. 15. Pp. 7423-7438.

Mishchenko, M.I. et al. (2007). Long-term satellite record reveals likely recent aerosol trend. Science. Vol. 315. Pp. 1543.

Mishchenko, M.I. et al. (2012). Aerosol retrievals from channel-1 and -2 AVHRR radiances: long-term trends updated and revisited. Journal of Quantitative Spectroscopy and Radiative Transfer. Vol. 113. Pp. 1974-1980. doi: 10.1016/j.jqsrt.2012.05.006.

Nakajima, T., Higurashi, A., Kawamoto, K., and Penner, J.E. (2001). A possible correlation between satellite-derived cloud and aerosol microphysical parameters. Geophysical Research Letters. Vol. 28. Pp. 1171-1174.

Nemery, B., Hoet, P.H.M., and Nemmar, A. (2001). The Meuse Valley fog of 1930: an air pollution disaster. The Lancet. Vol. 357. Pp. 704-708.

Ostrenga, D. (2010). README Document for MERRA Data Products. NASA Goddard Earth Sciences Data and Information Services Center (GES DISC). Last Revised: 4/11/2012. 58 pages.

Petty, G.W. (2006). A First Course in Atmospheric Radiation. 2nd Ed. Sundog Publishing. 2006, Madison, WI, USA. Book. ISBN: 0-972-90331-3.

Pitchford, M.L., Poirot, R.L., Schichtel, B.A., and Malm, W.C. (2009). Characterization of the winter Midwestern particulate nitrate bulge. Journal of the Air and Waste Management Association. Vol. 59. Pp. 1061-1069. doi: 10.3155/1047-3289.59.9.1061.

Platnick, S. et al. (2015). MODIS Cloud Optical Properties: User Guide for the Collection 6 Level-2 MOD06/MYD06 Product and Associated Level-3 Datasets. Version 1. 145 pages.

Prospero, J.M. et al. (1983). The atmospheric aerosol system: an overview. Reviews of Geophysics and Space Physics. Vol. 21. Pp. 1607-1629.

Prospero, J.M. and Lamb, P.J. (2003). African droughts and dust transport to the Caribbean: Climate change implications. Science. Vol. 302. Pp. 1024-1027. doi: 10.1126/science.1089915.

Pruppacher, H.R. and Klett, J.D. (1978). Microphysics of Clouds and Precipitation. D. Reidel Publishing Company. Dordrecht, Holland. Book. ISBN: 90-277-0515-1.

Pytharoulis, I. and Thorncroft, C. (1999). The low-level structure of African easterly waves in 1995. Monthly Weather Review. Vol. 127. Pp. 2266-2280.

Remer, L.A. et al. (2005). The MODIS aerosol algorithm, products, and validation. Journal of the Atmospheric Sciences. Vol. 62. Pp. 947-973.

Remer, L.A. and Kaufman, Y.J. (2006). Aerosol direct radiative effect at the top of the atmosphere over cloud free ocean derived from four years of MODIS data. Atmospheric Chemistry and Physics. Vol. 6. Pp. 237-253. doi: 10.5194/acp-6-237-2006.

Remer, L.A. et al. (2008). Global aerosol climatology from the MODIS satellite sensors. Journal of Geophysical Research. Vol. 113. D14S07. doi: 10.1029/2007JD009661.

Renard, J.J., Calidonna, S.E., and Henley, M.V. (2004). Fate of ammonia in the atmosphere – a review for applicability to hazardous releases. Journal of Hazardous Materials. Vol. B108. Pp. 29-60.

Ricchiazzi, P., Yang, S., Gautier, C., and Sowle, D. (1998). SBDART: A research and teaching software tool for plane-parallel radiative transfer in the Earth's atmosphere. Bulletin of the American Meteorological Society. Vol. 79. Pp. 2101-2114.

Ricchiazzi, P. (2002). Input documentation for SBDART (summer 2002 release). SBDART Read-Me. Institute for Computational Earth System Science. U. California - SB. Prepared by Paul Ricchiazzi. 43 pages.

Rienecker, M.M. et al. (2008). The GEOS-5 data assimilation system – Documentation of versions 5.0.1, 5.1.0, and 5.2.0. NASA Technical Report Series on Global Modeling and Data Assimilation, NASA/TM-2008-104606. Vol. 27. 92 pages.

Rienecker, M.M. et al. (2011). MERRA: NASA's Modern-Era Retrospective Analysis for Research and Applications. Journal of Climate. Vol. 24. Pp. 3624-3648. doi:10.1175/JCLI-D-0015.1.

Rodríguez, S. et al. (2015). Modulation of Saharan dust export by the North African dipole. Atmospheric Chemistry and Physics. Vol. 15. Pp. 7471-7486. doi: 10.5194/acp-15-7471-2015.

Rogers, R.R. and Yao, M.K. (1989). A Short Course in Cloud Physics. 3rd Ed. Butterworth-Heinemann. 1989, Oxford, U.K. Book. ISBN: 0-750-63215-1.

Rosenfeld, D. et al. (2008). Flood or drought: how do aerosols affect precipitation? Science. Vol. 321. Pp. 1309-1313. doi: 10.1126/science.1160606.

Ruckstuhl, C. et al. (2008). Aerosol and cloud effects on solar brightening and the recent rapid warming. Geophysical Research Letters. Vol. 35. L12708. doi: 10.1029/2008GL034228.

Salomonson, V.V., Barnes, W., and Masuoka, E.J. (2006). "Introduction to MODIS and an overview of associated activities". *Earth Science Satellite Remote Sensing: Science and Instruments Vol. 1*. Ed. Qu, J.J. et al. Springer New York, USA. Book. ISBN: 3-540-35606-1.

Sato, M., Hansen, J.E., McCormik, M.P., and Pollack, J.B. (1993). Stratospheric aerosol optical depths, 1850-1990. Journal of Geophysical Research. Vol. 98. Pp. 22987-22994.

Seinfeld, J.H. (1986). Atmospheric Chemistry and Physics of Air Pollution. Wiley-Interscience, 1986, New York, USA. Book. ISBN: 0-471-82857-2.

Seinfeld, J.H. (2004). Air pollution: a half century of progress. Environmental and Energy Engineering. Vol. 50. Pp. 1096-1108. doi: 10.1002/aic.10102.

Shaw, G.E. (1983). Sun Photometry. Bulletin of the American Meteorological Society. Vol. 64. Pp. 4-10.

Skinner, C.B. and Diffenbaugh, N.S. (2014). Projected changes in African easterly wave intensity and track in response to greenhouse forcing. Proceedings of the National Academy of Sciences. Vol. 111. No 19. Pp. 6882-6887. doi: 10.1073/pnas.1319597111.

Smirnov, A. et al. (2003). Effect of wind speed on columnar aerosol optical properties at Midway Island. Journal of Geophysical Research. Vol. 108. 4802. doi:10.1029/2003JD003879.

Smith, S.J. et al. (2011). Anthropogenic sulfur dioxide emissions: 1850-2005. Atmospheric Chemistry and Physics. Vol. 11. Pp. 1101-1116. doi: 10.5194/acp-11-1101-2011.

Stevens, G.L. (1978). Radiation profiles in extended water clouds. II: Parameterization schemes. Journal of the Atmospheric Sciences. Vol. 35. Pp. 2124-2132.

Stowe, L.L., Ignatov, A.M., and Singh, R.R. (1997). Development, validation, and potential enhancements to the second-generation operational aerosol product at the National Environmental Satellite, Data, and Information Service of the National Oceanic and Atmospheric Administration. Journal of Geophysical Research. Vol. 102. Pp. 16923-16934.

Streets, D.G., Wu, Y., and Chin, M. (2006). Two-decadal aerosol trends as a likely explanation of the global dimming/brightening transition. Geophysical Research Letters. Vol. 33. L15806. doi: 10.1029/2006GL026471.

Streets, D.G. et al. (2009). Anthropogenic and natural contributions to regional trends in aerosol optical depth, 1980-2006. Journal of Geophysical Research. Vol. 114. D00D18. doi: 10.1029/2008JD011624.

Su, W. et al. (2010). An estimate of aerosol indirect effect from satellite measurements with concurrent meteorological analysis. Journal of Geophysical Research. Vol. 115. D18219. doi: 10.1029/2010JD013948.

Su, W. et al. (2013). Global all-sky shortwave direct radiative forcing of anthropogenic aerosols from combined satellite observations and GOCART simulations. Journal of Geophysical Research. Vol. 118. Pp. 655-669. doi: 10.1029/2012JD018294.

Sutton, R.T., Dong, B., and Gregory, J.M. (2007). Land/sea warming ratio in response to climate change: IPCC AR4 model results and comparison with observations. Geophysical Research Letters. Vol. 34. L02701. doi: 10.1029/2006GL028164.

Thorncroft, C.D. and Blackburn, M. (1999). Maintenance of the African easterly jet. Quarterly Journal of the Royal Meteorological Society. Vol. 125. Pp. 763-786.

Twomey, S. (1974). Pollution and the planetary albedo. Atmospheric Environment. Vol. 8. Pp. 1251-1256.

Twomey, S. (1977). The influence of pollution on the shortwave albedo of clouds. Journal of the Atmospheric Sciences. Vol. 34. Pp. 1149-1152.

U.S. EPA. (2004a). Air quality criteria for particulate matter. Vol. 1, U.S. Environmental Protection Agency Final Rep. EPA 600/P-99/002aF. 900 pp. [Available online at https://cfpub2.epa.gov/ncea/risk/recordisplay.cfm?deid=87903.]

U.S. EPA. (2004b). Air quality criteria for particulate matter. Vol. 2, U.S. Environmental Protection Agency Final Rep. EPA 600/P-99/002bF. 1148 pp. [Available online at https://cfpub2.epa.gov/ncea/risk/recordisplay.cfm?deid=87903.]

Volz, F.E. (1969). Sum results of turbidity networks. Tellus. Vol. 21. Pp. 625-630.

von Storch, H. and Zwiers, F.W. (1999). Statistical analysis in climate research. Cambridge University Press. London, United Kingdom.

Wang, C. et al. (2012). Multidecadal covariability of North Atlantic sea surface temperature, African dust, Sahel rainfall, and Atlantic Hurricanes. Journal of Climate. Vol. 25. Pp. 5404-5415. doi: 10.1175/JCLI-D-11-00413.1.

Wang, J. and Christopher, S.A. (2003). Intercomparison between satellite-derived aerosol optical thickness and $PM_{2.5}$ mass: implications for air quality studies. Geophysical Research Letters. Vol. 30. doi: 10.1029/2003GL018174.

Wang, Y. et al. (2011). Long-term impacts of aerosols on precipitation and lightning over the Pearl River Delta megacity area in China. Atmospheric Chemistry and Physics. Vol. 11. Pp. 12421-12436. doi: 10.5194/acp-11-12421-2011.

Wang, Y., Khalizov, A., Levy, M., and Zhang, R. (2013). New directions: light absorbing aerosols and their atmospheric impacts. Atmospheric Environment. Vol. 81. Pp. 713-715. doi: 10.1016/j.atmosenv.2013.09.034.

Weber, S.A. et al. (2010). An improved method for estimating surface fine particle concentrations using seasonally adjusted satellite aerosol optical depth. Journal of the Air and Waste Management Association. Vol. 60. Pp. 574-585. doi: 10.3155/1047-3289.60.5.574.

Wielicki, B.A. et al. (1996). Clouds and the Earth's Radiant Energy System (CERES): An Earth Observing System Experiment. Bulletin of the American Meteorological Society. Vol. 77. Pp. 853-868.

Wielicki, B.A. et al. (1997). Clouds and the Earth's Radiant Energy System (CERES) Algorithm Theoretical Basis Document, Overview of Cloud Retrieval and Radiative Flux Inversion (Subsystem 4.0), release 2.2.

Wild, M. et al. (2005). From dimming to brightening: decadal changes in solar radiation at Earth's surface. Science. Vol. 308. Pp. 847-850.

Wild, M., Ohmura, A., and Makowski, K. (2007). Impact of global dimming and brightening on global warming. Geophysical Research Letters. Vol. 34. L04702. doi: 10.1029/2006GL028031.

Wild, M. (2012). Enlightening global dimming and brightening. Bulletin of the American Meteorological Society. Vol. 93. Pp. 27-37. doi: 10.1175/BAMS-D-11-00074.1.

Winker, D.M. et al. (2009). Overview of the CALIPSO mission and CALIOP data processing algorithms. Journal of Atmospheric and Oceanic Technology. Vol. 26. Pp. 2310-2323. doi: 10.1175/2009JTECHA1281.1.

Wu, M.-L. C. et al. (2009). African easterly jet: Structure and maintenance, Journal of Climate. Vol. 22. Pp. 4459-4480. doi:10.1175/2009JCLI2584.1.

Wu, M.-L. C. et al. (2012). African easterly jet: barotropic instability, waves, and cyclogenesis. Journal of Climate. Vol. 25. Pp. 1489-1510. doi: 10.1175/2011JCLI4241.1.

Xing, J. et al. (2013). Historical gaseous and primary aerosol emissions in the United States from 1990 to 2010. Atmospheric Chemistry and Physics. Vol. 13. Pp. 7531-7549. doi: 10.5194/acp-13-7531-2013.

Xiong, X., Wenny, B.N., and Barnes, W.L. (2009). Overview of NASA Earth Observing Systems Terra and Aqua moderate resolution imaging spectroradiometer instrument calibration algorithms and on-orbit performance. Journal of Applied Remote Sensing. Vol. 3. 032501. doi:10.1117/1.3180864.

Young, D.F. et al. (1997). Clouds and the Earth's Radiant Energy System (CERES) Algorithm Theoretical Basis Document, ERBE-like Averaging to Monthly TOA Fluxes (Subsystem 3.0), release 2.2.

Yan, H. et al. (2014). Long-term aerosol-mediated changes in cloud radiative forcing of deep clouds at the top and bottom of the atmosphere over the Southern Great Plains.

Atmospheric Chemistry and Physics. Vol. 14. Pp. 7113-7124. doi: 10.5194/acp-14-7113-2014.

Yu, H. et al. (2006). A review of measurement-based assessments of the aerosol direct radiative effect and forcing. Atmospheric Chemistry and Physics. Vol. 6. Pp. 613-666.

Yu, H. et al. (2013). A multimodel assessment of the influence of regional anthropogenic emission reductions on aerosol direct radiative forcing and the role of intercontinental transport. Journal of Geophysical Research. Vol. 118. Pp. 700-720. doi: 10.1029/2012JD018148.

Yu, H. et al. (2015). Quantification of trans-Atlantic dust transport from seven-year (2007-2013) record of CALIPSO lidar measurements. Remote Sensing of Environment. Vol. 159. Pp. 232-249. doi:10.1016/j.rse.2014.12.010.

Yuan, T., Li, Z., Zhang, R., and Fan, J. (2008). Increase of cloud droplet size with aerosol optical depth: an observation and modeling study. Journal of Geophysical Research. Vol. 113. D04201. doi: 10.1029/2007JD008632.

Zhang, J. and Reid, J.S. (2010). A decadal regional and global trend analysis of the aerosol optical depth using a data-assimilation grade over-water MODIS and Level 2 MISR aerosol products. Atmospheric Chemistry and Physics. Vol. 10. Pp. 10949-10963. doi: 10.5194/acp-10-10949-2010.

Zhao, T.X.-P. et al. (2008a). Study of long-term trend in aerosol optical thickness observed from operational AVHRR satellite instrument. Journal of Geophysical Research. Vol. 113. D07201. doi: 10.1029/2007JD009061.

Zhao, T.X.-P. et al. (2008b). Derivation of component aerosol direct radiative forcing at the top of atmosphere for clear-sky oceans. Journal of Quantitative Spectroscopy and Radiative Transfer. Vol. 109. Pp. 1162-1186. doi: 10.1016/j.jqsrt.2007.10.1006.

Zhao, T.X.-P., Chan, P.K., and Heidinger, A.K. (2013). A global survey of the effect of cloud contamination on the aerosol optical thickness and its long-term trend derived from operational AVHRR satellite observations. Journal of Geophysical Research. Vol. 118. Pp. 2849-2857. doi: 10.1002/jgrd.50278.